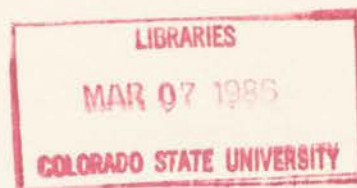


QC852  
C6  
no. 396  
ATSL



MESOSCALE  
BOUNDARY LAYER DEVELOPMENT  
OVER MOUNTAINOUS TERRAIN

David C. Bader

(Principal Investigator: Thomas B. McKee)



Atmospheric Science

PAPER NO.

396

DEPARTMENT OF ATMOSPHERIC SCIENCE  
COLORADO STATE UNIVERSITY  
FORT COLLINS, COLORADO

MESOSCALE BOUNDARY LAYER DEVELOPMENT  
OVER MOUNTAINOUS TERRAIN

by

David C. Bader

Research supported by the  
National Science Foundation  
under Grant ATM83-04328.

(Principal Investigator: Thomas B. McKee)

Department of Atmospheric Science  
Colorado State University  
Fort Collins, Colorado

November 1985

Atmospheric Science Paper No. 396

30852  
CL  
no. 396  
ATSL

ABSTRACT

MESOSCALE BOUNDARY LAYER DEVELOPMENT  
OVER MOUNTAINOUS TERRAIN

The diurnal evolution of the mesoscale boundary layer (~ 50 km) over gently sloping terrain upwind of a high mountain barrier is described using both observational data and results from numerical model simulations. Atmospheric sounding data are presented from two nights, one during the summer and the second during the winter, when the mesoscale nocturnal boundary layer development was observed. Subsequently, a series of two and three-dimensional numerical model experiments are presented which identify the important physical processes responsible for the observed features. A conceptual model of mesoscale boundary layer evolution is then presented that accounts for the principle dynamic mechanisms discerned from analysis of the observational and simulated cases.

Observational data from both nights reveal that the nocturnal boundary layer (NBL) extends 200-500 m above the valley ridgetops and plateaus and cools 1-4 K. Found within this layer are topographically induced thermal winds of  $1-5 \text{ m s}^{-1}$  which either produce mesoscale circulations or influence the prevailing synoptic wind fields. The summer night data reveal that when the prevailing geostrophic wind is less than  $7-10 \text{ m s}^{-1}$  at 500 mb and contains no component into the high barrier, a complete mountain-plain circulation forms over the plateaus

and ridges and down valley winds in the underlying valleys are strong. Contrasted with this is the winter case in which a much stronger geostrophic wind ( $\sim 15 \text{ m s}^{-1}$  at 500 mb) directed into the barrier inhibited the mountain-plain circulation. In this case, there was a wide mesoscale variability in nocturnal boundary layer structure.

One numerical experiment realistically simulated the diurnal evolution of the mesoscale boundary layer through a complete cycle encompassing the evening and morning transition periods. Additional simulations reveal that surface cooling and the shear between low-level thermal flows and the overlying winds produce a 300-500 m deep NBL 3-5 h after sunset. The nocturnal stable layer contains decoupled wind regions and can form a blocked wind region upwind of the barrier. In all cases, the nocturnal thermal wind component was  $4\text{-}5 \text{ m s}^{-1}$  directed away from the barrier. It is also demonstrated that full three-dimensional model configuration are necessary to adequately describe the evolution of three-dimensional boundary layer structure.

## ACKNOWLEDGMENTS

I am very fortunate to have benefitted from the help, guidance and encouragement given by my principal research adviser, Dr. Thomas B. McKee, throughout my graduate research program. His advice and involvement through all aspects of the work presented here as well as his editorial suggestions on early versions of this dissertation were invaluable. I am very grateful for the assistance provided by Mr. Gregory Tripoli with the numerical model and analysis of the model results. The success of this research is due in large part to his unselfish contribution of both time and ideas. I also appreciate the efforts of my co-adviser, Dr. William R. Cotton, who helped in the design of the numerical modeling experiments and provided many suggestions throughout this research endeavor. The criticisms and advice of my graduate committee members, Dr. Richard Johnson and Dr. Jon Peterka, were also valuable in improving the final version of this dissertation.

The contributions of the following individuals are also appreciated. John Kleist participated in all aspects of the data collection and reduction efforts and his ability to overcome instrument and computer problems was invaluable. Keeley Hanson was primarily responsible for the ASCOT 82 data in addition to participating in the field experiment. Nolan Doesken aided in the interpretation of the synoptic data and participated in the CSU 84 field experiment.

Jim Cowie, Mike Weissbluth, Ricky Jackson, Doug Wesley, Paul Wolyn and Cathy McKee all endured the cold during the CSU 84 field experiment. Discussions with Ray Arritt, Dr. Roger Pielke and Craig Tremback have proved enlightening and they have therefore contributed to this research with their ideas.

Finally, a special thanks goes to Odilia Bliss who performed the difficult and time-consuming task of assembling the final version of this dissertation from a disorganized collection of text pages, figures and word-processor files. She also participated in the ASCOT 82 field experiment and helped in the preparation for the CSU 84 experiment.

Judy Sorbie drafted the final versions of many of the figures and Duayne Barnhart provided photographic reproductions of the synoptic weather maps. This research was supported by the National Science Foundation (NSF) under grant ATM83-04328. Numerical model simulations were performed at the National Center for Atmospheric Research, which is sponsored by NSF.

## TABLE OF CONTENTS

<u>Chapter</u>	<u>Page</u>
I. INTRODUCTION.....	1
II. BACKGROUND.....	4
A. Boundary Layers Over Flat Terrain.....	4
1. Diurnal boundary layer evolution over flat terrain..	6
2. Ideal nocturnal boundary layer structure.....	9
3. Non-ideal effects on nocturnal boundary layers.....	13
B. Mesoscale and Local Effects of Mountainous Terrain.....	15
1. Ideal thermal circulations in mountainous terrain...	15
a. Slope winds.....	16
b. Hydrostatic mountain thermal circulations.....	23
2. Non-ideal circulations in mountainous terrain.....	28
III. OBSERVATIONS OF MESOSCALE BOUNDARY LAYER STRUCTURE.....	34
A. Data Collection and Reduction Procedures.....	36
B. ASCOT 82 Experiment.....	38
1. Synoptic weather conditions.....	38
2. ASCOT 82 observations.....	52
3. Analysis of observations.....	63
C. CSU 84 Experiment.....	66
1. Synoptic weather conditions.....	66
2. CSU 84 observations.....	80
a. Ca site data.....	80
b. Meeker site data.....	88
c. Rifle site data.....	97
3. Analysis of observations.....	105
D. Summary of Observational Program.....	109
IV. NUMERICAL MODELING OF MESOSCALE BOUNDARY LAYER EVOLUTION....	111
A. Model Description.....	114
1. Theoretical development of model equations.....	114
2. Finite differences.....	121
3. Model domain.....	121
4. Boundary conditions.....	123
5. Initialization.....	126

TABLE OF CONTENTS (continued)

<u>Chapter</u>	<u>Page</u>
IV. NUMERICAL MODELING OF MESOSCALE BOUNDARY LAYER EVOLUTION continued	
B. Description of Numerical Experiments.....	130
C. Results of Numerical Experiments.....	132
1. Results of sensitivity studies.....	132
a. Effects of turbulence parameterization, dynamic initialization and boundary conditions.....	132
b. Effects of ambient wind field.....	133
2. Simulation of mesoscale boundary layer evolution through a diurnal cycle.....	142
3. Factors affecting nocturnal boundary layer development.....	155
a. Effects of wind speed.....	163
b. Effects of afternoon boundary layer depth.....	173
c. Effects of wind direction.....	179
D. Analysis of Numerical Model Results.....	205
V. CONCEPTUAL MODEL OF MESOSCALE BOUNDARY LAYER EVOLUTION.....	219
VI. CONCLUSIONS AND SUGGESTIONS FOR FUTURE RESEARCH.....	225
A. Conclusions from Research.....	225
B. Suggestions for Future Research.....	228
REFERENCES.....	230
APPENDIX I. Rossby Similarity in the Atmospheric Boundary Layer.....	239
APPENDIX II. Model Sensitivity Experiments.....	244
A. Test of Model Initialization Procedure.....	244
B. Tests of Turbulence Closure.....	246
C. Test of Horizontal Grid Spacing.....	248

## LIST OF SYMBOLS

$\alpha$	-- cross-isobaric wind angle
$\pi$	-- normalized pressure; natural constant
$\rho$	-- dry air density
$\theta$	-- potential temperature
$\Delta$	-- mixing length
A, B, C	-- boundary layer similarity functions
$c_p, c_v$	-- constant pressure and constant volume specific heats of dry air
f	-- Coriolis parameter
$F_r$	-- Froude number
G	-- ground conducted heat flux
g	-- gravitational acceleration
H	-- elevation of model top
h	-- nocturnal boundary layer depth; height of hill or valley depth
$K_M$	-- momentum mixing coefficient
$K_S$	-- scalar mixing coefficient
k	-- von Karmen constant
L	-- Obukov length scale
$z$	-- vertical mixing length
N	-- Brunt Väisälä frequency
p	-- absolute pressure

$q^2$  -- twice turbulent kinetic energy  
 $R$  -- gas constant of dry air; net surface radiative flux  
 $R_i$  -- Richardson number  
 $S$  -- surface heat flux  
 $T$  -- temperature  
 $t$  -- time  
 $u_i$  -- Cartesian velocity tensor  
 $u_g$  -- geostrophic wind  
 $u_*$  -- surface friction velocity  
 $u, v, w$  -- Cartesian velocity components  
 $u^*, v^*, w^*$  -- transformed velocity components  
 $x_i$  -- Cartesian spatial tensor  
 $x, y, z$  -- Cartesian spatial axes  
 $x^*, y^*, z^*$  -- transformed spatial axes  
 $z_s$  -- surface elevation

## CHAPTER I

### INTRODUCTION

The dynamic and thermal effects of mountainous terrain influence atmospheric circulations extending in scale from a few tens of meters to thousands of kilometers. Therefore, it is not surprising that mountain meteorology has been a research interest to scientists for many years, dating back to the early studies of slope circulations done by Wenger (1923). Since that time, the pace of research has accelerated to meet a growing need for more detailed information about the meteorological structure of mountain atmospheres. As industrial activity and the population increases in these regions, this need becomes more acute. This information is essential to such diverse industries as agriculture, energy production, mining, timber and tourism. Additionally, urban planners and others concerned with air quality related issues must deal with complex atmospheric circulations in order to best identify potential air pollution problems.

Coupled with the increased research effort has been the development of new research tools. Innovations in instrumentation have enabled investigators to measure meteorological variables far above the surface. These include aircraft platforms, automated meteorological towers and portable sounding stations which can be easily operated in remote locations. Also, recent advances in the design of high speed, large memory digital computers has prompted the formulation and use of sophisticated numerical models to simulate atmospheric processes in

complex terrain. In addition, physical models have been constructed in wind tunnels and water tanks in which idealized complex terrain flows can be observed and controlled on a smaller scale.

In this paper, the results of research focused on one problem in mountain meteorology is presented. The diurnal evolution of a meso- $\beta$  scale (~50 km) boundary layer in northwestern Colorado is examined using both analyses of observed structure and numerical model results. Located in this region are vast reserves of recoverable oil shale and it is projected that a large oil shale industry will develop in this currently sparsely populated area. At night, a stably stratified boundary layer forms over the larger scale topographic features and separates the synoptic flow from the local circulations in the smaller scale valleys and depressions. During the day, a surface based mixed layer can develop and recouple the small and large scale flows. Although not much is currently known about the mesoscale boundary layer structure, it is critically important in this area where future air quality problems must be anticipated and abated. This is particularly true of the nocturnal stable layer, which has the greatest potential for causing air quality problems.

Atmospheric sounding data were analyzed for two cases when the evolution of the boundary layer was observed. The first set of observations was collected over a single site in a narrow mountain valley over a period encompassing a summer night and the following morning when the synoptic scale winds were light. Using a combination of data collected both in the valley and through the mesoscale boundary layer above the valley, the relationships between the valley and mesoscale circulations were explored. In the second case, a series of

simultaneous soundings over three sites were used to examine the mesoscale boundary layer evolution through the evening transition period on a winter night when the synoptic winds were much stronger.

Subsequently, the results of a numerical modeling program are presented with the goal of aiding in the interpretation of the observations and developing a conceptual model of the mesoscale boundary layer structure. For this program, a fully elastic, non-hydrostatic primitive equation model was first employed to simulate the diurnal evolution of the mesoscale boundary layer over an idealized representation of the terrain found in the region studied. Attention was then focused on the effects of wind speed, wind direction and season on the evolution of the nocturnal boundary layer through the analysis of six additional simulations of the evening transition period. From the combined results of the observational and modeling programs, insight into the physical processes responsible for the evolution and structure of the mesoscale boundary layer over mountainous terrain was achieved.

## CHAPTER II

### BACKGROUND

Research of the atmospheric boundary layer structure over complex terrain integrates the study of boundary layers over flat terrain with that of the thermal and mechanical effects of uneven topography on atmospheric circulations. The current state of knowledge in all of these areas has been gained through a history of both observational and theoretical studies. A comprehensive review of all of the research performed to date is beyond the scope of this dissertation. However a summary of the previous work which is pertinent to the present study is presented.

#### A. Boundary Layers Over Flat Terrain

The atmospheric boundary layer (ABL) consists of the layer of air adjacent to the earth's surface in which the surface effects are significant over time periods of hours to days. The simplest boundary layer structure is found over flat terrain where the surface is horizontally homogeneous, the effects of water substance are insignificant and the atmospheric flow field is stationary and barotropic. Although these conditions are rarely met, they form the basis for the development of a theoretical framework to describe the ABL using the concepts of boundary layer fluid mechanics. The fundamental theory stems from von Karmen's (1930) mixing length hypothesis of fluid turbulence. Panofsky and Dutton (1984) describe turbulence as:

"... a type of fluid flow that is strongly rotational and apparently chaotic. Turbulence separates nearby parcels of air and thus mixes fluid properties. It has eddy structures arranged in a continuous spectrum of sizes and intensities."

These motions are inherently three-dimensional and exist on temporal and spatial scales much smaller than the prevailing flow field. The ABL structure is maintained by the vertical transport of heat and momentum in the eddies (turbulent flux) to and from the surface. Atmospheric turbulence is generated through shear and static (convective) instabilities and dissipated by viscosity and static stability. One commonly used parameter which describes the level of turbulence in the atmosphere is the gradient Richardson number,  $Ri$ , given by

$$Ri = \frac{g}{\theta} \frac{\partial\theta/\partial z}{(\partial u/\partial z)^2 + (\partial v/\partial z)^2}, \quad (1)$$

where  $g$  is the gravitational acceleration,  $\theta$  is the potential temperature and  $u$  and  $v$  are the horizontal wind components.  $Ri$  is a normalized ratio of the dominant turbulence production terms, vertical wind shear and static stability. In statically unstable regimes ( $Ri < 0$ ), turbulent motions are generated by both shear, or mechanical production, and convection, or buoyant production. In the case of stable stratification ( $Ri > 0$ ), buoyant production is replaced by suppression and mechanical generation of breaking Kelvin-Helmholtz (K-H) waves (Thorpe, 1972) is the primary source of turbulence. If the stratification is sufficiently strong with respect to the vertical shear, the production of turbulence is totally suppressed. Miles (1961) and Howard (1961) used linear wave theory to determine that at  $Ri \geq Ri_c = 0.25$  the growth of K-H waves ceases in Boussinesq fluids. Although atmospheric flows are not truly linear,  $Ri_c$  values observed and

calculated for atmospheric cases are very near this value (Merrill, 1977).

Most studies of atmospheric turbulence attempt to parameterize its effects on the mean atmospheric thermodynamic and dynamic fields. The early work of Rossby and Montgomery (1935), which dealt with the deviations of flow from geostrophy in the neutrally stratified ABL, initiated the development of the currently utilized similarity theory for the boundary layer. They partitioned the boundary layer into a shallow surface or inner layer and a deeper outer or Ekman layer, so named for its resemblance to the theoretical wind profile formulated by Ekman (1927). Their work has been restated in its currently used form by Kasanski and Monin (1961) and Blackadar and Tennekes (1968). Since real boundary layers are seldom neutrally stratified, diabatic extensions to Rossby similarity were added later by Zilitinkevich (1972) and Zilitinkevich and Deardorff (1974) who matched Monin-Obukov surface layer similarity (Monin and Yaglom, 1971) to Blackadar and Tennekes' solution. A summary of Rossby similarity and its extensions can be found in Appendix I. In neutrally stratified, barotropic flow, the heat flux is negligible and the vertical wind shear generated by the flux of momentum into the surface layer maintains the turbulence structure in the outer layer against dissipation by viscosity. If the flow field remains stationary, steady-state is achieved and the ABL depth can be calculated from the values of surface stress and geostrophic wind.

#### 1. Diurnal boundary layer evolution over flat terrain

Over land the ABL undergoes a diurnal heating and cooling cycle shown schematically in Figure 1. Starting at midday, when the surface heat flux is positive from solar heating, a super-adiabatic surface

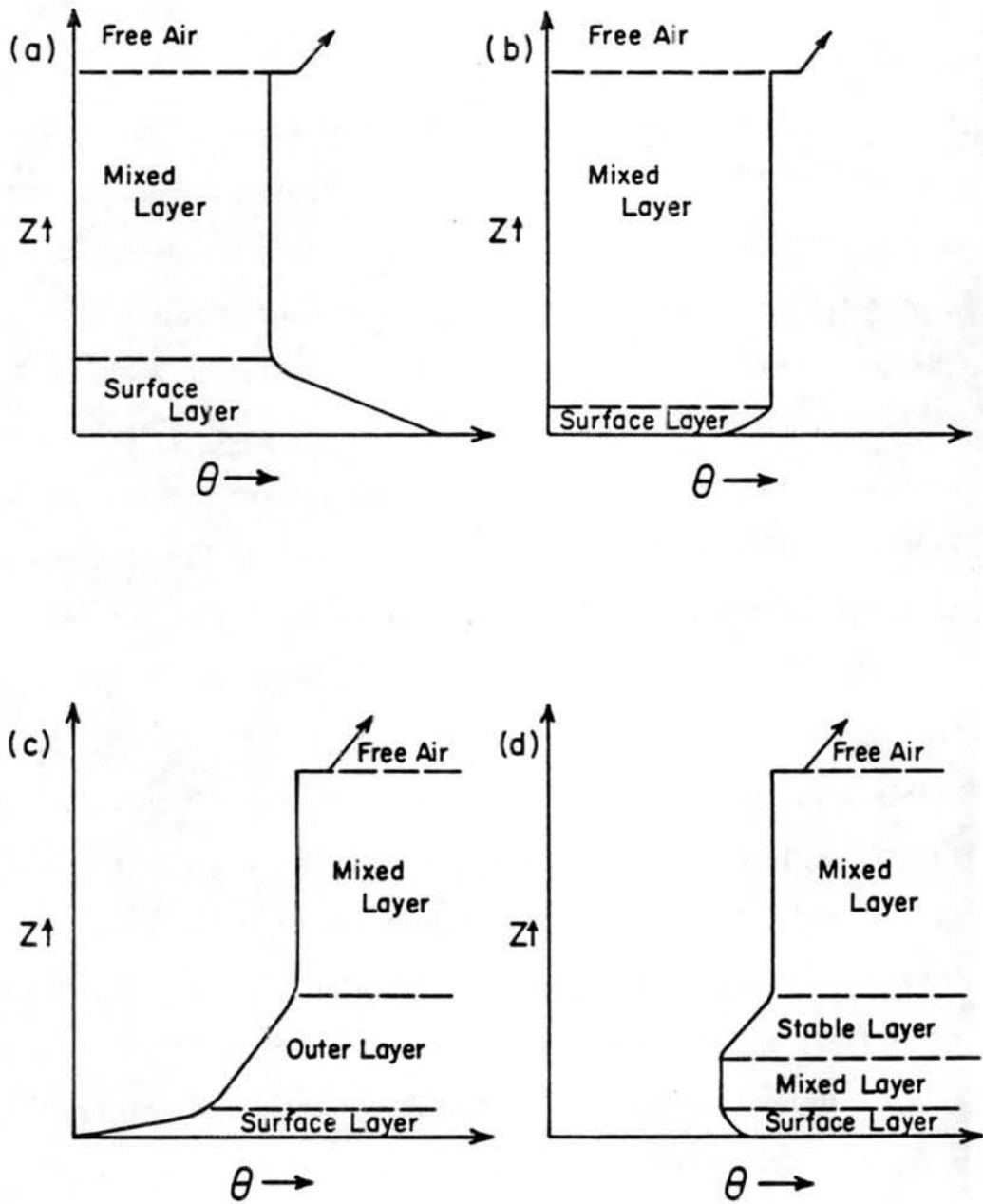


Figure 1. Schematic diagram of the diurnal boundary cycle over flat terrain for a) late afternoon, b) early evening, c) late night and d) early morning.

layer underlies a near neutral, deep convectively mixed layer capped by a strong potential temperature inversion 1-2 km above the surface (Fig. 1a). The excess of turbulent energy generated by the surface heating is transported to the inversion level by convective plumes (Warner and Telford, 1967; Lenschow and Stephens, 1980). This energy is utilized to entrain some of the free air above the inversion layer and causes the ABL to grow. Simple one-dimensional models of the growth of the convective boundary layer have been formulated by Ball (1960), Lilly (1968), Tennekes (1973) and Stull (1973). A good review of the physics of the convective boundary layer over flat terrain can be found in Banta (1982). Near sunset, the surface radiational cooling becomes stronger than the rapidly decreasing solar heating and the surface heat flux reverses direction. This point marks the beginning of an evening transition lasting one to two hours during which a cooled nocturnal stable layer replaces the lower part of the daytime convective layer. In this period, the daytime surface layer collapses as the super-adiabatic daytime lapse rate is supplanted by a stable nocturnal one (Fig. 1b) (Delage, 1974). Unlike the convective case, where the static instability in the surface layer dominated the generation of turbulent energy, shear production of turbulence in the nocturnal surface layer acts to mix the cooled surface air upward and thereby stabilize the boundary layer. Since the stable stratification inhibits the vertical transfer of surface layer turbulence, nocturnal boundary layers are usually only 50-300 m deep (Melgarejo and Deardorff, 1974) and form under the remnants of the daytime mixed layer (Fig. 1c). After sunrise, solar heating again becomes stronger than the radiational cooling at the surface and the heat flux becomes positive. At this time, a surface

based convective layer starts growing into the nocturnal stable layer (Fig. 1d). This morning transition ends when the stable layer is destroyed in the late morning and the ABL structure again resembles that shown in Fig. 1a.

## 2. Ideal nocturnal boundary layer structure

The most basic nocturnal boundary layer (NBL) structure consists of three layers shown in Figure 2 (Mahrt, 1981). The surface layer obeys Monin-Obukov similarity and has very strong wind shear and a very stable lapse rate.  $Ri$  values are relatively low and this layer is the source of turbulent energy for the NBL. Above the surface layer, the outer layer has a nearly constant vertical shear and lapse rate. The excess surface layer turbulent energy is expended as the cooler air is mixed upward against the stratification. Although  $Ri$  values in this layer are higher than those in the surface layer, they remain below the critical value (Zeman, 1979). At the top of the outer layer,  $Ri$  values approach the critical value and the flow field loses the effects of surface friction. Blackadar (1957) first documented an acceleration of the winds at this level resulting from the loss of downward momentum flux. The resulting wind maximum, commonly referred to as the nocturnal jet, oscillates with the inertial period as explained by Delage (1974). Because the shear vanishes at the nose of the jet, no turbulent fluxes can pass through this level. Between the outer layer and the mixed layer left over from daytime heating lies a transition layer, typically extending to a height 125-200% of the elevation of the jet maximum, which shows some degree of cooling (Mahrt et al., 1979). The structure of this layer is not well understood nor is there positive agreement as to the cause of the observed cooling. Possible explanations include

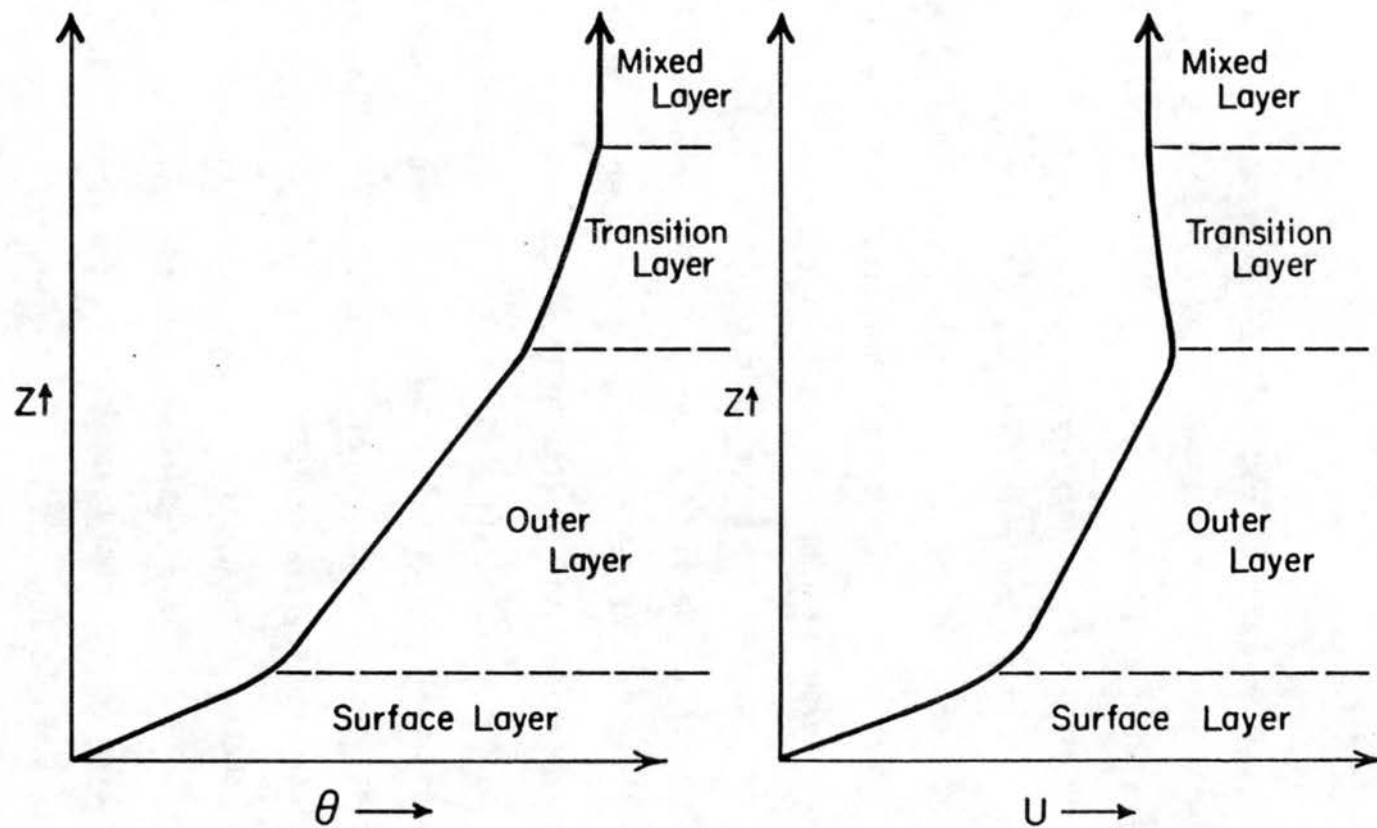


Figure 2. Ideal nocturnal boundary layer structure over flat terrain.

sporadic turbulence propagating upward from the layer below (Mahrt, 1981), clear air radiative cooling (Andre and Mahrt, 1982) and advection due to slight baroclinicity or small terrain inhomogeneities (Nieuwstadt and Driedonks, 1979). While the depth of the surface and outer layers achieve a near steady-state structure several hours after the surface cooling begins, the transition layer deepens throughout the night (Garratt and Brost, 1981).

Mathematical expressions defining the NBL height are difficult to formulate because of the relatively poor understanding of the turbulent structure in stable layers, particularly in regions where the turbulence is neither continuous nor stationary, such as the transition layer. Consequently, most definitions apply only to the top of the continuous turbulence or outer layer and do not consider the transition layer at all. Early attempts at parameterizing the NBL depth used the bulk Richardson number  $Ri_B$  defined by

$$Ri_B = \frac{g}{\theta} \frac{(\theta_h - \theta_s) h}{u_g^2}, \quad (2)$$

where  $h$  is the elevation of the top of the outer layer,  $u_g$  is the geostrophic wind speed and  $\theta_h$  and  $\theta_s$  are the potential temperatures at the top and bottom of the NBL, respectively. Hanna (1969) proposed that the atmosphere adjusted to maintain a critical value of  $Ri_{BC} = 0.75$  in the steady-state NBL. From  $Ri_{BC}$  and known or estimated surface heat flux and geostrophic wind speed values, one could compute the steady-state NBL depth. This approach is limited because of the uncertainty of  $Ri_{BC}$ .

Zilintinkevich (1972, 1975) used similarity theory to define the steady-state depth of the turbulent NBL,  $h_s$ , by

$$h_s = d (Lu_*/f)^{1/2} \quad , \quad (3a)$$

$u_*$  is the surface layer friction velocity and  $f$  is the Coriolis parameter.  $L$  is the Monin-Obukov length, defined as

$$L = \frac{u_*^3 \theta}{kg \overline{w'\theta'_s}} \quad , \quad (3b)$$

where  $k$  is the von Karmen constant ( $\sim 0.4$ ), and  $\overline{w'\theta'_s}$  is the magnitude of the surface kinematic heat flux. Values of the constant,  $d$ , range from 0.22 (Wyngaard, 1975) to 0.74 (Nieuwstadt and Tennekes, 1981). However, since the surface heat flux never achieves a constant value, the steady-state assumption may not be strictly valid (Zeman, 1979).

Alternatively, Nieuwstadt (1980) proposed the prognostic relaxation relation

$$dh/dt = -\frac{1}{T_D} [h(t) - h_s(t)] \quad , \quad (4a)$$

where  $h_s$  is defined by (3), and  $T_D$  is the turbulent time scale given by

$$T_D = \frac{\theta_h - \theta_s}{\partial \theta_s / \partial t} \quad . \quad (4b)$$

$T_D$  is on the order of several minutes during the transition period and lengthens to several hours late at night. Yu (1978) compared results from similar equations to data from the Wangara experiment and found their performance was generally poor. Mahrt et al. (1982) reasoned that for relationships such as (3) and (4) to be valid, profiles of the turbulent fluxes must be used to define  $h$ .

More recently, simple one-dimensional parameterizations of NBL structure have been developed for use in larger scale numerical models. Wetzel (1982) accounts for the transition layer cooling in an ad hoc

fashion, thereby eliminating the need for radiative transfer calculations. Stull (1983a, b) uses a modified similarity approach to extend the NBL beyond the coter layer, incorporating radiative cooling effects empirically. On the other hand, Yamada (1979) includes the effects of clear air radiative transfer in his NBL parameterization to explicitly account for cooling in the transition layer. All three models perform comparably when tested against data from the Wangara experiment.

### 3. Non-ideal effects on nocturnal boundary layers

Unfortunately, even a small degree of baroclinity or slight terrain slope can significantly alter the basic three level structure (Caughey et al., 1979). Brost and Wyngaard (1978) used a higher-order turbulence model to show that terrain slopes on the order of 1-2 degrees can change the NBL structure. Nieuwstadt and Driedonks (1979) demonstrated through scale analysis that advection is important unless

$$\partial u/\partial x + \partial v/\partial y \ll 3 \times 10^{-5} \text{ s}^{-1} \quad (5a)$$

and

$$\partial \theta/\partial x + \partial \theta/\partial y \ll 3 \times 10^{-5} \text{ K m}^{-1} \quad (5b)$$

criteria which are not met generally. Recently, researchers at the Boulder Atmospheric Observatory have studied the non-ideal NBL structure to ascertain the importance of other factors not considered in the basic three level conceptual model (Kaimal, 1983).

The stable stratification of nocturnal boundary layers also permits the generation and propagation of internal gravity waves. The generation and breaking of Kelvin-Helmholtz waves has previously been discussed as the principal source of turbulence in the NBL. Because of the close similarity between K-H waves and the longer gravity waves,

interactions between the wave and turbulence structures can modulate NBL behavior (Einaudi and Finnegan, 1981a, b). Mahrt et al. (1979) found that the elevation of the nocturnal jet maximum oscillated in time as gravity waves propagated through the stable layer. Previously, wave activity was difficult to detect because the time and space scales of wave motions are very close to those of turbulent eddies. However, the use of fast response microbarographs (Merrill, 1977) and data from acoustic sounding systems (Eymard and Weill, 1979) have enabled researchers to observe the wave structure of the NBL. Using mathematical techniques which separate the short term variability due to waves from that due to turbulence, Finnegan et al. (1984) showed that there can be substantial conversion of gravity wave energy to turbulence in the NBL. Conversely, Chimonas and Grant (1984a, b) demonstrated with a numerical model how shorter wavelength K-H waves can excite longer gravity modes instead of being reduced to turbulent eddies.

The structure of most nocturnal boundary layers is still not very well understood. The NBL is rarely in steady-state, although most current models are based largely on the steady-state assumption. Additionally, boundary layer theory breaks down when terrain inhomogeneity or advection is important. The presence of gravity waves introduces still another modulating effect on both the mean and turbulent NBL structure. Very little is also known about the evening transition period when the NBL structure first develops and the mean and turbulent time scales are similar. However, with time a more detailed understanding of NBL behavior will evolve as these problems are investigated.

## B. Mesoscale and Local Effects of Mountainous Terrain

Most local and mesoscale terrain induced circulations can be divided into two categories depending upon the principal forcing mechanism giving rise to the circulation (Atkinson, 1981). Those which are mechanically forced arise from the dynamic interaction between the gradient level wind and elevated terrain. Included in this group are mountain waves, downslope wind storms, lee circulations and similar phenomena which will not be considered here. The thermally forced circulations result from the elevated heating and cooling of the mountain topography during the course of the diurnal cycle. These are typically best observed when the larger scale wind fields are weak and include what are commonly called slope and mountain-valley wind systems. Additionally, there are other atmospheric phenomena which result from the interaction of the thermal circulations with the gradient wind field. Analysis of terrain induced motions is complicated because one must not only consider the characteristic dynamic scales of the atmosphere but also account for the natural time and length scales of the topographic forcing. Of particular relevance to this study are the smaller meso- $\beta$  and meso- $\gamma$  scale (Orlanski, 1975) boundary layer flows in complex terrain.

### 1. Ideal thermal circulations in mountainous terrain

Mountain thermal circulations form as a consequence of the larger diurnal temperature change of the air near elevated or sloping topography compared to air at the same elevation away from the terrain. Many of the concepts upon which the current models of mountain boundary layer evolution are based were developed from observational and

theoretical studies of Alpine wind systems during the period between 1920-1950. Wenger (1923) applied Bjerknæs' circulation theorem (see Holton, 1977) to a cross-section of air lying over a two-dimensional slope and the adjacent low plain. Figure 3 shows conceptually his results with the air cooled by the mountains at night flowing down the slope toward the plain and the reverse situation during the day when solar heating results in the warming of the mountain air. However, it was the later studies by Wagner (1938), Ekhardt (1944, 1948) and Defant (1949) which integrated extensive observations to develop a comprehensive theoretical framework of mountain wind systems. Three thermal regimes were identified in the boundary layer over mountainous terrain, each containing a different thermal wind system. Figure 4 shows these three systems schematically during both the daytime and nighttime periods. Immediately above the surface are the slope winds. These are small scale, buoyancy driven flows which tend to move parallel to the fall line of the topography. The hydrostatic circulations commonly labeled mountain and valley winds develop along the axes of mountain valleys in response to the diurnal temperature changes of the valley air volume. On a larger scale still is the mountain-plain circulation which forms because of the heating and cooling effects of the mountain land mass as a whole. Although not shown in the figure, compensating flows, also known as "anti-winds", are required by continuity to complete the circulation in all three wind systems based on the Alpine model. A more complete description of these systems as well as a discussion of their interactions follows.

a. Slope winds. Slope winds are the small scale thermal circulations which develop in the surface layer over sloping topography.

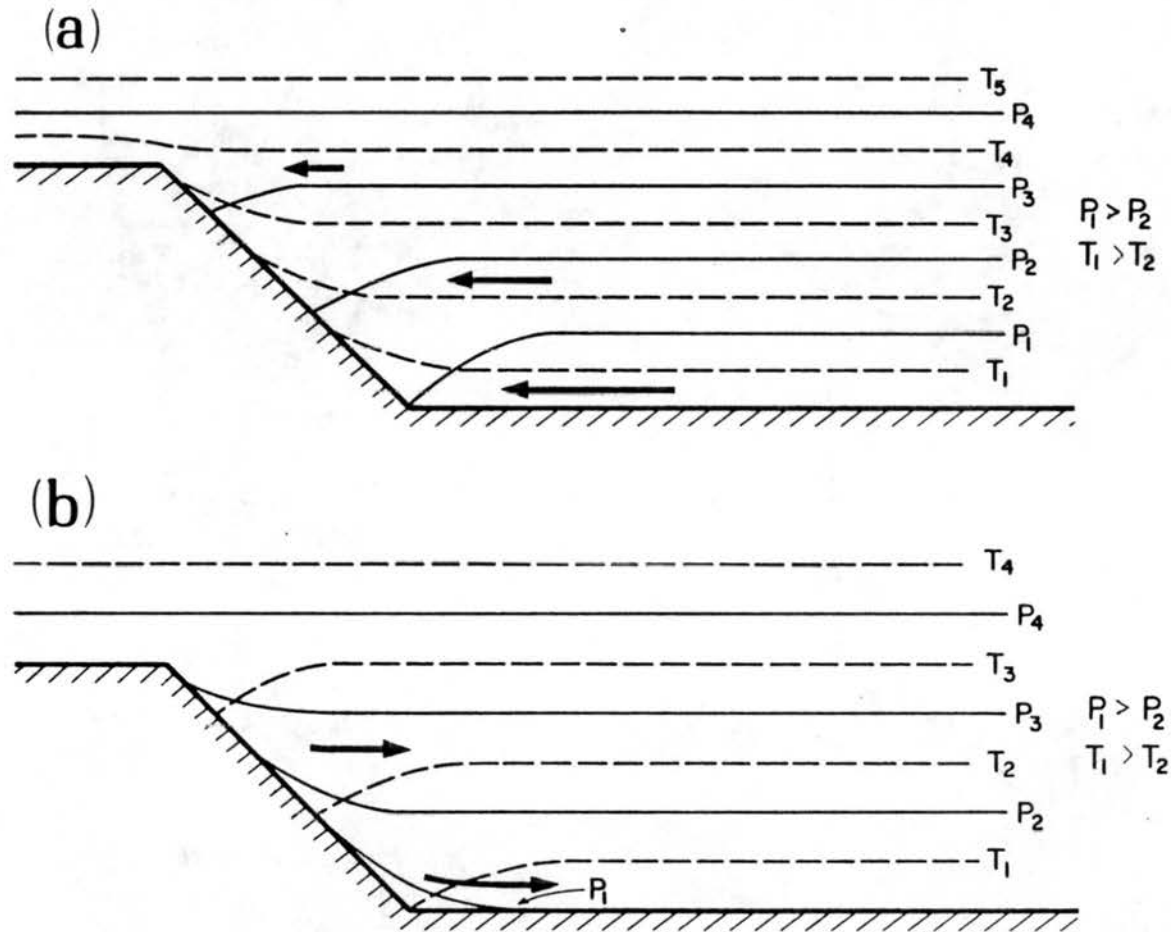


Figure 3. Pressure and temperature fields over two dimensional slope and adjacent plain for a) daytime circulation and b) nighttime circulation.

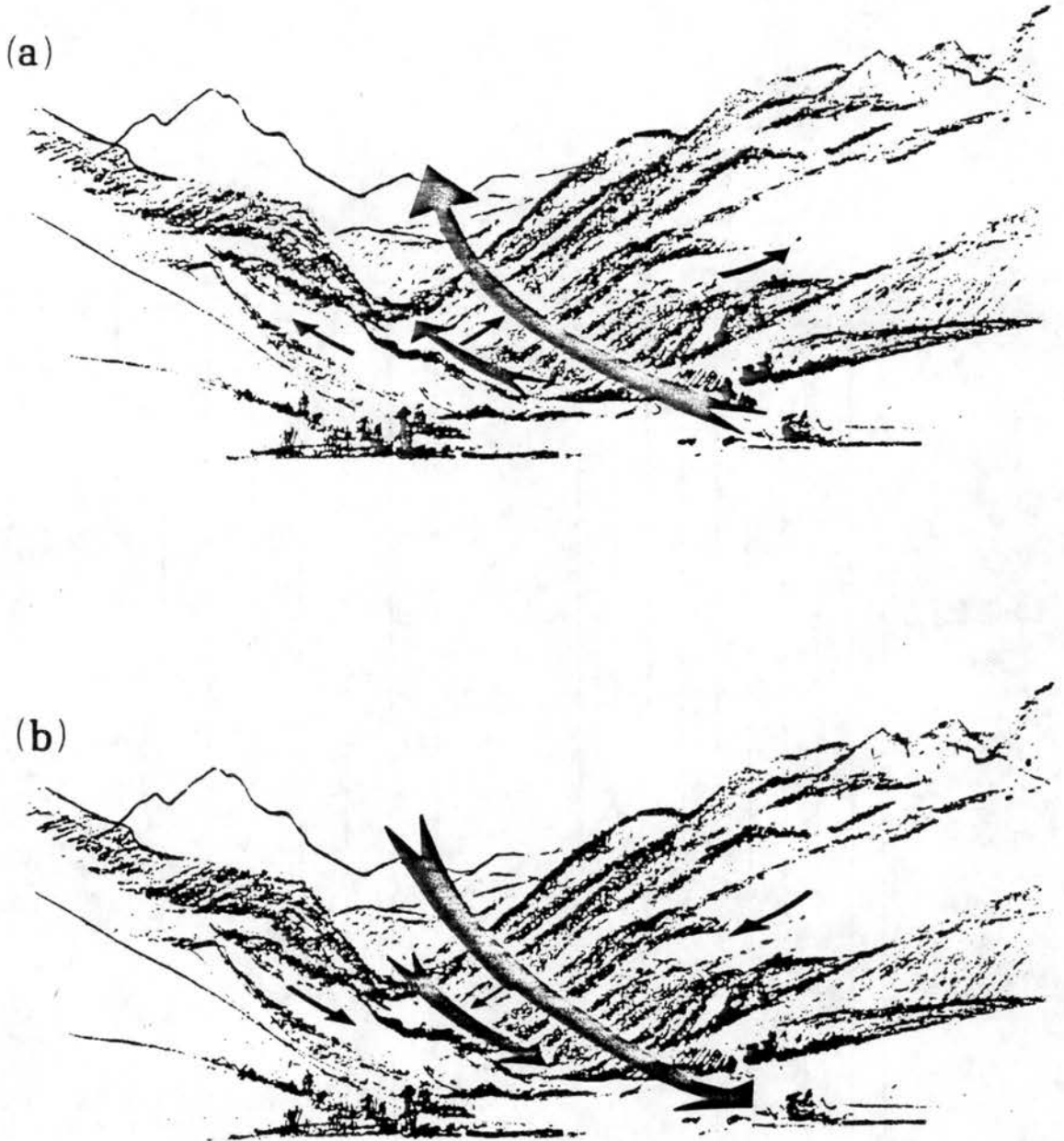


Figure 4. Schematic illustration of slope, valley and mountain-plain wind systems for a) daytime circulations and b) nighttime circulations.

Air density perturbations resulting from the heat exchange with the underlying surface produce the buoyant accelerations which force the slope flow. The transition period for the reversal of the slope flow in the early morning and early evening is usually rapid, typically occurring 30-60 minutes after the reversal of the surface sensible heat flux (Defant, 1949; Banta, 1982; McNider and Pielke, 1984). Earlier work concentrated on the nocturnal downslope flow regime because it is physically much easier to describe. However, more recent studies have yielded a great deal of information about upslope flow as well.

The negative buoyancy in the surface layer over a cooled, inclined surface causes air in the layer to move down the fall line of the terrain. For the most part, the downslope flow layer is stably stratified and turbulence is weak, but continuous. However, the top and bottom of the flow layer remain highly turbulent. The weak overlying static stability and the shear at the top of the flow layer enable it to entrain some of the ambient air and thereby retard the flow. At the surface, the high shear continues to support the heat flux into the ground and maintain the flow against turbulent "friction" at the top. Although downslope flows can extend over a large horizontal distance (Hootman and Blumen, 1984), they are weak and very shallow, usually less than 50 m deep with speeds less than 5 m/s (Atkinson, 1981). Consequently, the return or anti-downslope wind is difficult to discern from observations. Theoretically, steady state would be achieved if the rate of cooling at the surface is balanced by the rate of warm air entrainment at the top. Probably one of the earliest models of steady state downslope flow was Prandtl's (1942) analytical expression for flow down an infinite slope. From given values of surface temperature

perturbation, slope and ambient stratification, the steady state downslope wind profile could be computed. The model assumed a constant eddy mixing coefficient, and was not formulated to deal with the time dependent nature of the flow during the transition period.

Nevertheless, Defant found excellent agreement between observations of downslope winds taken on the sidewalls of the Inn Valley in Austria and predictions using Prandtl's model.

More sophisticated models include time dependent analytical and finite difference formulations which better describe both the temporal and spatial variation of observed downslope wind behavior. Mannins and Sawford (1979) used hydraulic theory to develop a non-linear, two-dimensional model of downslope flow. Their results show that the depth of the downslope layer increases with distance down the slope and confirm that entrainment at the top is the dominant mechanism opposing the gravitational acceleration of the flow layer. Observations support both conclusions; Moll (1935) and Doran and Horst (1983) found thicker downslope layers farther down the slope and Fitzjarrald (1984) clearly demonstrated the effects of entrainment on retarding the downslope flow. Fleagle (1950) used a time dependent analytical equation set to model the observed oscillatory nature (Heywood, 1933) of downslope wind velocities in the first few hours after sunset. Based on his calculations, Fleagle attributed this oscillation to an overshooting of the neutral buoyancy level by parcels in the slope flow as they move down the incline in a stably stratified environment; an analog to the harmonic oscillation of an underdamped mass-spring system. McNider (1982) qualified this explanation and demonstrated through scale analysis that this effect alone cannot account for the observed

behavior. Doran and Horst (1981) used a hydraulic model similar to that of Mannins and Sawford to reproduce observed oscillations with a period of 1 h. However, the non-linear and time dependent nature of the numerical solution make it difficult to determine a single mechanism causing the oscillation. Recently, more sophisticated turbulence closure and advection parameterization schemes have been applied to versions of Prandtl's one-dimensional model and have produced realistic results based on a limited number of comparisons to observations (Rao and Snodgrass, 1981; Garrett, 1983). McNider and Pielke (1984) applied a three-dimensional mesoscale model to both the nocturnal slope and along-valley wind systems. They found agreement between the numerical results and theoretical slope flow calculations, including the appearance of a compensating upslope layer above the surface based downslope wind.

Daytime upslope layers are much more difficult to describe theoretically. They first form in a shallow convective surface layer lying under the remnants of the nocturnal inversion present at sunrise. Unlike the negatively buoyant downslope flow, which is confined to the surface layer by gravity, daytime sensible heating of the air in the surface layer produces positive buoyant accelerations which tend to lift the parcels vertically away from the slope. Despite this, upslope winds are a persistent feature of the diurnal boundary layer cycle over sloped terrain. Therefore, there must be a restraining force that confines the air to the slope layer. One possibility is that the overlying stability from the previous night's inversion layer causes the air to lose its buoyancy a short distance above the slope and not rise any higher. This would especially be true in the first several hours after sunrise when

the boundary layer is still stably stratified and the surface layers over the slopes are shallow. Banta (1982) proposed an alternative mechanism whereby a hydrostatic pressure gradient directed horizontally presses the air against the slope. Davidson (1961) probably documented the best observed case of steady-state upslope flow with measurements showing both a well defined upslope wind layer with a compensating downslope wind above it.

Because of the convective instability of upslope flows, they are highly turbulent and can extend much deeper than the nocturnal downslope flows found over the same topography, typically extending to heights of several hundred meters (Atkinson, 1981). As a result, numerical models of upslope flows are much more difficult to formulate. Interestingly, Defant (1949) applied Prandtl's slope flow equations to the steady-state upslope flow over the same terrain as he used for the downslope calculations and found good agreement in the lowest 30 m. Above this level however, the model assumption of layered flow was not valid and the agreement became increasingly worse with altitude. Thyer (1966) and Orville (1964) used vorticity models to simulate the development of upslope winds generated by surface heating. Unfortunately, Thyer's simulations became computationally unstable after only two minutes of simulated time. However, they do yield qualitatively realistic results showing an upslope wind above the surface under a weak return flow. Orville used a more computationally stable set of equations to obtain solutions for flow after more than an hour of simulated time. He was also able to produce an upslope flow layer but found that the compensating return flow was weak and diffuse. Gal-Chen and Sommerville (1975a, b) used a system of anelastic primitive equations to simulate

the development of a convective upslope layer under the remnants of the nocturnal stable layer. Later, Bader and McKee (1983) modeled the early morning development of slope flows over valley sidewalls in the presence of a stable layer. Their simulations reveal that the upslope wind does not initially form as a continuous flow over the length of the sidewall but rather develops in sections which connect later in the morning as the surface heating intensifies. By midday, when the stable layer is destroyed, a deep slope circulation is well developed with upslope wind speeds near 5 m/s and weaker compensating winds above the upslope layer. However, no one to date has modeled the complete diurnal slope flow cycle encompassing both transition periods when the flow direction reverses.

b. Hydrostatic mountain thermal circulations. On a larger scale than the slope winds are the hydrostatic wind systems that form both the mountain-valley circulations, which run parallel to the valley axes, and the still larger mountain-plain circulation, which develops over entire mountain ranges and their adjacent lowlands. The valley wind systems result from the greater diurnal temperature range of the valley boundary layer than that of the boundary layer over the adjacent plain at the valley mouth. The mountain-plain circulation similarly develops because of the larger diurnal temperature change of the mountain boundary layer than in the free air above the boundary layer over the surrounding lowland areas. Whereas the slope circulations reverse quickly after the surface heat flux reverses direction, the larger scale circulations usually require several hours to become established. This is due to the longer time required to reverse the mesoscale temperature gradients than the relatively rapid temperature transition in the shallow surface

layers over the slopes. Wagner (1938) realized that the slope flows were responsible for mixing the air heated or cooled over the terrain surfaces to form the deeper valley and mountain boundary layers. At night, the air cooled next to ground slides down the inclined surfaces of the mountain range and collects in the low lying basins and valleys to form cold air pools which typically extend to the height of the surrounding terrain. After sunrise, when the surface sensible heat flux again becomes positive the nocturnal stable layers are destroyed by the redistribution of warm upslope air.

Defant (1949) showed graphically this influence of the slope circulations in the development of the valley wind system in the classic diagram displayed in Figure 5. Although lacking in many of the details, this illustration is useful in understanding conceptually the effects of the slope wind system in the development of the along valley circulation. In this model, warming and cooling of the valley airmass is accomplished through cross-valley slope circulations. Of particular importance is the lag between the reversal of the slope circulations and the corresponding valley circulations in the early morning and early evening. In the same paper, Defant computed the time required to completely cycle the volume of air in a unit valley cross-section through the slope flows using Prandtl's slope flow equations. He found good agreement between his model computations and the observed length of the valley transition periods of three to five hours. Since that time, observational studies by Davidson and Rao (1958, 1963), Whiteman and McKee (1977; Whiteman, 1980, 1982), Brehm and Freytag (1982) and others have all been concerned with understanding the valley boundary layer evolution through the diurnal cycle. The compensating return flow above

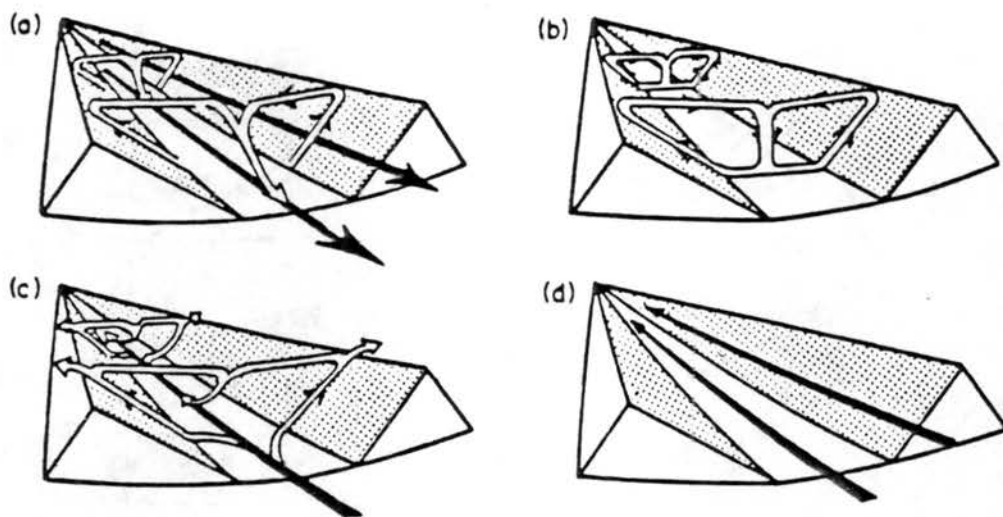


Figure 5. Schematic representation of the diurnal cycle of slope and valley winds (from Defant, 1949).

- (a) Air flow in the morning at sunrise. The upslope winds begin (white arrows). The mountain wind (black arrows) is still present in the valley. The pressure drop is in the down-valley direction. Temperature: valley is cold, plain is relatively warm. Changes in temperature (until situation shown in b): valley is becoming warmer, plain is becoming cooler.
- (b) Air flow in the forenoon (about 9 am). The upslope winds are strong. The system is in a state of transition from mountain wind to valley wind. Pressure drop: zero. Temperature: equalized. Changes in temperature (until the situation shown in c): valley is rapidly becoming warmer, temperature over the plain is changing slightly.
- (c) Air flow from noon to early afternoon. The upslope winds are decreasing. The valley wind is fully developed. The pressure drop is in the up-valley direction. Temperature: valley is warm, plain is relatively cold. Changes in temperature (until the situation shown in d): essentially none.
- (d) Air flow in the late afternoon. The upslope winds have died out. The strength of the valley wind is about the same as in c. The valley wind extends to the sides of the slopes. The pressure drop is in the up-valley direction. Temperature: valley is warm, plain is relatively cold. Changes in temperature (until the situation shown in e): valley is slowly cooling.

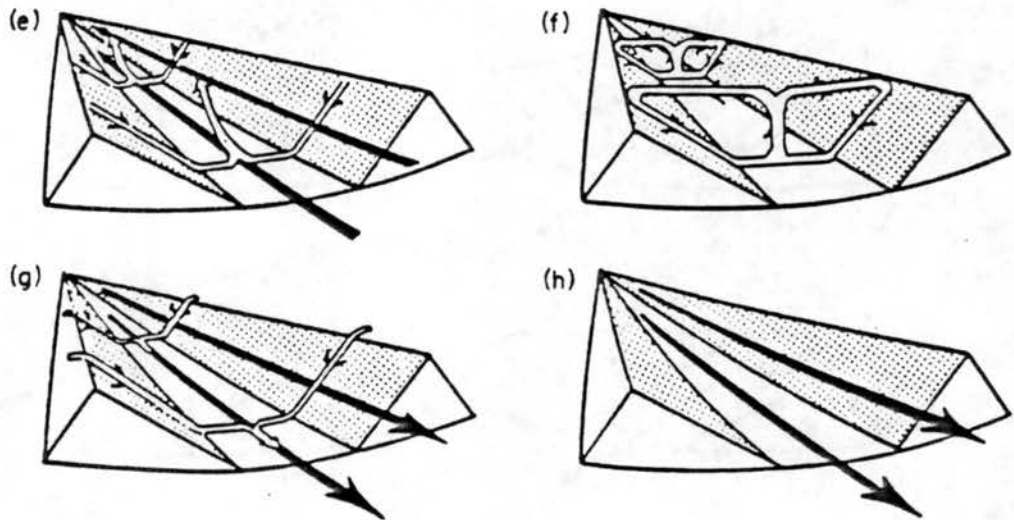


Figure 5 continued. Schematic representation of the diurnal cycle of slope and valley winds (from Defant, 1949).

- (e) Air flow in the evening. The downslope winds are beginning. The valley wind is decreasing. The pressure drop is still in the up-valley direction. Temperature: it is slightly warmer in the valley than it is over the plain. Changes in temperature (until the situation shown in f): the valley is cooling rapidly; the plain is cooling only slightly.
- (f) Air flow from late evening through the first half of the night. Downslope winds are present. The system is in a state of transition from valley wind to mountain wind. Pressure drop: zero. Temperature (until the situation shown in g): valley continues to cool rapidly.
- (g) Air flow at night. Mountain wind is present along with the downslope winds. The pressure drop is in the down-valley direction. Temperature: valley is cold, plain is relatively warm. Changes in temperature (until the situation shown in h): valley is cooling; plain is cooling slightly but is warm relative to the valley.
- (h) Air flow from night until morning. The downslope winds have died out. The mountain wind extends to the sides of the slopes. The pressure drop is in the down-valley direction. Temperature: cold in the valley, warmer over the plain. Changes in temperature (until the situation shown in a): there are only slight changes in the valley and over the plain.

the valleys was observed and documented by Buettner and Thyer (1966) in an exhaustive study of valley circulations in the Carbon River valley in Washington. They measured the anti-winds for both the nocturnal down-valley flow as well as the daytime up-valley flow. In both cases, they noted that the valley winds filled the valley to ridgetop and that the overlying return flows were weaker and occupied a layer about as thick as the valley depth. In most cases however, the return flows are masked by the overlying mountain-plain or gradient winds.

Mountain-plain circulations are the largest of the terrain induced thermal wind fields. They flow over the smaller scale slope and valley winds, often masking them. Whiteman (1980) identified a daytime flow above the valley wind directed toward the main mountain barrier. It has long been suspected that the daytime toward-mountain winds are responsible for triggering the summer convective storms observed on the lee side of the Rocky Mountains (Dirks, 1969). Holzworth and Fisher (1979) documented climatologically the increased daytime boundary layer depth over mountainous locations compared to lowland stations. Raymond and Wilkening (1981) observed a large mesoscale updraft region through such a deep boundary layer over a large mountain range. Banta (1984) also observed boundary layer evolution over mountainous terrain which was conducive to storm initiation. This wind system is often difficult to discern from the overlying gradient wind field at night when the boundary layer shrinks and the cold surface layer air tends to collect in the low lying valleys and basin. However, Barr and Clements (1981) reported on observations showing a deep nocturnal circulation above the local valleys in the region under study in the present investigation.

Theoretical studies of the larger scale mountain wind systems have included both analytical and numerical model calculations. Gleeson (1953) formulated an analytical model of cross-valley winds, but his results yielded no quantitative information. Thyer (1966) attempted to solve numerically the Boussinesq equations for valley flow, but his solutions became numerically unstable after only 120 s of integrated time. However, his model results do show the appearance of both valley and slope winds as were described earlier. Egger (1981) used a simple numerical model to obtain theoretically consistent slope and valley circulations. McNider and Pielke (1984) used a hydrostatic model to simulate the formation of the nocturnal slope and valley wind systems, however they were unable to produce the strong inversions observed by Whiteman (1981). This was most probably due to the difficulty in formulating a turbulence parameterization which works well in nocturnal stable layers, a problem shared by most mesoscale models. Bader and McKee (1983, 1985) used a non-hydrostatic boundary layer model developed by Tripoli and Cotton (1982) to realistically simulate the cross-valley evolution of the daytime valley boundary layer structure. Extension of the model to include along-valley structure revealed the nature of the interactions of the along-valley and cross-valley wind systems during the morning transition period (Bader et al., 1983).

## 2. Non-ideal circulations in mountainous terrain

Unfortunately, most flows observed in complex terrain settings do not follow the conceptual framework encompassing the basic thermal circulations. For example, Start et al. (1975) observed that even the well developed nocturnal down-valley wind was not stationary, because it contained a core "jet" that meandered from side to side as it moved down

the valley axis. However, extensions of this theory can help explain many of the observed characteristics if consideration is given to the dynamic and thermal interactions of these wind systems with gradient flow. Recent improvements in both numerical and physical modeling capability have significantly enlarged the types of the problems for which a theoretical understanding can be gained. These include decoupled wind systems, flow over non-ideal topography, blocking of stratified flows and particularly, the complex nature of the circulation systems during the morning and evening transition periods.

Flow interactions and decoupling have been the object of several investigations. Tang (1976) used an analytical model to describe both daytime and nighttime steady-state cross-valley wind structures in the presence of an ambient wind blowing across the valley. His results show the development of separated flow regions on the slope where the thermal circulation tends to oppose the ambient flow (windward slope for downslope winds, lee slope for upslope winds). Doran and Horst (1983) reported on observations showing the existence of a drainage flow down a two-dimensional hill which was decoupled from the overlying flow. Yamada (1983) successfully simulated the development of the observed structure using a hydrostatic primitive equation model containing a higher order turbulence closure. The complex nature of winds found near the confluence of several separate nocturnal drainage flows has been studied by several investigators involved in the U.S. Department of Energy's ASCOT program (see Dickerson and Gudiksen, 1981). Recent investigations by Whiteman (1982) and Banta and Cotton (1981; Banta, 1984) reveal the coexistence of several decoupled wind systems separated by stable layers in complex terrain settings. These multiple wind

systems become turbulently coupled with the overlying gradient level winds once the stable layer is destroyed near midday, but not before they have a significant impact upon the boundary layer evolution. In the former case, the complex structure of the evolving daytime boundary layer within a mountain valley has serious air pollution dispersion consequences (Whiteman et al., 1984). In the latter case, the decoupled flow systems appear to be a necessary condition leading to convective storm development later in the day. Prognostic model simulations of both situations using a non-hydrostatic primitive equation model (Tripoli and Cotton, 1982) have been very useful in the interpretation of the observational data (Banta, 1982; Bader and McKee, 1985). Arritt and Pielke (1984) used a hydrostatic model (McNider and Pielke, 1984) to examine the effects of ambient flow across a valley top on the evolution of the nocturnal slope and valley flow. Their results also show that local cooling produces surface based slope flows opposing the overlying wind. Wind tunnel studies of even more complicated flow situations beyond the capability of numerical models, including thermal effects, are reviewed by Cermak (1984).

Bell and Thompson (1980) used both a numerical model and a physical model to investigate the ability of the synoptic wind to dynamically sweep out the stable air mass in a valley. In their simulations, the lapse rate both within and over the valley is the same and there is effectively no surface heat or momentum exchange. Based upon potential flow theory, their results show that dynamic interaction of the in-valley and over-valley air is characterized by the internal Froude number,

$$Fr = \frac{u}{Nh} \quad , \quad (6)$$

where  $N$  is the Brunt-Vaisalla frequency,  $h$  is the valley depth and  $u$  is the free stream cross-valley wind speed above the valley.  $Fr$  is a ratio of the inertial and buoyant forces in the flow. At low values, the buoyant forces dominate and the air in the valley remains stagnant. Above a critical value of  $Fr$ ,  $Fr_c$ , the stable air mass is dynamically swept out by the wind above the valley as the inertia in the flow overcomes the static stability in the valley. From the results of both physical and numerical experiments, they determined a value of  $Fr_c = 1.4$ . Since the flow in the models used was inviscid and predominantly non-turbulent, these results are no longer valid as  $N$  becomes very small and turbulence becomes important. It also appears that non-linear wave instability was the primary mechanism allowing the flow to penetrate the valley and sweep out the air.

Another type of separated flow phenomenon occurs upwind of large barriers when the boundary layer is stably stratified. Again,  $Fr$  values are commonly used to describe the flow where  $u$  is the speed of the barrier normal wind far upstream and  $h$  is the barrier height. In this case,  $Fr_c$  is defined as the value of  $Fr$  above which all flow passes over the barrier and below which some of the flow is blocked and separated from the main streamflow. The value of  $Fr_c$  is weakly dependent on barrier geometry but is on the order of unity (Baines, 1984). Using idealized topography, Long (1955) determined  $Fr_c$  to be  $1/\pi$  in both analytical and laboratory models of stratified flow. Kityabashi (1977) found  $Fr_c$  to be 2.3 in wind tunnel experiments, but used a slightly different definition of  $Fr$  which was based on surface flow properties. Kao (1965) introduced the concept of a dividing streamline for blocked

flow (Figure 6) which separates the stagnant region from the over-barrier flow. Hunt and Snyder (1980) defined the height of the dividing streamline,  $h_c$ , as

$$h_c = h (1 - Fr) \quad . \quad (7)$$

This definition implicitly assumes a  $Fr_c$  value of 1. Tank studies by Lee et al. (1984) appear to verify this relation. McNider and Arritt (1984) caution against strict application of (7) in instances where the interaction of the nocturnal slope flow with the approaching wind may be important.

The complexities of flow in mountainous terrain are vast and, for the most part, not well understood except in the ideal and nearly ideal situations just described. However, progress is being made in gaining an understanding of a broader range of atmospheric problems in complex terrain regions by integrating results from previous studies with new investigative programs, of which this paper is one small part. A number of problems still need to be addressed as work proceeds to fill the large gap that still exists between what is known and what is yet to be learned. These include the effects of flow interaction on the different scales of motion, the effects atmospheric radiative transfer and surface energy relationships among others. The purpose of the present investigation is to examine the dry dynamical processes contributing to the development of a mesoscale boundary layer overlying the local scale slope and valley circulations.

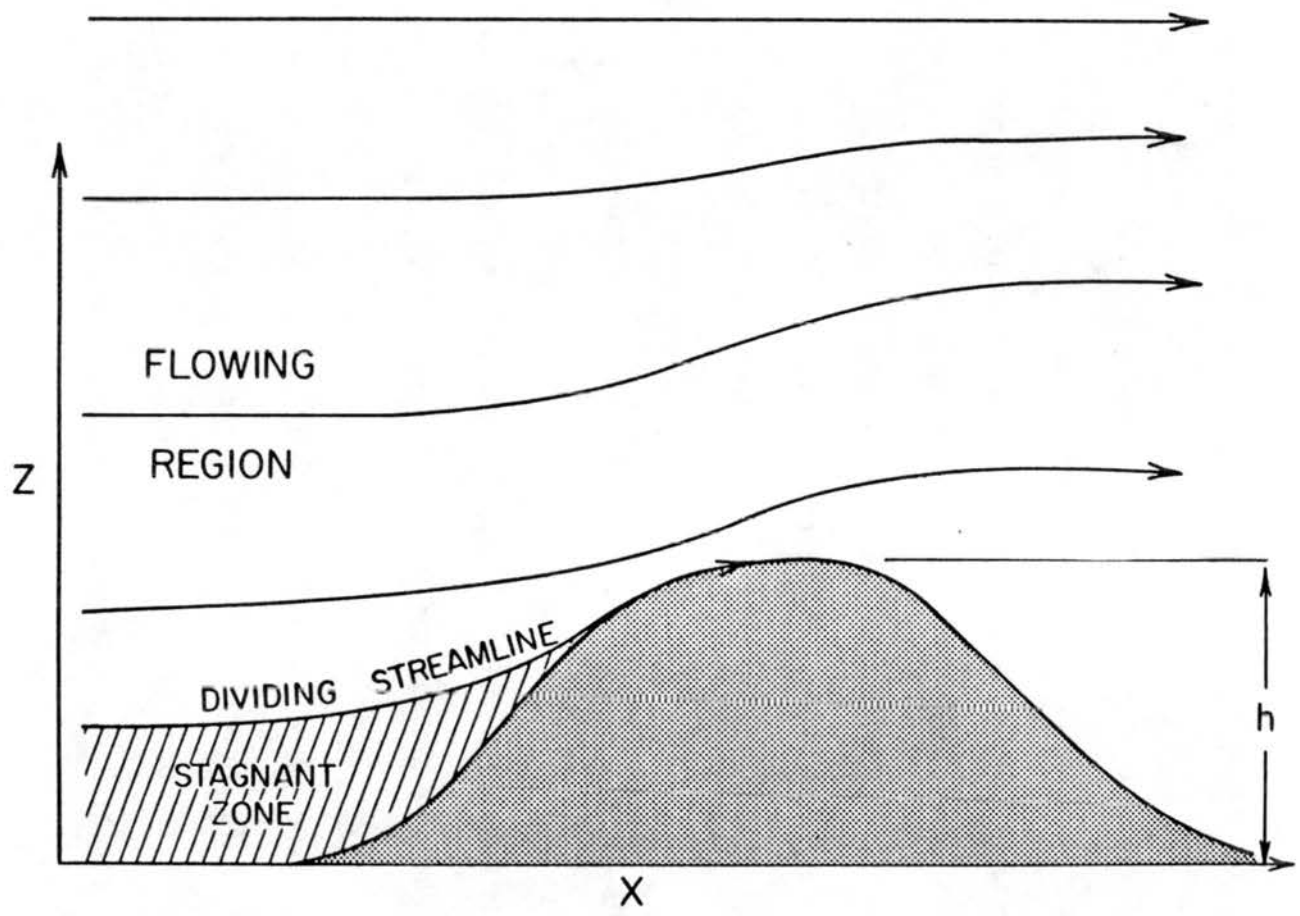


Figure 6. Schematic representation of flow over a two-dimensional barrier with a stagnant region of blocked flow below the dividing streamline.

## CHAPTER III.

### OBSERVATIONS OF MESOSCALE BOUNDARY LAYER STRUCTURE

Several different types of meteorological data were collected on two occasions when the evolution of the mesoscale boundary layer was observed. The principal data sets were vertical soundings of pressure, temperature and wind from several stations in the area shown in Fig. 7. This region in northwestern Colorado could be the site of extensive future development because it contains nearly all of the recoverable shale oil found in the state. As can be seen, the terrain generally slopes upward toward the east before encountering the high barriers shown by the shaded regions (elevations above 9000 ft MSL). Three major river systems pass through this part of the state. To the south, the Colorado River runs through a gap in the high terrain as it enters the area. Running through the region depicted in the center of the map is the White River and its tributaries which have their headwaters in the elevated barrier to the east. Farther north, the Yampa River drains a wide basin in the corner of the state before merging with the Green River near the Utah border. The primary region of interest in this study lies between the Colorado and White Rivers and west of the high barriers. The topography in this area consists of many narrow and deep creek and river valleys embedded in a high, gently sloping land mass known as the Roan Plateau.

Two separate field experiments were undertaken to identify the mesoscale circulations and examine the seasonal boundary layer

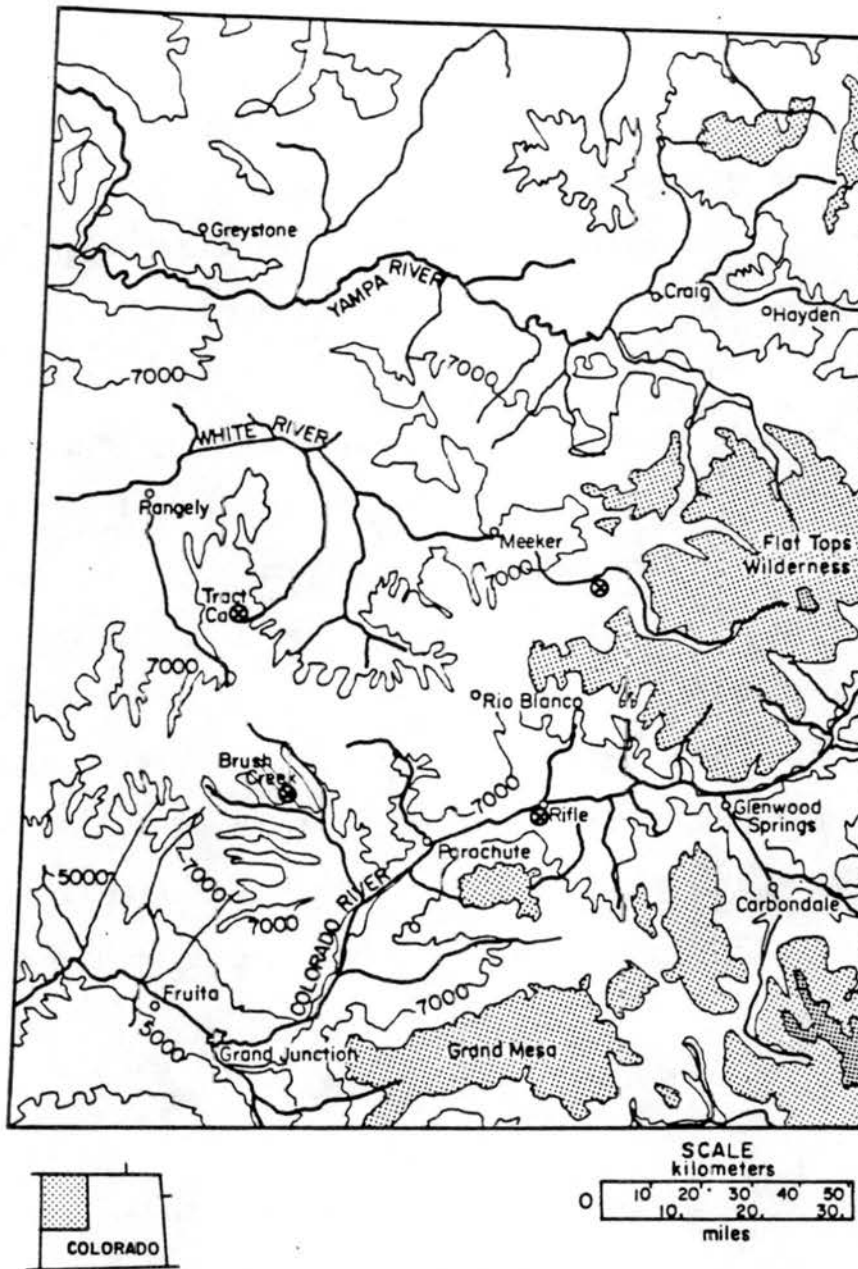


Figure 7. Map of study region in northwest Colorado. Contour interval is 2000 ft MSL and cross-hatched areas represent topography higher than 9000 ft MSL.

variability between summer and winter. The first observational period, ASCOT 82, commenced on the evening of 30 July 1982 and continued through the following morning. During this time, deep vertical soundings were taken to levels above 500 mb in conjunction with a cooperative study of local wind systems in the Brush Creek Valley undertaken by the Department of Energy's ASCOT program. The second observational period, CSU 84, started on the afternoon of 20 January 1984 and continued through the following morning as well. For this experiment, periodic deep vertical soundings were taken simultaneously from three sites; one located at Rifle, a second located near oil shale tract Ca and a third placed upstream from Meeker at a resort on the White River. Wind data above 1 km AGL collected with an experimental microwave wind profiler located at Craig were also available for this period. The exact location of the sounding stations for both periods are shown by the X marks in Fig. 7. Additionally, upper air soundings collected by the National Weather Service (NWS) rawinsonde station at Grand Junction (GJT) were used to supplement data collected during both field exercises.

#### A. Data Collection and Reduction Procedures

The deep vertical soundings were taken with free balloon-borne sondes (Airsondes<sup>®</sup>)<sup>1</sup> instrumented to measure absolute pressure, temperature and, in the case of the first experiment, wet bulb temperature. The pressure sensor was an electronic aneroid barometer accurate to 1 mb absolute pressure. Both wet bulb and dry bulb measurements were made with electronic thermistors accurate to 0.5°C

---

<sup>1</sup> Airsonde is a trademark of AIR, Inc., Boulder, CO.

over the range observed in both field programs. The information was relayed to a portable ground receiver by a small FM transmitter carried in the instrument package at a rate of 11 data scans per minute. Initial processing was performed in the field by a microprocessor located in the ground station. Data were recorded by the microprocessor onto an audio cassette tape as well as printed in real-time on a printing calculator. Prior to launch, each package was checked against surface pressure and temperature references in order to establish an absolute baseline. The sondes were carried aloft by standard 30 g pilot balloons overinflated to give an ascent rate of  $0.2 \text{ m s}^{-1}$ . When possible, a single meteorological theodolite was used to optically track each sonde with measurements accurate to 0.1 degrees being recorded at 30 s intervals. As part of the local wind study in the Brush Creek Valley, high resolution vertical profiles of wind and temperature below the valley ridgetop ( $z < 650 \text{ m AGL}$ ) were also collected during the ASCOT 82 experiment with a tethered balloon sounding instrument package which utilizes the same ground station described previously. The temperature sensors in this system are very similar to those in the upper-air sondes and pressure measurements were accurate to 0.1 mb. Additionally, the tethered system is capable of wind measurements accurate to  $0.2 \text{ m s}^{-1}$  in speed and 5 degrees in direction. More details about the tethered balloon system are available in Whiteman (1980).

Baseline air temperatures were measured with high resolution mercury thermometers and wet bulb temperatures were measured with an Assman psychrometer. For the ASCOT 82 experiment and for the Ca and Meeker sites in the CSU 84 experiment, surface pressure was measured with high resolution aneroid microbarometers. All three sites during

the CSU 84 experiment were equipped with recording microbarographs accurate to 0.5 mb. All pressure instruments were referenced to a mercurial barometer both before and after each experiment to check their performance. Data reduction was simple and straightforward. Temperature and pressure measurements were corrected according to baseline references. The corrected sounding data were then integrated hydrostatically to yield height profiles of temperature, pressure, potential temperature and, in cases when wet-bulb sondes were used, relative humidity. Wind computations were made by correlating theodolite readings with sonde elevations. The resulting profiles were then subjectively analyzed to eliminate obviously bad data.

## B. ASCOT 82 Experiment

### 1. Synoptic weather conditions

The ASCOT 82 experiment occurred during a period of climatically typical late summer weather in western Colorado. A prevailing southwesterly synoptic flow, commonly called the southwest monsoon, brought moist air from the Pacific Ocean into the inter-mountain region of the western U.S. As a result, afternoon and evening convective storms appeared frequently in areas west of the high mountain barriers. However, a break in the convective activity during the period between 29-31 July permitted the execution of the first observational experiment. Figures 8-10 show the National Meteorological Center (NMC) upper-air synoptic analyses for 1200 GMT (LST + 7 h), 30 July; 0000 GMT, 31 July; and 1200 GMT, 31 July. The NMC surface analyses are not used for two reasons. First, the entire study region lies near or above the 850 mb level. Moreover, the adjustment that is used to reduce observed

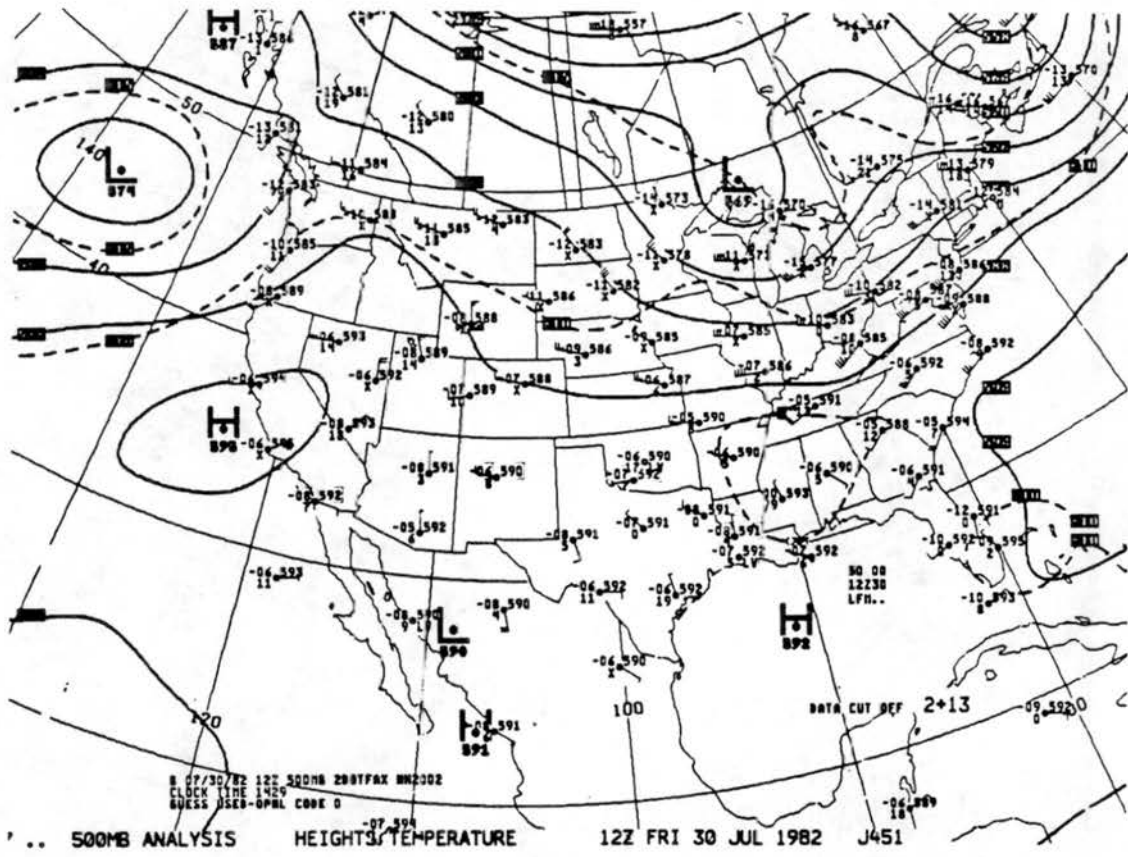


Figure 8a. National Meteorological Center (NMC) analysis for 1200 GMT on 30 July 1982 for 500 mb.

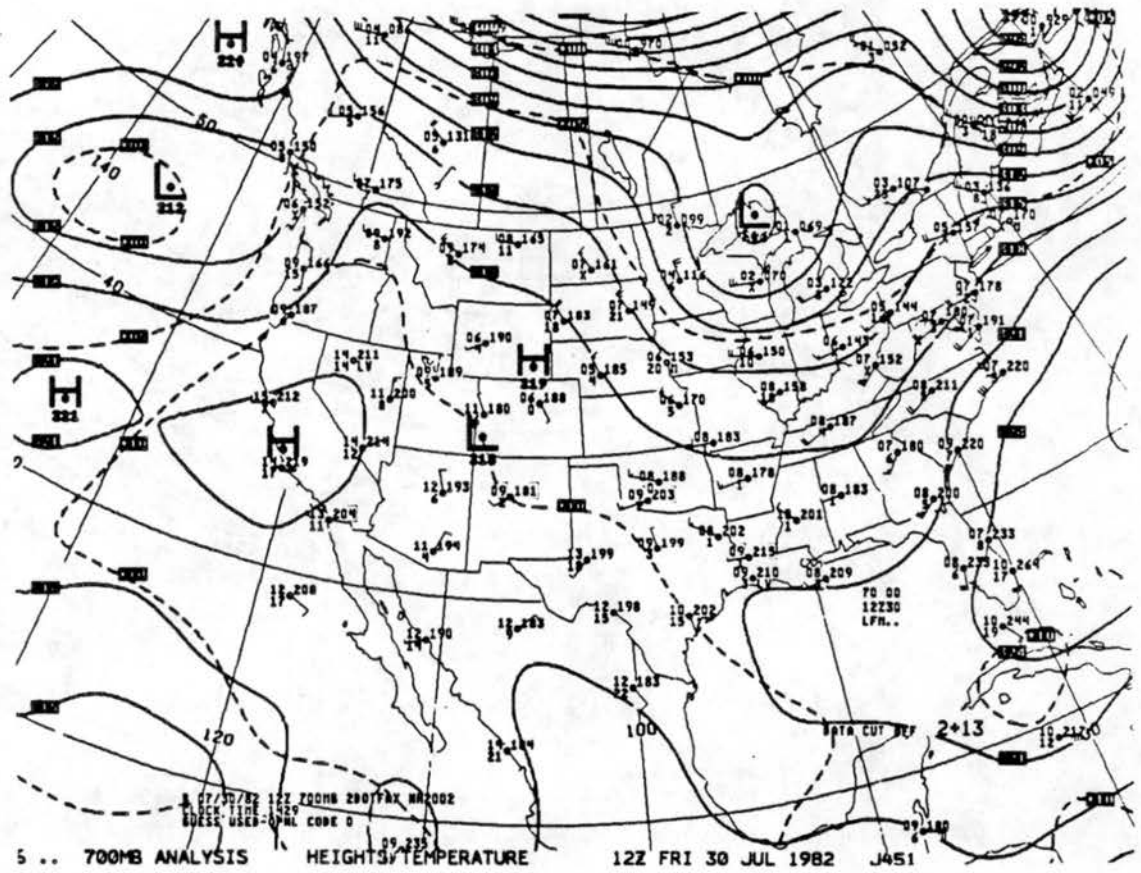


Figure 8b. NMC analysis for 1200 GMT on 30 July 1982 for 700 mb.

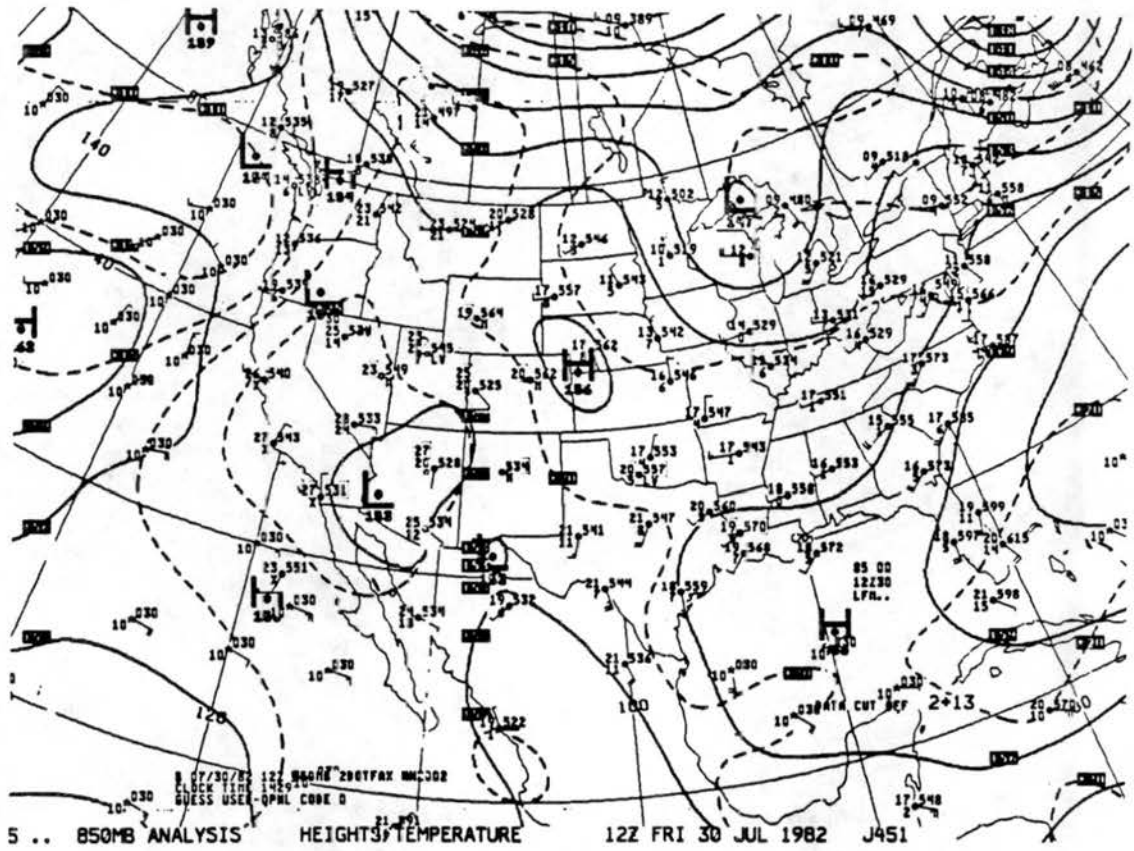


Figure 8c. NMC analysis for 1200 GMT on 30 July 1982 for 850 mb.

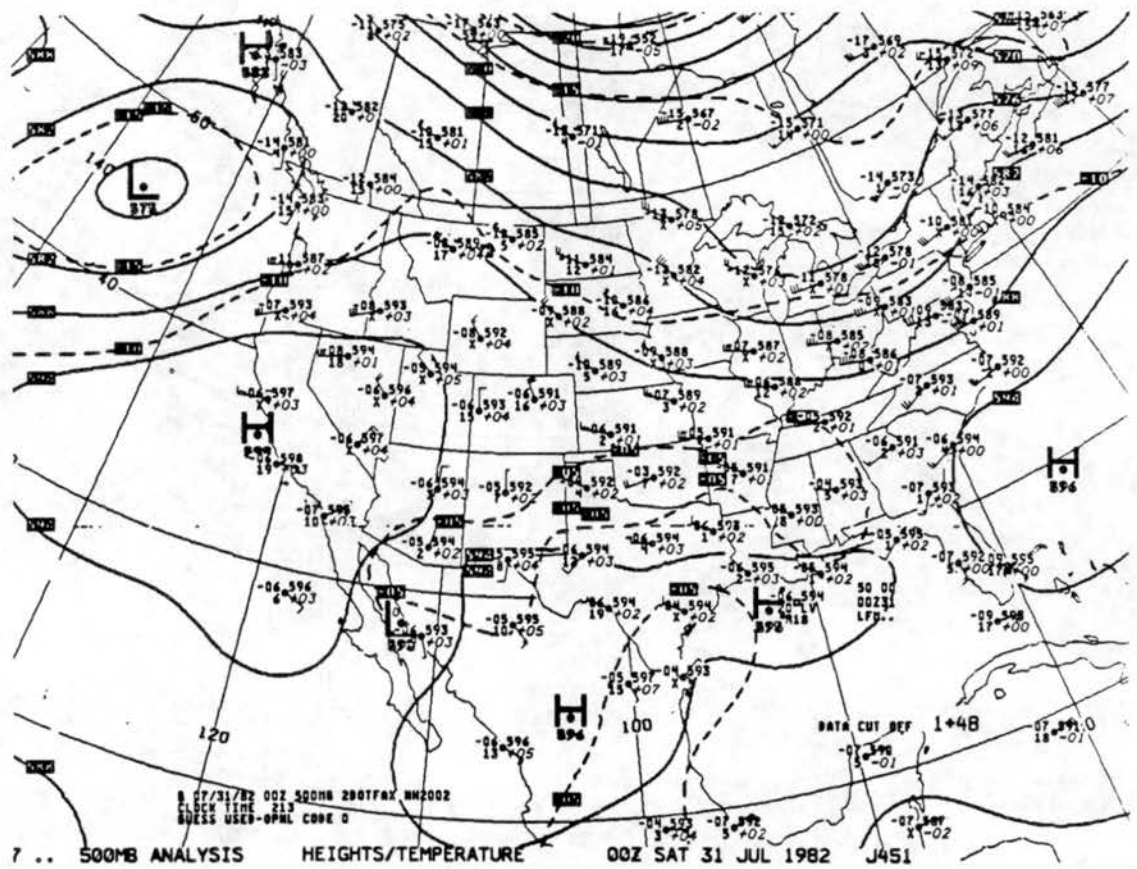
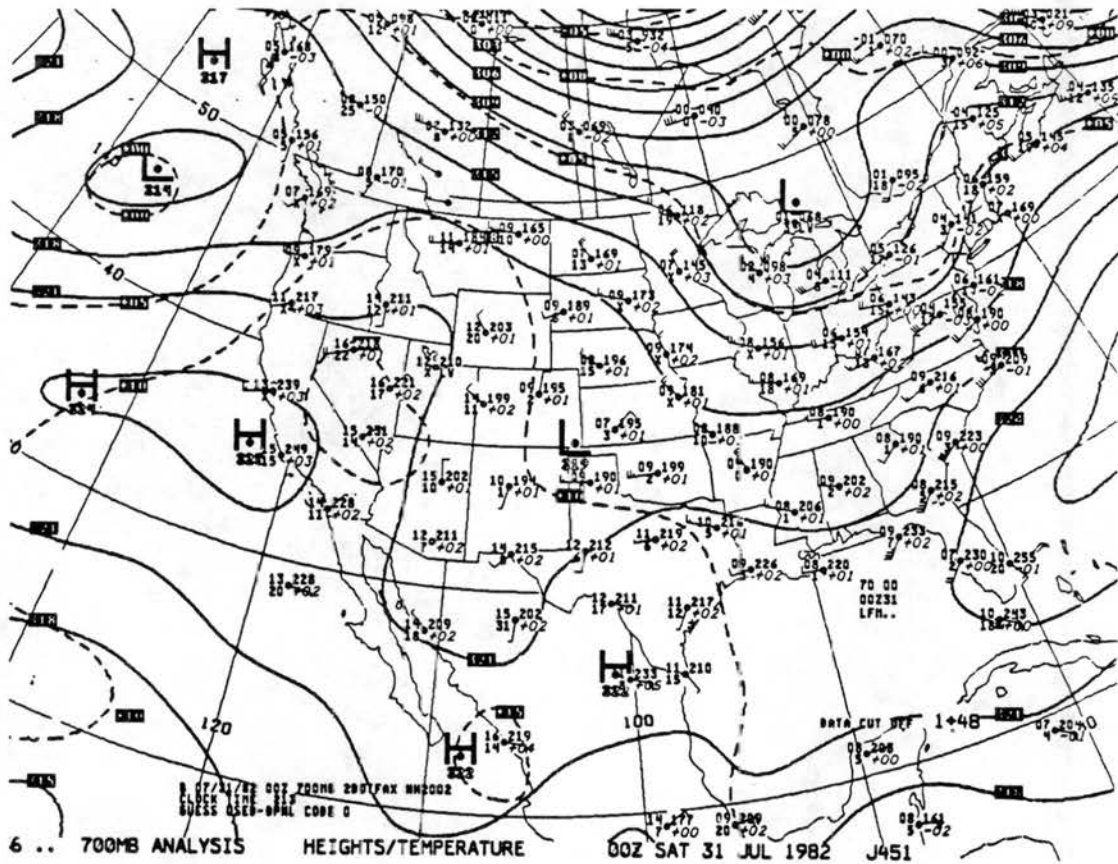


Figure 9a. NMC analysis for 0000 GMT on 31 July 1982 for 500 mb.



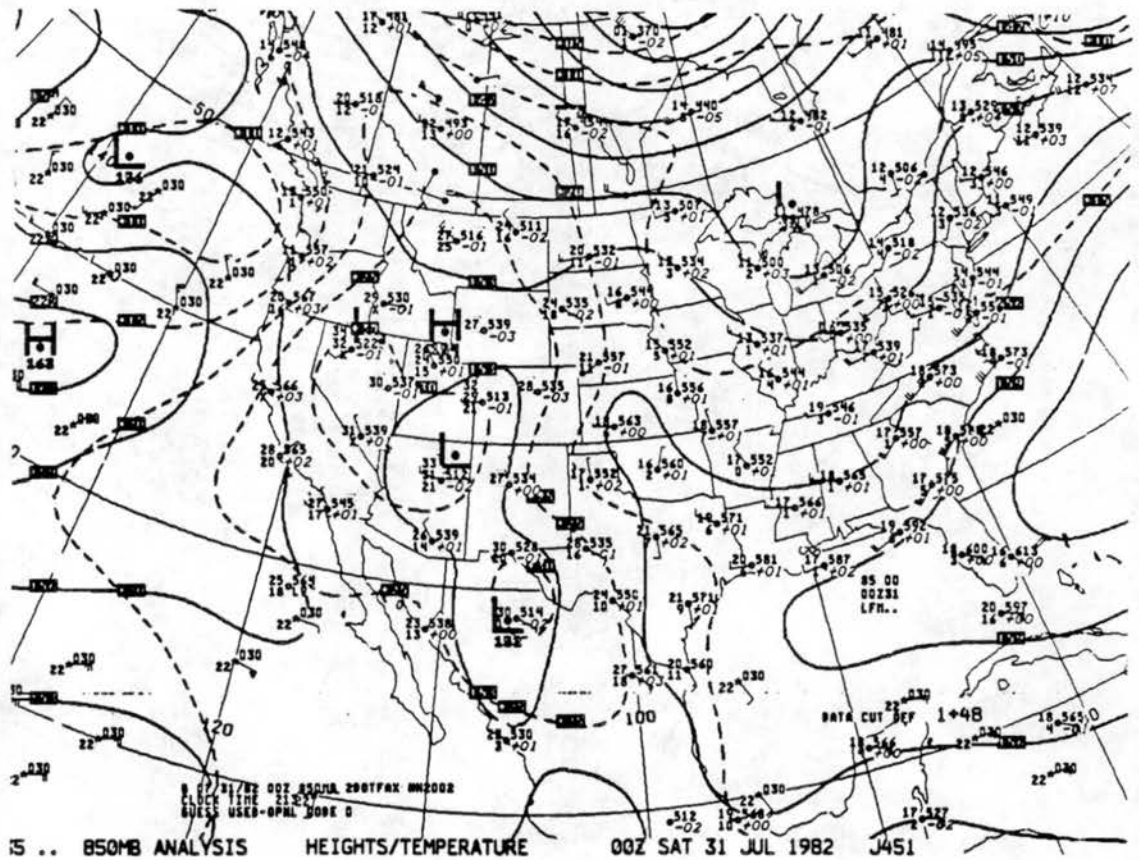


Figure 9c. NMC analysis for 0000 GMT on 31 July 1982 for 850 mb.

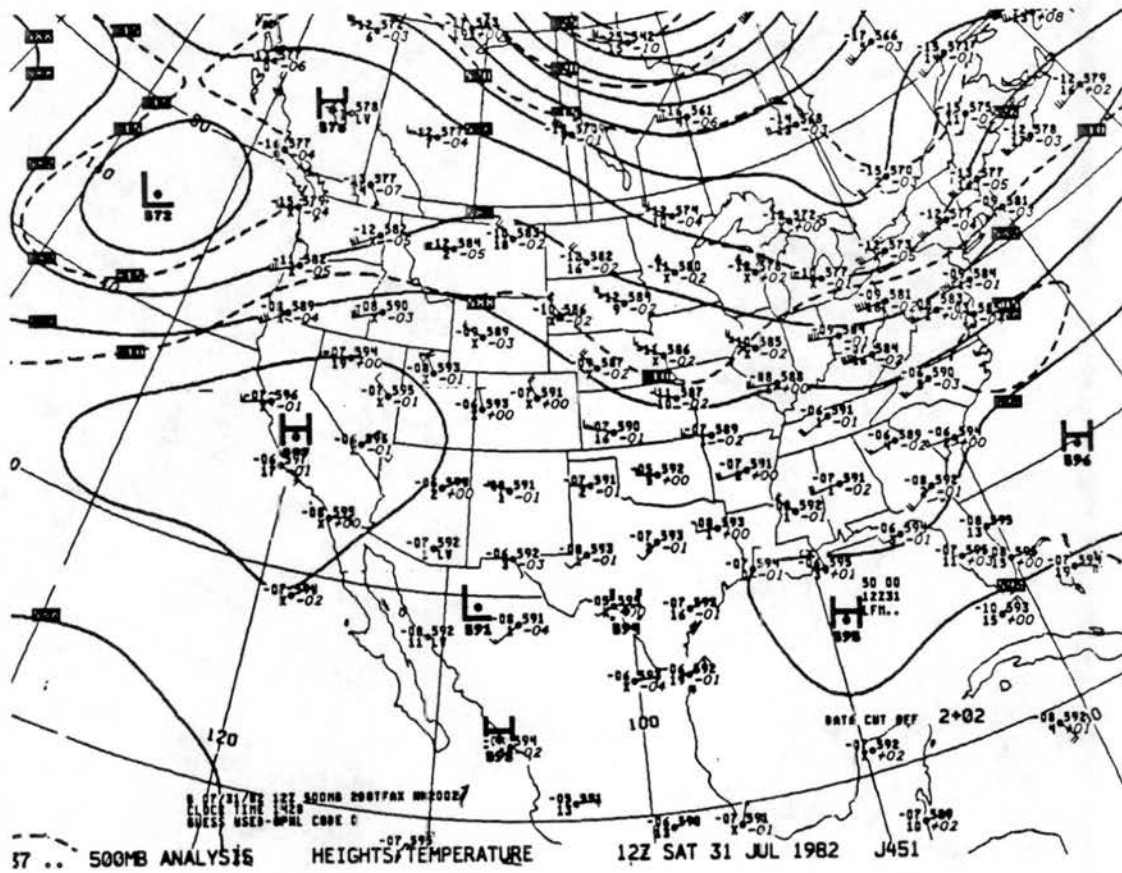


Figure 10a. NMC analysis for 1200 GMT on 31 July 1982 for 500 mb.

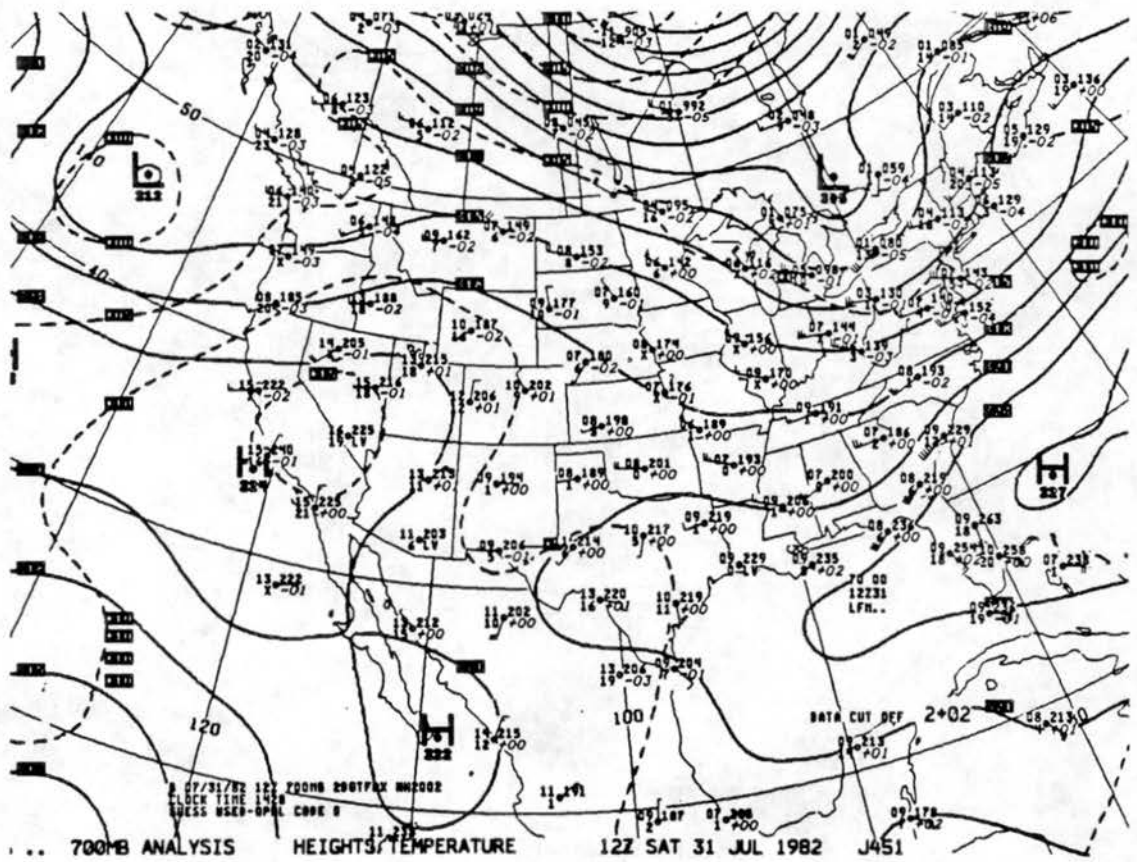


Figure 10b. NMC analysis for 1200 GMT on 31 July 1982 for 700 mb.



station pressures to sea-level equivalent values can lead to fictitious synoptic surface weather features on analyzed maps. Unfortunately, the density of the NWS rawinsonde stations does not provide the high resolution afforded by the surface data network, but this is not a great problem for this period when synoptic-scale forcing was weak. As can be seen, the southwest was dominated by a large subtropical high-pressure band with nearly stationary geopotential and temperature fields. At the GJT station, the 24 h observed temperature changes were  $1^{\circ}\text{C}$  or less at all three levels with height rises of 30 m at 700 mb and 40 m at 500 mb mostly resulting from the deep boundary layer heating during the day. The synoptic winds as well as geopotential height and temperature gradients were weak, making the situation nearly ideal for observations of local and mesoscale thermal circulations.

Figure 11 displays the GJT 0000 GMT rawinsonde data for 31 July, which was launched near 1600 LST on the afternoon of 30 July (rawinsonde launch times at GJT precede the actual synoptic reporting time by 1 h). The Grand Junction NWS weather station is located in the Colorado River Valley slightly northeast of the city at the Grand Junction airport. Station elevation is 1472 m MSL (4830 ft MSL), which is approximately 500 m lower than the tops of the nearby valley sidewalls. As a result, the GJT sounding data below 500 m AGL is often very strongly influenced by the local wind and thermal structure produced within the river valley, which may show little resemblance to the larger mesoscale and synoptic scale structures above the surrounding ridgetops. The sounding shows the existence of a very deep, surface based convective boundary layer (CBL) with potential temperatures of 318-319 K. From the coarse resolution rawinsonde data, the capping inversion at the top the CBL is

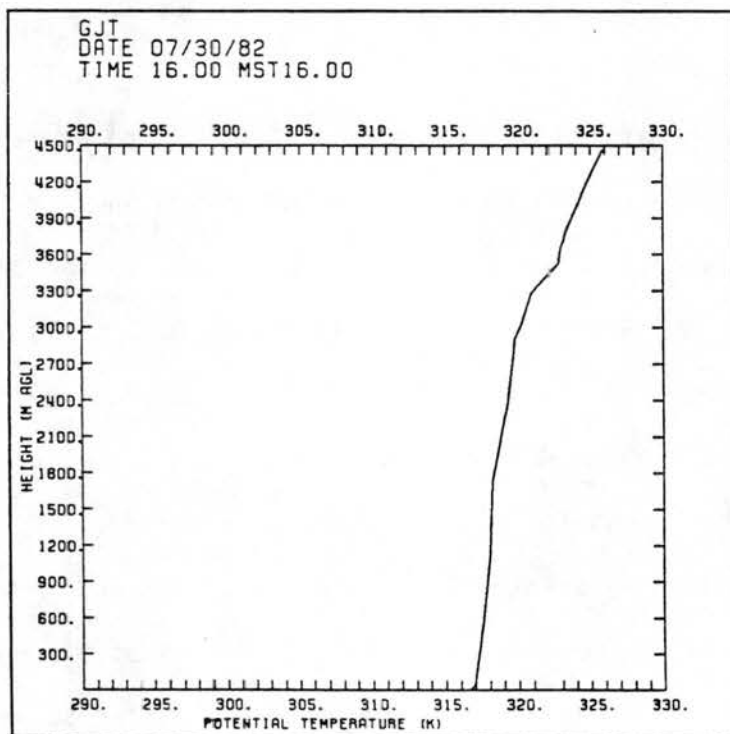
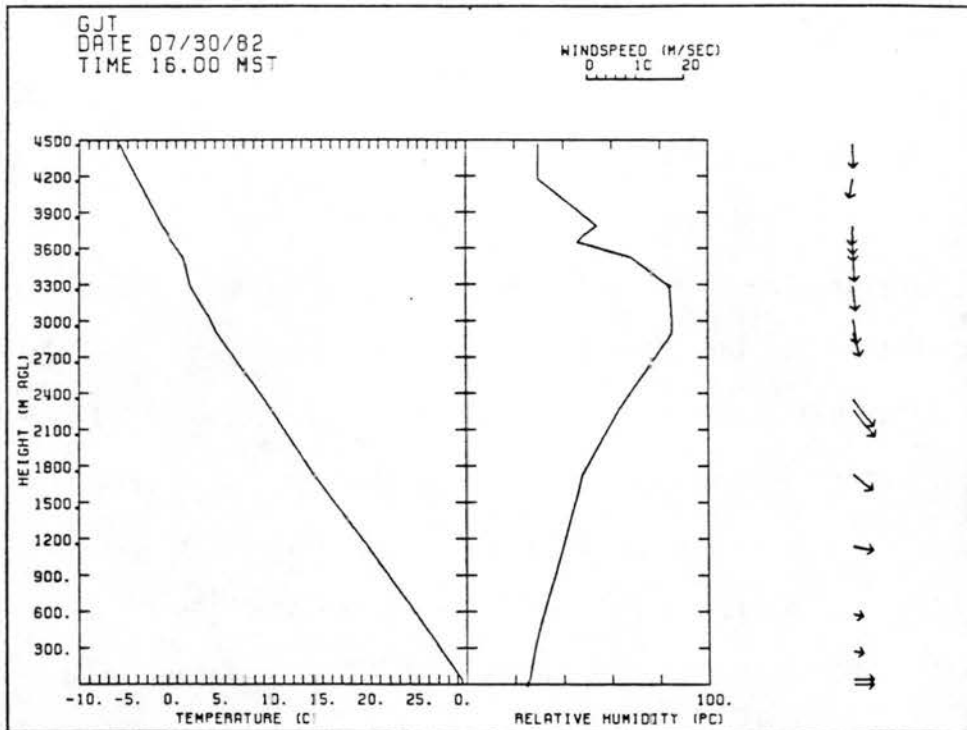


Figure 11. National Weather Service (NWS) Grand Junction (GJT) rawinsonde sounding for 1600 LST on 30 July 1982.

not apparent. However, the coincidence of an inflection in the potential temperature profile with the elevation of the relative humidity maximum would locate the top of the CBL at 2800 m AGL. Winds are light and westerly up to 1200 m AGL before increasing in speed as they develop a northerly component with height. Above the inferred top of the CBL, the winds exhibit a predominantly northerly direction, showing a distinct directional shear across the mixed layer top, an observation consistent with ideal boundary layer behavior.

Contrasted with the 0000 GMT sounding is the 1200 GMT sounding taken 12 h later (Fig. 12). During the night, a distinct two layer structure has replaced the well-mixed CBL present the previous afternoon. The lower layer extends to 1000 m AGL and has a nearly uniform potential temperature lapse rate of  $3.0 \text{ K km}^{-1}$ . It is topped by a thin, nearly isothermal region which separates it from an adiabatic layer that extends to 2000 m AGL. Another isothermal transition region, possibly the remnants of the capping inversion from the previous day, lies between 2000 and 2300 m AGL and separates the adiabatic layer from the free air above it. All levels below 2300 m also exhibit some degree of cooling from the 0000 GMT sounding, showing significant effects at levels well above what is consistent with typical nocturnal boundary layer (NBL) behavior. The east-northeast winds in the very lowest part of the sounding are the local down-valley flows. However, the east winds between 600 and 1200 m AGL are not associated with the valley circulation and appear to be part of the larger scale mountain-plain circulation formed in response to the cooling of the elevated land to the east. Unfortunately, only two data points were available in the overlying layer, but they display a transition from the easterly

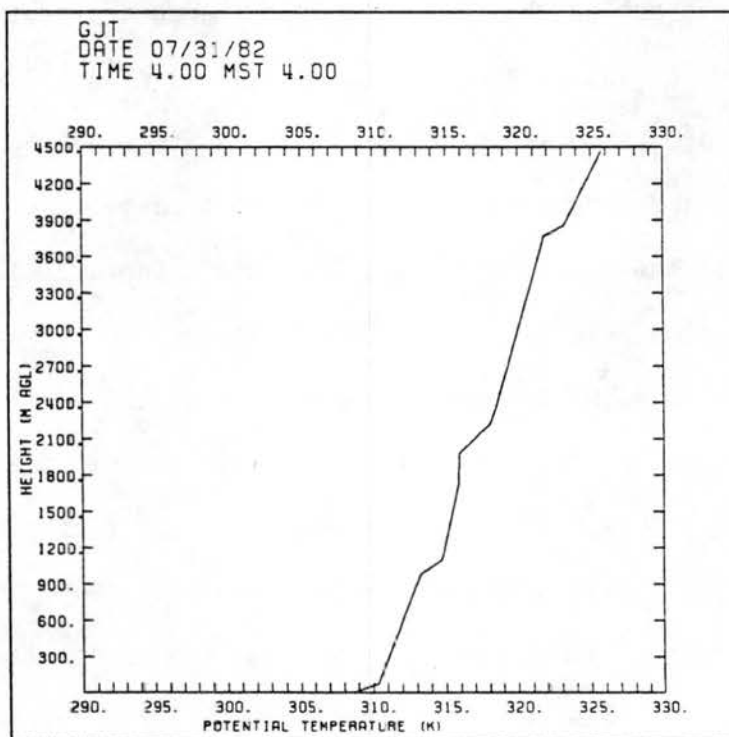
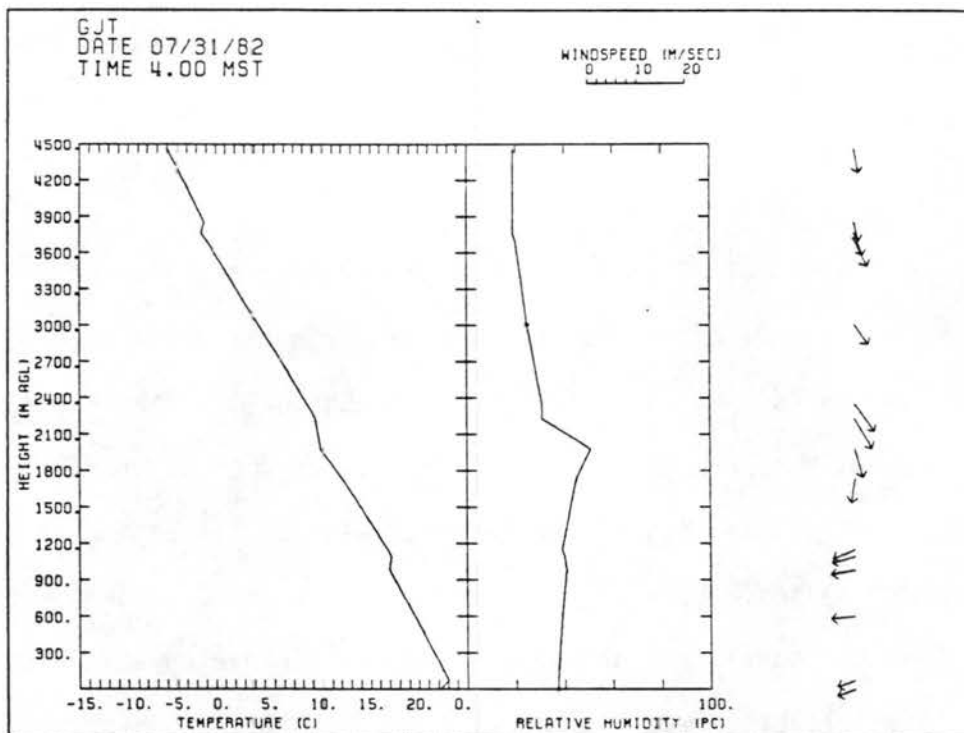


Figure 12. NWS GJT rawinsonde sounding for 0400 LST on 31 July 1982.

direction found in the lower layer to northwest winds in the free air at higher elevations.

## 2. ASCOT 82 observations

The ASCOT 82 observational site was located in the Brush Creek Valley approximately 2.5 km upstream from the confluence of Brush and Roan Creeks. Cut into the southern edge of the Roan Plateau, this valley is nearly geometrically ideal with smooth, uniformly sloping sidewalls along its entire length. With the exception of several small side canyons, the valley floor width linearly decreases with distance from the confluence and lies 650 m below ridgetop at the observational site; elevation was 1783 m MSL (5850 ft MSL), 311 m above GJT. Table 1 lists information about each sounding taken during the observation period which lasted from 1700 LST on 30 July to 0900 LST on 31 July.

Figure 13 shows the 1900 LST upper-air sounding taken near the start of the experiment. Although local sunset was not until about 1930 LST, the valley floor was shaded and surface cooling had formed a very shallow inversion layer under the deep, well mixed CBL extending to 2400 m AGL. CBL temperatures were between 317 and 318 K, which are slightly cooler than the 318-319 K range seen in the GJT 0000 GMT sounding. This difference appears to be real, as the deviations from the GJT potential temperatures at elevations above the inversion layer range from 0.1-1.2 K warmer, revealing the mesoscale influence of differential boundary layer heating. The high resolution airsonde sounding does reveal a well defined 2 K capping potential temperature inversion 2400 m AGL, which clearly marks the top of the CBL. Based on this observation, the inferred elevation of the CBL top estimated from the GJT sounding appears to be correct. However, the winds observed in

Table 1.  
Times of ASCOT 82 Soundings

<u>Sounding Time</u>	<u>Sounding Type</u>	<u>Release Time</u>
1800 LST	Tethersonde	1756 LST
1900 LST	Airsonde	1842 LST
2000 LST	Tethersonde	2011 LST
2100 LST	Tethersonde	2059 LST
2200 LST	Tethersonde	2159 LST
2300 LST	Airsonde	2251 LST
0000 LST	Tethersonde	0001 LST
0100 LST	Tethersonde	0057 LST
0200 LST	Tethersonde	0155 LST
0300 LST	Tethersnde	0303 LST
0400 LST	Airsonde	0353 LST
0500 LST	Tethersonde	0500 LST
0600 LST	Tethersonde	0556 LST
0700 LST	Tethersonde	0656 LST
0800 LST	Airsonde	0801 LST
0900 LST	Tethersonde	0904 LST

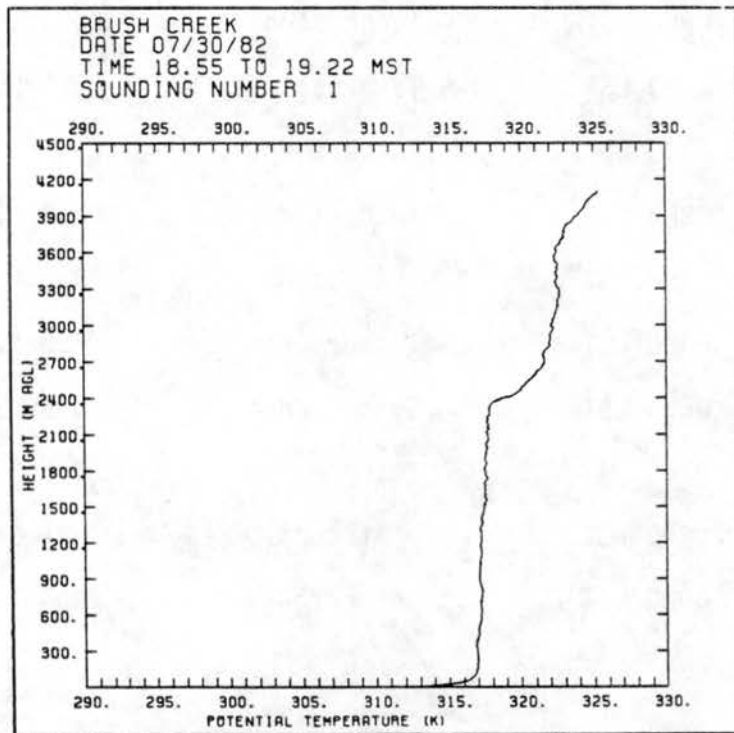
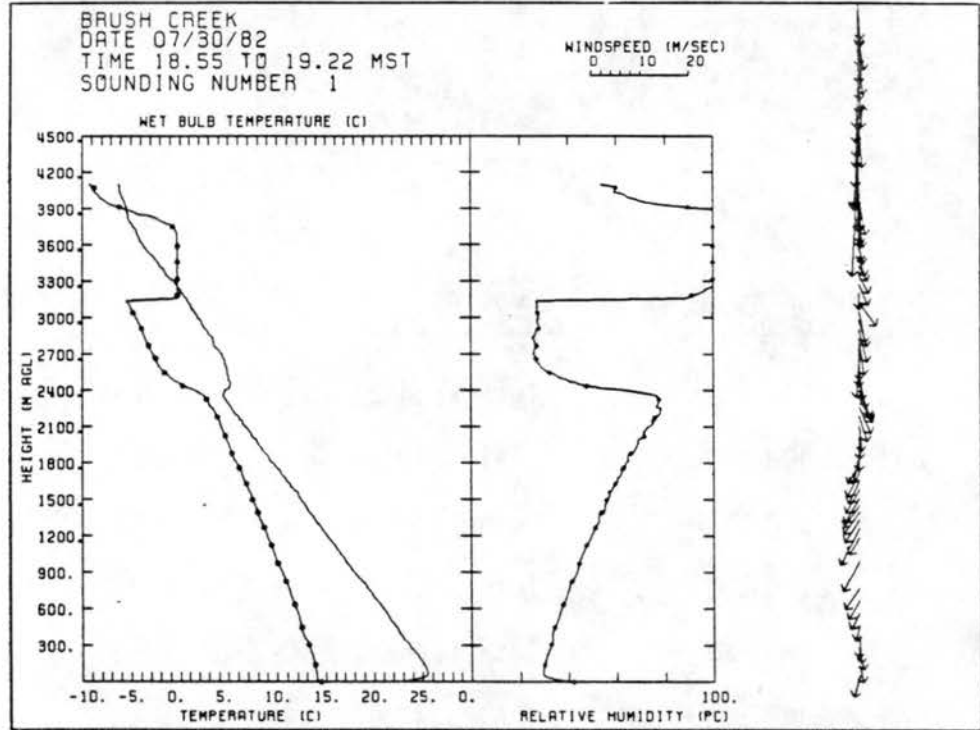


Figure 13. Brush Creek site airsonde sounding for 1900 LST on 30 July 1982 (solid pattern - dry bulb temperature and circle pattern - wet bulb temperature).

this sounding differ greatly from the GJT wind profile. Whereas the GJT winds in the lower CBL were predominantly westerly with speeds less than  $5 \text{ m s}^{-1}$ , winds in the same layer over the Brush Creek site were northeasterly with speeds of  $5\text{-}10 \text{ m s}^{-1}$ . Near the top of the CBL the winds rotated smoothly to a northwest direction, as was found in the GJT profile. Across the inversion layer, the winds abruptly shifted to north, similar to the GJT observations. The appearance of the northeast wind component is consistent with the ageostrophic effect produced by the differences in observed CBL temperatures between Brush Creek and GJT. Another possibility is that the observed winds could be the result of dynamic interactions between the nearby terrain and the mixed layer wind field, but this cannot be fully determined without more data. The west winds above GJT are more easily explained as part of the daytime mountain-plain circulation forced by the elevated terrain of Grand Mesa to the east of Grand Junction.

The airsonde sounding taken at 2300 LST reveals that a 1000 m deep stable layer has formed under the neutral layer remaining from the daytime CBL (Figure 14). A surface based inversion layer extends to 300 m and is topped by a nearly isothermal layer that extends to the valley ridgetops at 600 m AGL. In the transition layer between 600 m AGL and 1000 m AGL, the air has cooled  $0\text{-}2^\circ\text{C}$  in the 4 h from the previous sounding, a change too large to be attributed to clear air radiational cooling. Below ridgetop, the winds were blowing primarily down-valley. Above this level, however, wind data were not available below 2000 m AGL due to the difficulties encountered in tracking the balloons at night. Winds immediately below the top of the mixed layer were still northeasterly and they shifted to northerly above the

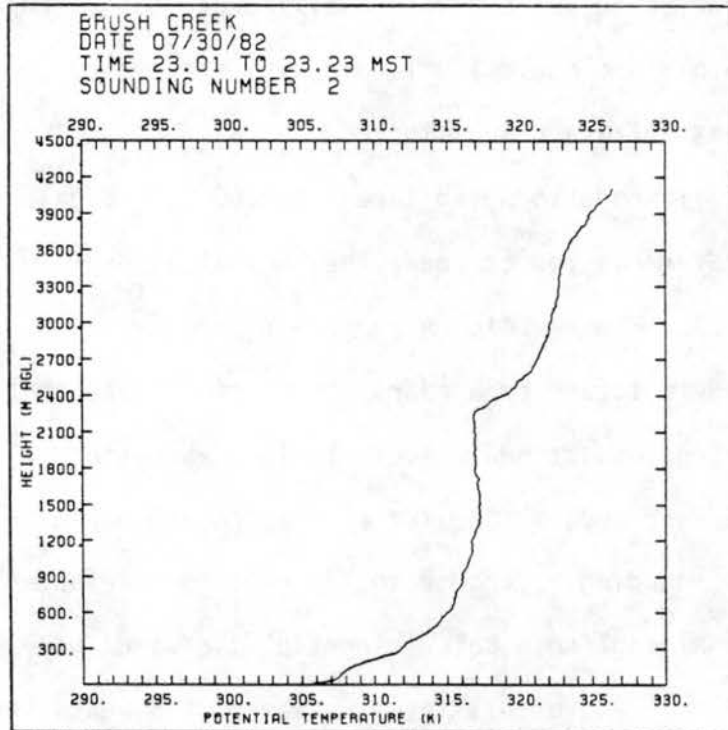
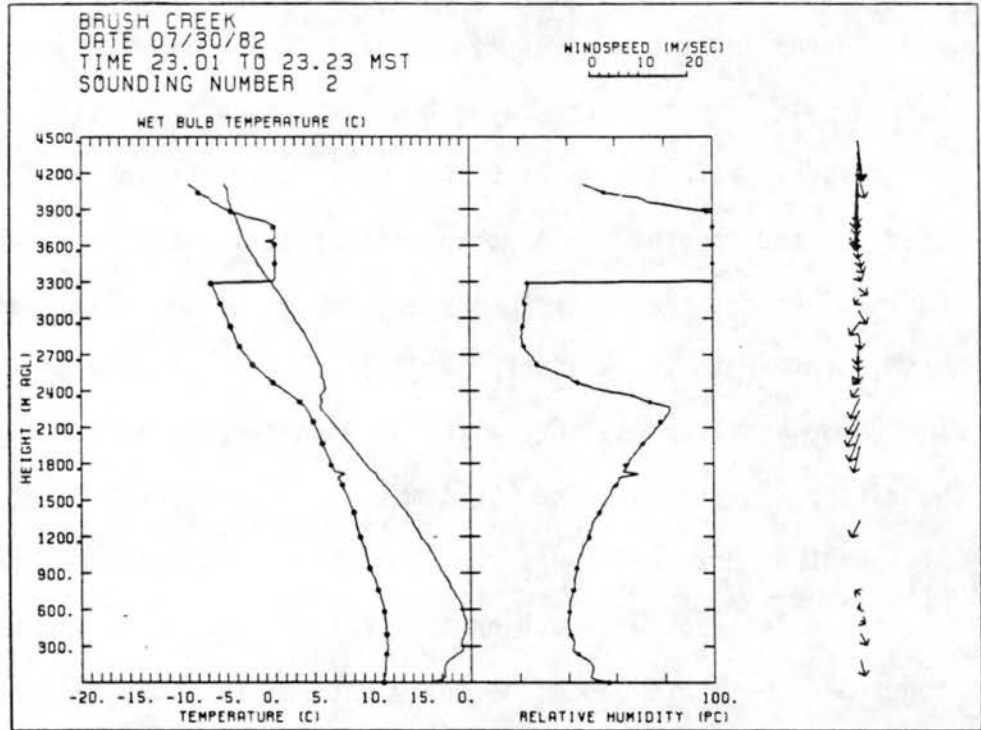


Figure 14. Brush Creek site airsonde sounding for 2300 LST on 30 July 1982 (solid pattern - dry bulb temperature and circle pattern - wet bulb temperature).

inversion, as was observed in the previous sounding. At this time, the level of the capping inversion is 100 m lower than it was at 1900 LST and it was slightly more diffuse.

Figure 15 shows the 0400 LST airsonde measurements taken 5 h later. The isothermal layer extends above the surface inversion to ridgetop, much like the structure seen in the 2300 LST profile. However, the 400 m deep transition layer evident previously has disappeared and the top of the mixed layer has descended to 2000 m AGL, 400 m lower than its level at 1900 LST. Approximately 30 m of the descent can be attributed to diabatic compression with the remainder resulting from adiabatic subsidence. Wind data below 1800 m AGL were sparse due to the same difficulties mentioned before, but winds above this level show a shift to a northwest orientation from the northeast direction observed in the earlier soundings. The descent of the mixed layer top is consistent with the GJT 0400 LST sounding data which were collected simultaneously with the airsonde measurements. This subsidence appears to be the part of the mesoscale nocturnal mountain-plain circulation in the absence of any larger scale baroclinic forcing. Neff (1983) believed similar effects could be produced in a single profile by a large scale gravity wave. This explanation, though possible, is discounted for several reasons. First, the near neutral stability both above and below the mixed layer top would not favor propagation of such a large amplitude disturbance. Second, the onset of the subsidence occurred before 2300 LST as evidenced by the 100 m descent of the mixed layer top at that time. Last, the descent was observed at both GJT and Brush Creek, an unlikely coincidence in the case of a gravity wave. Observations taken during the Dischma Valley Experiment (see Whiteman and Dreisetel,

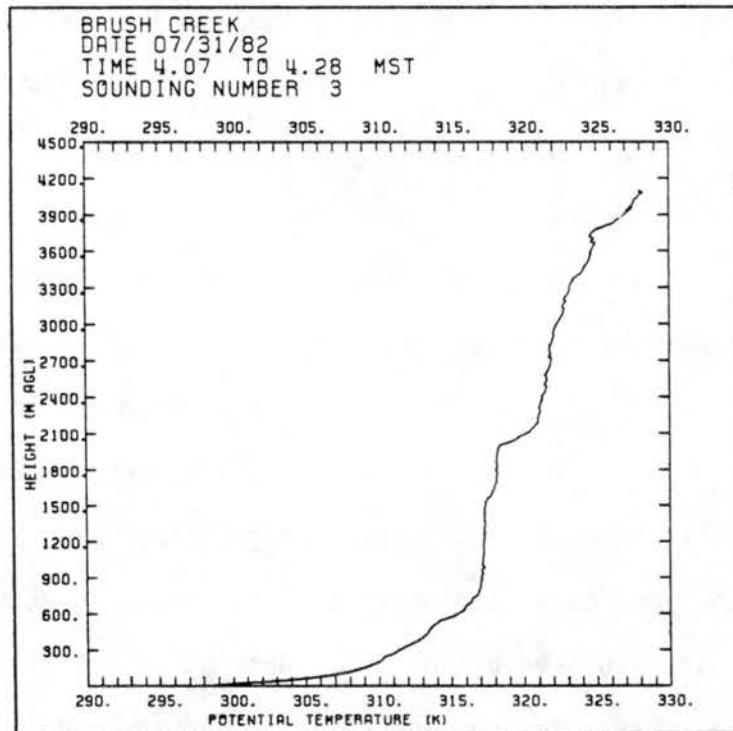
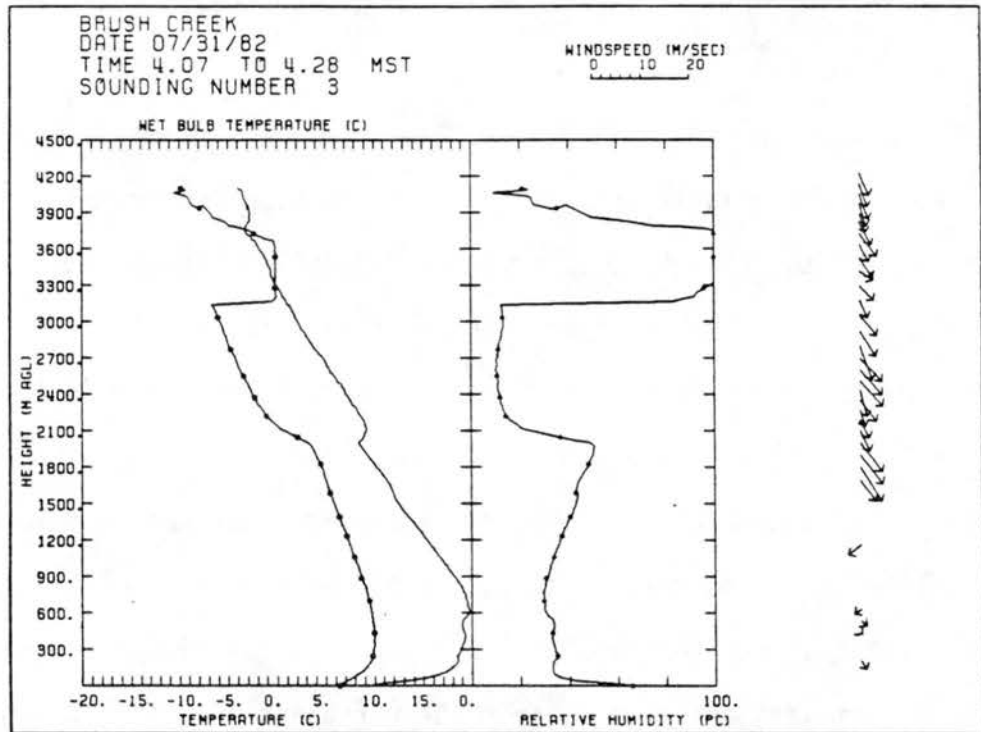


Figure 15. Brush Creek site airsonde sounding for 0400 LST on 31 July 1982 (solid pattern - dry bulb temperature and circle pattern - wet bulb temperature).

1984) show a similar subsidence through the night above an alpine valley in Switzerland (Whiteman, 1985).

Local sunrise on 31 July was a few minutes before 0600 LST. Figure 16 shows the airsonde sounding taken at 0800 LST in which light, up-valley (southeast) winds have appeared in the valley, although the speeds were less than  $2.0 \text{ m s}^{-1}$ . Winds between ridgetop and 1400 m AGL were light from the south-southeast before shifting abruptly to northwesterly above this level. Their appearance coincides with the  $1\text{-}2^\circ\text{C}$  cooling and resulting stabilization of the layer between ridgetop and 1800 m AGL. The stable region remaining from the capping inversion has risen to 2200 m AGL, showing a reversal in the subsidence observed throughout the night. Since it is still too early for the onset of lifting associated with the reversal of the mountain-plain circulation to occur, another factor must be the cause of the observed rise. The development of the westerly geostrophic wind component could be responsible, since a west wind would force convergence on the upwind side of the high terrain. This effect has been simulated in model experiments to be presented in a later chapter. The southerly winds above ridgetop were most probably the remnants of a nocturnal circulation induced by the large elevated terrain region to the south of the observational site.

Figure 17 displays the tethered balloon soundings taken at 2200 LST, 0300 LST, 0600 LST, 0700 LST and 0900 LST in the Brush Creek Valley. The first sounding shows the fully developed nocturnal structure typically observed in the Brush Creek Valley. The surface based inversion extends to 150 m AGL and underlies a deeper, quasi-isothermal layer. Strong down-valley (northwest) winds appear in the

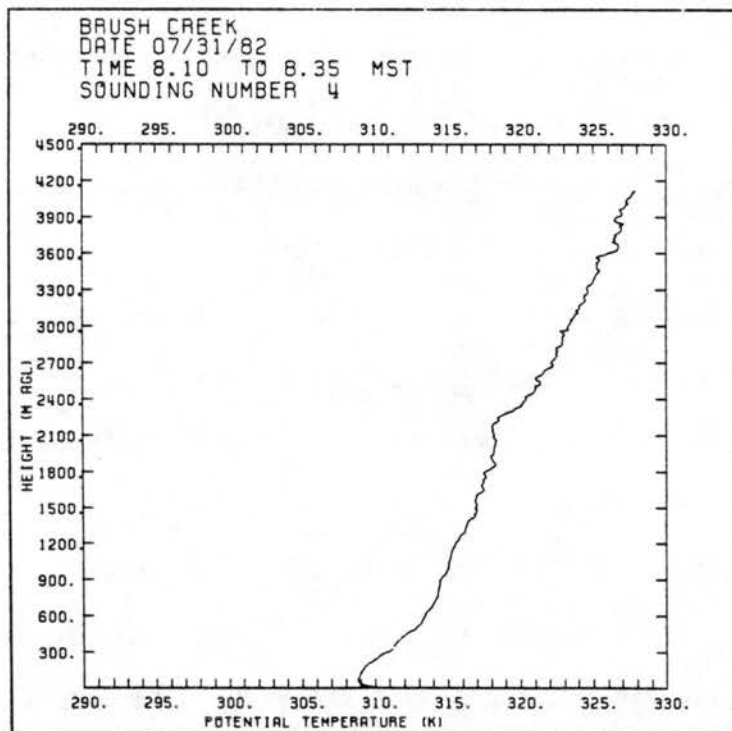
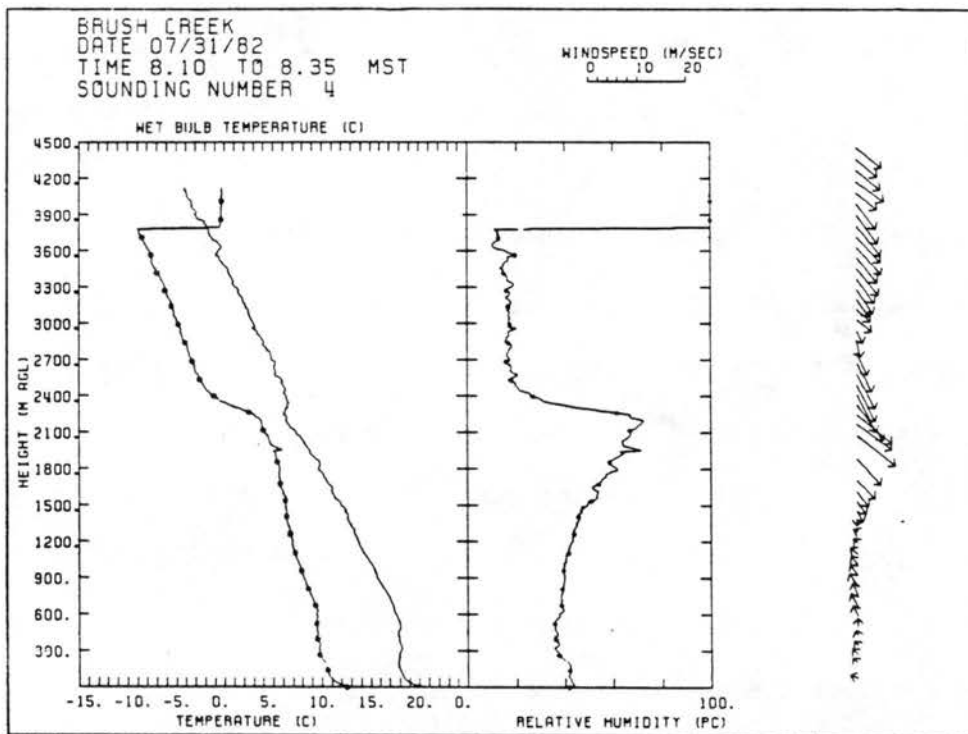


Figure 16. Brush Creek site airsonde sounding for 0800 LST on 31 July 1982 (solid pattern - dry bulb temperature and circle pattern - wet bulb temperature).

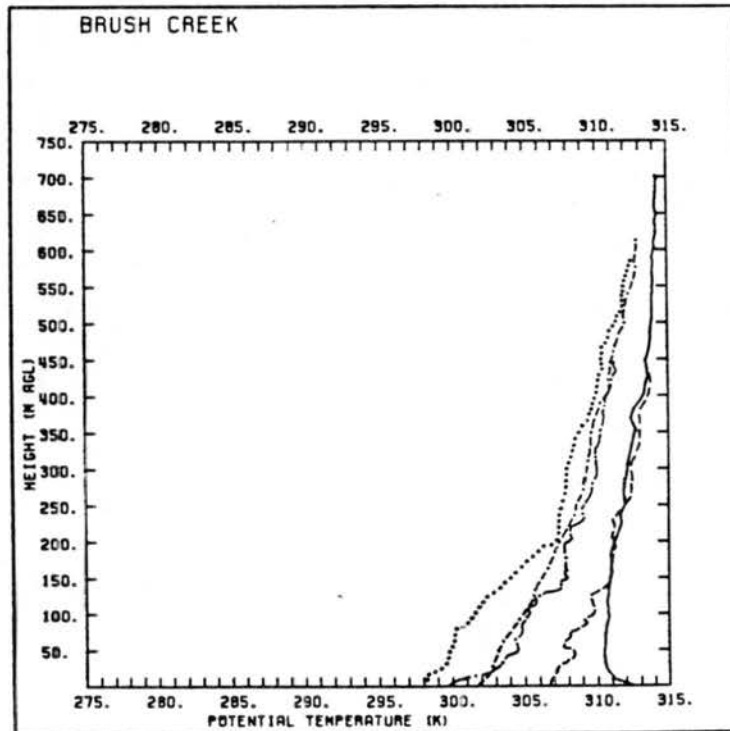
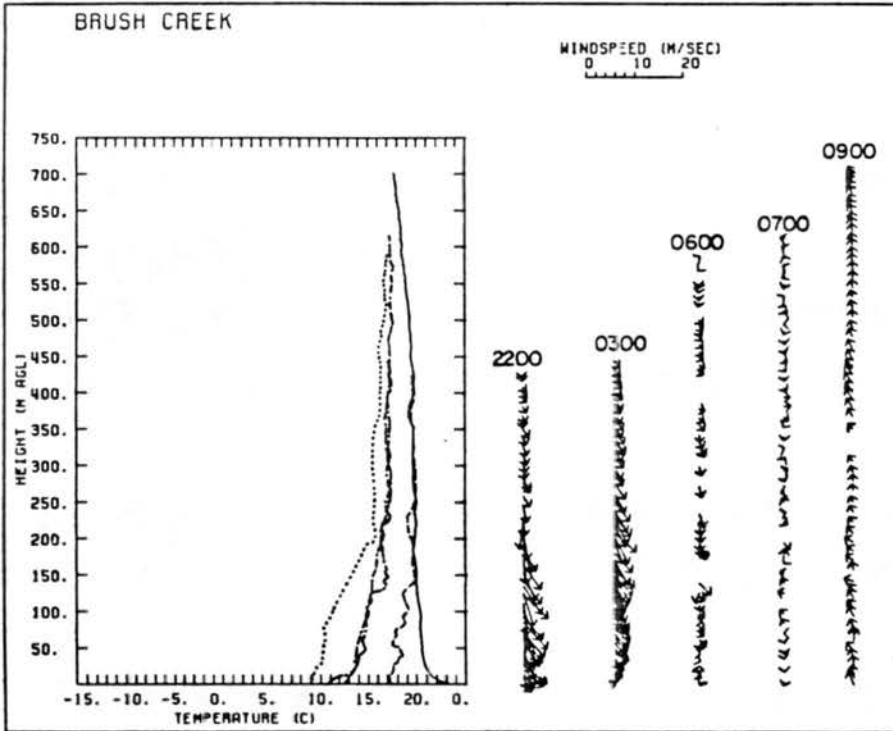


Figure 17. Brush Creek tether sonde soundings for 30-31 July 1982 for times 2200 (---), 0300 (·-·), 0600 (···), 0700 (·-·-·) and 0900 (—).

inversion layer with a maximum of  $7.5 \text{ m s}^{-1}$  at 80 m AGL. Speeds decrease steadily with height to near  $5.0 \text{ m s}^{-1}$  at 200 m AGL, then abruptly weaken to less than  $2.0 \text{ m s}^{-1}$  while retaining the down-valley orientation above this level. By 0300 LST, the surface based valley inversion layer has deepened to 230 m AGL. While the maximum wind speed has decreased to  $6.2 \text{ m s}^{-1}$ , the wind profile through the inversion layer has much less shear and generally higher speeds than was observed earlier. Wind speeds rise sharply from less than  $1.0 \text{ m s}^{-1}$  near the surface to above  $4.0 \text{ m s}^{-1}$  at 78 m AGL then increase more gradually to the maximum at 200 m AGL. Above this level, the speeds drop off slowly with height to values near  $2.0 \text{ m s}^{-1}$  at the top of the sounding at 450 m AGL.

At 0600 LST, the surface inversion is 200 m deep and the winds in the valley have weakened considerably since 0300 LST. Below 50 m AGL, wind speeds are less than  $1.0 \text{ m s}^{-1}$ . Winds between 50 m AGL and 200 m AGL are down valley and gradually increase in speed with height, reaching a maximum of  $3.6 \text{ m s}^{-1}$  near the top of the inversion layer. As before, an isothermal layer fills the valley to ridgetop and contains down-valley winds with speeds generally below  $0.5 \text{ m s}^{-1}$ . Near the top of the sounding, winds are lighter still and the direction shifts slightly from northwest to north. By 0700 LST, the surface had warmed  $2.5^\circ\text{C}$ , showing that the morning transition period had already begun. The surfaced based inversion layer was weakened but still intact and extended to 250 m AGL. The overlying isothermal layer still filled the valley to ridgetop and winds through the depth of the sounding were light and variable. The last tethered balloon sounding showed that by 0900 LST, the morning transition was complete in the valley. A

neutrally stratified layer extended through the valley depth and the winds were predominantly up-valley in the lowest 500 m before rotating slightly to south near ridgetop.

### 3. Analysis of observations

Figure 18 illustrates the evolution of the mesoscale boundary layer thermal structure as deduced from the series of airsonde soundings launched from the Brush Creek site. The contoured fields are deviations of the airsonde observations of potential temperature from the 0000 GMT GJT rawinsonde values and show the evolution of the mesoscale boundary layer thermal structure. At 1900 LST, the CBL temperatures were slightly cooler than the GJT values. Above the inversion at 4100 m MSL (2400 m AGL), the situation reversed and the Brush Creek values were 1-2 K warmer. This contrast helps locate the mixed layer top in this cross-section, although the profiles presented before give better definition. By 2300 LST, the valley layer has cooled significantly as would be expected, but a 300 m deep layer above ridgetop (ridgetop elevation is marked by the broken line at 2500 m MSL) has had potential temperature losses greater than 1 K as well. The appearance of the cold layer between 3500 and 4000 m MSL does not appear to be connected to the surface and is probably a transient mesoscale phenomenon. The descent of the mixed layer is clearly evident in the subsequent soundings as is the attainment of a quasi-steady, slowly developing mesoscale nocturnal boundary layer extending 500-600 m above ridgetop. A 1.5-2.0 K increase between 4000 m MSL and 5000 m MSL can be seen to have occurred late at night because of the warm air advection above the boundary layer. Below the mixed layer top, however, the atmosphere did not show any warming and a cooling through all levels is apparent in the later soundings.

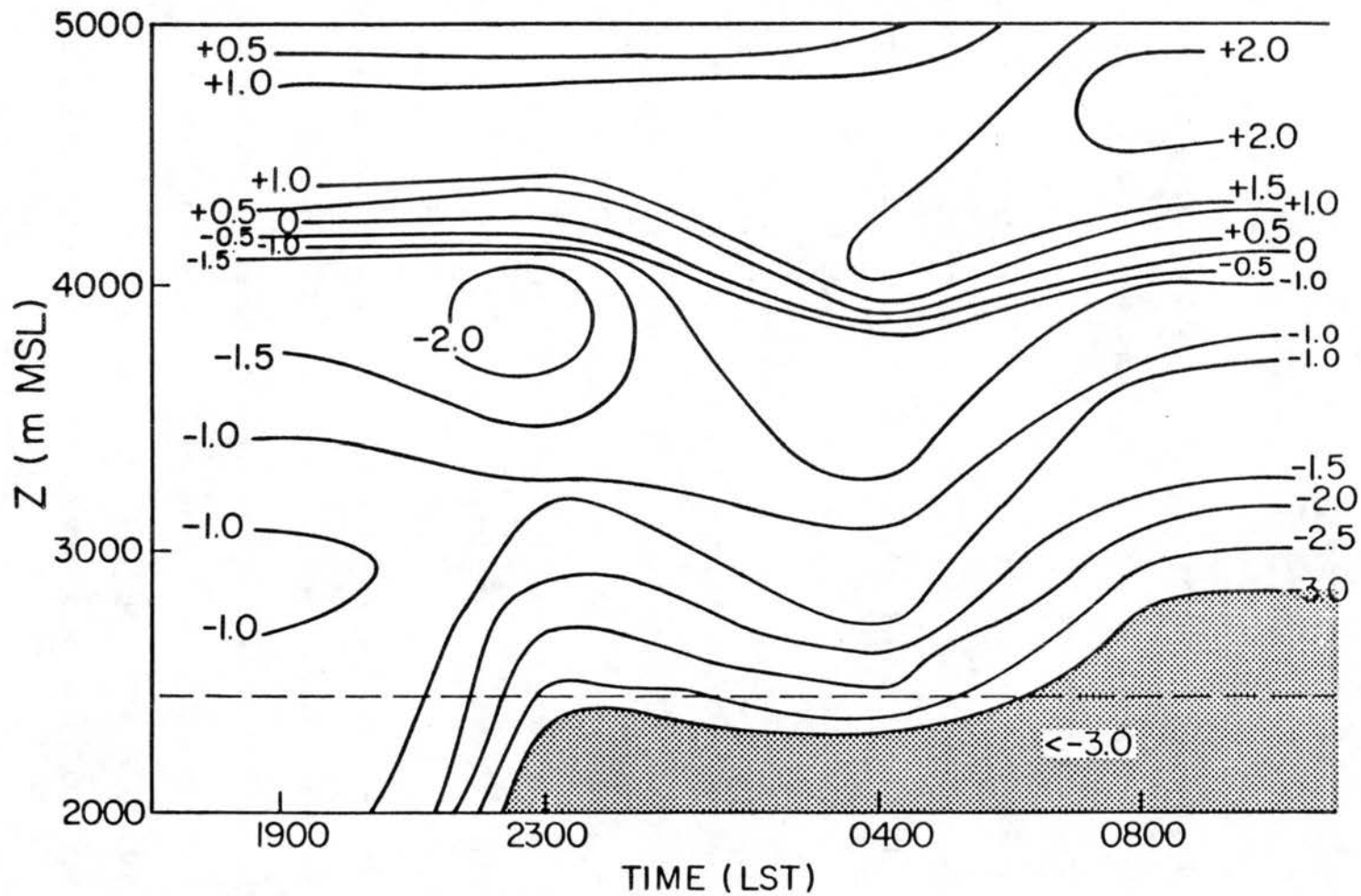


Figure 18. Deviations of potential temperature observed in Brush Creek site airsonde soundings from 0000 GMT 31 July 1982 NWS GJT rawinsonde observations for the period 30-31 July 1982.

The descent of the mixed layer top ceases simultaneously with the advent of the warming and a slight increase in the capping inversion elevation is evident in the morning sounding. The warm air advection does imply a weak synoptic scale disturbance not apparent on the NMC analyses which could be responsible for the late night geostrophic wind shift from northeast to northwest.

The evolution of the valley wind and thermal structure is related to the NBL development occurring simultaneously over the surrounding ridges of the Roan Plateau. Even before sunset, the valley started to cool and a shallow inversion developed. By 2200 LST, 2.5 h after sunset, the nocturnal stable layer and down-valley wind was well established in the valley as the layer above ridgetop had also cooled and stabilized slightly through a deep layer. By 0400 LST, the valley winds had strengthened and deepened as a noticeable subsidence of the mesoscale boundary layer was observed. As hypothesized previously, this could be the descending branch of the mountain-plain circulation as mass is lost to feed both the valley winds in the area and the larger scale terrain induced thermal circulations of the mesoscale nocturnal boundary layer itself. Before sunrise, however, a shift occurred in the geostrophic wind and lifting replaced the subsidence documented earlier. At the same time, the valley winds weakened dramatically before the start of the morning transition shortly after sunrise. Even 1 h after sunrise, the mesoscale boundary layer still exhibited its nocturnal structure with a 600 m deep stable layer containing thermal winds which opposed the prevailing synoptic scale winds. This observed nocturnal boundary layer is very different from ones observed over the plains. Over the plains, the NBL is typically very stable and less than 200 m

deep with only a 50-100 m deep overlying transition layer to separate it from the free air. In the case just presented, the boundary layer extends 500-600 m above the plateau and forms as a result of the influence of the mountainous terrain in the area.

### C. CSU 84 Experiment

#### 1. Synoptic weather conditions

In sharp contrast to the weak synoptic scale flow pattern observed in the ASCOT 82 experiment, the conditions during the CSU 84 winter experiment showed a moderately strong upper-level synoptic flow field. Figures 19-21 show the NMC upper-air analyses for 1200 GMT, 20 January; 0000 GMT, 21 January; and 1200 GMT 21 January which encompasses the period before and during the observational experiment. As can be seen, northwest Colorado is slightly to the anti-cyclonic side of the primary polar jet axis with a strong northwest geostrophic flow. At 1200 GMT (0700 LST) on 20 January, an upper atmospheric short wave had already passed the study region and was located over the high plains east of the mountains. Warm air advection continued throughout the day, resulting in 12 h observed height rises over GJT of 30 m at 700 mb and 80 m at 500 mb. At 0000 GMT, 1 h after the start of the observational period, the upper level synoptic pattern appeared to be nearly stationary and barotropic, the conditions necessary for the observation of boundary layer evolution. However, a weak disturbance marked by the perturbation in the temperature field at 500 mb appears to be passing slightly to the north of the study region. The pattern changes little by 1200 GMT on the following morning with a slight shift of the winds to a more westerly direction from the northwest orientation of the previous afternoon.

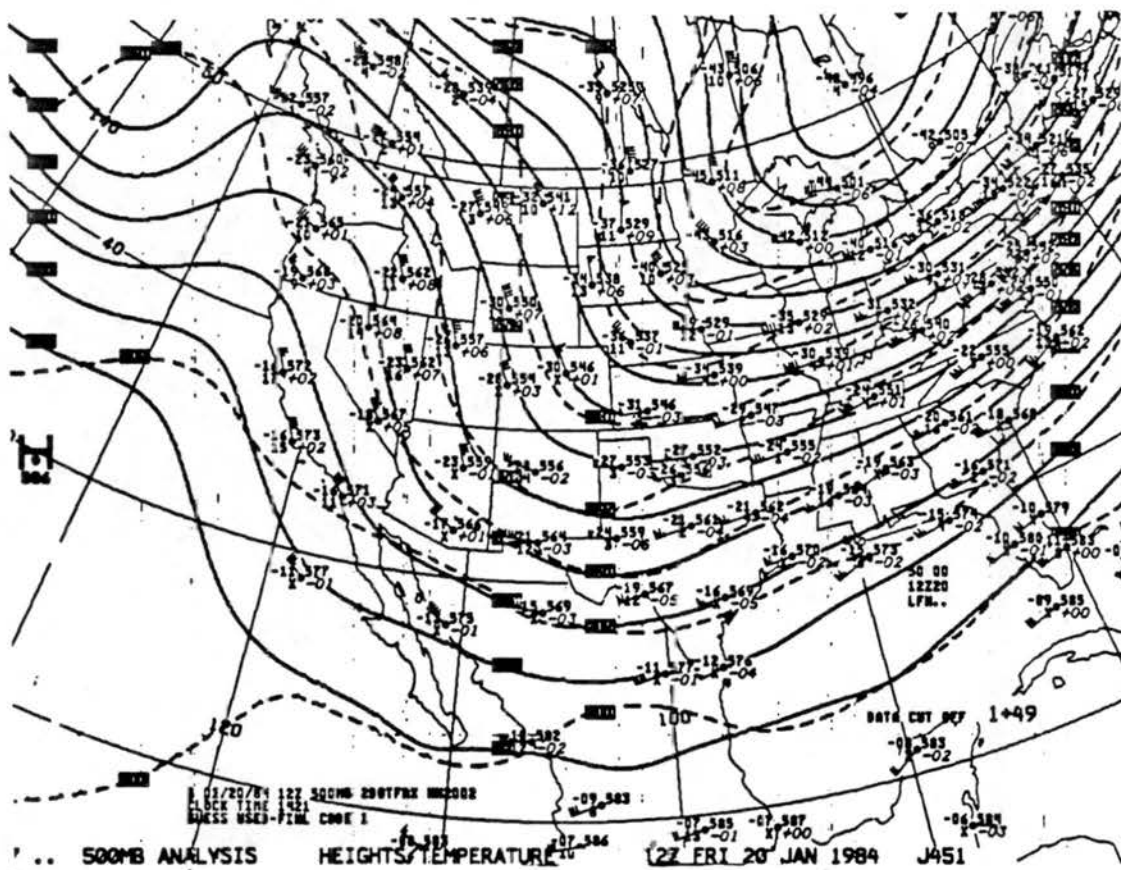


Figure 19a. NMC analysis for 120C GMT on 20 January 1984 for 500 mb.

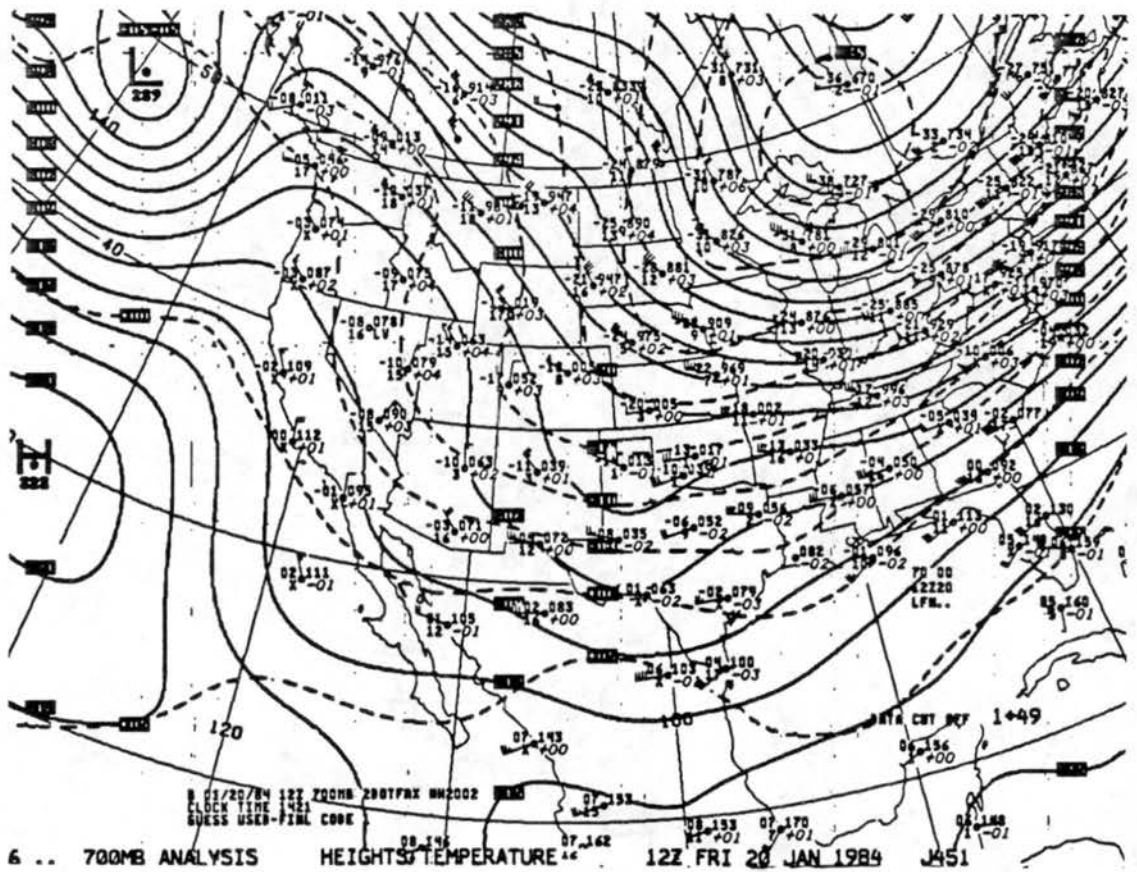


Figure 19b. NMC analysis for 1200 GMT on 20 January 1984 for 700 mb.

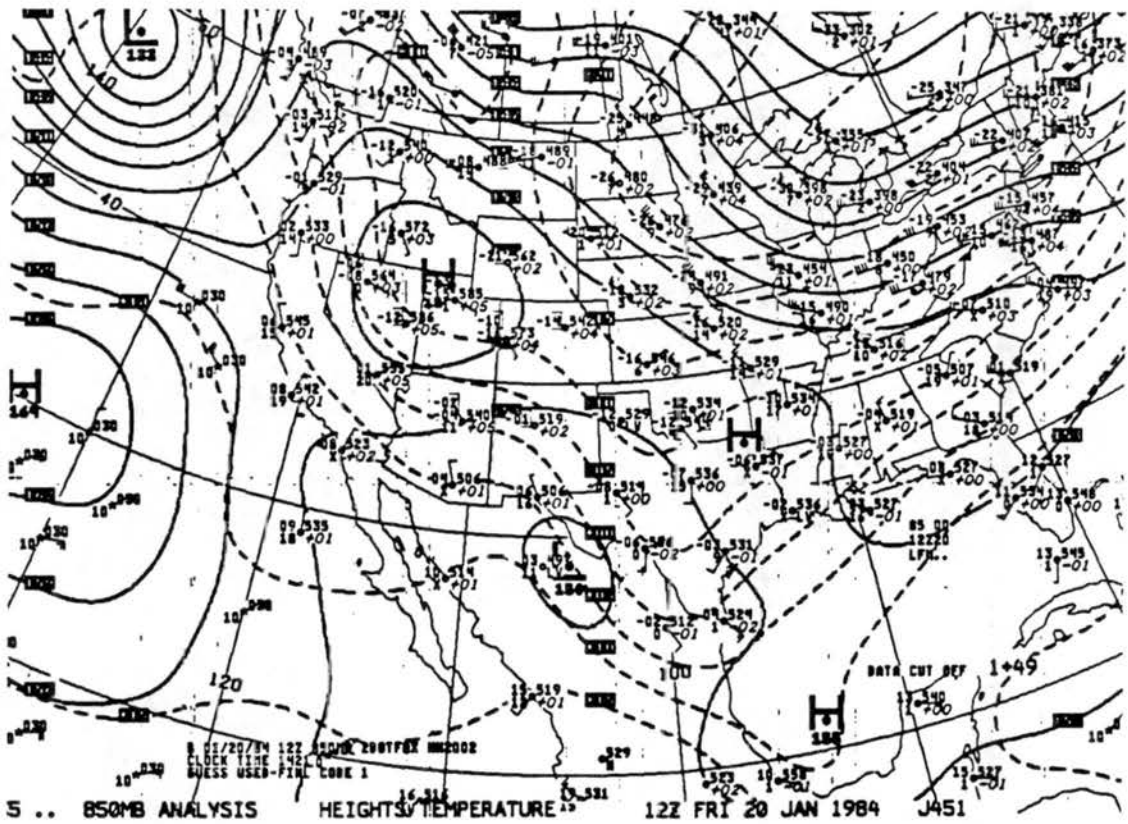


Figure 19c. NMC analysis for 1200 GMT on 20 January 1984 for 850 mb.

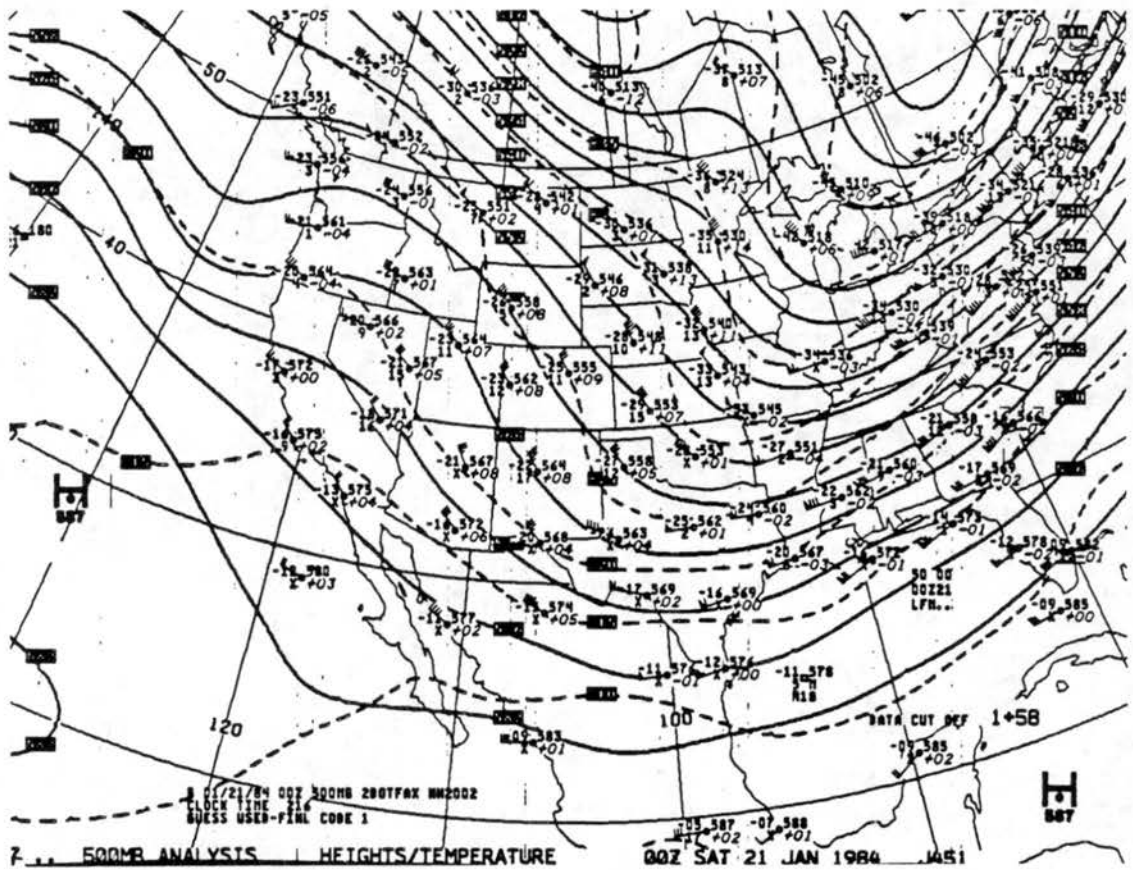


Figure 20a. NMC analysis for 0000 on 21 January 1984 for 500 mb.

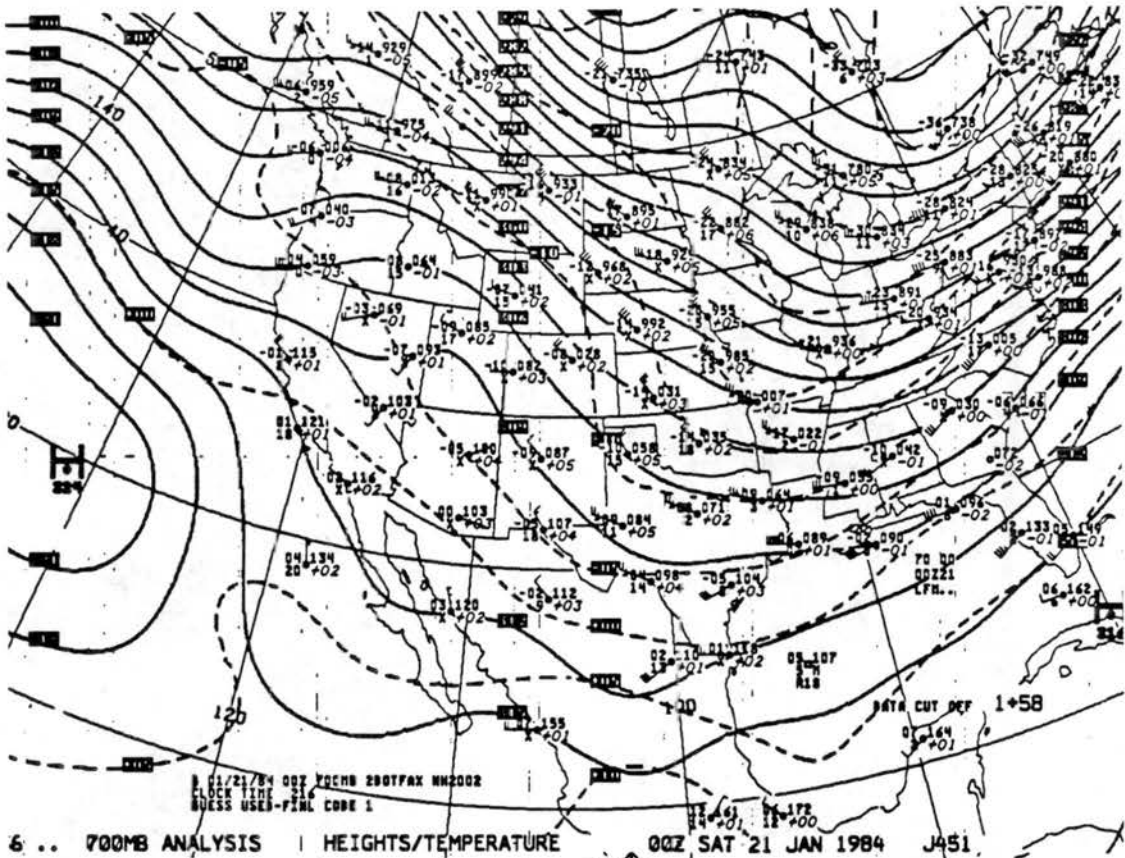


Figure 20b. NMC analysis for 0000 GMT on 21 January 1984 for 700 mb.

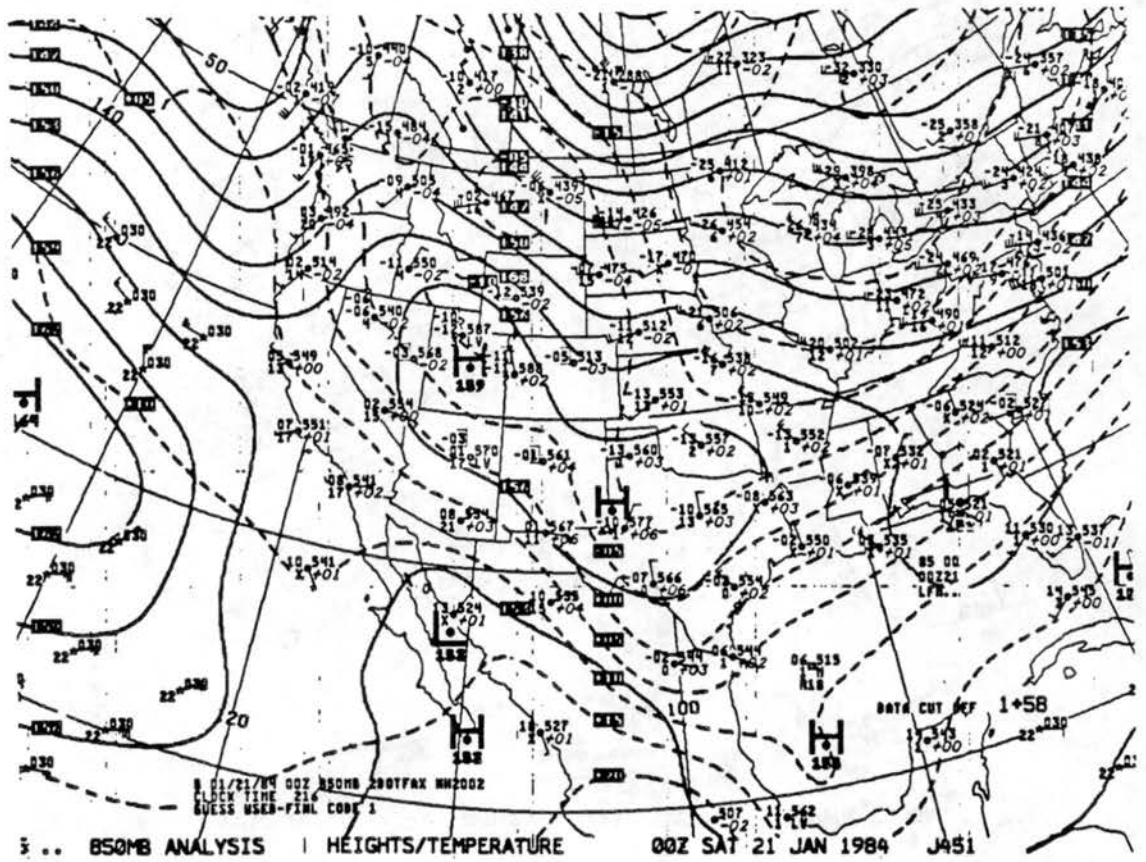


Figure 20c. NMC analysis for 0000 GMT on 21 January 1984 for 850 mb.

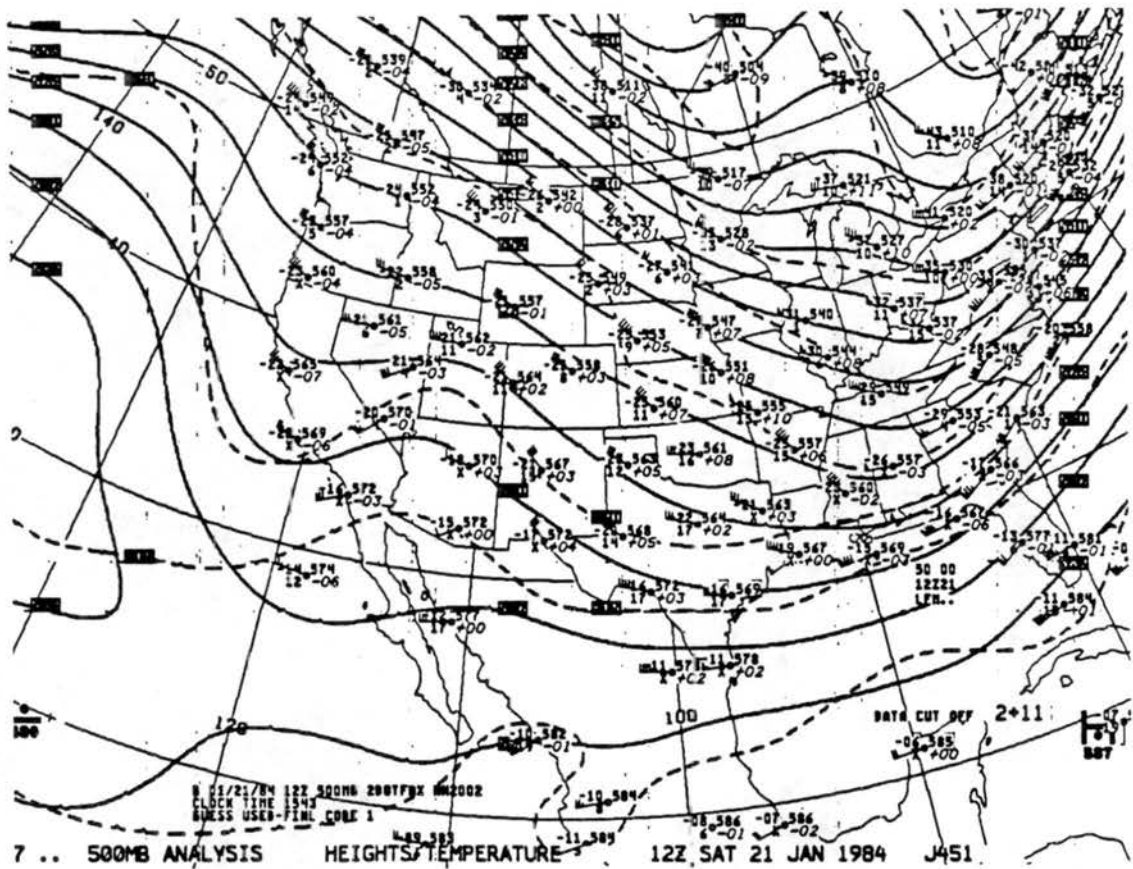


Figure 21a. NMC analysis for 1200 GMT on 21 January 1984 for 500 mb.

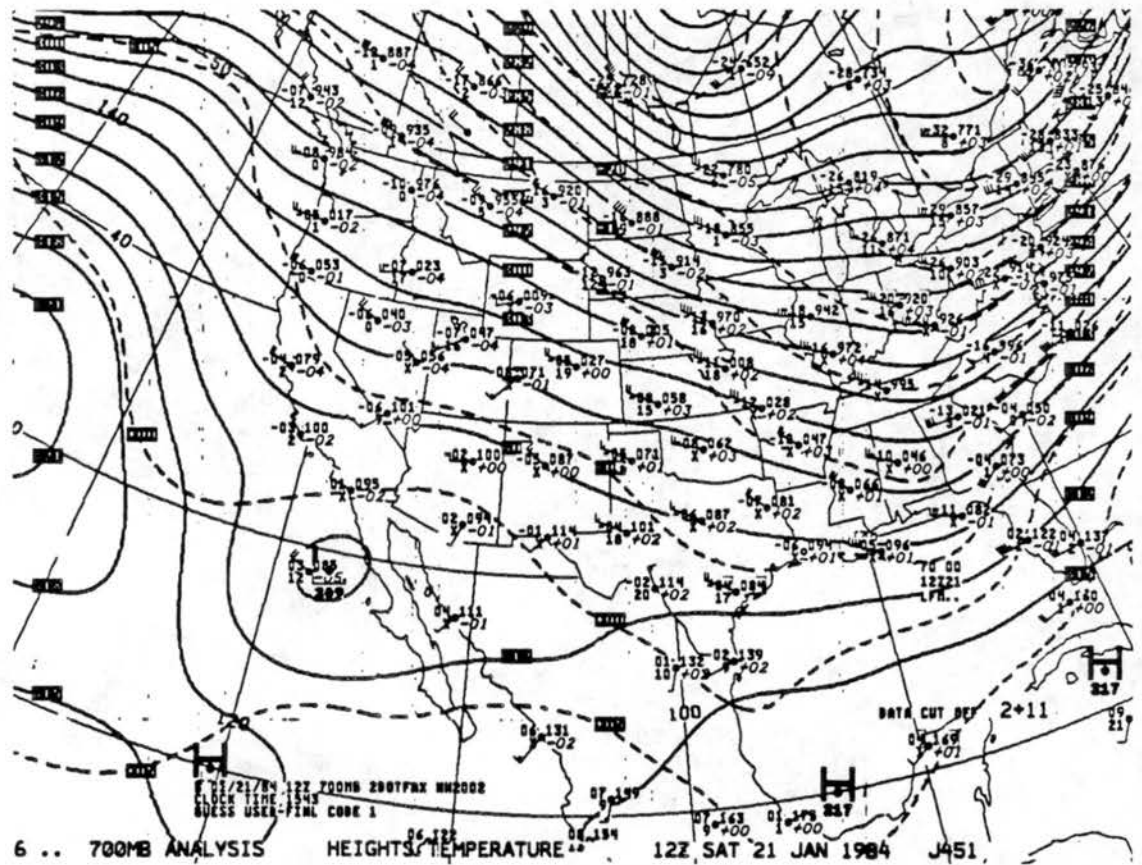


Figure 21b. NMC analysis for 1200 GMT on 21 January 1984 for 700 mb.



Figure 22 shows the 21 January 0000 GMT observations from the GJT rawinsonde launched near 1600 LST on 20 January. The entire profile is stable and there is no evidence of a well mixed CBL as was observed in the summer experiment. The entire northwest portion of the state had received a large amount of snow 5 days before from a major winter storm that crossed the Rocky Mountains. Temperatures since the storm had remained cold enough to prevent any substantial amount of melting to occur and 9 in (23 cm) of snow was still on the ground at GJT. The high surface albedo inhibited the daytime boundary layer development, resulting in the deep stable profile with the only deviation being a 20 m deep unstable layer immediately above the surface. A 2.0°C inversion layer fills the river valley and is topped by a weakly stable region between 500 m AGL and 1400 m AGL, which resulted from the limited boundary layer heating that occurred throughout the day. This layer is capped by very strong 300 m deep inversion layer which separates the weakly stable air from the free atmosphere above it. Winds below 1000 m AGL are very light and of variable direction, except for the up-valley (northwest) wind at the surface. Near 1000 m AGL, a 3.4 m s<sup>-1</sup> south wind is observed and the speeds steadily increase with height above this level. The direction rotates to northwest above the inversion, and speeds reach 15.0 m s<sup>-1</sup> at 4000 m AGL. Humidities are not shown in the soundings from this experiment because the air was so cold that it could not hold much water substance. Dew-point depressions were greater than 9.0°C through the depth of the sounding, verifying that air was indeed very dry. Additionally, the airsonde observations during this field experiment did not include wet-bulb measurements because the sub-freezing temperatures cause the thermistor reservoir to

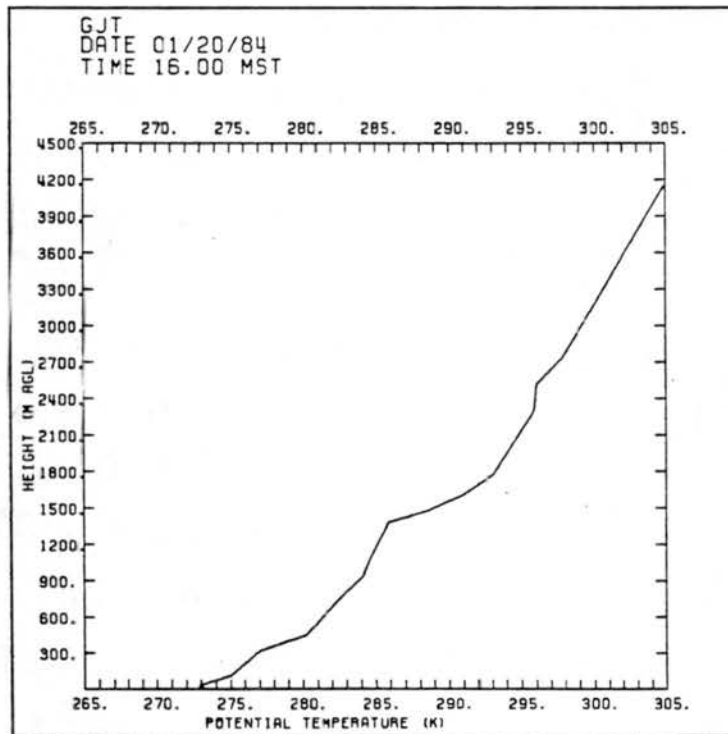
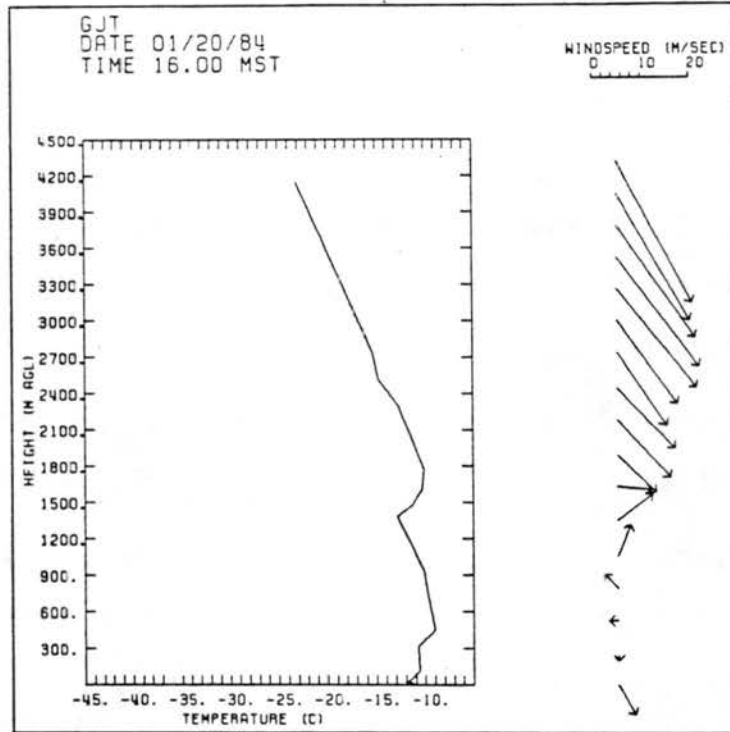


Figure 22. NWS GJT rawinsonde sounding for 1600 LST on 20 January 1984.

freeze and render it useless. Local sunset was a few minutes after 1700 LST and surface observations at GJT showed that the sky remained clear through the night.

The 1200 GMT sounding from GJT is shown for comparison in Figure 23. A multiple layer structure has formed in the lowest 1500 m of the sounding and the free atmosphere has warmed  $3^{\circ}\text{C}$  at all levels, showing warm air advection not evident on the NMC analyses. A  $10^{\circ}\text{C}$ , 250 m surface inversion is present in the lower valley and is surmounted by a 400 m deep weakly stable layer that extends above ridgetop. A second inversion layer lies between 650 m AGL and 900 m AGL and is topped by a 300 m deep isothermal region, which is separated from the free atmosphere by still another, thin inversion layer at 1200 m AGL. Winds in the valley exhibited typical down-valley (southeast) behavior. Above ridgetop, winds were south to southeast with speeds between  $5.0\text{ m s}^{-1}$  and  $7.0\text{ m s}^{-1}$  before changing to southwest above 1500 m AGL. In the free atmosphere above this level, the winds rotated smoothly with height to a northwest direction with speeds near  $10.0\text{ m s}^{-1}$  at 3000 m AGL increasing steadily to  $15.0\text{ m s}^{-1}$  at 4000 m AGL, very similar to the values observed the previous afternoon. This veering of the upper level winds with height is consistent with the  $3^{\circ}\text{C}$  advective warming observed in the temperature profiles. Also, an elevated layer between 4800 m AGL and 5800 m AGL had dew-point depressions less than  $6^{\circ}\text{C}$  from temperatures which ranged between  $-25^{\circ}\text{C}$  and  $-30^{\circ}\text{C}$ . The upper-level wind data from the remote profiler near Craig shows a similar pattern of the winds above 3000 m MSL (1530 m AGL at GJT) throughout the night. Winds were predominantly northwesterly at the start of the observational period and backed slightly to a more westerly orientation by the following morning.

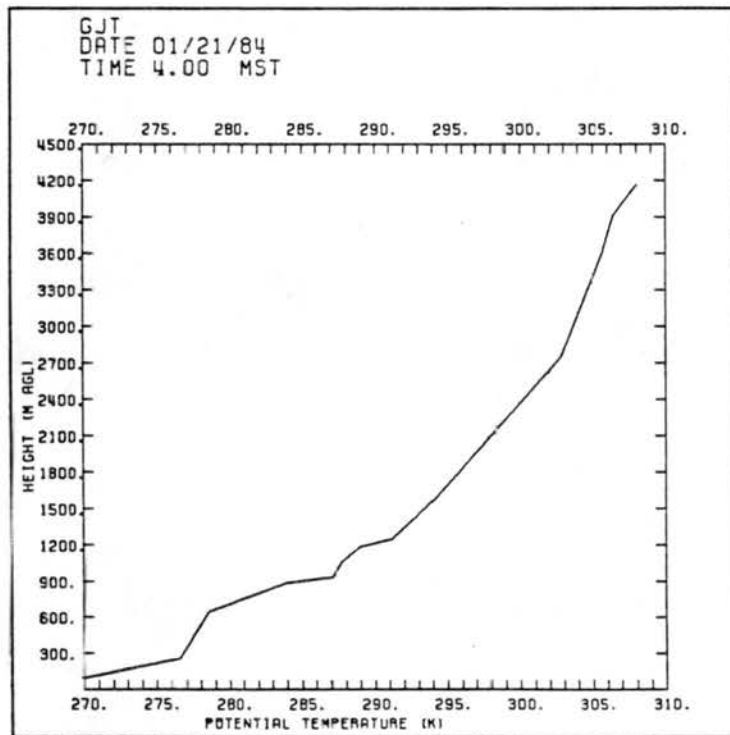
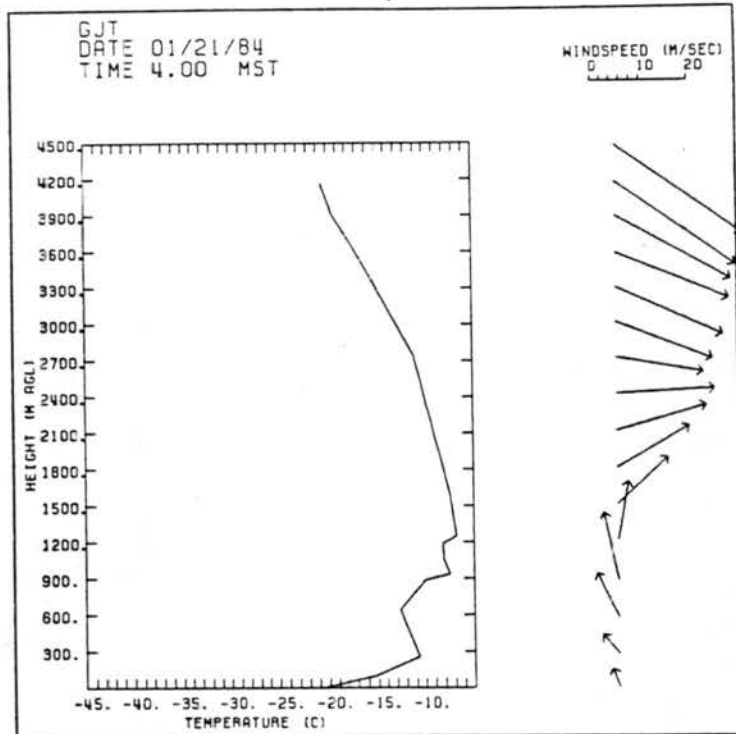


Figure 23. NWS GJT rawinsonde sounding for 0400 LST on 21 January 1984.

Speeds were comparable to those recorded by the GJT rawinsonde at all levels for which data are available.

## 2. CSU 84 observations

Table 2 lists pertinent information about the airsonde soundings taken at each of the three sites during the observational period. Soundings were taken every two hours starting at 1600 LST on 20 January and continuing through 1000 LST on the morning of 21 January, except for a break period between 2300 LST and 0600 LST during which no soundings were made. It was thought that the NBL would be fully developed before the break and that little change would occur before the start of the morning transition period after sunrise around 0720 LST. Sky cover remained clear prior to the break at all three sites, but high thin clouds were present over part of the study region by the resumption of data collection at 0600 LST. These clouds slowly spread and thickened throughout the morning and produced nearly overcast skies at all sites by the conclusion of the observational period at 1100 LST. The cloud layer appeared first over the high terrain east of the Ca site and could be the result of the orographic lifting of the elevated moist layer observed in the GJT sounding. Records obtained from the continuously operating microbarographs at each site revealed that starting around 0100 LST, surface pressure fell at a steady rate of  $0.55 \text{ mb h}^{-1}$  at all three locations, a trend that continued throughout the morning. This pressure fall preceded a weak synoptic scale short wave which passed through the region on the following day.

a. Ca site data. The Ca site was located on the Rio Blanco Oil Shale Co. lease tract at one of the three meteorological tower sites (M1) used in the study by Barr and Clements (1981). The location was

Table 2.  
Times of CSU 84 Soundings

<u>Sounding Time</u>	<u>Release Time (LST)</u>		
	<u>Ca</u>	<u>Meeker</u>	<u>Rifle</u>
1600 LST	1637	1612	1614
1800 LST	1818	1812	1802
2000 LST	2006	2022	2003
2200 LST	2206	2207	2210
0600 LST	0617	0556	0612

slightly to the east of a very sharp and narrow ridge called the Cathedral Bluffs on the western edge of the Roan Plateau. Site elevation was 2240 m MSL (7350 ft MSL) and the main ridgeline of the Cathedral Bluffs was near 2635 m MSL. The topography in the immediate vicinity of the site slopes gradually northeast toward the Yellow Creek and is embedded with many small creek valleys. Although not used in this analysis, the tower measurements were used to verify the airsonde readings during the experiment. The area was still covered with 5-10 inches of snow from the storm earlier in the week.

Figure 24 shows the 1600 LST airsonde sounding data collected above Ca. A very shallow 3°C inversion layer underlies a 550 m deep mixed layer. Topographic winds in the lowest 100 m were from the south with speeds near  $3.0 \text{ m s}^{-1}$ . Above 150 m AGL the winds rotated to a southwesterly direction in the upper part of the CBL with speeds of  $3.0\text{-}4.0 \text{ m s}^{-1}$ . The winds shift abruptly to the northwest above a 150 m deep inversion layer between 550 m AGL and 690 m AGL, and slowly increase in speed with height from  $5.6 \text{ m s}^{-1}$  at 735 m AGL to over  $10.0 \text{ m s}^{-1}$  above 1150 m AGL. Except for two small perturbations at 1100 m AGL and 1800 m AGL, the lapse rate above the inversion is near constant at  $4.6 \times 10^{-3} \text{ }^\circ\text{C m}^{-1}$ . By 1 h after sunset, a 300 m deep isothermal layer has developed over the shallow surface inversion (Figure 25). The neutral layer is still present between 300 m AGL and 550 m AGL, but the base of the overlying inversion has descended 40 m since the last sounding. Unfortunately, wind data was not available for most of this sounding except for two observations of light south winds below 400 m AGL and the  $5.0\text{-}7.0 \text{ m s}^{-1}$  west-northwest winds observed between 750 m AGL and 1400 m AGL.

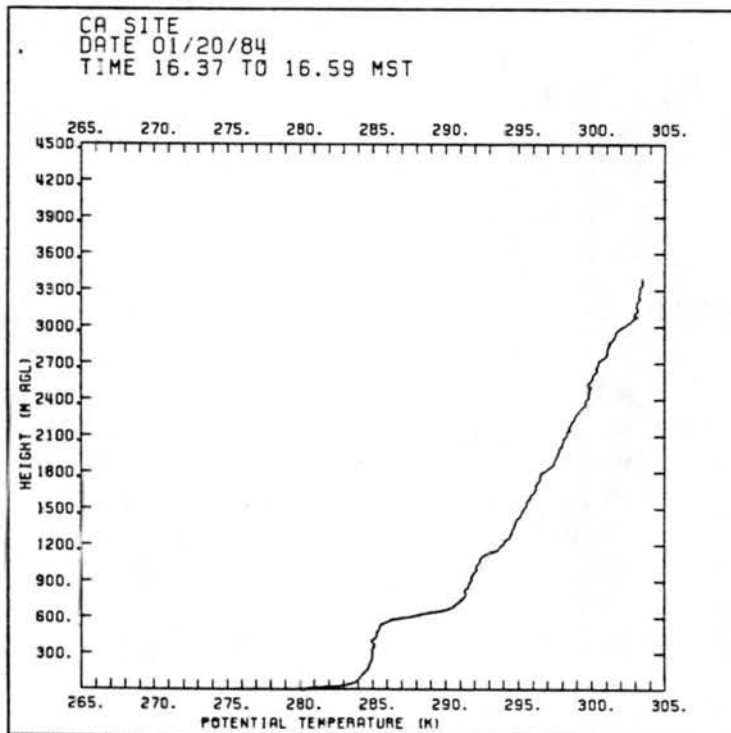
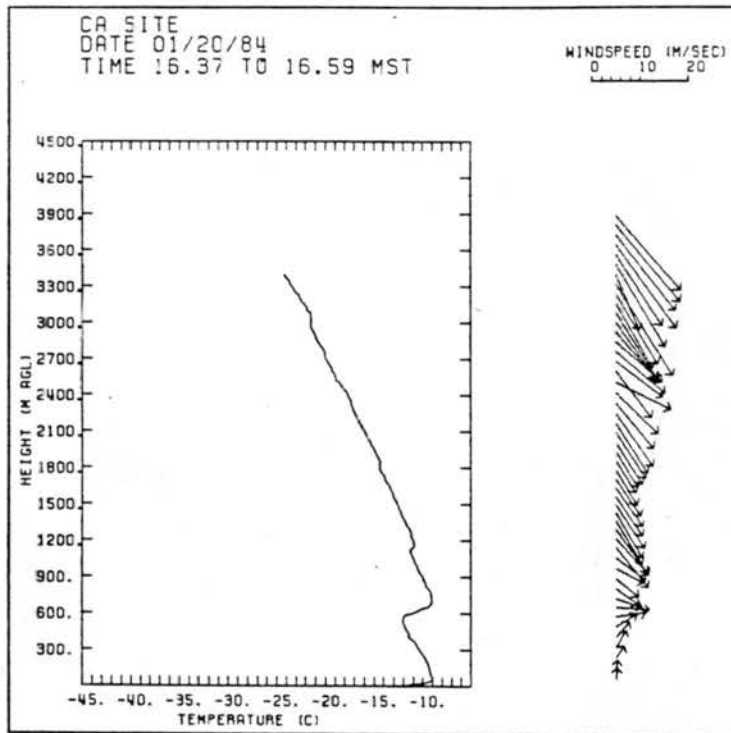


Figure 24. Ca site airsonde sounding for 1600 LST on 20 January 1984.

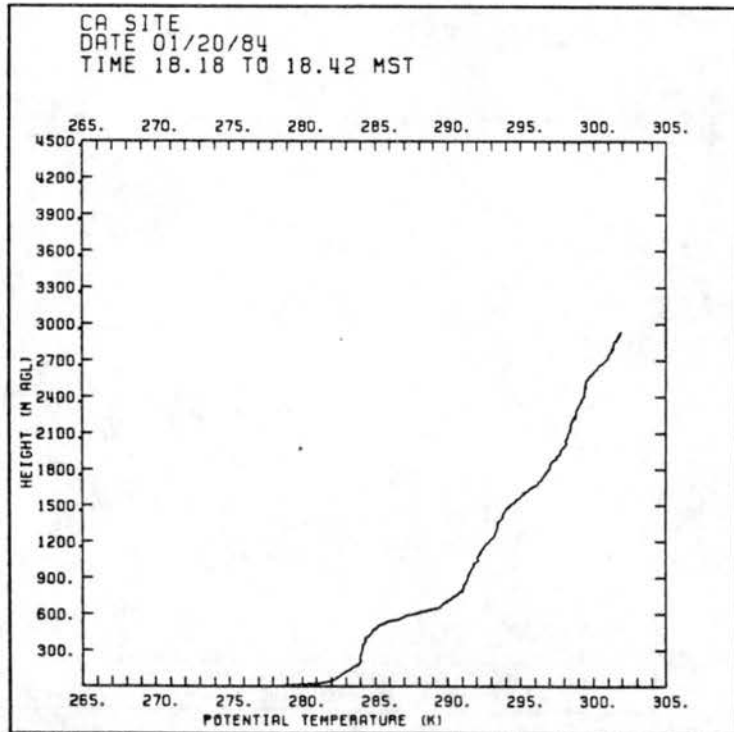
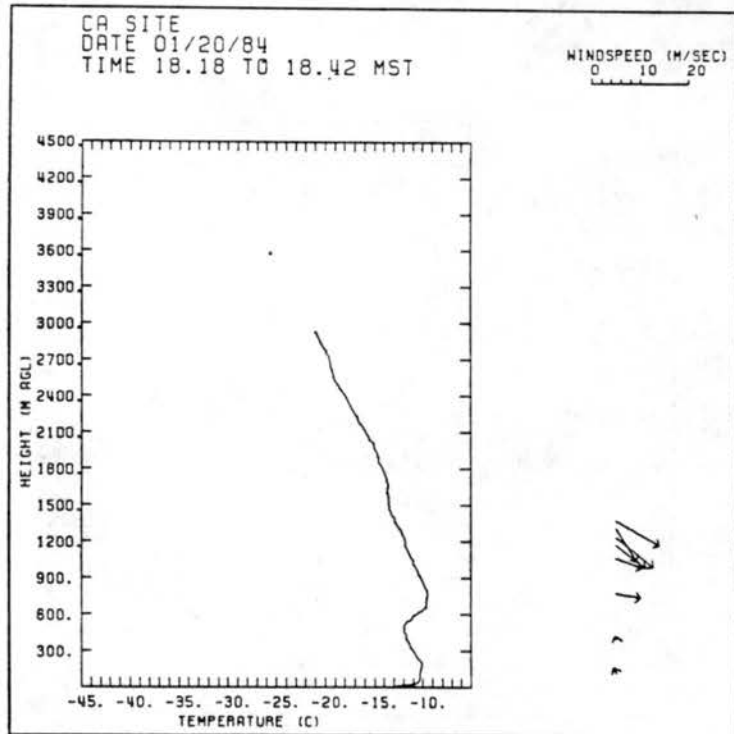


Figure 25. Ca site airsonde sounding for 1800 LST on 20 January 1984.

The 2000 LST sounding shows a significant change from the one just 2 h previously (Figure 26). The neutral layer has warmed and stabilized while the surface temperature has dropped  $3.5^{\circ}\text{C}$  to  $-16.2^{\circ}\text{C}$ . This combination has resulted in a 250 m deep surface based inversion layer topped by a deep, nearly isothermal region which extends to 770 m AGL. Winds in the surface inversion layer are southerly drainage flows from the local topography with speeds less than  $3.0\text{ m s}^{-1}$ . In the deep isothermal region,  $2.0\text{--}3.0\text{ m s}^{-1}$  winds from the west are present below 600 m AGL with a southwesterly  $4.0\text{--}5.0\text{ m s}^{-1}$  flow above this level. The winds above 1200 m AGL exhibited the prevailing northwest direction with speeds very near those recorded earlier.

The 2200 LST observations reveal a complex multiple layer vertical structure (Figure 27). The surface inversion consisted of an extremely stable shallow surface layer topped by a weaker inversion layer extending to 500 m AGL. Surface temperature continued to fall and reached  $-18.0^{\circ}\text{C}$  by launch time while the temperature at 500 m AGL had risen  $2.2^{\circ}\text{C}$  since the 2000 LST sounding. A near neutral layer extending from 500 m AGL to 700 m AGL has formed in response to the lower level warming. Above 700 m AGL, the thermal structure exhibits little change from the 2000 LST observations. Winds below 900 m AGL were from the southwest with speeds ranging from  $4.0\text{ m s}^{-1}$  at 613 m AGL to  $6.8\text{ m s}^{-1}$  at 864 m AGL. Above this level, the wind direction rotated smoothly to the northwest with height, with a  $5.7\text{ m s}^{-1}$  west wind at 1665 m AGL and a  $6.8\text{ m s}^{-1}$  northwesterly flow at 2000 m AGL. The record obtained from the microbarograph at Ca showed that the surface pressure fell at a nearly constant  $0.25\text{ mb h}^{-1}$  starting at 1900 LST and continued until the sharper decline commenced near 0100 LST. From 1600-1900 LST, surface

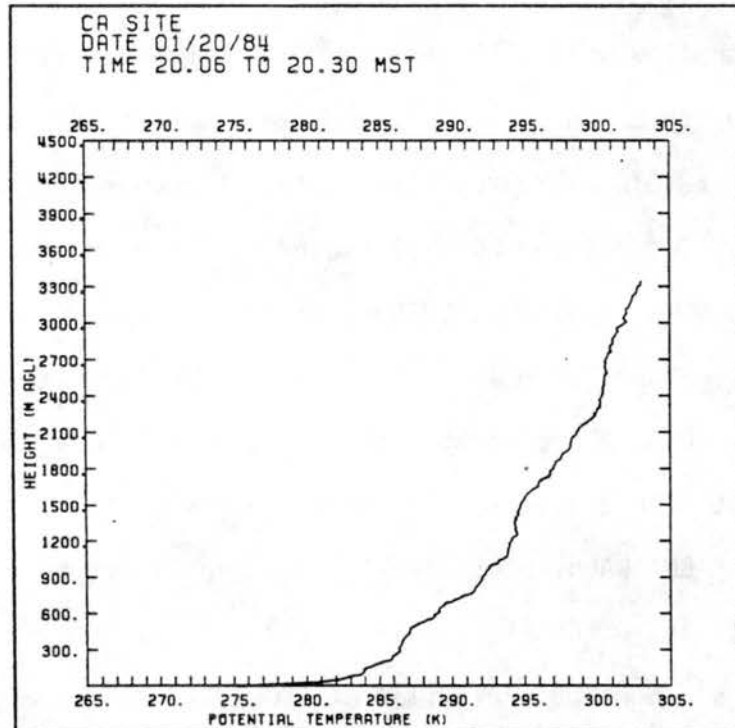
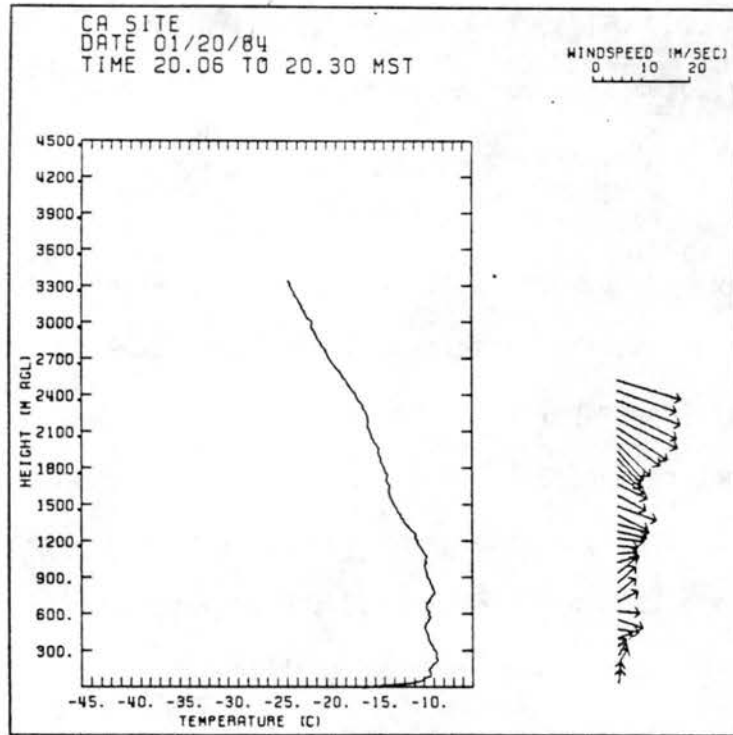


Figure 26. Ca site airsonde sounding for 2000 LST on 20 January 1984.

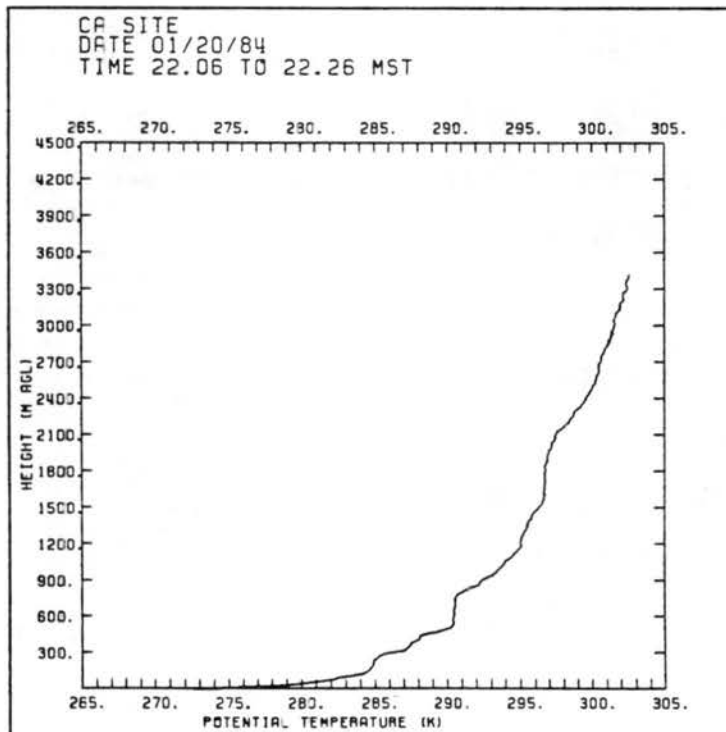
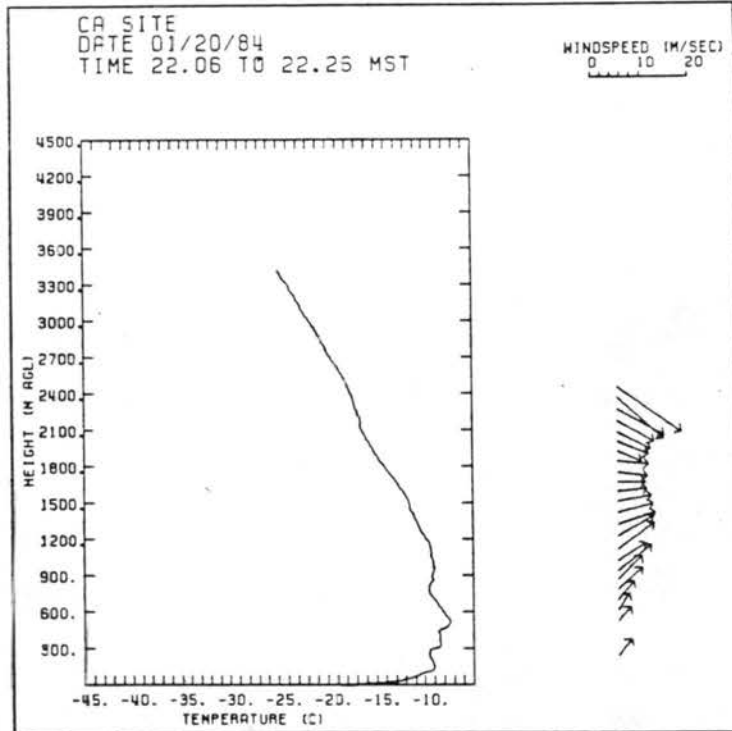


Figure 27. Ca site airsonde sounding for 2200 LST on 20 January 1984.

pressure values remained nearly constant with no evidence of small or large scale disturbances.

Figure 28 displays data from the first sounding following the break at 0600 LST, which exhibits evidence of warm air advection similar to that observed in the GJT 1200 GMT upper-air data. Significant warming has occurred at all levels above 600 m AGL. Observed temperature increases ranged from 4.5°C near 800 m to 1.5°C in a thin layer between 1100 m AGL and 1300 m AGL. Above 1500 m AGL, the temperature difference between soundings varied from 3.0°C to 5.0°C. The surface temperature had also increased to -15.2°C, but the warm air advection maintained the surface based inversion to 700 m AGL. Below 1000 m AGL, winds were moderately strong from the southwest with speeds above 10.0 m s<sup>-1</sup> before becoming more westerly with height. A maximum of 14.8 m s<sup>-1</sup> near 640 m AGL appears to be associated with the top of the inversion layer just 60 m higher. Above the maximum, the profile exhibits very little speed or directional shear with west-southwest winds between 10.5 m s<sup>-1</sup> and 12.1 m s<sup>-1</sup> evident from 700-1700 m AGL. Because of the difficulty in separating boundary layer processes from the synoptic scale baroclinic effects, continued analysis of subsequent soundings would be fruitless.

b. Meeker site data. The Meeker sounding site was southeast of the town on the White River at the confluence of North Elk Creek. Due to the site's valley bottom location, surface elevation was only 6850 ft MSL (2088 m MSL), but mountain masses with a large area above 9000 ft MSL (2743 m MSL) were immediately to the north and south. Additionally, a long ridge with an elevation over 8000 ft MSL (2438 m MSL) was just 15 km to the west of the site and surrounded the

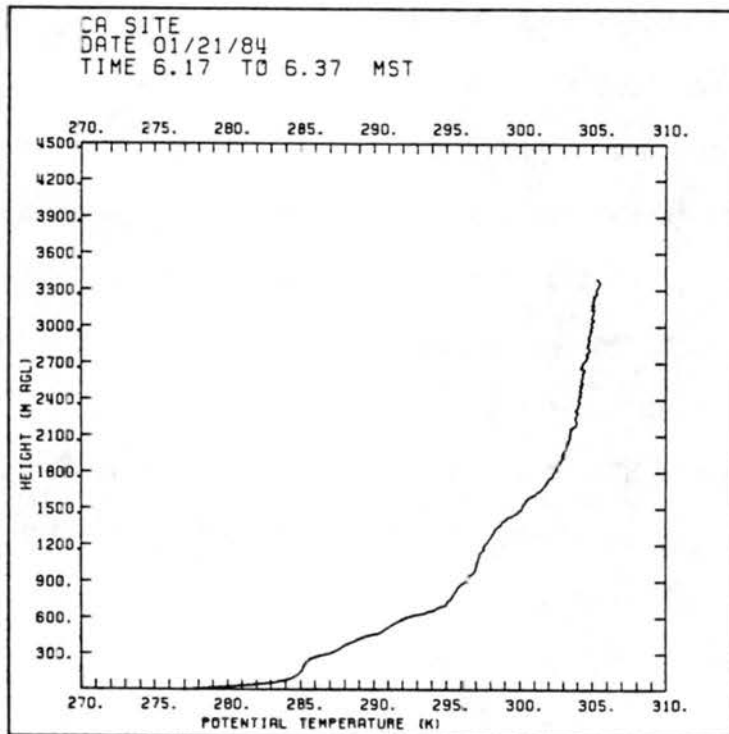
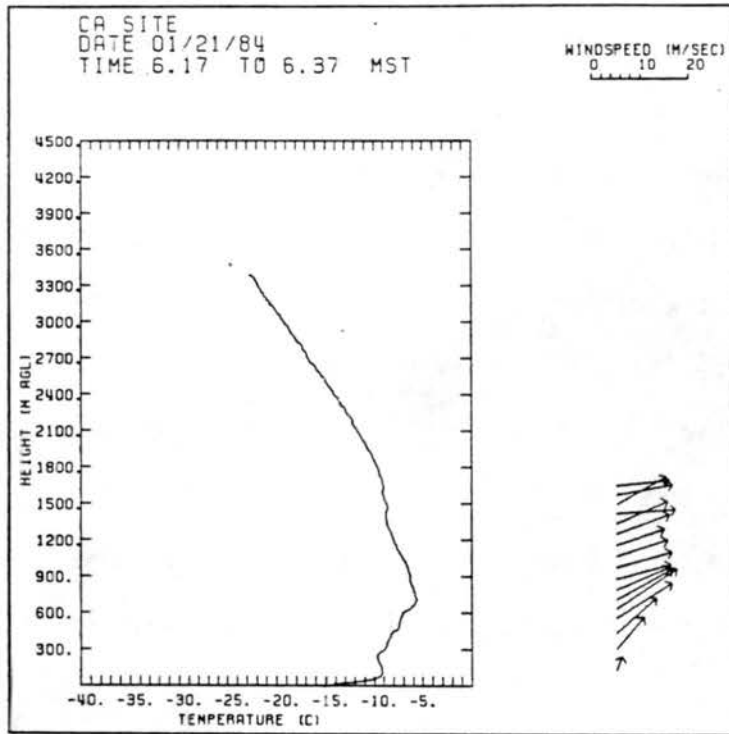


Figure 28. Ca site airsonde sounding for 0600 LST on 21 January 1984.

location with high terrain. The valley ridgetops were not as clearly defined as in the Brush Creek case, but the steeply sloping terrain on either side gives way to a more gentle slope near 400 m AGL. A great deal of difficulty was encountered in collecting wind data from the Meeker site, mainly due to the extreme cold encountered in this valley location. The eyepiece on the theodolite routinely fogged over from condensation and the formation of a thin radiative ground fog in the valley bottom prevented the tracking of the balloon higher than several hundred meters above the surface on several occasions through the night. The problems were exacerbated by the deep snow still remaining from the earlier storm.

As is shown in Figure 29, the surface inversion had already developed and extends to 180 m AGL by the start of the observational period near 1600 LST. A nearly neutral layer left over from the daytime valley boundary layer lies above the surface inversion. It is topped by a shallow isothermal layer with a base 480 m AGL. Between 600 m AGL and 930 m AGL is another neutral layer, most probably the CBL which resulted from the limited daytime sensible heating from the snow-covered surfaces in the region. The CBL is not capped by a strong inversion as was found in the ASCOT 82 experiment but rather is surmounted by the free atmosphere with a very limited but smooth transition zone between the two layers. Wind observations correlate well with the observed thermal structure, a  $0.8 \text{ m s}^{-1}$  down-valley (northeast) flow in the surface inversion layer and  $2.3\text{-}2.9 \text{ m s}^{-1}$  south winds in the CBL. Although sunset was not until 1 h later these south winds were the beginning of a thermal circulation initiated by the cooling of the elevated terrain south of the site, which was already shaded. Considering the very

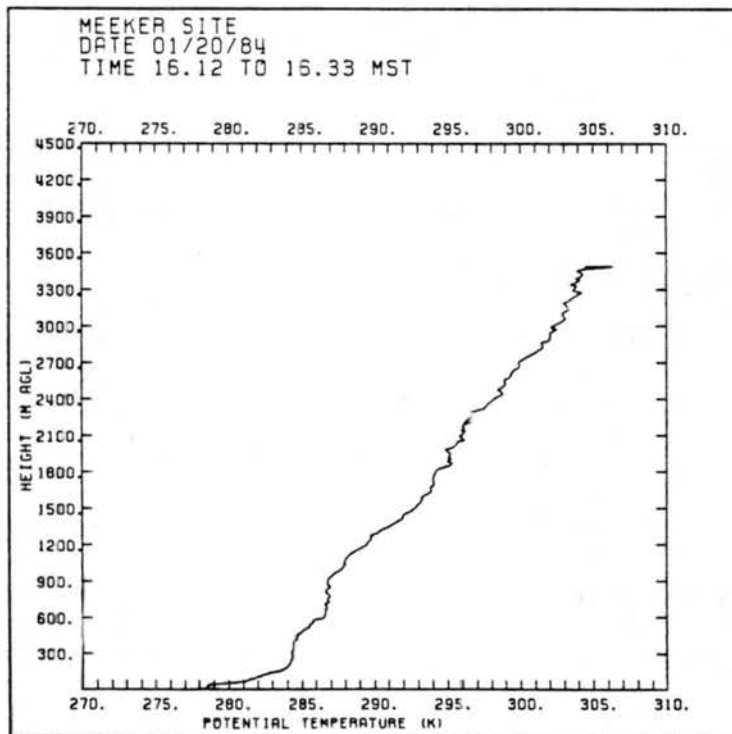
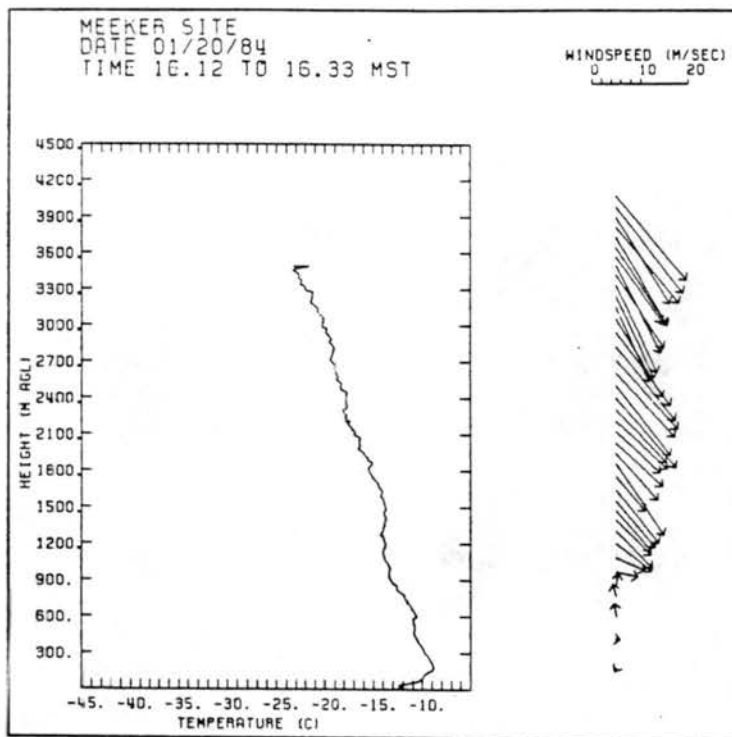


Figure 29. Meeker site airsonde sounding for 1600 LST on 20 January 1984.

limited degree of solar heating resulting from the high surface albedo and low mid-winter solar elevation angle, it is likely that the sensible heat flux reversed direction 2-3 h prior to sunset. Above the CBL top, the winds shifted to the strong synoptic scale northwesterly flow also found in the GJT and Ca soundings.

By 1800 LST, the surface inversion had grown to 220 m AGL, and the neutral layer above it had cooled and stabilized (Figure 30). At this time, the surface temperatures were extremely cold (near  $-20^{\circ}\text{C}$ ), making data collection difficult for both the instruments and the observers. A nearly isothermal layer with a temperature near  $-10.5^{\circ}\text{C}$  occupied the region between 220 m AGL and 615 m AGL. The neutral layer remaining from the CBL extended from the top of the isothermal region to 750 m AGL, 180 m lower than the top in the earlier sounding. This could be the result of subsidence, which is consistent with potential temperature values between 750 m AGL and 1800 AGL. This could occur despite the west wind component since the principal convergence region was probably farther upwind of the high barriers than the Meeker site. Above 750 m AGL, the atmospheric lapse rate remains practically unchanged since 1600 LST. The low level down-valley flow has strengthened to  $1.4\text{ m s}^{-1}$  at 135 m AGL. The south winds present above the valley at 1600 increased in speed to  $3.0\text{--}6.0\text{ m s}^{-1}$  and developed a small easterly component below 600 m AGL. As before, the winds above the top of the neutral layer were from the northwest with speeds increasing steadily with height from  $6.0\text{ m s}^{-1}$  at 1000 m AGL to  $13.0\text{ m s}^{-1}$  at 2000 m AGL.

Unfortunately, thermal data from the 2000 LST sounding (Figure 31) were only available to 1870 m AGL and wind data were completely absent.

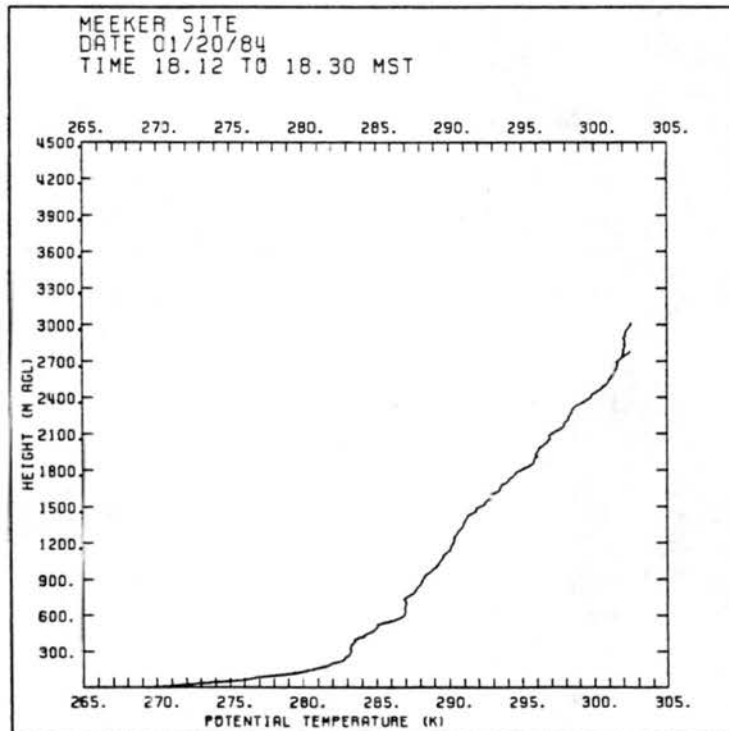
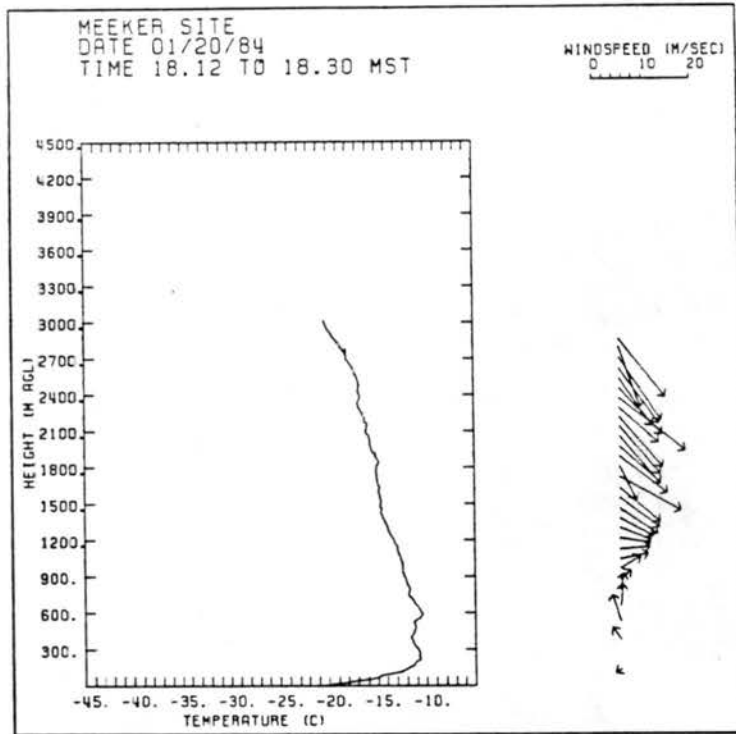


Figure 30. Meeker site airsonde sounding for 1300 LST on 20 January 1984.

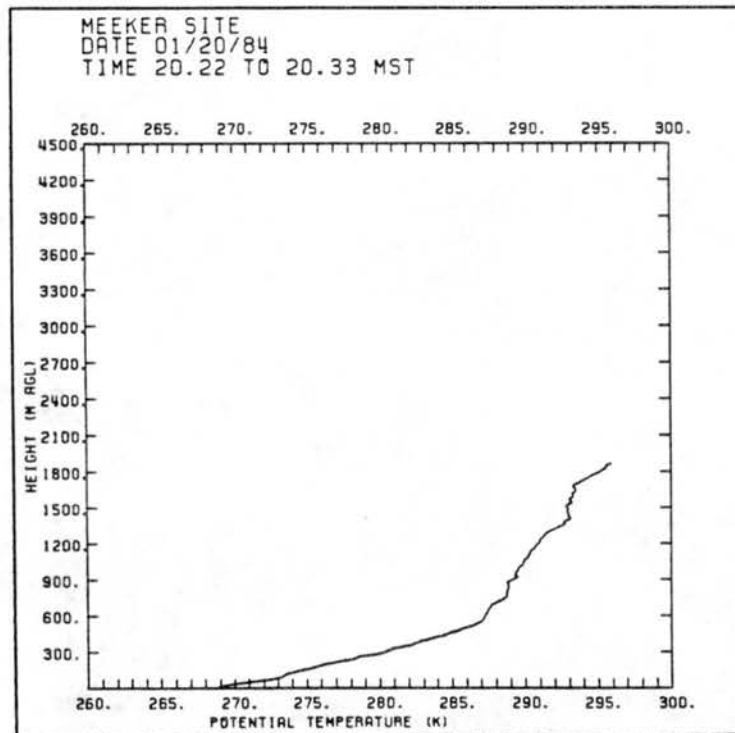
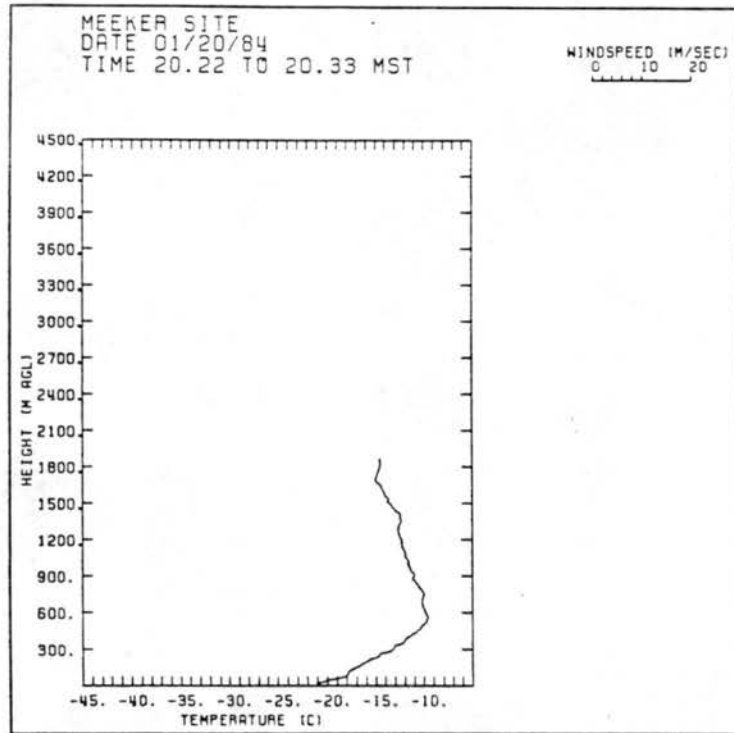


Figure 31. Meeker site airsonde sounding for 2000 LST on 20 January 1984.

Nevertheless, the observed temperature profile shows a dramatic change from the previous sounding at 1800 LST. The sounding exhibits a simpler two layer structure which differs significantly from the multiple layers seen just 2 h earlier. The lowest 600 m has continued to cool and stabilize to form a deep inversion layer. Above the surface inversion, the atmospheric lapse rate is the same as that observed above the CBL in the earlier profiles, but the temperatures are 1.0-2.0°C warmer at all levels for which there are data. Again, this observation is consistent with a continued subsidence of the layer below 1800 m AGL, but also could be the result of larger scale advection. The absence of data above 1800 m AGL makes better analysis to determine the true cause difficult.

The 2200 LST sounding (Figure 32) reveals several significant changes in the boundary layer thermal structure which have occurred since 2000 LST. The surface based inversion layer extends to 450 m AGL, near the top of the valley. Above the valley, a 750 m deep quasi-isothermal transition layer separates the valley inversion from the free atmosphere. The stabilization necessary to form the isothermal layer resulted from a 1.0-2.0°C cooling of the layer between 450 m AGL and 800 m AGL with a 1.0-2.0°C warming in the layer between 800 m AGL and 1200 m AGL. The limited wind data available from this sounding shows that the down-valley flow continues below the inversion level with the south-southwest winds continuing immediately above the valley.

Windspeeds are somewhat unreliable but appear to range between  $2.0 \text{ m s}^{-1}$  and  $4.0 \text{ m s}^{-1}$  in the valley flow and  $4.0 \text{ m s}^{-1}$  and  $6.0 \text{ m s}^{-1}$  above it.

The microbarograph record from the Meeker site indicated that the pressure was very steady throughout the evening, rising less than 0.5 mb between 1700 LST and 0000 LST. Around 0100 LST, the pressure started to

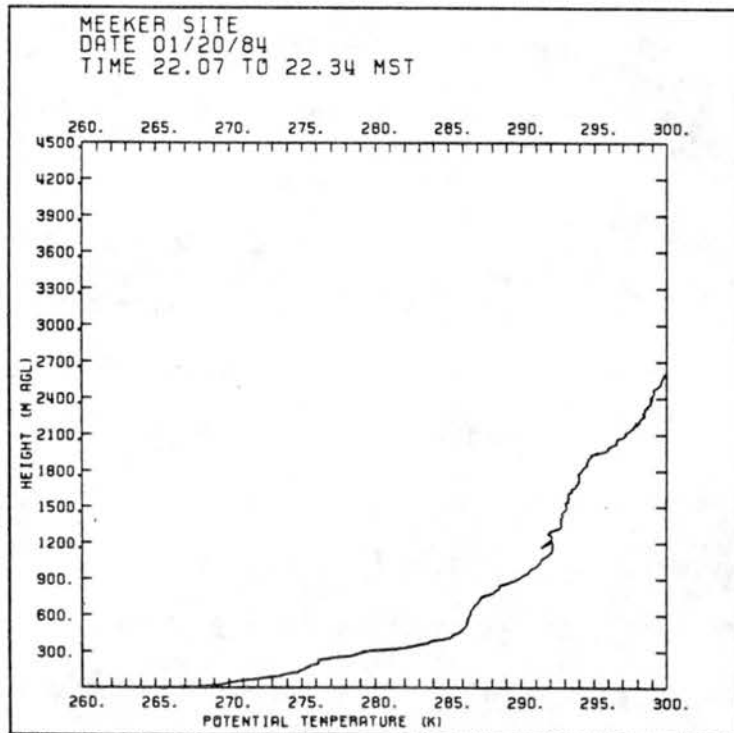
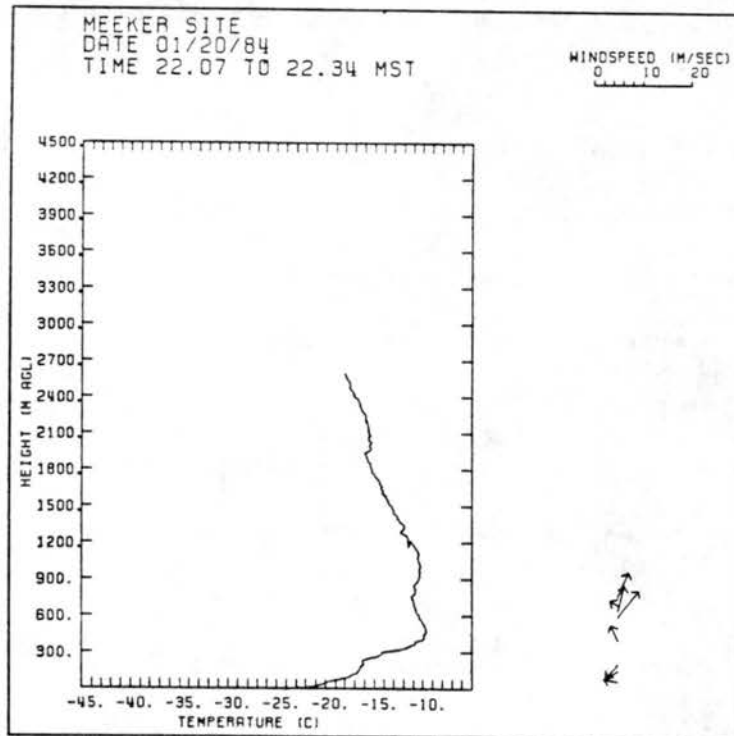


Figure 32. Meeker site airsonde sounding for 2200 LST on 20 January 1984.

fall, marking the onset of the synoptic scale change described previously. Figure 33 displays the 0600 sounding data which shows evidence of the disturbance. At all levels above 300 m AGL, the atmosphere has warmed 2.0-3.0°C, similar to the changes observed at the Ca site. The surface inversion layer has remained intact with its embedded down-valley winds, but the layer above it has warmed and contains a strong southwest wind. As before, the continued analysis of data collected later would be of little value to this study because of the obvious baroclinic effects on the boundary layer.

c. Rifle site data. The Rifle sounding site was located approximately 2.0 km south of the town center on the opposite side of the Colorado River in an area known as the South Rifle Metro District. As can be seen in Figure 7, the Colorado River Valley widens slightly to the east of the Rifle area to form a small basin. Southwest of the city is a large landform known as Battlement Mesa which has a large area above 9000 ft MSL (2745 m MSL). The site was in the valley bottom and elevation was 5345 ft MSL (1630 m MSL). A small mesa with a peak elevation of 6000 ft MSL (1830 m MSL) rose abruptly to the south of the site and valley depths immediately to the west of the site were 500-600 m. As was found at the other locations, several inches of snow were on the ground at the start of the observational period. The observations from the Rifle site formed the most complete data set from the experiment with very few gaps in either wind or thermal data.

Figure 34 displays the first sounding taken at Rifle near 1600 LST. Except for an 80 m deep superadiabatic surface layer, the atmosphere is stably stratified through its entire depth. A nearly isothermal layer extends to 700 m AGL, above which is a slightly less stable region with

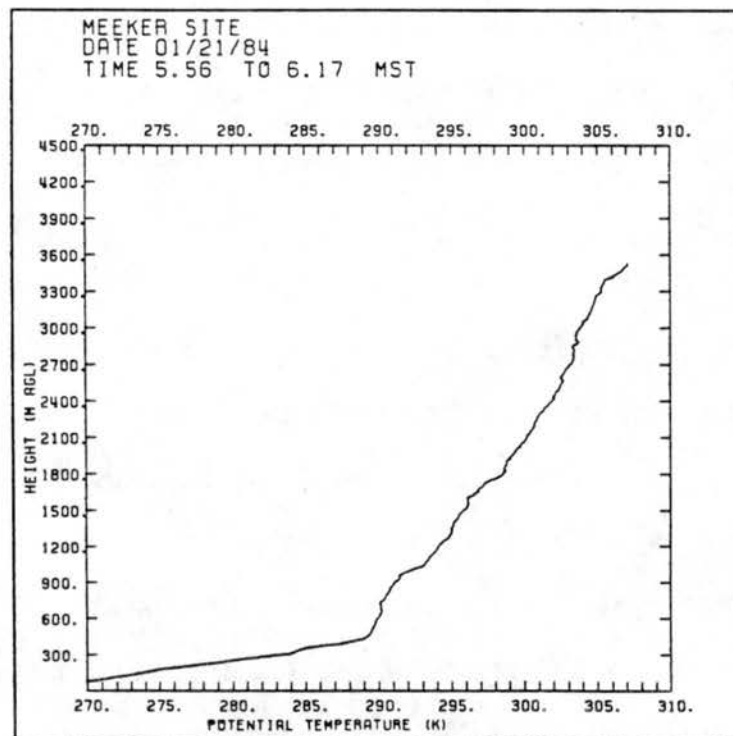
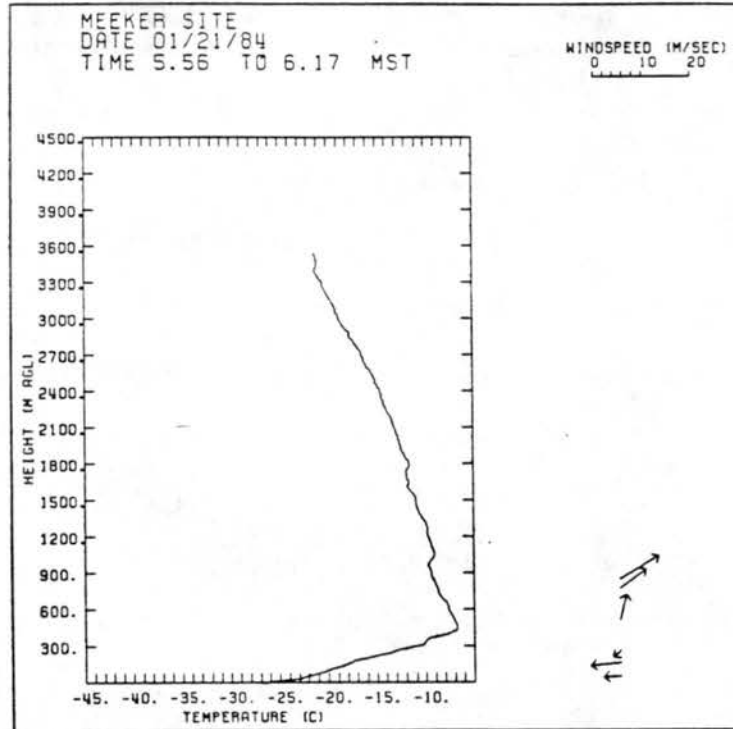


Figure 33. Meeker site airsonde sounding for 0600 LST on 21 January 1984.

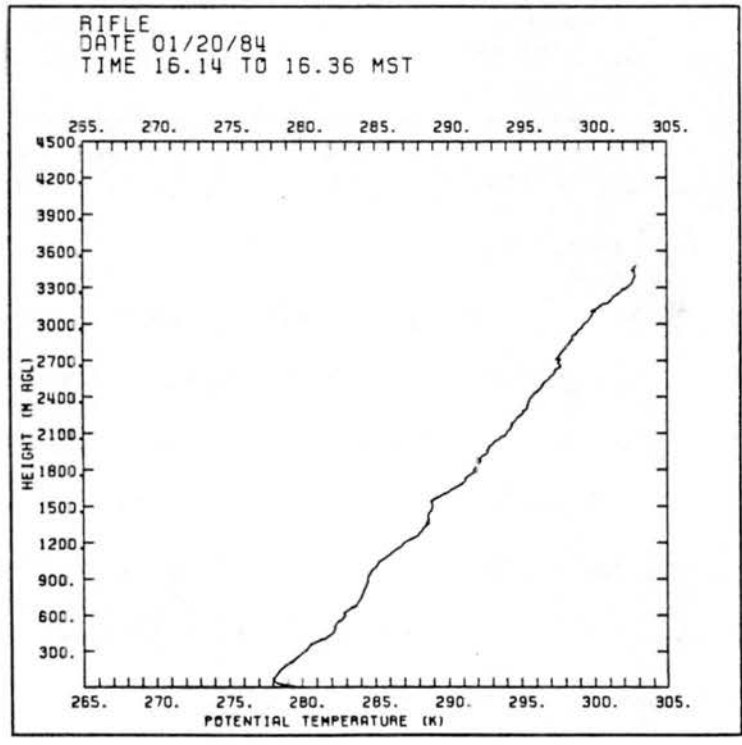
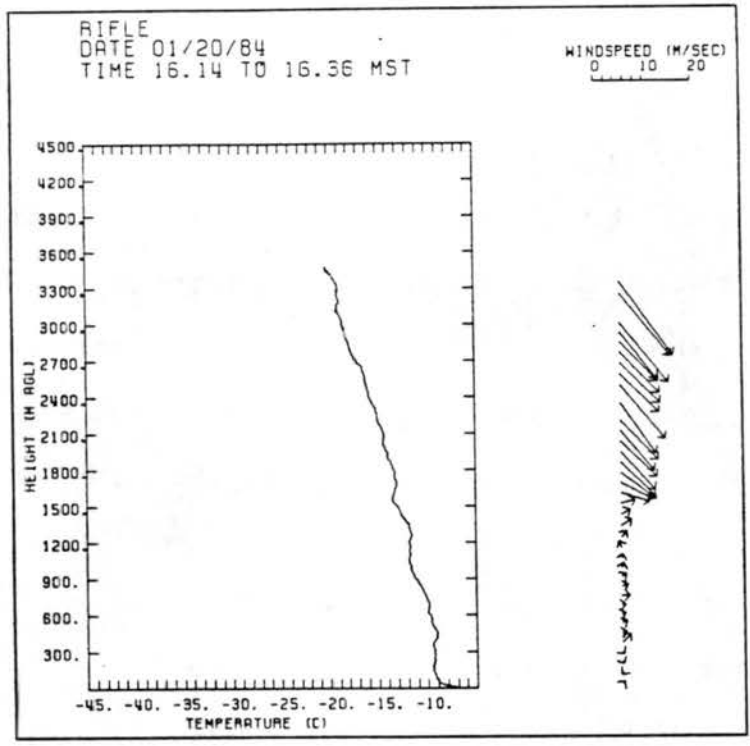


Figure 34. Rifle site airsonde sounding for 1600 LST on 20 January 1984.

a lapse rate of  $4.0 \times 10^{-3} \text{ }^\circ\text{C m}^{-1}$ . Between 1290 m AGL and 1530 m AGL is a nearly neutral layer capped by a 150 m deep weak inversion layer. The height of the base of the shallow mixed layer coincides with the elevation of the high terrain of Battlement and Grand Mesa, suggesting that this layer may be an elevated CBL produced by the daytime heating of these landforms. Winds below the elevated neutral layer are generally very weak from the southwest with speeds less than  $1.5 \text{ m s}^{-1}$ . Within the mixed layer the winds retain the southwest direction but increase in speed to  $2.0\text{-}3.0 \text{ m s}^{-1}$ . However, they shift abruptly to the prevailing northwest synoptic flow above the capping inversion layer with speeds over  $10.0 \text{ m s}^{-1}$  at 2000 m AGL.

The profile has changed significantly by the next sounding taken at 1800 LST (Figure 35). Below 1200 m AGL, the air has cooled slightly while above 1200 m AGL the temperature has increased. Additionally, a surface based inversion layer which extends from the ground to 200 m AGL has replaced the shallow convective layer observed in the 1600 LST sounding. Between 200 m AGL and 750 m AGL is a deep isothermal layer which underlies a nearly neutral layer reaching 1100 m AGL. A 400 m weak inversion layer separates the mixed layer from the free atmosphere above it. Below the top of the surface inversion, the down-valley (northeast) winds are weak with speeds less than  $2.0 \text{ m s}^{-1}$ . Between 600 m AGL and 900 m AGL a  $1.5\text{-}2.1 \text{ m s}^{-1}$  southwesterly flow appears which turns to the southeast above 1000 m AGL. Above 1400 m AGL, the synoptic flow first appears as a  $4.5 \text{ m s}^{-1}$  southwest wind which smoothly rotates with height to a northwest orientation by 1800 m AGL. Average  $Ri$  values are above 1.0 in the lower part of the sounding but drop to below 0.3 near the top of the mixed layer before increasing again higher in the profile.



The 2000 LST sounding shows that the atmosphere has changed little since 1800 LST (Figure 36). The surface has cooled to  $-17.5^{\circ}\text{C}$  and a well developed down-valley flow is present below the surface inversion top at 400 m AGL. The winds shift slightly to a southeasterly orientation with speeds of  $2.0\text{--}2.3\text{ m s}^{-1}$  in the isothermal layer between 500 m AGL and 750 m AGL. The winds were nearly calm from 750 m AGL to 900 m AGL and the cooling of the elevated mesas has resulted in the development of a  $2.0\text{ m s}^{-1}$  south wind in the remnants of the mixed layer below 1300 m AGL. As before, Ri values achieve a minimum below 0.3 near the elevated inversion base.

Two hours later the continued cooling of the air below the 1200 m AGL level and the warming above it has resulted in the profile taken from the 2200 LST sounding (Figure 37). The surface temperature has continued to fall reaching  $-22.1^{\circ}\text{C}$  at the start of the sounding. The surface inversion reaches 380 m AGL, slightly lower than the previous sounding. A deep, nearly isothermal region lies between the inversion top and 1100 m AGL before it encounters a 500 m deep inversion layer which has resulted from the upper level warming. The wind profile also shows two decoupled regions above and below 1200 m AGL. Above the  $3.0\text{--}4.0\text{ m s}^{-1}$  down-valley flow in the surface inversion layer, a nearly uniform  $2.0\text{ m s}^{-1}$  southeast wind extends to 1000 m AGL before rotating through a thin layer to the prevailing west to southwest winds in the free air. Ri values below 0.2 are found in this high shear zone, and indicate the maintenance of turbulent flux through the layer.

The surface pressure at Rifle rose over 1.0 mb between the start of the experiment at 1600 LST and 2100 LST, then remained nearly constant until 0100 LST, the onset of the steady pressure fall which continued

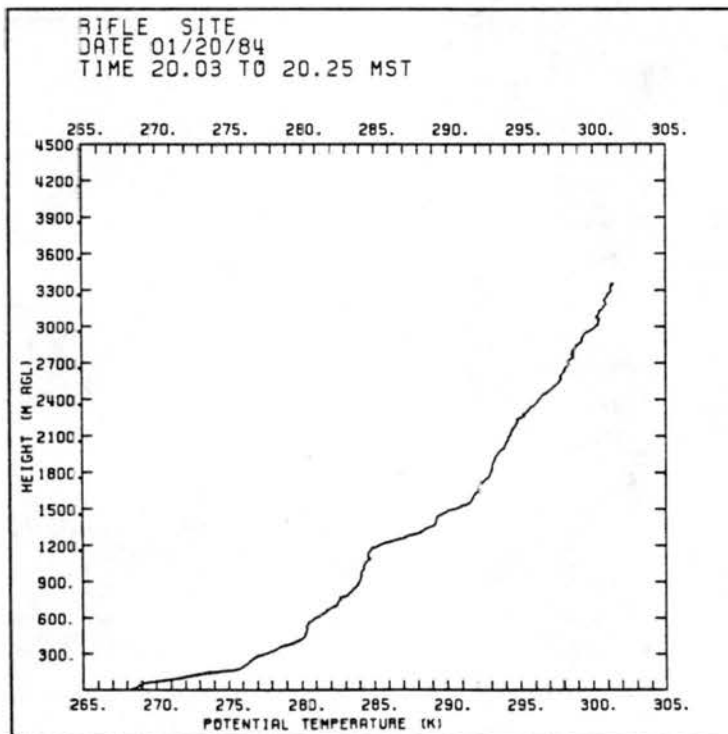
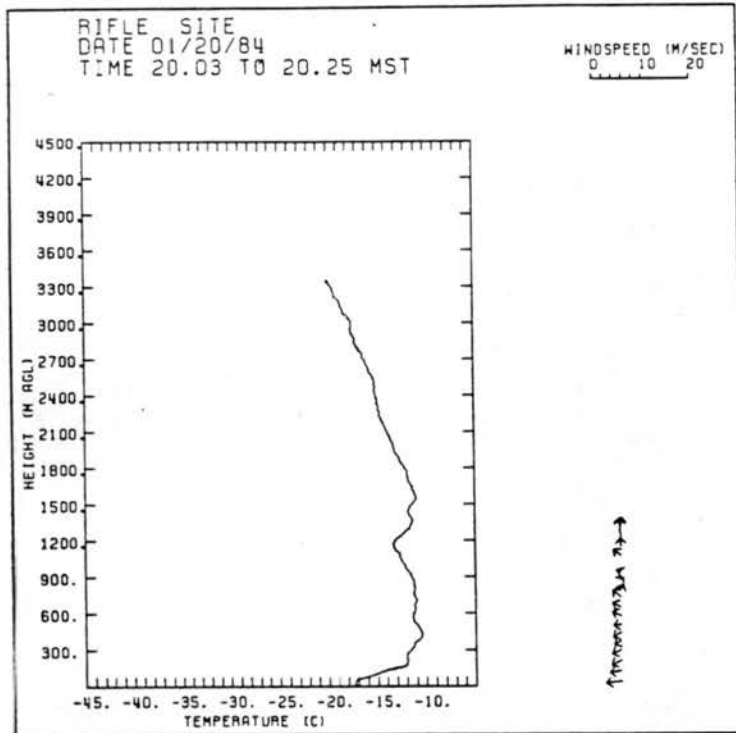


Figure 36. Rifle site airsonde sounding for 2000 LST on 20 January 1984.

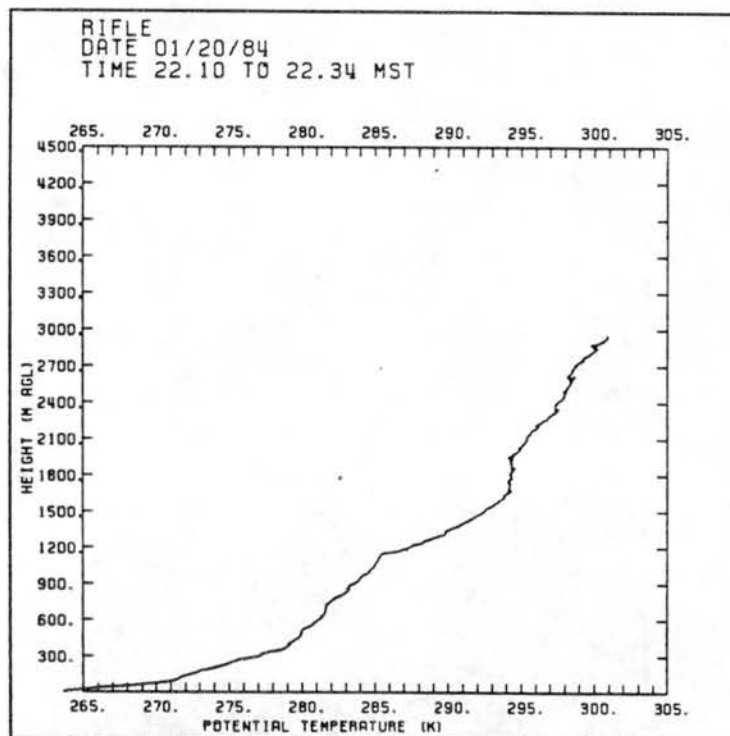
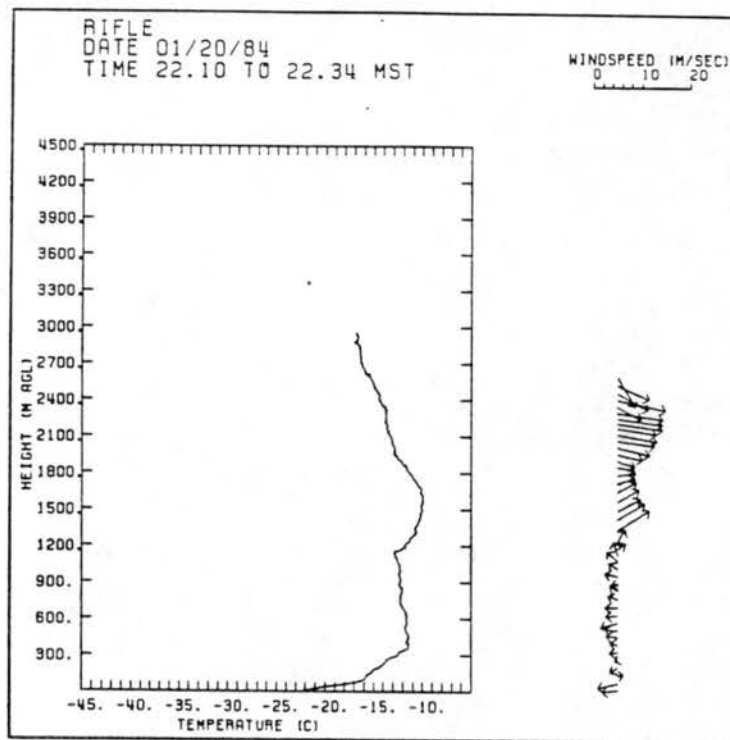


Figure 37. Rifle site airsonde sounding for 2200 LST on 20 January 1984.

through the morning. The 0600 sounding shown in Figure 38 reveals that large scale changes observed at the other two sites were present at Rifle as well. The valley layer continued to cool despite the warm air advection that occurred simultaneously above it. Temperature changes of 2.0-3.0°C at higher elevations were similar to those observed over the other two sites. The temperature and wind profiles still exhibit a decoupled two layer structure with the dividing height slightly lower than before at 1150 m AGL. The surface inversion layer extends up to this level with a free atmospheric lapse rate at higher elevations. The winds in the lowest 600 m were still down-valley with speeds of 1.0-3.0 m s<sup>-1</sup>. Above the valley, the winds turn easterly with a 7.8 m s<sup>-1</sup> maximum at 712 m AGL. In the free air above the inversion, the winds changed to the prevailing westerly flow with speeds over 10.0 m s<sup>-1</sup>.

### 3. Analysis of observations

Figure 39 shows the simultaneous evolution of the boundary layer structures above each of the three sites in the experiment from 1600 LST to 2200 LST, before the influence of the synoptic scale disturbance was significant. The contoured fields are the deviations of the observed potential temperatures from the GJT 0000 GMT sounding data taken near the start of the experiment. Generally, the observed potential temperatures at Meeker were 1.0-2.0 K colder than at the same elevation at Ca, but the overall evolution of the thermal structure is very similar, with a slight synoptic scale warming trend occurring above the local topographic features. The observed differences are probably the result of the larger scale topographically induced cooling occurring over the Meeker site, which was surrounded by high terrain. The apparent adiabatic descent of the temperature profile indicated

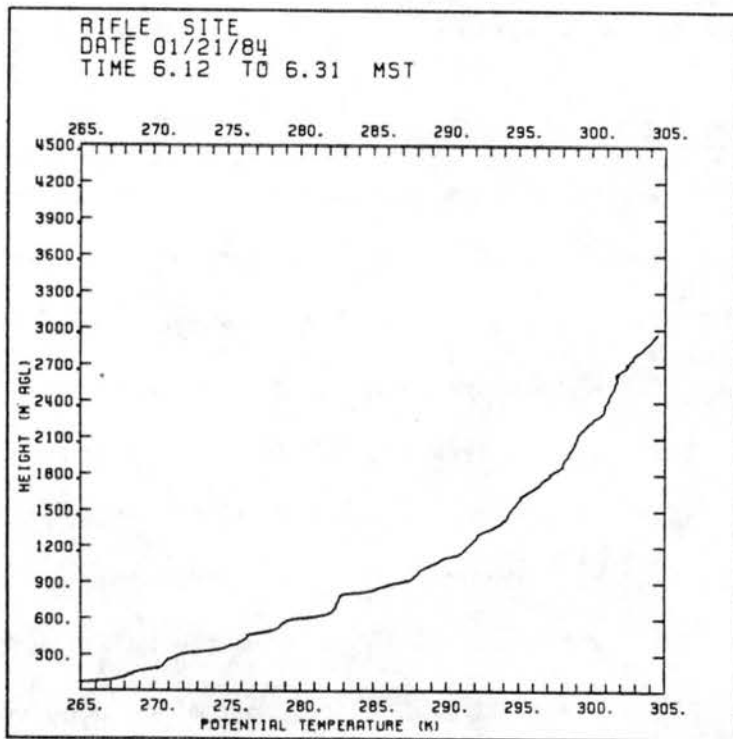
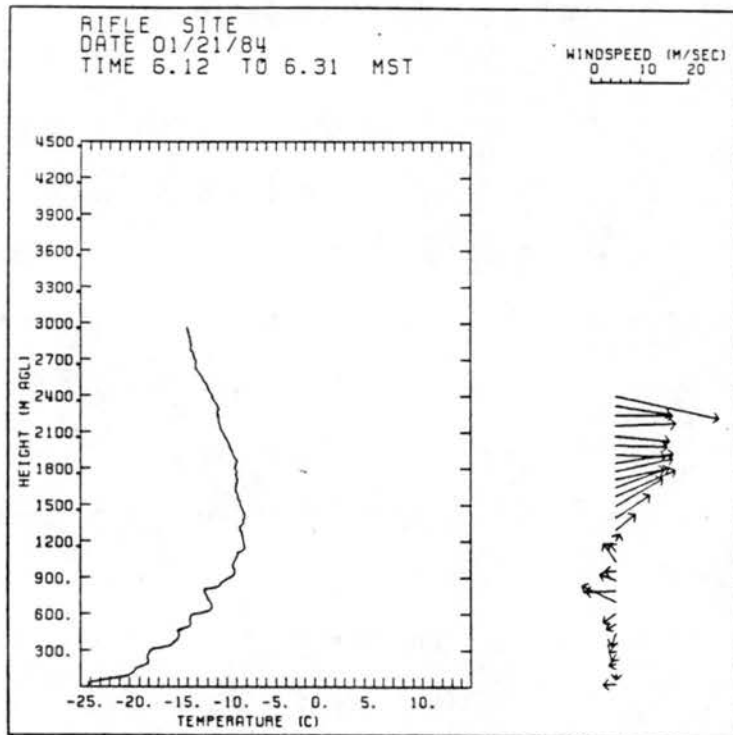


Figure 38. Rifle site airsonde sounding for 0600 LST on 21 January 1984.

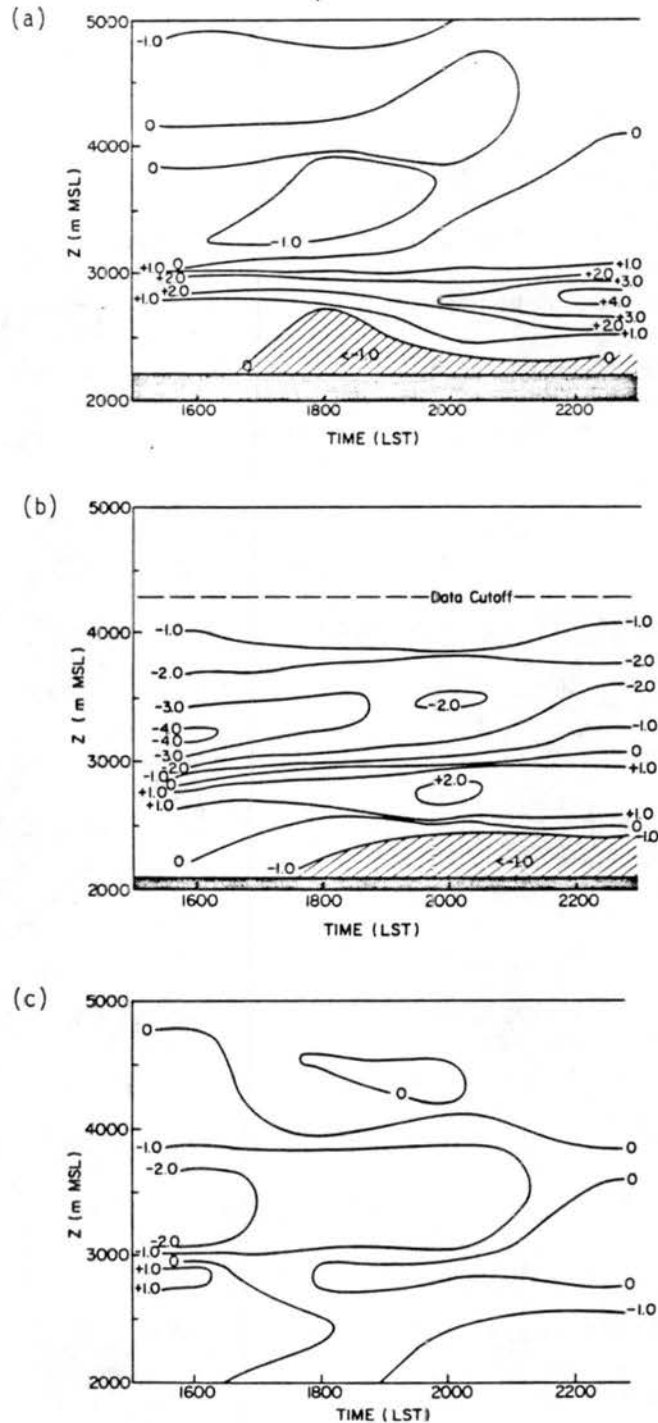


Figure 39. Deviations of potential temperature observed in: a) Ca site airsonde soundings; b) Meeker site airsonde soundings; and c) Rifle site airsonde soundings from 0000 GMT 21 January 1984 NWS GJT rawinsonde observations for the period 20-21 January 1982.

mesoscale subsidence at the Meeker site which was not present at either of the other sites. The most striking feature is the obvious difference between the development of the boundary layer above the Rifle site from the other two. Whereas the layer between 2500 m MSL and 3000 m MSL gradually warmed 1-4°C at both Meeker and Ca, potential temperature values decreased nearly 1°C in the same layer over Rifle. This difference is attributed to a cooling on a scale that is larger than the local valley scale, but does not encompass an area as large as the study region.

Associated with this difference in thermal structure is the appearance of the blocked flow region below 2835 m MSL (1200 m AGL) at Rifle and the decoupling and cooling of the boundary layer from the free atmosphere above it. The Ca site is 50 km to the east of the 9000 ft MSL terrain and was too far upwind of the high terrain during the experiment to be influenced by its cooling. The development of a mesoscale boundary layer started soon after sunset when the surface cooling was strongest, but the growth ceased within several hours as the strong synoptic level winds overpowered the boundary layer processes. At the Meeker site, which was surrounded on three sides by terrain over 9000 ft MSL, local valley scale wind and thermal structure became fully developed less than 4 h after sunset, but the overlying mesoscale boundary layer never fully developed, although a large scale cooling did offset some of the advective warming. Additionally, from the limited wind data from the site it could be determined that topographically induced winds were present through a thin layer above the valley. These effects would probably be more pronounced had a deeper CBL developed during the day so that the boundary layer processes could be buffered from the free air aloft, as in the ASCOT 82 experiment.

#### D. Summary of Observational Program

The data collected from these two field experiments unquestionably show the development of nocturnal boundary layers which are of a scale larger than the local valleys and much deeper than the 100-300 m deep layers typically found over flat terrain. In both cases presented here, the depth of the topographical influence does not exceed the elevations of the large mountain masses in the region which typically extend to 9,000-10,000 ft MSL (2740-3050 m MSL). In the ASCOT 82 experiment, a 1-3 K cooling was observed in a 600 m deep layer with its bottom located at the valley ridgeline and its top reaching 3000 m MSL. Additionally, the development of this mesoscale nocturnal boundary layer caused the weak synoptic scale north wind to become dynamically decoupled from the southerly topographically induced flow above the Roan Plateau. The valley scale boundary layer was influenced by the development of the mesoscale NBL above the valley, which in turn was related to the synoptic scale flow. Early on, the valley winds were over  $6 \text{ m s}^{-1}$  as a well developed mountain-plain circulation was present over the plateau. Later, when a synoptic wind shift inhibited this circulation, the valley winds weakened to nearly half their earlier speeds.

During the CSU 84 experiment, the blocked flow layer observed at Rifle extended 1500 m above the valley floor to the elevation of the high terrain downwind of the site. In this case, the mesoscale boundary layer structure was much more complex, exhibiting a high degree of variability. At the Ca site, the synoptic scale flow overpowered the boundary layer processes. A limited cooling occurred at the Meeker site with temperatures in the mesoscale boundary layer being 1-2°C colder than at Ca. The Rifle site data exhibited the greatest mesoscale

boundary layer effects, with cooling and topographically induced winds present through a deep layer above the valley. This type of structure should be expected to develop during the winter when the daytime boundary layer depth does not exceed the height of the large scale terrain and the synoptic scale winds are relatively strong.

The large contrast between the two cases presented implies that a large variability can be expected between observed cases of boundary layer evolution. Causes of this variability include gradient level wind speed and direction, afternoon CBL depth, differential heating and other mesoscale influences. For example, on several other nights for which data were taken during the ASCOT 1982 field study, boundary layer development was disturbed by mesoscale circulations which remained after early evening convective storms had dissipated. However, some common features should be anticipated as well, such as a boundary layer cooling that extends several hundred meters above the ridges and plateaus and a deviation of the wind field from the synoptic scale flow through this layer. Obviously, more data would be helpful in better defining the common aspects of nocturnal boundary layer evolution in the study region, however analyses of these two cases do present significant insight toward understanding its basic development. Using these observations as a base, it is useful to employ a numerical model to help in understanding the mechanisms responsible for creating the observed structures and subsequently to investigate the causes for structural variability. Therefore, emphasis of the current study shifts at this point to the design and results of a numerical modeling program that explores these questions.

## CHAPTER IV

### NUMERICAL MODELING OF MESOSCALE BOUNDARY LAYER EVOLUTION

Sophisticated numerical models which describe complex non-linear atmospheric processes have become an invaluable tool in many branches of meteorology, including the study of the atmospheric boundary layer. By controlling the initial and boundary conditions in model simulations, relationships between atmospheric forcing and feedback mechanisms can be discerned on time and space scales not possible in even the most complete observational program. When properly integrated, modeling and observational studies can be designed to complement one another to yield information not available from either observations or model results alone. In order to attain this goal properly, one must give careful consideration to the types of processes to be simulated and subsequently select or formulate a numerical model which is capable of performing the desired simulations. Once this is achieved, the modeling program should be designed using the information already obtained from analysis of field data. Caution must be used in the analysis of the results by recognizing the deficiencies inherent in the model and relating the simulated processes to real atmospheric phenomena.

There are two philosophies used in the design of a numerical modeling program to simulate observed atmospheric characteristics. The first approach, which is the one more often used, is to simulate the details of the observed structure on a case by case basis with the goal of reproducing specific sets of observations. The main advantage of

this method is the ability to verify the model computations with actual data and thereby give credibility to the model formulation. Unfortunately, the model results are often difficult to analyze due to the complexity of the very specific boundary conditions necessary to reproduce the observed case. As could be seen in the two cases presented in the previous chapter, a wide variability even exists in observed behavior at the same location. Alternatively, one can design a modeling program with the goal of producing idealized structures that are still representative of actual observational cases to determine the dominant forcing and feedback mechanisms contributing to the observed structures. Although it loses the high degree of verification found in case studies, this approach allows for the simplification of the specified boundary conditions to produce a realistic but controlled "laboratory-type" simulation resulting in a more general picture of the primary physical processes. For these reasons, this method is more appropriate for the current study due to the very complex nature of the mesoscale boundary layer evolution. Another advantage of this approach is the ability to design simulations to explain the causes for the observed variability by altering the simplified boundary conditions between simulations.

The two goals in the present use of the model are to simulate the complete diurnal cycle of the mesoscale boundary layer evolution over the study region and to explore the causes for the observed variability in NBL development. To accomplish these goals, six two-dimensional (2-D) and two three-dimensional (3-D) simulations were run using idealized representations of terrain and conditions in the observational study region (Table 3). One 2-D simulation detailed the evolution of

Table 3.  
Model Simulation Information

Case	$L_m$ (km)	$L_p$ (km)	$D_x$ (km)	$h$ (m)	$\Delta t_\ell$ (s)	$\frac{\Delta t_\ell}{\Delta t_s}$	$\Delta X$ (m)	$U_o$ ( $ms^{-1}$ )	$V_o$ ( $ms^{-1}$ )
1	60	12.75	150	127	3	6	375	0	N/A
2	60	12.75	150	127	3	6	375	5	N/A
3	120	42.75	300	427	3	6	375	5	N/A
4	60	12.75	150	127	3	6	375	3	N/A
5	60	12.75	150	127	3	6	375	7	N/A
6	60	12.75	150	127	3	6	375	5	N/A
7	60	12.75	150	127	3	3	750	3.5	3.5
8	60	12.75	150	127	3	3	750	0	5

the mesoscale boundary layer from sunset until noon on the following day. The remaining 2-D and both 3-D numerical experiments were run to examine the effects of wind speed, wind direction and afternoon CBL depth on the development of the NBL through the evening transition period. The model was forced in these simulations by both a prescribed external wind field and a specified surface heat flux function which approximates the diurnal cycle.

#### A. Model Description

The Colorado State University Three-Dimensional Cloud/Mesoscale Model (Tripoli and Cotton, 1982) was selected to carry out the model program. Originally developed to perform simulations of cumulus convection (Cotton and Tripoli, 1978; Tripoli and Cotton, 1980), the model was later extended to perform detailed simulations of boundary layer flow in complex terrain (Banta, 1982; Bader and McKee, 1983, 1985). This model uses a fully elastic and non-hydrostatic primitive equation set employed in a terrain following coordinate system, making it ideal for this type of study. Additionally, recent improvements to the model (Tremback et al., 1985) have increased its capability to simulate a wider variety of mesoscale phenomena. Since it has changed substantially since the publication of the original papers, a brief description of the model follows which includes modifications made specifically for this study.

##### 1. Theoretical development of model equations

The model equations are formulated to describe perturbations about a dry, hydrostatic, quiescent base state. Finite difference forms of the momentum equation, thermodynamic energy equation, and a combination

of the ideal gas relation and continuity equation were used to predict velocity, potential temperature and normalized pressure. Absolute pressure and temperature were computed from diagnostic relationships involving the predicted quantities. Following the notation of Tripoli and Cotton (1982) and others, any variable  $A$  can be decomposed as

$$A = \bar{A} + A'' , \quad (8a)$$

where the overbar represents an ensemble average value resolvable on the time and space scales of the model simulation and the double prime denotes an unresolvable turbulent fluctuation about this average. The mean value can be further decomposed as

$$\bar{A} = A_0(z) + \bar{A}' , \quad (8b)$$

where  $A_0$  is the temporally and horizontally invariant base state and  $A'$  is the resolvable deviation from this state.

Because it is conserved in dry adiabatic processes, potential temperature is used as the thermodynamic variable and is defined by Poisson's equation,

$$\theta = \frac{T}{\pi} \quad (9)$$

in which  $\theta$  is the potential temperature,  $T$  is the temperature and  $\pi$  is the normalized pressure (hereinafter referred to simply as "pressure") defined by

$$\pi = \left( \frac{p}{p_{00}} \right)^{R/c_p} . \quad (10)$$

Here,  $p$  is absolute pressure, the constant  $p_{00}$  is a reference pressure, usually taken to be 1000 mb ( $10^5$  Pa), and  $R$  and  $c_p$  are the gas constant

and constant pressure specific heat of dry air, respectively. Using (10), the ideal gas relation

$$p = \rho RT , \quad (11a)$$

can be rewritten as

$$\pi = \left( \frac{R}{p_{00}} \rho \theta \right)^{R/c_v} , \quad (11b)$$

where  $\rho$  is the dry air density and  $c_v$  is the constant volume specific heat of dry air which is related to  $c_p$  and  $R$  by  $c_p = c_v + R$ . The base state is assumed to obey both (11b) and the hydrostatic relation and is therefore defined by

$$\pi_0 = \left( \frac{R}{p_{00}} \rho_0 \theta_0 \right)^{R/c_v} \quad (12)$$

and

$$\pi_0 = - \frac{g}{(c_p \theta_0)} \quad (13)$$

where  $\pi_0$ ,  $\rho_0$  and  $\theta_0$  are the base state pressure, density and potential temperature.

The formulation of the elastic pressure equation is described in detail by Klemp and Wilhelmson (1978). Summarizing their development, the time derivative of (11b) is combined with the compressible continuity equation,

$$\frac{\partial \rho}{\partial t} + \frac{\partial}{\partial x_j} (\rho u_j) = 0 , \quad (14)$$

then approximated to yield

$$\frac{\partial \bar{\pi}}{\partial t} + \frac{R\pi_0}{c_v \rho_0 \theta_0} \frac{\partial}{\partial x_j} (\rho_0 \theta_0 \bar{u}_j) = 0 . \quad (15)$$

Justification for the approximations is made in the original paper, but basically they allow for mean mass adjustments to domain average temperature changes which do not affect the dynamics in model simulations. The momentum equation is

$$\begin{aligned} \frac{\partial \bar{u}_i}{\partial t} + \frac{c_p \theta_0 \partial \bar{\pi}'}{\partial x_i} = g \frac{\bar{\theta}'}{\theta_0} \delta_{i3} - \frac{1}{\rho_0} \frac{\partial}{\partial x_j} (\rho_0 \bar{u}_i \bar{u}_j) \\ + \frac{\bar{u}_i}{\rho_0} \frac{\partial}{\partial x_j} (\rho_0 \bar{u}_j) - \frac{\partial}{\partial x_j} \overline{u_j'' u_j''} \end{aligned} \quad (16)$$

where  $u_i$  is the  $i$ th component of the velocity vector,  $g$  is the gravitational acceleration and  $\delta_{i3}$  is the Kroneker delta function. Here, the buoyancy term,  $-\bar{\rho}'/\rho_0$ , has been approximated by  $\bar{\theta}'/\theta_0$ , based on a linearization of (11b) and scale analysis of the resulting terms as described by Pielke (1984). Completing the basic model equation set, the dry thermodynamic energy equation is described by

$$\frac{\partial \bar{\theta}}{\partial t} = - \frac{1}{\rho_0} \frac{\partial}{\partial x_j} (\rho_0 \bar{u}_j \bar{\theta}) + \frac{\bar{\theta}}{\rho_0} \frac{\partial}{\partial x_j} (\rho_0 \bar{u}_j) - \frac{\partial}{\partial x_j} (\overline{\theta'' u_j''}) . \quad (17)$$

The terms in the pressure equation and on the lhs of the momentum equation comprise the acoustically active or elastic terms capable of propagating sound waves. The terms on the rhs of (16) and in the thermodynamic energy equation describe the non-acoustic processes, such as advection and diffusion, which are active on the longer gravity wave time scale.

The turbulent flux terms are parameterized using an eddy viscosity closure scheme in which the mixing coefficients are determined from prognostic turbulent kinetic energy (TKE) equations formulated by Yamada (1983). This approach offers some of the advantages afforded by higher-order closure schemes (Mellor and Yamada, 1982) without a great increase

in computational expense. Unlike fully diagnostic closure schemes, the effects of inhomogeneous and non-stationary turbulence fields can be included. In this parameterization, two coupled equations are used to predict  $q^2 = \bar{u}_j''^2$  (twice TKE) and product of  $q^2$  and the turbulent length scale,  $\ell$ , and are written for this model as

$$\begin{aligned} \frac{\partial \bar{q}^2}{\partial t} = & -\frac{1}{\rho_0} \frac{\partial}{\partial x_j} (\rho_0 \bar{q}^2 \bar{u}_j) + \frac{\bar{q}^2}{\rho_0} \frac{\partial}{\partial x_j} (\rho_0 \bar{u}_j) - \frac{\partial}{\partial x_j} (\overline{u_j'' q^2''}) \\ & - \left( \overline{u_j'' u_m''} \frac{\partial \bar{u}_m}{\partial x_j} \right) + \frac{g}{\theta_0} \delta_{j3} \overline{u_j'' \theta''} - \frac{(\bar{q}^2)^{3/2}}{B_1 \ell} \end{aligned} \quad (18)$$

and

$$\begin{aligned} \frac{\partial \bar{q}^2 \ell}{\partial t} = & -\frac{1}{\rho_0} \frac{\partial}{\partial x_j} (\rho_0 \bar{q}^2 \ell \bar{u}_j) + \frac{\bar{q}^2 \ell}{\rho_0} \frac{\partial}{\partial x_j} (\rho_0 \bar{u}_j) \\ & - \frac{\partial}{\partial x_j} [\overline{u_j'' (q^2 \ell)''}] - \ell F_1 \left\{ \left( \overline{u_j'' u_m''} \frac{\partial \bar{u}_m}{\partial x_j} \right) \right. \\ & \left. + \frac{g}{\theta_0} \delta_{j3} \overline{u_j'' \theta''} - \frac{(\bar{q}^2)^{3/2}}{B_1} [1 + F_2 \left( \frac{\ell}{kz} \right)^2] \right\} \end{aligned} \quad (19)$$

where  $B_1$ ,  $F_1$  and  $F_2$  are empirical constants. The turbulent flux terms are evaluated from

$$\overline{u_i'' u_j''} = -K_M \frac{\partial \bar{u}_i}{\partial x_j} \quad (20.a)$$

and

$$\overline{s'' u_j''} = -K_S \frac{\partial \bar{s}}{\partial x_j} \quad (20.b)$$

here  $s$  represents any scalar quantity ( $\theta$ ,  $q^2$ ,  $q^2 \ell$ ) and  $K_M$  and  $K_S$  are the momentum and scalar mixing coefficients defined by

$$K_M = (\bar{q}^2)^{1/2} \Delta S_M \quad (21.a)$$

and

$$K_S = 1.2 K_M \quad (21.b)$$

The mixing length,  $\Delta$ , is simply  $(q^2_x/q^2)$  for vertical flux quantities and the horizontal grid spacing otherwise. The stability function  $S_M$  is defined for the momentum and thermodynamic energy equations by

$$S_M = 1.96 \frac{(0.1912 - Ri_f)(0.2341 - Ri_f)}{(1 - Ri_f)(0.2231 - Ri_f)} \quad (22.a)$$

where

$$Ri_f = \begin{cases} 0.6588[Ri + 0.1776 - (Ri^2 - 0.3211 Ri + 0.03156)^{\frac{1}{2}}] & Ri < Ri_c \\ Ri_c & Ri \geq Ri_c \end{cases} \quad (22.b)$$

and  $Ri_c = 0.19$ .  $S_M$  is simply set to 0.4 (the neutral limit) for the turbulence equations. This formulation differs slightly from that used by Yamada in two ways. First, except for the specification of the mixing length, horizontal diffusion is handled in a similar fashion as the vertical diffusion. The original closure had a crude parameterization for horizontal diffusion in simulations with very small grid aspect ratios. In the simulations described in this chapter, the grid aspect ratios vary between 0.14 and 1.33, necessitating a more sophisticated horizontal turbulence parameterization. Secondly,  $S_M$  was empirically determined to be 0.2 for the turbulence equations from neutral channel flow experiments (Mellor and Yamada, 1984). However, it was believed that setting  $S_M$  to 0.4 would make the diffusion of the turbulence quantities more consistent with the diffusion of the other scalar fields. Sensitivity tests with the model in several configurations revealed that the parameterization was not overly

diffusive in stable environments, a problem frequently encountered with many parameterizations (see Appendix II).

The inclusion of uneven topography at the lower boundary was accomplished using a terrain following coordinate system developed by Gal-Chen and Sommerville (1975) and extended by Clark (1977). Known as a "sigma-z" system, it results from the transformations

$$x^* = x \quad (23.a)$$

$$y^* = y \quad (23.b)$$

$$z^* = \frac{z - z_s(x,y)}{H - z_s(x,y)} H \quad (23.c)$$

where  $x$ ,  $y$  and  $z$  are the standard Cartesian independent spatial variables,  $x^*$ ,  $y^*$  and  $z^*$  are the corresponding transformed spatial variables,  $z_s$  is the height of the surface and  $H$  is the height above the model reference level of the model domain top. From Clark, the spatial derivative of any quantity  $A$  can be written as

$$\frac{\partial A}{\partial x_i} = \frac{1}{a} \frac{\partial}{\partial x_j^*} (ab^{ij}A) \quad (24.a)$$

$$a(x^*) = 1 - z_s(x^*)/H = \frac{\partial z}{\partial z^*} \quad (24.b)$$

where the transformation tensor,  $b^{ij}$ , is defined by

$$b^{ij} = \begin{bmatrix} 1 & 0 & \frac{1}{a} \frac{\partial z_s}{\partial x} \left( \frac{z^*}{H} - 1 \right) \\ 0 & 1 & \frac{1}{a} \frac{\partial z_s}{\partial y} \left( \frac{z^*}{H} - 1 \right) \\ 0 & 0 & \frac{1}{a} \end{bmatrix} \quad (25)$$

## 2. Finite differences

The model equations were integrated on a staggered mesh described by Tripoli and Cotton (1982). This type of grid centers scalars in each grid box with velocity components defined normal to the sides. When used with standard fourth-order advection, this system is very effective at properly describing gravity wave propagation. A time differencing scheme described by Klemp and Wilhelmson (1978) was used to separately integrate the acoustic and non-acoustic terms in the predictive equations. After the non-acoustic terms were integrated over a  $2\Delta t_1$  timestep using a leap-frog scheme, the acoustically active terms were stepped forward for a specified number of smaller  $\Delta t_s$  time steps using a semi-implicit scheme to complete the integration. An Asselin filter was then employed to prevent solution separation. The time steps for both the acoustic and non-acoustic tendency computations were chosen to avoid exceeding linear stability criteria and are shown for each simulation in Table 3. A more detailed description of the finite difference methods can be found in Tripoli and Cotton (1982) and Klemp and Wilhelmson (1978).

## 3. Model domain

Figure 40 shows the domain used in the model simulations. The topography chosen is an idealized representation of an east-west cross-section through the observational study region. The model reference level ( $z_s = 0$ ) is coincident with a flat plain on the western edge of the domain which is bounded on the east by a long, gently sloping section with a 1% grade. A 500 m high blocking ridge on the eastern end of the domain is connected to the long sloping plain by a more steeply sloping ramp with an 8% slope. Two configurations were used in this

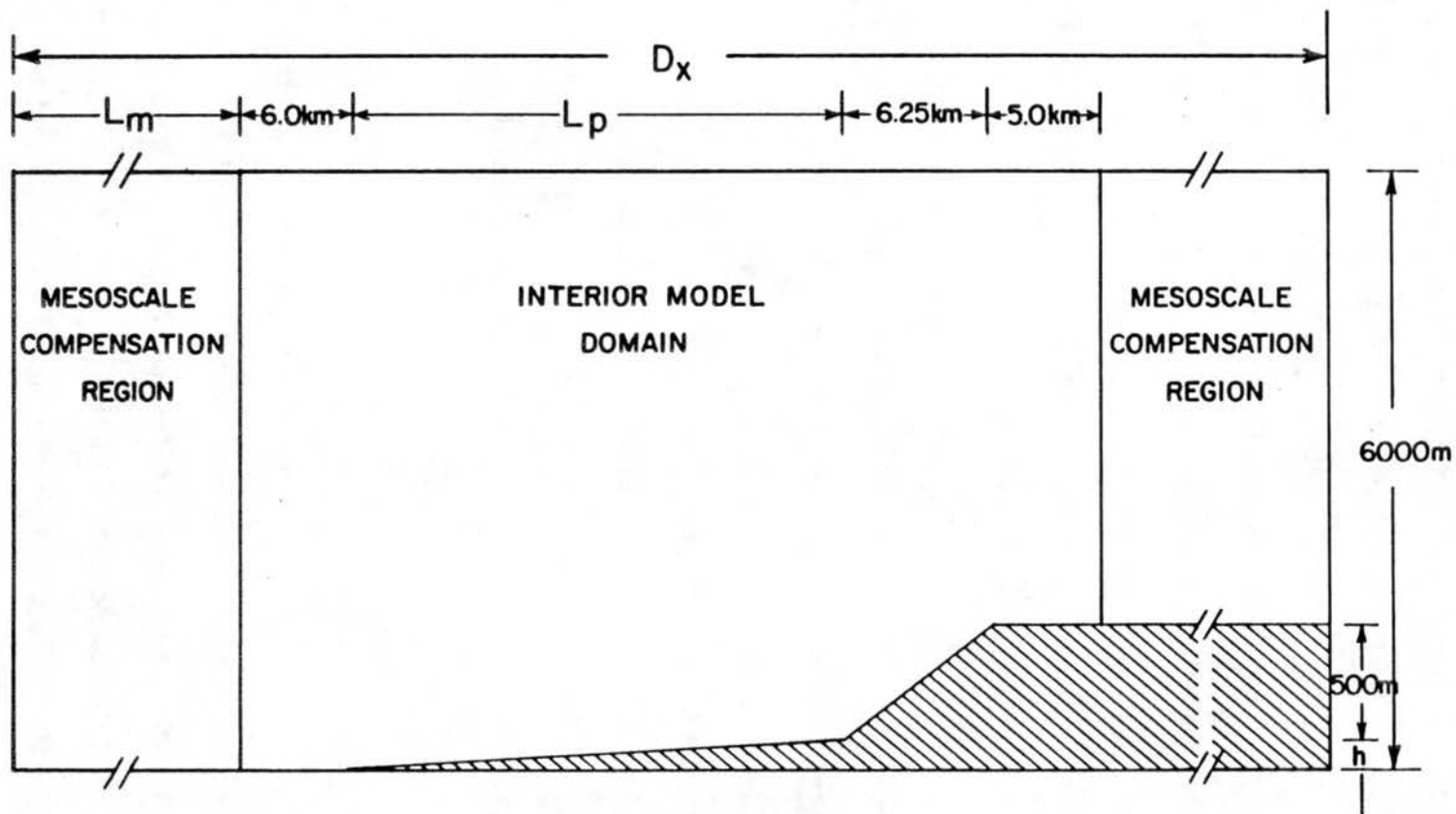


Figure 40. Model domain (not to scale).

study which differed only by the length of the long sloping plain. A shorter section with a total horizontal projected length,  $L_D$ , of 12.75 km was used in preliminary sensitivity experiments as well as in the intercomparison study of factors influencing the evolution of the NBL structure. The single simulation detailing the complete diurnal mesoscale boundary layer cycle uses a longer section with  $L_D = 45.75$  km for reasons to be explained in a subsequent section. The mesoscale compensation regions (MCRs) on the lateral sides are used in conjunction with the boundary conditions and will be described later. In the 3-D simulations, topography is infinitely slab-symmetric in the north-south ( $y$ ) direction and the model domain through a horizontal cross-section is square with an interior domain width of 30 km. The horizontal model top is 6.0 km above the low plain in all simulations. Horizontal grid spacing is a constant 375 m in the interior model domain in the 2-D simulations and 750 m in the 3-D simulations. Vertical grid spacing above the lowest topography is a constant 50 m in the lowest 10 levels then telescopes logarithmically to include 22 additional levels below the model top. Vertical grid spacing above the elevated terrain is computed using the coordinate transformation functions to form a rectangular grid in  $z^*$  coordinates.

#### 4. Boundary conditions

The top boundary condition is based on a formulation by Klemp and Durran (1984) and allows for the radiation of vertically propagating gravity waves. For mesoscale and local scale model simulations, it is desirable to have open lateral boundary conditions as well. However, these boundary conditions tend to produce artificial outflow accelerations when coupled with the dynamic formulation of the model

equations. An alternative method developed by Tripoli and Cotton (1982) for determination of quantities at the lateral boundaries coupled the Orlanski (1976) radiation boundary condition with a mesoscale adjustment. The MCRs inhibit domain-scale trends produced by the Orlanski condition at the interior domain boundaries by providing a crude mesoscale adjustment through pressure and temperature feedbacks. Additionally, the imposed wind profiles are prescribed only at the outer boundaries and the MCR acts as a buffer between the externally specified winds and the interior model domain. The only constraints on the momentum field in the interior domain result from total mass conservation requirements at the inflow and outflow boundaries. Scalar quantities and vertical velocities are defined in the MCR for each level at a point midway between the interior and exterior domain boundaries. No gradient is assumed to exist beyond these points.

The surface layer parameterization was adapted from a formulation by Louis (1979) based on the flux-profile relationships developed by Businger et al. (1971). In all simulations, the surface is assumed to be dry, a condition frequently observed in western Colorado. Surface friction velocity is computed for the bottom grid boxes based on the horizontal velocity components and a specified surface potential temperature flux. Separate relations were developed for the computation of surface potential temperature flux for the nighttime and daytime regimes. For the nocturnal phase, a simple one layer soil heat budget is used. From climatological records of observed diurnal temperature ranges in western Colorado, the surface temperature is approximated by

$$T_s = T_{s0} + \Delta T_s e^{-b(t-t_{ss})} \quad (26)$$

where  $t_{ss}$  is the time of sunset,  $\Delta T_s$  is the nocturnal temperature change, and  $b$  is a time constant (set to 4 h in the simulations described here). A simple heat budget of the form

$$S + G + R = 0 \quad (27)$$

where  $G$  is the conduction term,  $R$  is the net longwave radiative flux and  $S$  is the sensible heat transfer from the ground to the air is used. The conduction term is computed by assuming that the temperature 1.0 m below the surface did not change significantly during the night and that the thermal conductivity,  $a$ , of the soil layer between this depth and the surface is  $0.010 \text{ W(mK)}^{-1}$  (Sellers, 1965). Based on these assumptions,

$$G = - \frac{a(T_s - T_{s0})}{1 \text{ m}} \quad (28)$$

The net radiative flux is computed from the difference between the upward black-body radiative flux emitted from the surface and a prescribed constant atmospheric downward flux of  $300 \text{ W m}^2$  taken from climatological averages computed from Denver rawinsonde soundings. From the computed values of  $R$  and  $G$ , the surface potential temperature flux  $\overline{w''\theta''_s}$  is diagnosed from (27) and the relation

$$\overline{w''\theta''_s} = - \frac{S}{\rho_0 c_p} \quad (29)$$

In this simple formulation there is no forced realization imposed on the surface temperature described by (26) and the computed model temperatures. The time history of the calculated nocturnal surface

potential temperature flux is shown in Figure 41a. The computed values compare favorably with recent values measured in the study area (Gudiksen, 1985). To simulate the wintertime conditions desired in the shallow boundary layer case (Case 6), the same cooling function is used, but  $t_{ss}$  is replaced by  $t_{ss}+3$  h in (25) to reduce the strong initial cooling.

The daytime potential temperature flux is described by

$$\overline{w''\theta''_s} = \overline{w''\theta''_{sMAX}} \sin \frac{\pi(t-t_{sr})}{\tau} \quad (30)$$

where  $t_{sr}$  is the time of sunrise. The amplitude of the heating function,  $\overline{w''\theta''_{sMAX}}$ , is set to  $0.25 \text{ K m s}^{-1}$  and the daylength,  $\tau$ , is set to 12 h. This heating function (Figure 41b) has been successfully used in previous studies of valley-scale boundary layer evolution and appears to be quite realistic, although the phase of the model surface flux may deviate up to 1 h from that actually observed.

## 5. Initialization

For all of the simulations except one (Case 6 in Table 1), the base state sounding input to the model consisted of a 1.5 km deep surface based neutral layer underlying a free atmosphere layer extending to the model top (Figure 42a). For Case 6, which was the simulation exploring the effects of afternoon CBL depth on NBL evolution, a surface based stable layer was present initially (Figure 42b). At the external lateral boundaries, the logarithmic wind profile shown in Figure 43 was imposed linearly with time over a 15 min dynamic initialization period from a quiescent state at the start of the simulation. This was followed by a 45 min dynamic adjustment period with no surface heating

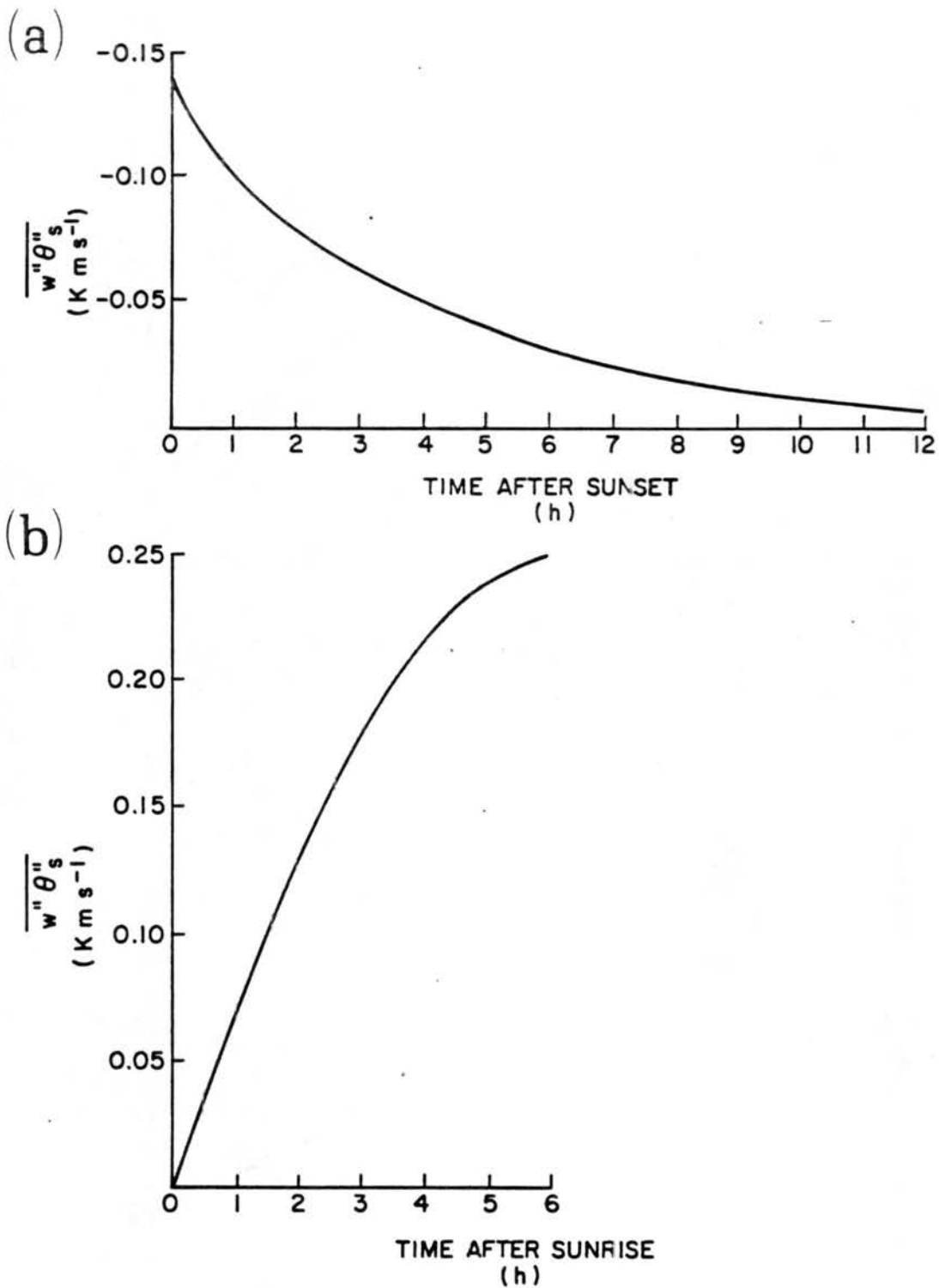


Figure 41. Computed model potential temperature flux for a) nighttime and b) daytime.

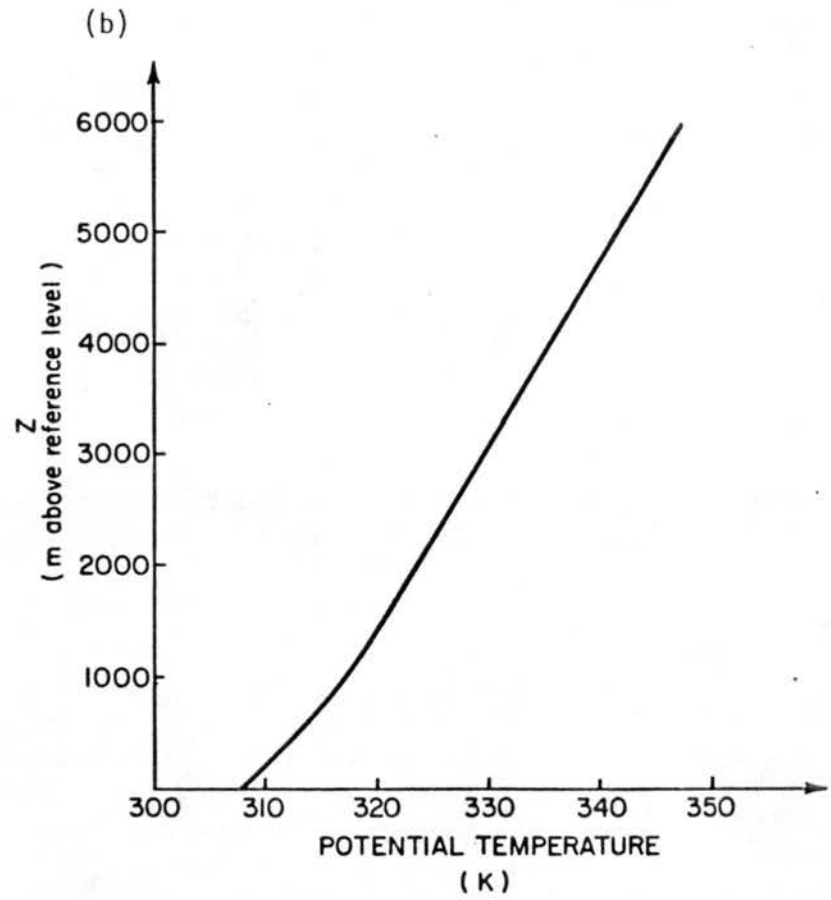
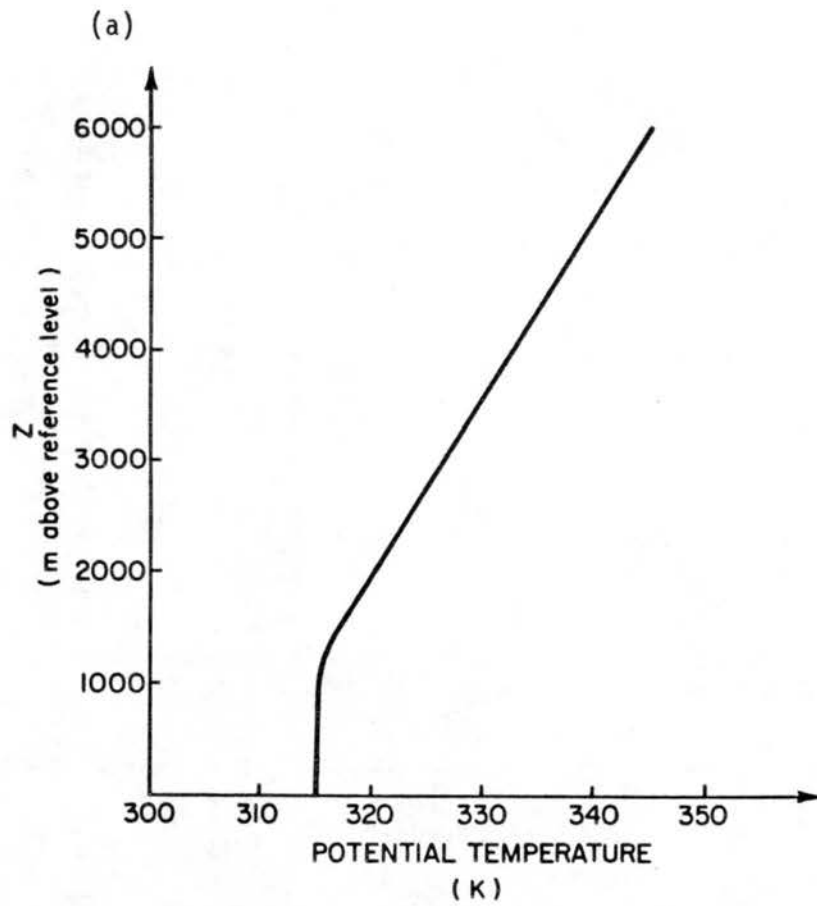


Figure 42. Base state model sounding for  
 a) Cases 1-5 and 7-8 and b) Case 6.

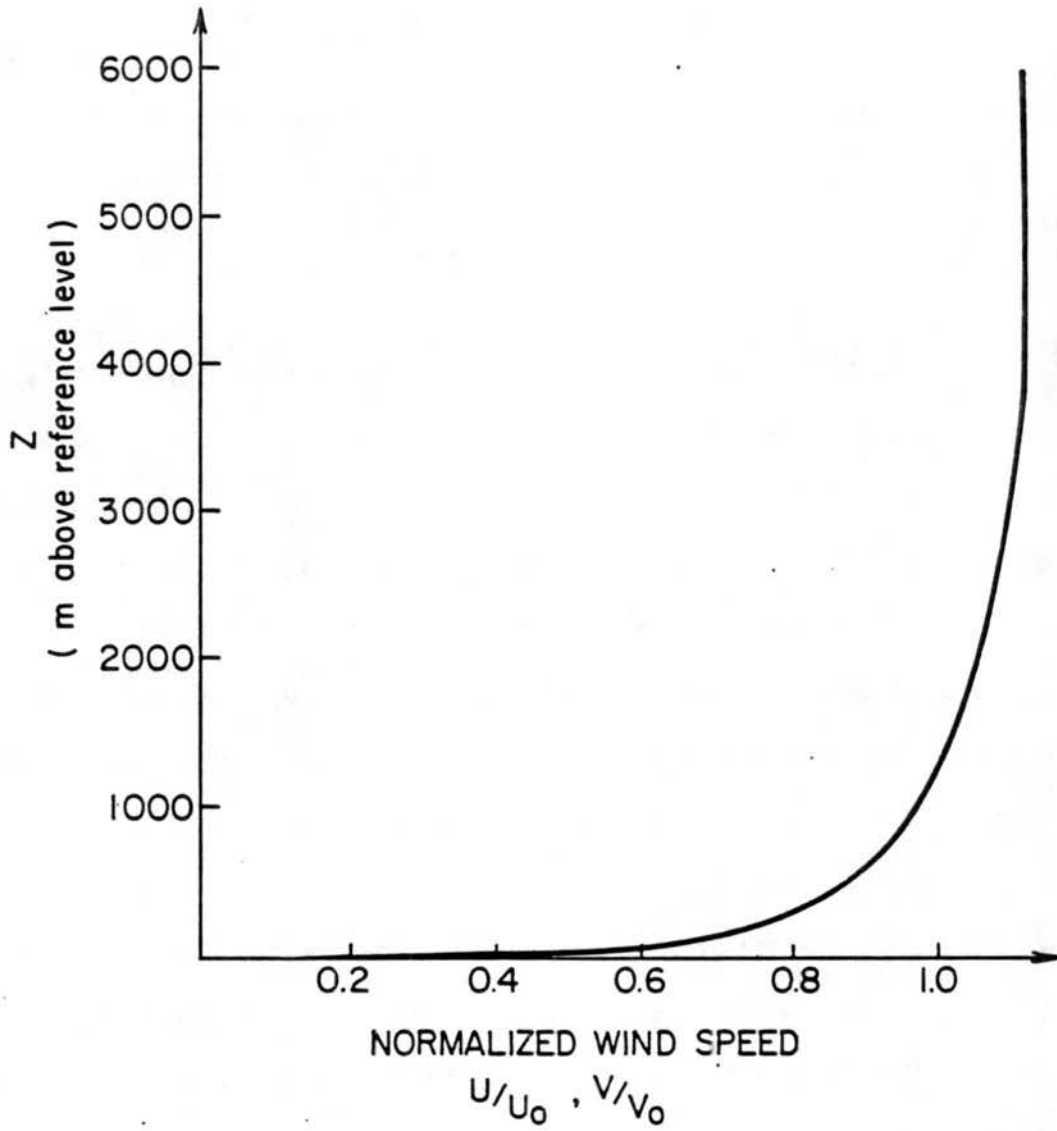


Figure 43. Imposed external wind field profile for model simulations.

or cooling. Values of  $u_0$  and  $v_0$  appear in Table 1. Sensitivity tests (see Appendix II) confirmed that the model had achieved a steady state at this time for the deep neutral layer simulations. Following the 1 h dynamic initialization-adjustment in Case 6, a 3 h heating period was initiated with  $\overline{w''\theta''}_s$  set to  $0.10 \text{ K m s}^{-1}$  to develop a shallow CBL. Model sunset marked the end of the initialization process in all cases and surface cooling was initiated at that time.

### B. Description of Numerical Experiments

The modeling program was undertaken in three parts. First, several 2-D sensitivity experiments were run to insure that the model was correctly initialized and that it would not produce any unrealistic dynamic or thermodynamic features. The most significant result from the sensitivity analysis was the determination that an ambient wind must be present to correctly simulate NBL evolution. This was revealed by comparing a reference simulation initiated with a deep surface-based neutral layer and a  $5 \text{ m s}^{-1}$  westerly geostrophic wind to one with no initial winds. Although the primary emphasis of the research program was on mesoscale NBL development, it was determined that a good test of the full model, including the surface layer parameterization, would be the simulation of the mesoscale boundary layer evolution through a complete diurnal cycle. Consequently, the second part of the model study consisted of a single 2-D simulation which started at sunset and continued through noon the following day. The last part of the modeling program focused on the effects of season and geostrophic wind on the evolution of the mesoscale NBL, particularly through the evening transition period when non-linear effects are the most important. Four

2-D and two 3-D simulations were intercompared for this purpose. One of the 2-D experiments was the reference simulation. Two more of the 2-D simulations were initiated identically except for differences in the geostrophic wind speed. The fourth two-dimensional simulation was designed to determine the seasonal differences in NBL evolution, which is determined primarily by afternoon CBL depth. The two 3-D experiments examined the effects of geostrophic wind direction on the development of the NBL. The first was initialized with a  $5 \text{ m s}^{-1}$  southwest wind and the second with a  $5 \text{ m s}^{-1}$  south wind. A summary of all eight simulations appears in Table 3.

As mentioned previously, two domains were used with total interior domain widths of 30 km and 60 km. Although the length of the actual sloping plain in the study region is approximately 60 km long, it was hoped that the shorter length of 12.75 km used in the narrow domain adequately represented its effects for several reasons. First, the fine resolution of the 2-D experiments made the addition of extra grid columns computationally more expensive. Second, even with the doubling of the horizontal grid spacing in the 3-D experiments, the narrow domain was the largest which could be reasonably used due to the computational costs associated with the 3-D simulations. Although the model realistically simulated the evolution of the NBL structure during the first 8 h after sunset in the narrow domain, the unrealistic pooling of cold air near the west boundary and the development of the relatively larger scale daytime convective circulations necessitated using the wider domain in the diurnal cycle simulation.

### C. Results of Numerical Experiments

Model output included instantaneous fields of all model variables saved every 10 min on permanent computer file and printed fields of selected variables every 30 min. Additionally, profiles of 10 min averages for selected quantities for a single grid location were also calculated from instantaneous model fields at every timestep. The contour-vector plots appearing in Figures 44-45, 47-51 and 53 were taken from the instantaneous fields on file and only show the lowest 14 levels for increased resolution. In these figures, the vertical coordinate is exaggerated 24 times with respect to the horizontal (48 times in Figure 46). The wind vectors are true in both speed and direction, which results in an apparent flow normal to the topography in some of the plots.

#### 1. Results of sensitivity studies

a. Effects of turbulence parameterization, dynamic initialization and boundary conditions. Several sensitivity experiments were run to test the turbulence parameterization, initialization procedure, terrain configuration and the lateral boundary conditions. The turbulence parameterization was tested by running the model in two different configurations. In the first, the terrain was removed and the surface cooling parameterization was instituted following the 1 h initialization period. The model formed a very shallow surface based inversion with most of the cooling limited to a 150 m deep layer. From this result, it was determined that the Yamada scheme was not overly diffusive. The second test used the narrow domain model terrain shown in Figure 40, but the turbulent flux terms were computed using a Smagorinsky type

diagnostic mixing coefficient (Cotton and Tripoli, 1978). In this configuration, the model failed to respond properly and quickly suppressed all turbulent fluxes in even slightly stable regions despite the presence of strong wind shear. Clearly, in this case the effects of turbulent flux terms had a significant impact on the model solution so that the choice of a physically realistic and well documented scheme such as the Yamada closure became necessary.

The test of the initialization procedure continued a simulation using the narrow domain with  $u_0 = 5 \text{ m s}^{-1}$  for several hours in the absence of surface heating or cooling. From a comparison of model fields taken at different times, it could be seen that the model had achieved a near steady state 30 min after the start of the run. The longer adjustment time was added as a precaution against any undetected instabilities. This same simulation was used to determine if the lateral boundary conditions produced any artificial circulations in time, and it was found that they remained stable. Another test of both the boundary conditions and the Yamada turbulence closure consisted of maintaining the speed profile but reversing the direction of the wind field in a separate run, thereby having the wind blow from the high to the low terrain. As before, the boundary conditions remained stable and did not produce any artificial circulations. Appendix II provides more detail of these experiments.

b. Effects of ambient wind field. The most significant finding from the model sensitivity experiments was the importance of the ambient winds in producing realistic model solutions. In previous simulations of valley flows, the wind field above the valley had little effect on the circulations below ridgetop due to the sheltering of the valley air

mass by terrain. However in this case, the boundary layer was not isolated from the overlying wind field by topographical features. Figure 44a-d shows the results when the model was run for 2 h without an external wind field (Case 1). The simulation started with a quiescent wind field and a deep surface based neutral layer (Figure 44a). After 30 min, the cooling was confined to the lowest model layer which showed a 3.9-4.3 K potential temperature decrease. As a result, a shallow drainage developed with speeds near  $2.0 \text{ m s}^{-1}$  over the steep slope slowing to  $0.5 \text{ m s}^{-1}$  over the sloping plain, but it was confined to the lowest layer as well (Figure 44b).

The shear produced by the drainage enabled a limited amount of vertical mixing of the very stable surface air to cool the layer between 50 m AGL and 100 m AGL 0.5 K over the length of the sloping plain and 2.0 K over the steep slope after 1 h (Figure 44c). Because of the slightly deeper cold layer and the slope of the terrain, the drainage flow present just above the surface weakened and an easterly cold thermal circulation appeared 100 m AGL over both slopes with speeds of  $1.5 \text{ m s}^{-1}$  over the western end of the sloping plain increasing to over  $4.0 \text{ m s}^{-1}$  above the eastern end and the steeply sloping section. The distinction between this type of circulation and a drainage flow is that it is produced by hydrostatic pressure gradients and not strictly by buoyancy forces, analogous to the difference between slope and mountain-plain winds. The evening transition period appears to have reached its final phases at this time as the differences in the simulated fields after 2 h (Figure 44d) show that the cooling and deepening of the stable layer with the imbedded easterly winds was proceeding at a much slower rate than initially and had reached a quasi-steady state.

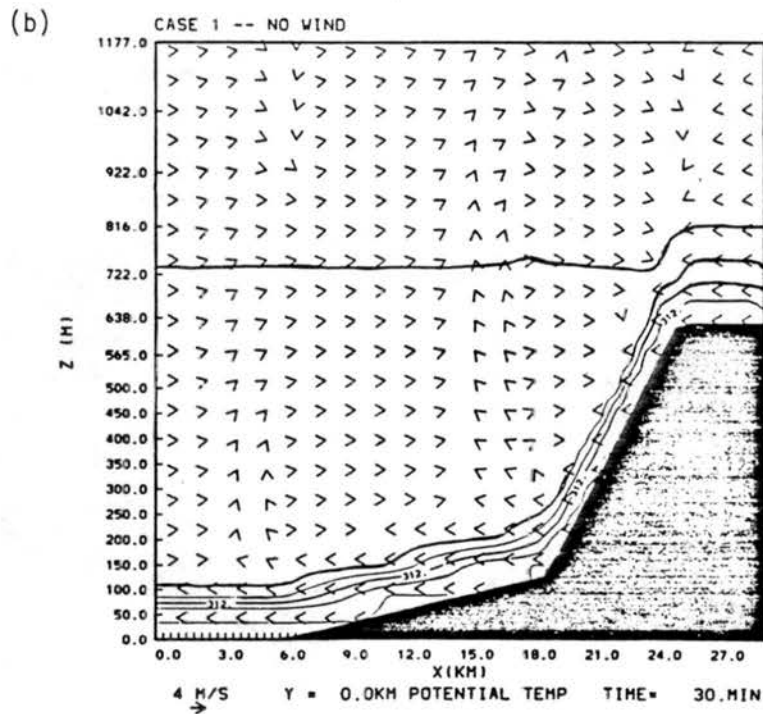
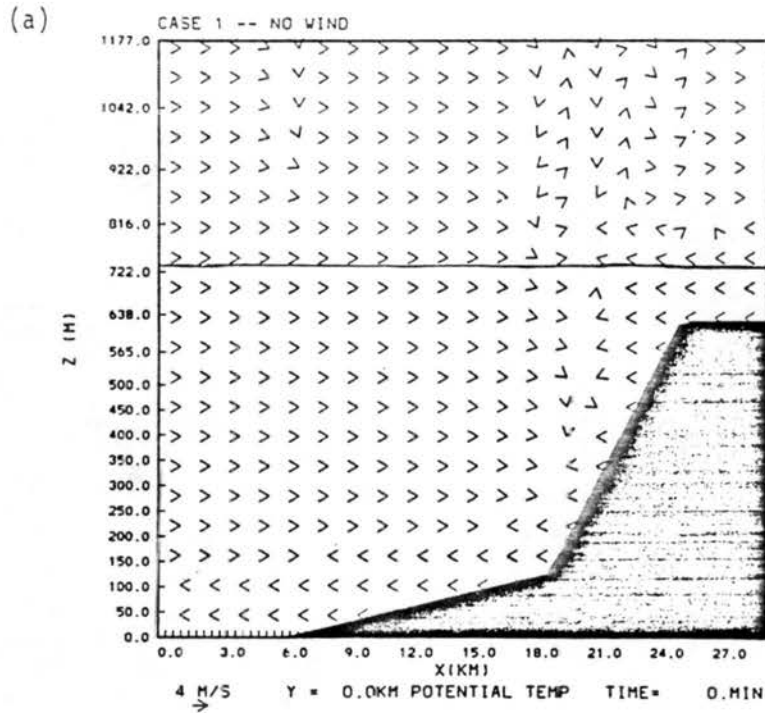


Figure 44. Wind and potential temperature fields for Case 1 (contour interval - 1 K) for (a) at sunset and (b) at sunset + 0.5 h.

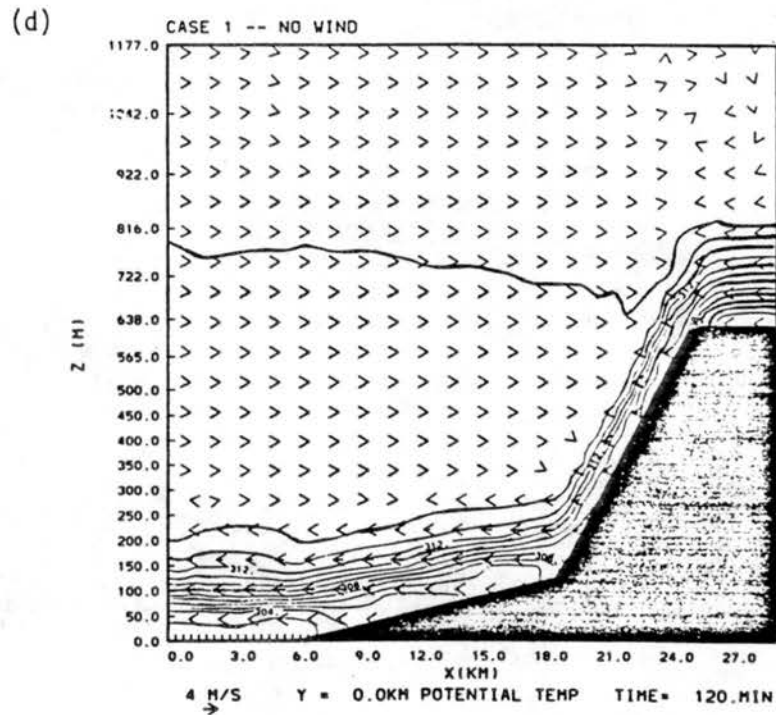
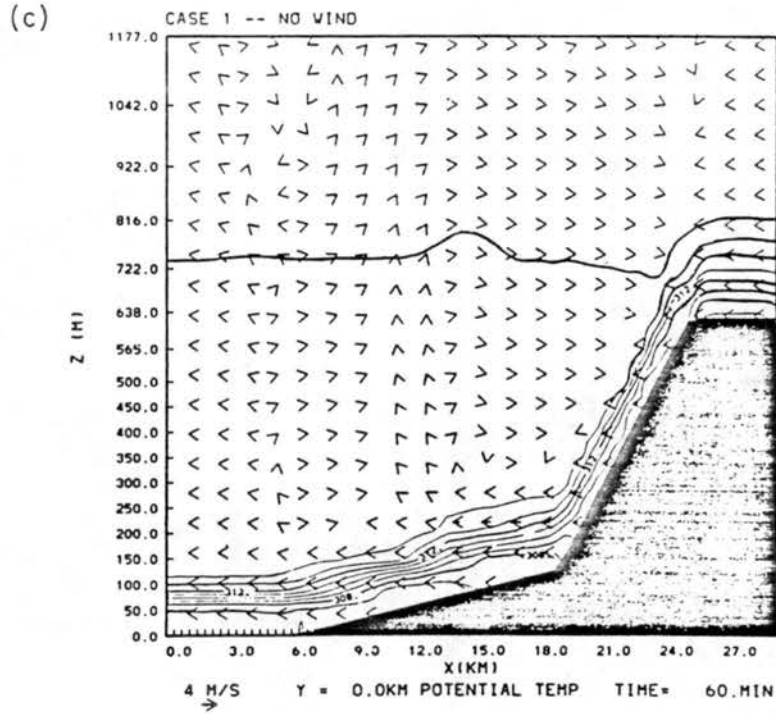


Figure 44. Wind and potential temperature fields for Case 1 (contour interval = 1 K) for (c) at sunset + 1 h and (d) at sunset + 2 h.

Contrasted with these results is the solution from the Case 2 simulation initialized with  $u_0 = 5 \text{ m s}^{-1}$ , a relatively light geostrophic wind speed (Figure 45a-h). Figure 45a shows the model state at sunset. The initial mixed boundary layer is 1300 m deep over the lower terrain and 700 m deep over the blocking ridge to the east, showing little potential temperature gradient across the domain. Over the flat terrain to the east and the low elevation sloping plain, the initially west wind increases in speed with height following the external logarithmic profile. To conserve mass at the inflow and outflow boundaries, the model produced a slight acceleration of the winds above the high terrain on the eastern side of the domain. Speeds were  $5.0 \text{ m s}^{-1}$  at 25 m AGL and increased to a maximum of  $7.5 \text{ m s}^{-1}$  at 530 m AGL as opposed to  $4.1 \text{ m s}^{-1}$  and  $4.8 \text{ m s}^{-1}$  at the same elevations farther upwind. Above the maximum, the speeds decreased with height above the high terrain to become more uniform across the domain. The appearance of this jet coincides with the top of the neutral layer and does not appear to adversely affect the simulations.

By 30 min after sunset (Figure 45b), surface cooling has produced a 125 m deep stable layer with a  $0.5\text{-}0.7 \text{ m s}^{-1}$  drainage flow that extends midway up the steep slope. This easterly drainage has replaced the  $2.0\text{-}3.0 \text{ m s}^{-1}$  west wind present initially. Over the upper part of the steep slope and the ridge to its east, the winds remain westerly but the speeds have decreased to less than  $1.0 \text{ m s}^{-1}$ . Unlike the previous case, the strength of the drainage remained unchanged 1 h after sunset (Figure 45c), but the depth of the stable layer increased as the shear produced by the overlying winds opposing the drainage flow acted to mix the cold surface air upward. The horizontal velocity convergence formed in

response to the adverse pressure gradient compensated for the downward component of the slope flow. By this time, the drainage flow extends over the entire length of the steep slope and a stable layer formed over the high plateau to the east. The vertical grid resolution in the model is probably inadequate to completely resolve the details of these very shallow layers produced early in the evening transition period. However, the bulk effect of the simulated layer structure is realistic.

Figure 45d shows the boundary layer 90 min after sunset. The strength of the low level drainage flow increased to  $1.0 \text{ m s}^{-1}$  as the increased depth of the stable layer removed the frictional effects of the overlying westerly winds. An easterly cold thermal wind formed with a maximum speed of  $3.4 \text{ m s}^{-1}$  75 m AGL at  $x = 10.0 \text{ km}$ . This coincided with the location of a perturbation in the potential temperature field associated with the buildup of cold air above the low flat plain on the western end of the domain. Farther to the east, the thermal wind speeds averaged  $2.0 \text{ m s}^{-1}$  and appeared at the top of a very stable surface based layer which underlies a much deeper and less stable transition layer reaching 200 m AGL over the sloping plain. The depth of the stable layer above the steeper slope is only 100 m deep as much of the air cooled there has drained westward. The two layer thermal structure and the horizontal convergence became even more evident 2 h after sunset (Figure 45e). A strongly stable surface inversion extended 125 m AGL over the length of the low sloping terrain with its top following the slope of the underlying topography. The lapse rate ( $\partial\theta/\partial z$ ) through this layer was  $0.07 \text{ K m}^{-1}$  as opposed to  $0.01 \text{ K m}^{-1}$  in the 100 m deep overlying transition layer. The top of the transition layer did not exhibit the slope found at the top of the surface based layer but was

nearly horizontal and decreased in thickness with increasing surface elevation. Drainage wind speeds remained between  $0.5$  and  $1.0 \text{ m s}^{-1}$ . The elevated thermal circulation maintained speeds near  $2.0 \text{ m s}^{-1}$  at  $75 \text{ m}$  AGL with the winds turning westerly above this level. The effects of the stable air mass on the boundary layer flow field can be seen by following the horizontal train of vectors  $225 \text{ m}$  above the reference level from west to east in Figure 45e. At this level over the flat plain on the west, the air was still in the mixed layer overlying the stable transition region. Farther to the east, however, the cooler air was more elevated and produced an adverse pressure gradient to the geostrophic wind, thereby forcing horizontal convergence and flow reversal near the blocking barrier. At this point, the evening transition period was nearly complete as the nocturnal flow regime became established and the boundary layer evolved more slowly.

By  $3 \text{ h}$  after sunset, a  $200 \text{ m}$  deep pool of very stable air had developed over the flat plain from the accumulation of cold air moving away from the higher terrain (Figure 45f). Potential temperatures in the lowest layer were  $299 \text{ K}$  over the flat plain and increased slightly with increased surface elevation. Although the surface inversion was still  $75 \text{ m}$  deep over the sloping plain, the total depth of the stable layer extended to  $275 \text{ m}$  above the reference level as vertical mixing and advection of the cold air continued in the transition layer. As before, the top of the transition layer was nearly horizontal showing a slight upward tilt from west to east, but with significantly less slope than the underlying topography. Easterly winds extended through a  $125 \text{ m}$  deep layer above the sloping plain with the maximum near  $2.0 \text{ m s}^{-1}$  still at  $75 \text{ m}$  AGL, the top of the surface inversion. Shears ranging from

$0.05 \text{ s}^{-1}$  in the lower part of the transition layer to  $0.02 \text{ s}^{-1}$  at the top of the transition layer continued to mix the cold air vertically. At 275 m above the reference level, the average horizontal velocity convergence between  $x = 5.0 \text{ km}$  and  $x = 15.0 \text{ km}$  was  $1.7 \times 10^{-4} \text{ s}^{-1}$ , approximately the amount needed to compensate for the vertical component of the slope flow. Drainage off of the steeply sloping section prevents a deep stable layer from forming, although a 200 m deep slightly stable layer has developed by this time over the elevated plateau to the east.

The boundary layer structure changes little in the next hour and achieved the state shown in Figure 45g 4 h after sunset. Since it appears that the boundary layer was evolving very slowly at this point, much can be gained by detailing the quasi-steady structure produced by the model. The low level drainage flow starts nearly 2/3 up the steep slope to the east with speeds of  $0.2 \text{ m s}^{-1}$  which increase to  $0.7 \text{ m s}^{-1}$  1.5 km down the slope. From this point to the intersection with the sloping plain at  $x = 18.75 \text{ km}$ , the drainage flow speeds vary little. Although the speeds are less than  $1.0 \text{ m s}^{-1}$  above the drainage over the steep slope, they remained westerly throughout the simulation thus far. Over the sloping plain, the drainage flow weakens slightly to  $0.5 \text{ m s}^{-1}$  but is very constant over the entire length of the plain and continuing onto the short flat section to the west. The easterly wind maximum still was located 75 m AGL over the terrain west of the steep slope. Easterly wind speeds decreased from  $1.8 \text{ m s}^{-1}$  at the maximum to  $0.5 \text{ m s}^{-1}$  at 125 m before becoming westerly above this level. The wind profile over the entire lower region encompassing both the flat and sloping plains was remarkably constant from one location to another. From 175 m AGL to 375 m AGL, the westerly wind speed increased sharply

with height from  $1.2 \text{ m s}^{-1}$  to  $4.3 \text{ m s}^{-1}$  then increased more gradually at higher elevations.

Potential temperature values at 25 m AGL were near 300 K under the cold pool on the west and increased linearly with distance up the sloping plain to 311 K at the base of the steep slope. Interestingly, the surface layer was nearly adiabatic over the steep slope leading to the high plateau; potential temperature values at 25 m AGL increased only 1.5 K from base to summit, although the total change in elevation was 500 m. Above the western plain, the vertical potential temperature structure exhibited the two level pattern seen earlier in the simulation. The lapse rate between 25 m AGL and 125 m AGL was  $0.1 \text{ K m}^{-1}$ , about twice as stable as would be realistically expected of nocturnal boundary layers over flat terrain. This was primarily due to the very large amount of cooling which occurred in the lowest model layer. However, between 175 m AGL and 325 m AGL, the lapse rate was  $0.017 \text{ K m}^{-1}$ , a value in the range of those typically found in the observational program. Above 325 m AGL, the boundary layer was nearly neutrally stratified with little change in potential temperature occurring in the 4 h since sunset. At  $x = 15.0 \text{ km}$ , the potential temperature structure was similar, but the lower layer exhibited a much more realistic profile. Like the profile over the flat plain, the lowest layer extended to 125 m AGL, but the lapse rate at this location was a more realistic  $0.06 \text{ K m}^{-1}$ . Between 175 m AGL and 325 m AGL, the lapse rate was near  $0.01 \text{ K m}^{-1}$  or isothermal in absolute temperature. Above the transition layer, the atmosphere was nearly neutrally stratified as would be expected. Over the steeper slope and high

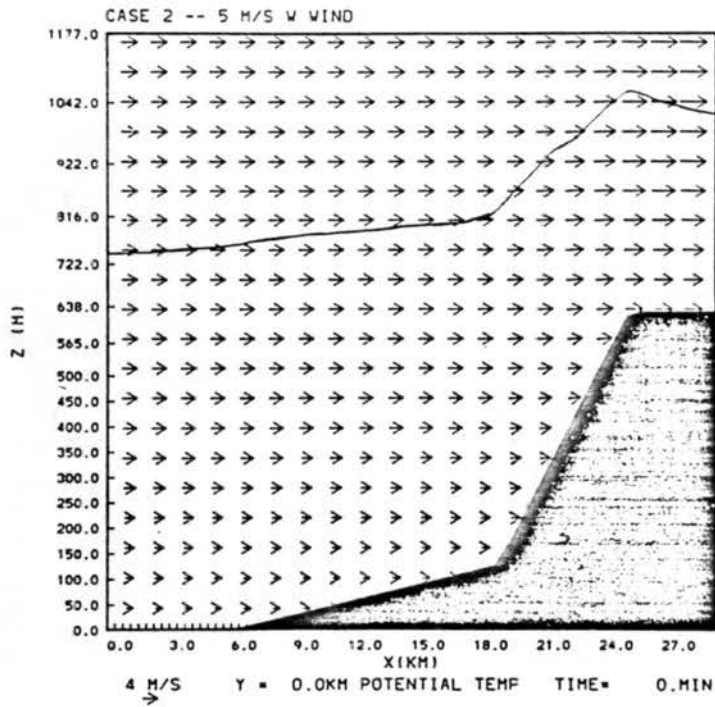
plateau, potential temperatures were only 2.0-3.0 K cooler than the neutral layer and the stable layer was just 125 m deep.

Figure 45h shows the boundary layer 5 h after sunset. As can be seen, the boundary layer evolution was very slow at this point with the transition layer slightly cooler and deeper than 1 h before this time. Figure 46 shows 30 min averages of the dominant terms in the thermodynamic energy equation in a column located at  $x = 15.0$  km. The advective and vertical diffusion terms were of the order of  $10^{-4} - 10^{-3} \text{ K s}^{-1}$ , three orders of magnitude higher than the horizontal diffusion contribution, although the total cooling rates were small. Typically, the advection terms were of like magnitude, but opposite in sign, resulting in the vertical diffusion term providing a substantial amount of the total cooling. Analysis of the simulation past this point would be redundant, since a quasi-steady state had been reached. It was obvious from a comparison of the results of this simulation with those from the no wind case that vertical wind shear is necessary to properly diffuse the cold air upward and build the transition layer. The absence of an ambient wind removes the shear and prevents the model from realistically simulating NBL development. In reality, small scale circulations and terrain features which are not resolved in the model would combine to mix the cold air vertically in "no wind" situations to a greater depth than was simulated in Case 1.

## 2. Simulation of mesoscale boundary layer evolution through a diurnal cycle.

There were two purposes for simulating the complete diurnal boundary layer evolution despite the emphasis of this study on NBL behavior. First, insight into the morning transition period had been

(a)



(b)

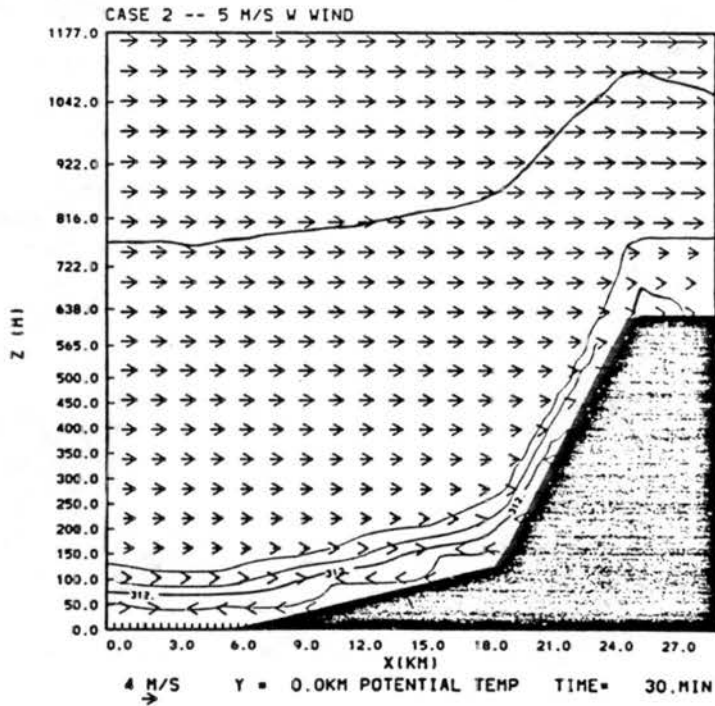


Figure 45. Wind and potential temperature fields for Case 2 (contour interval - 1 K) for (a) at sunset and (b) at sunset + 0.5 h.



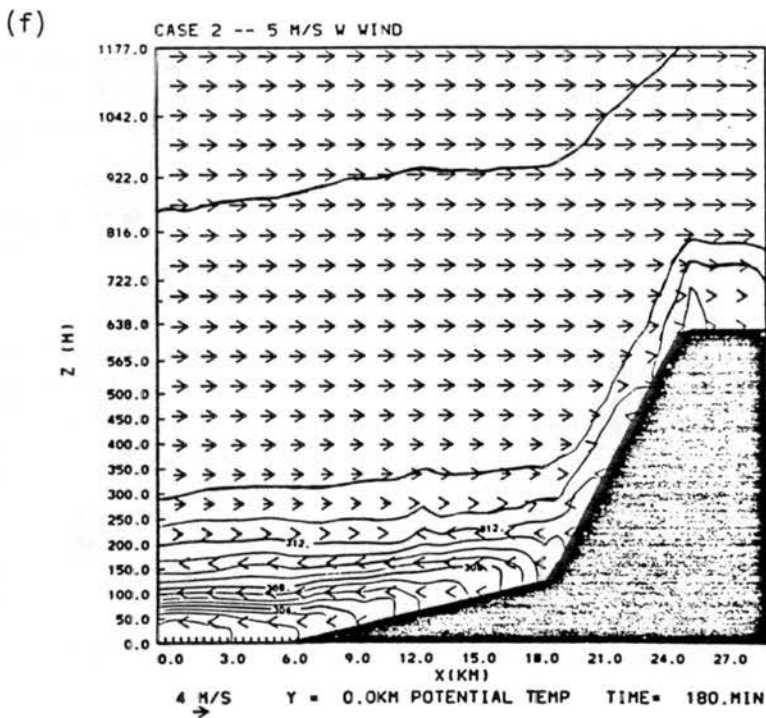
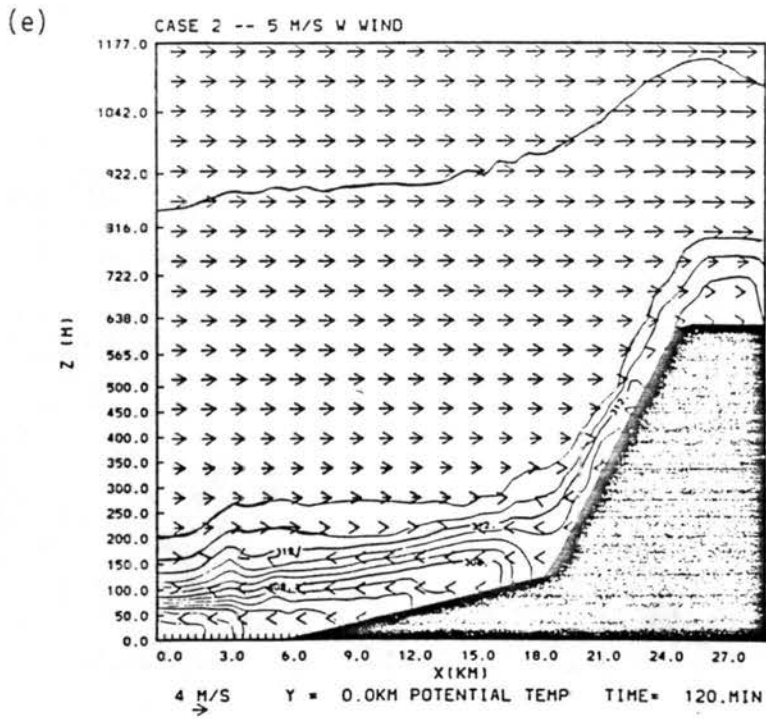
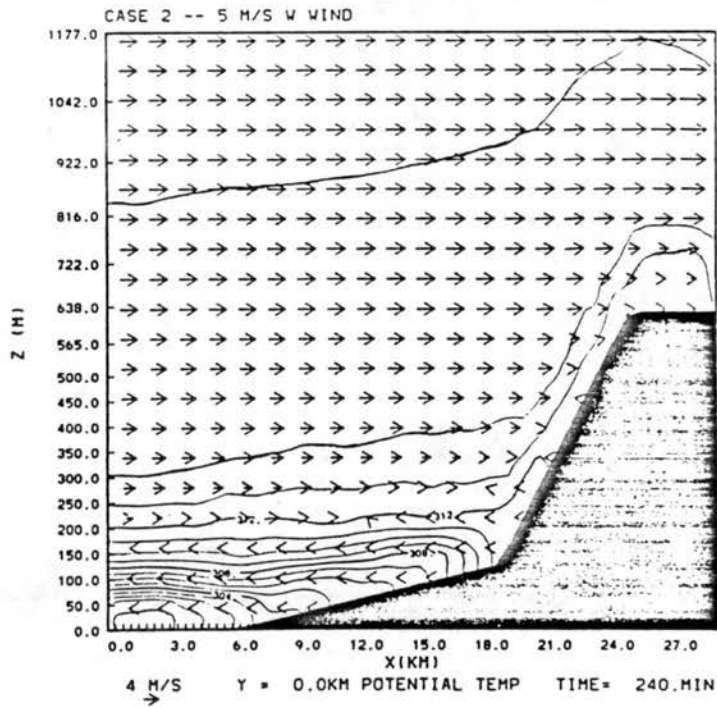


Figure 45. Wind and potential temperature fields for Case 2 (contour interval - 1 K) for (e) at sunset + 2 h and (f) at sunset + 2.5 h.

(g)



(h)

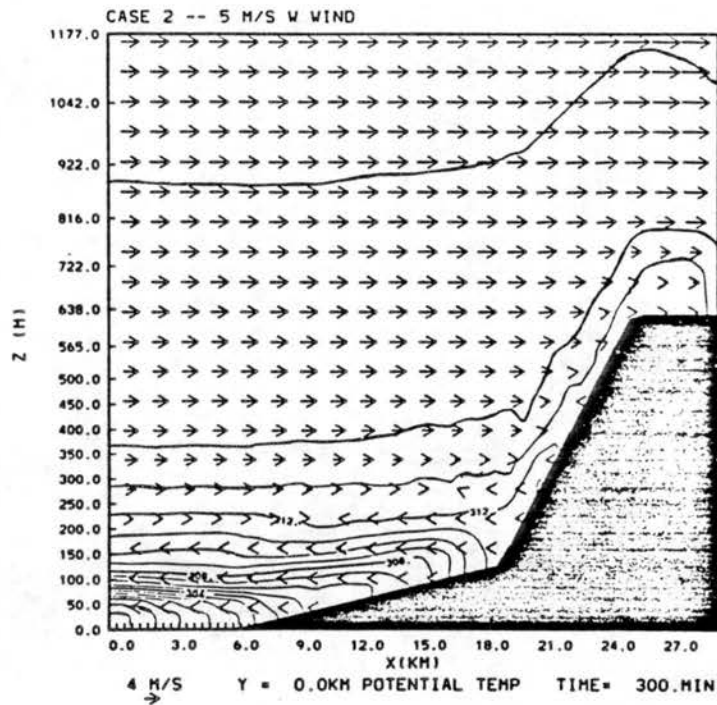


Figure 45. Wind and potential temperature fields for Case 2 (contour interval - 1 K) for (g) at sunset + 3 h and (h) at sunset + 5 h.

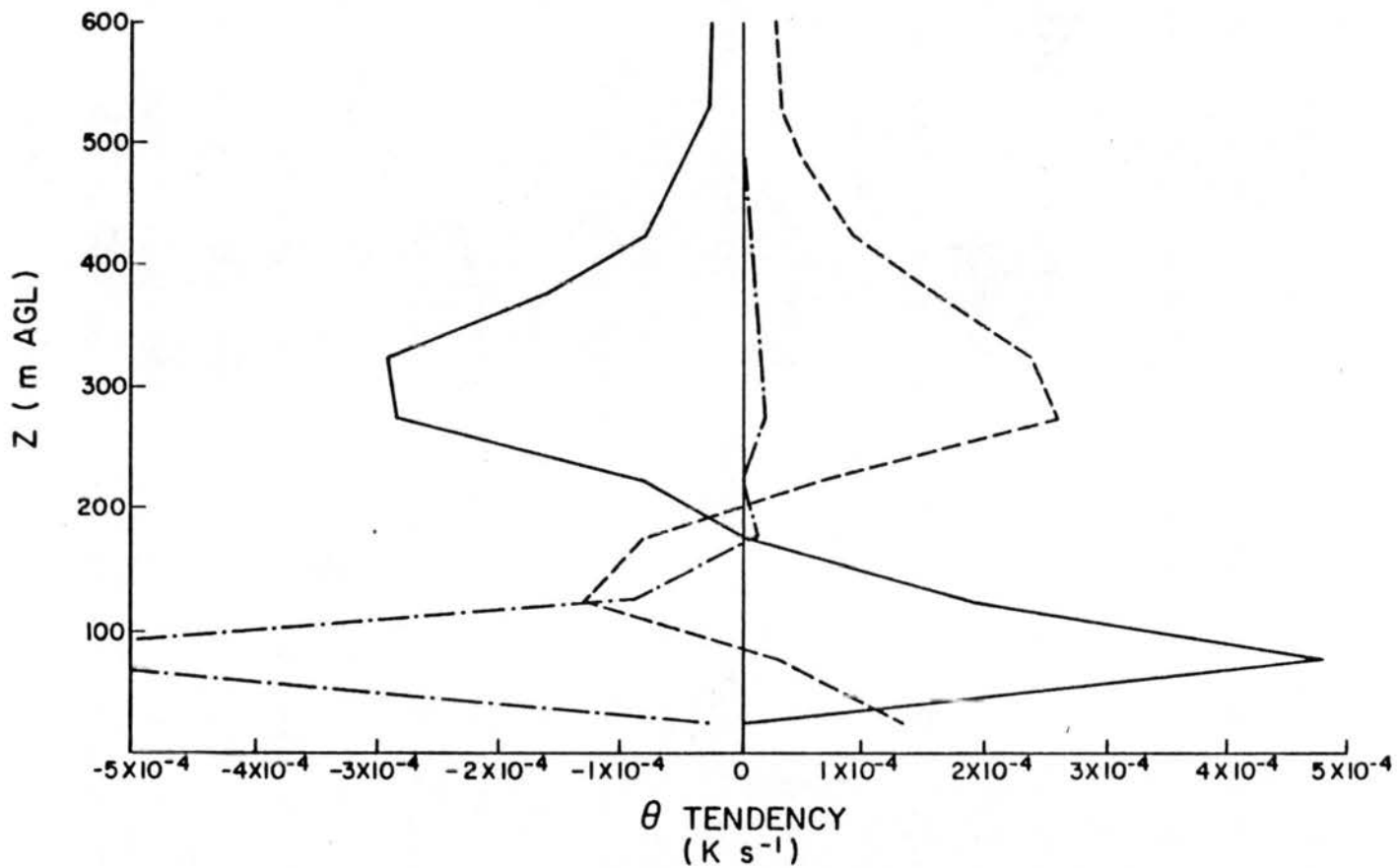


Figure 46. Thirty minute average values of the dominant  $\theta$  tendency terms. (solid line = horizontal advection along  $z^*$  surface, dashed line = vertical advection and broken line = vertical sub-grid scale diffusion.)

gained through analysis of earlier model studies on both the valley scale and a slightly larger scale in an elevated mountain basin (Bader and McKee, 1983, 1985; Banta, 1982). A comparison of the morning transition over the mesoscale terrain to these earlier studies was appropriate, despite the absence of a complete observational data set. Secondly, the validity of the model formulation and configuration used in the program could be tested by simulating the diurnal structure in the absence of larger synoptic scale changes. The first attempt at this simulation used the narrow domain configuration, but the solution was unrealistic in the last several hours before sunrise. The cold air pool over the flat plain slowly built eastward late at night until an excessively stable inversion layer extended over the sloping plain. This was due to the continued drainage of cold air onto the plain and the inability of the lateral boundary condition to allow the flow to continue westward as would happen in reality. Because of this problem, the longer slope domain was used which was more representative of the actual terrain in the observational study region.

Following the initialization of the model with  $u_0 = 5 \text{ m s}^{-1}$ , surface cooling was initiated with the boundary layer structure shown in Figure 47a. Because the total domain was twice as wide as the narrow domain, the width to depth ratio was changed in the plotting program to keep the same vertical resolution. Consequentially, slopes appear steeper than in the previous figures. The addition of the extra section of sloping plain added 300 m to the total height of the high plateau, but the difference in elevation between the base of the steep slope leading to the plateau and the plateau summit was kept at 500 m. The wind profile over the flat plain followed the externally imposed

logarithmic distribution. Over the sloping plain, the wind profile adjusted to maintain its logarithmic shape, but with more shear so that the velocities became nearly horizontally uniform 1000 m above the reference level with a speed near  $4.6 \text{ m s}^{-1}$ . The initial wind speeds over the plateau were  $1.0\text{-}1.5 \text{ m s}^{-1}$  higher than in the narrow domain case as a result of the velocity adjustment necessary to conserve total mass flow, but this effect was insignificant. The initial neutral layer top was 1300 m above the reference level and was nearly horizontal across the domain, with a slight increase in height over the higher terrain to the east.

The early part of the simulation proceeds similarly to the narrow domain case (hereinafter referred to as the reference case). After 30 min (Figure 47b) the lowest grid layer cooled  $3.0\text{-}4.0 \text{ K}$  and a  $0.4\text{-}0.6 \text{ m s}^{-1}$  drainage flow developed along the length of the sloping plain and steep slope to its east. By 1 h after sunset (Figure 47c), the cooling extended to 75 m AGL above the long slope and resulted in a decrease in wind speed of  $1.0 \text{ m s}^{-1}$  at this level. A weaker stable layer was also developing over the high plateau from the diffusion of cold surface air upward in the presence of the strong shear. After 2 h, the two layer thermal structure evident in the reference case appeared in this simulation as well (Figure 47d). The cold surface inversion layer was 125 m deep over the lower terrain encompassing both the flat and sloping plains. The lapse rate through the lowest 100 m was  $0.1 \text{ K m}^{-1}$  while in the 50-100 m deep transition layer it was  $0.013 \text{ K m}^{-1}$ . A  $1.1\text{-}1.3 \text{ m s}^{-1}$  cold thermal flow developed at the top of the surface inversion layer, producing strong shears near  $0.04 \text{ s}^{-1}$  in the layer between 125 and 225 m AGL. Like the reference case, a perturbation in the potential

temperature appeared at the junction of the flat and sloping plains due to the velocity convergence of the low level east winds from the higher terrain.

Three hours after sunset, the evening transition was complete with the two layer wind and thermal structure firmly established over the sloping plain (Figure 47e). The layer of easterly winds reached 125 m AGL over a horizontal area from  $x = 41.0$  km to the western boundary. East of this point, the west wind speeds had dramatically decreased since sunset and were less than  $0.5 \text{ m s}^{-1}$ . Below this level, the wind profile had changed very little in the previous hour. Potential temperature values at 25 m AGL increased slightly with distance east from the base of the sloping plain. Over the steeper slope, the 25 m AGL values varied slightly from 310 K near the base to 311.5 K at the summit. The surface inversion layer still extended to 125 m AGL with the top of the transition layer reaching 225 m AGL. Two hours later (Figure 47f), the thermal structure very much resembled that found in the reference experiment at the same time. The growing transition layer displayed a decrease in thickness from west to east, much like the tilt that was seen in the reference case, although it is much more evident here because of the increased sloping plain length and the more exaggerated plot. Velocities in and above the transition layer were also similar to those in the reference simulation. One major difference between this simulation and the reference case was the speed of the wind maximum at the top of the surface inversion layer. Whereas the speed increased slightly from east to west in the previous simulation, the total change was less than  $0.3 \text{ m s}^{-1}$ . The increased length of the sloping plain in this experiment allowed for a parcel to

accelerate in the pressure gradient through a greater distance before encountering the convergence region over the flat plain. Subsequently, the speeds in this simulation increased in speed from  $2.0 \text{ m s}^{-1}$  to over  $5.0 \text{ m s}^{-1}$  near the base of the sloping plain.

After this time the boundary layer structure changed much more slowly as the surface cooling rate decreased. Figure 47g shows the simulated fields 9 h after sunset. The surface inversion layer had grown slightly over the sloping plain to 175 m AGL, but was deeper over the flat plain where it reached 275 m AGL. The lowest layer potential temperatures over the flat region had cooled to an unrealistically low value of 285 K. The  $Ri_c$  value had been exceeded continuously for several hours, preventing the diffusion of the cooled air upward. Above this layer, however, the potential temperature profile is more typical of those observed over low-lying regions in the study area. The transition layer was not well defined with the lapse rate changing continuously with height. A weak westerly  $0.5\text{-}0.7 \text{ m s}^{-1}$  wind was present at 25 m AGL. Easterly winds existed through a layer between 75 m AGL and 225 m AGL having a maximum speed of  $2.5\text{-}2.7 \text{ m s}^{-1}$  in the layer center. Above the easterly layer, the west winds increased in speed from  $1.9 \text{ m s}^{-1}$  at 275 m AGL to  $5.0 \text{ m s}^{-1}$  at 870 m AGL.

Over the sloping plain, the isentropes in the surface inversion layer closely followed the slope of the underlying terrain. Thermal structure had changed little in the past 4 h. Potential temperature values in the lowest 100 m AGL actually rose  $1.0\text{-}1.5 \text{ K}$  as the cooling rate could not compensate for the advective warming in the drainage flow. Except near either end of the sloping plain, very little gradient remained along the surface. The top of the transition layer was more

horizontal, causing its thickness to decrease with distance from the flat plain, as was noted earlier. Similarly, very little change occurred over the steep slope and high plateau, except for a slight warming in the lower layers due to the drainage of the colder air westward. The corresponding wind structure over the sloping plain was also very uniform. East winds were present below 125 m AGL with a maximum of  $3.0\text{-}3.2\text{ m s}^{-1}$  at 75 m AGL. Strong shears were present as the easterly flow sharply decreased in speed to  $0.2\text{ m s}^{-1}$  at 175 m AGL and shifted to a westerly  $2.0\text{ m s}^{-1}$  flow at 225 m AGL. Above this level, the wind speed increased with height, reaching  $5.0\text{ m s}^{-1}$  at 680 m AGL.

By sunrise, the surface cooling had decreased to such an extent that mass adjustment had sharply reduced the pressure gradients driving the easterly winds. As a result, the isentropic surfaces were horizontal and the strong inversion layer was limited to the region over the flat plain and adjacent section of the sloping plain (Figure 47h). Westerly flow was reestablished in the lowest 125 m AGL over the flat plain due to the reduced strength of the drainage and cold thermal flows. Despite this, elevated weak east winds were still present in a layer between 175 m AGL and 275 m AGL. Easterly flow did not appear in any level west of  $x = 17.8\text{ km}$ . Above the flat plain, the two-level thermal structure was more pronounced than earlier, with a strong surface inversion layer reaching 175 m AGL topped by a much less stable transition layer extending to 680 m AGL. The lapse rate through the lower layer was  $0.075\text{ K m}^{-1}$  while the lapse rate through the transition layer varied from  $0.015\text{ K m}^{-1}$  in the region overlying the inversion layer to  $0.007\text{ K m}^{-1}$  near its top.

Over the sloping plain, lapse rates were similar to those in the transition layer. The strong surface inversion containing the drainage flow present earlier could not be maintained against turbulent shear at the top or the mass adjustment which occurred to weaken the east-west pressure gradient. The layer of easterly winds above the surface was 125 m deep with maximum velocities between  $1.0 \text{ m s}^{-1}$  and  $2.3 \text{ m s}^{-1}$ , a 50% speed reduction from earlier. Above the east winds, the westerlies increased in speed with height, producing moderately strong shear values of  $0.024 \text{ s}^{-1}$ . TKE values indicated that the transition layer was turbulent through its depth, with more vigorous turbulence near the top of the layer where the stability was much weaker. Over the steep slope and high plateau, the drainage wind was overpowered by the prevailing westerly flow mixing through the nearly adiabatic layer above the surface, although the westerly speeds between 25 m AGL and 75 m AGL were generally less than  $2.0 \text{ m s}^{-1}$ , compared to the  $4.0\text{-}5.0 \text{ m s}^{-1}$  present at 125 m AGL.

One hour after the initiation of surface heating (model sunrise), the westerly surface flow over the flat plain penetrated to  $x = 26.0 \text{ km}$  (Figure 47i). Speeds in the easterly flow layer decreased to less than  $1.5 \text{ m s}^{-1}$  and potential temperatures 25 m AGL rose 2.0-3.0 K, with little change above the lowest layer. Over the sloping plain, easterly wind speeds declined and the east wind layer was only 100 m deep. East of  $x = 20.0 \text{ km}$ , surface heating produced a neutral layer extending to 75 m AGL at the western end and reaching over 500 m AGL near the base of the steep slope. An along-slope potential temperature gradient also became established as a deeper CBL quickly developed over the upper part of the slope. Over the steep slope, the weak heating was sufficient to

remove the overlying weakly stable layer and allow the westerly winds to diffuse to the surface. Two hours after sunrise (Figure 47j),  $0.5\text{--}1.5\text{ m s}^{-1}$  east winds remained in a thin layer between 175 m and 225 m above the reference level and extended from the flat plain to  $x = 23.0\text{ km}$ . This region corresponds to the top of the weakened nocturnal surface inversion layer which remained over the lower elevations. A 75 m deep CBL developed under the inversion base and the synoptic westerly flow was reinforced at the surface by the warm thermal wind along the sloping plain. Wind speeds at 25 m AGL varied between  $0.5\text{ m s}^{-1}$  and  $2.0\text{ m s}^{-1}$ , indicating the flow was quite turbulent, as would be expected. CBL depth increased with distance east of the flat plain, a result of the weaker overlying sunrise stability at higher elevations. Above 175 m AGL, the wind profile was much more horizontally uniform, except for the region on the eastern side of the domain still under the influence of the inversion layer.

Figure 47k shows the boundary layer structure 3 h after sunrise. By this time, the increased surface heating rate had eliminated all easterly flow, although a region of weak westerly flow with speeds less than  $1.0\text{ m s}^{-1}$  was present above the flat plain. The influence of the nocturnal surface inversion was also still apparent at that time, with a strong stable layer capping the cold 75 m deep CBL over the flat plain. East of  $x = 40.0\text{ km}$ , the boundary layer was neutrally stratified to 1300 m AGL with a fully mixed velocity profile. West of this location, the remnants of the quasi-isothermal transition layer overlying the surface based CBL extended to 750 m above the reference level. One hour later, the CBL over the plain had grown to 275 m AGL and was still capped by a strong 2 K inversion (Figure 47l). Except for the weaker

winds under the plains inversion, strong westerly flow was present through the model depth, with speeds increasing smoothly with height from near  $2.0 \text{ m s}^{-1}$  at 25 m above the reference level to over  $5.0 \text{ m s}^{-1}$  at 1200 m. Wind speeds were  $0.5 \text{ m s}^{-1}$  higher near the surface where thermal effects were strongest.

The morning transition was nearly complete 5 h after sunrise (Figure 47m). The boundary layer was neutrally stratified east of  $x = 35.0 \text{ km}$  and an east west potential temperature gradient was developing in response to the heating of the high plateau. As a result, wind speeds in the lowest 700 m above the reference level had increased  $1.0\text{-}2.0 \text{ m s}^{-1}$  in the preceding hour. The last remnants of the nocturnal stable layer were still present over the flat plain and lower section of the sloping plain, but were nearly destroyed by the growing CBL. An hour later (Figure 47n), the daytime boundary layer was nearly fully developed with a well mixed westerly flow once again present through the depth of the CBL and only a thin and weakly stable region remaining from the NBL. Wind speeds over the sloping plain ranged from  $2.0\text{-}3.0 \text{ m s}^{-1}$  at 25 m AGL and increased in speed with height to over  $5.0 \text{ m s}^{-1}$  at 600 m AGL. CBL potential temperatures over the eastern half of the domain were near 315 K, the initial CBL temperature at sunset. Both the wind and potential structure very closely resembled the initial state at sunset, thereby completing the diurnal cycle.

### 3. Factors affecting nocturnal boundary layer development.

Five simulations were executed to determine the effects of wind speed, direction and initial CBL depth on the NBL evolution. Wind speed effects were examined in Cases 4 and 5, which were initialized identically to the reference case (Case 2) except that  $u_0$  was set to

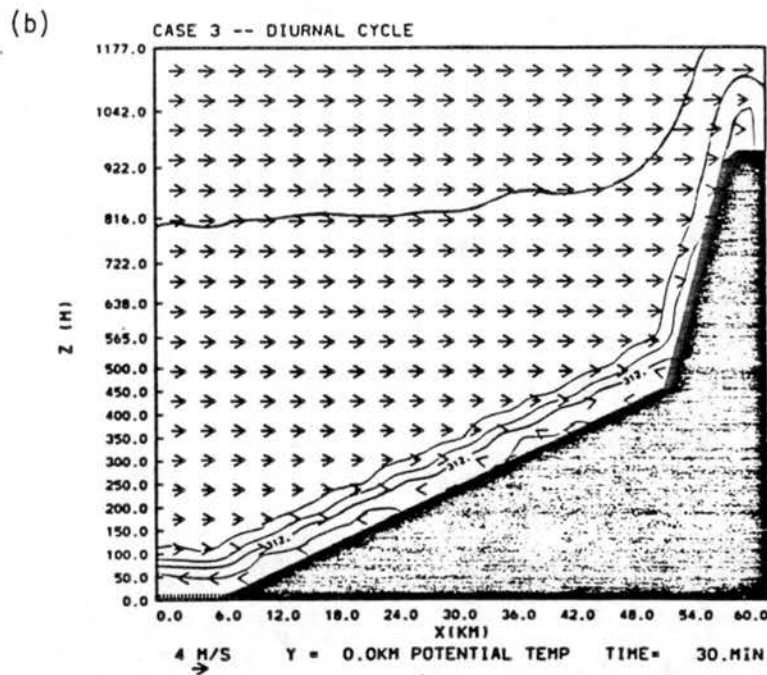
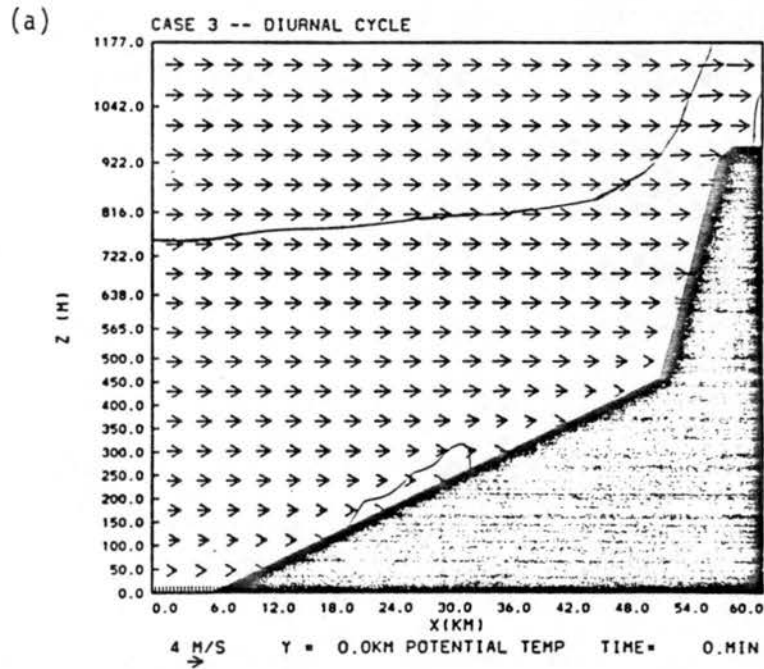


Figure 47. Wind and potential temperature fields for Case 3 (contour interval - 1 K) for (a) at sunset and (b) at sunset + 0.5 h.

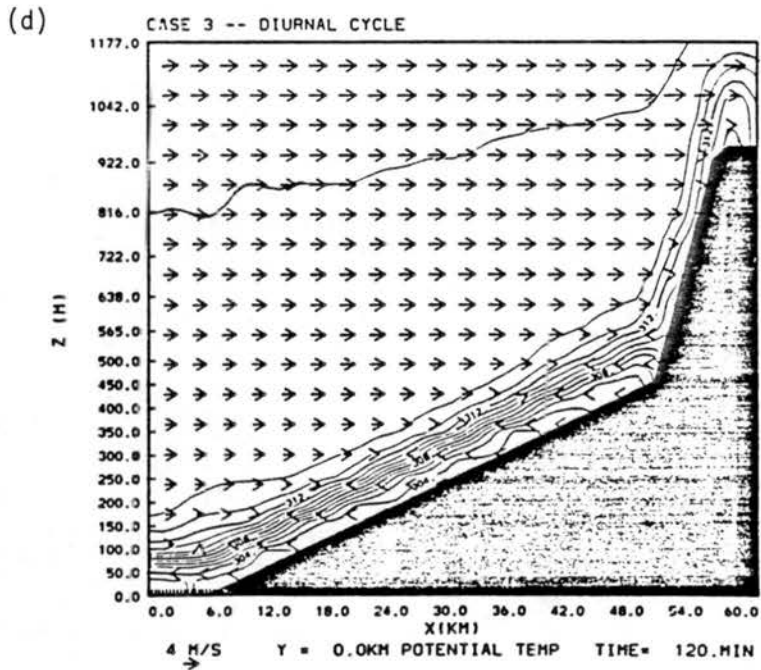
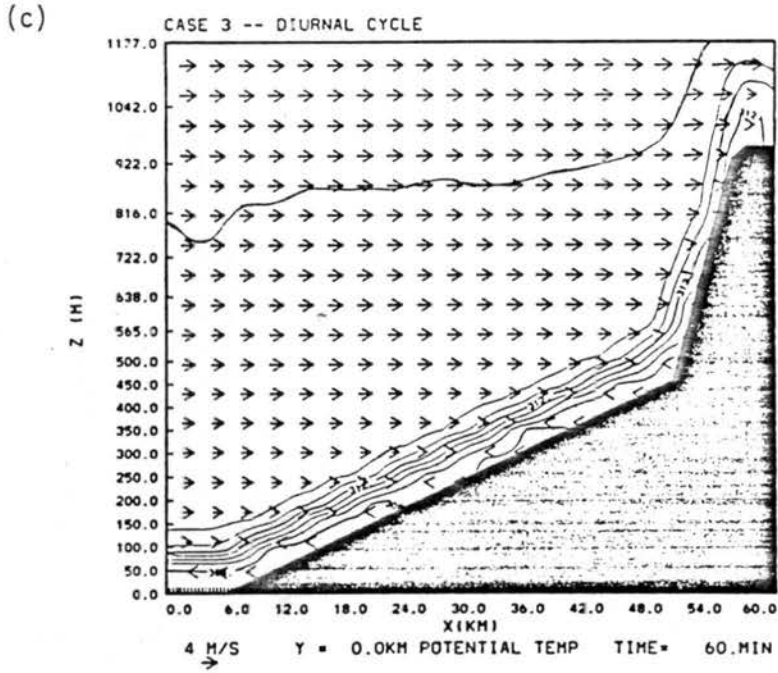
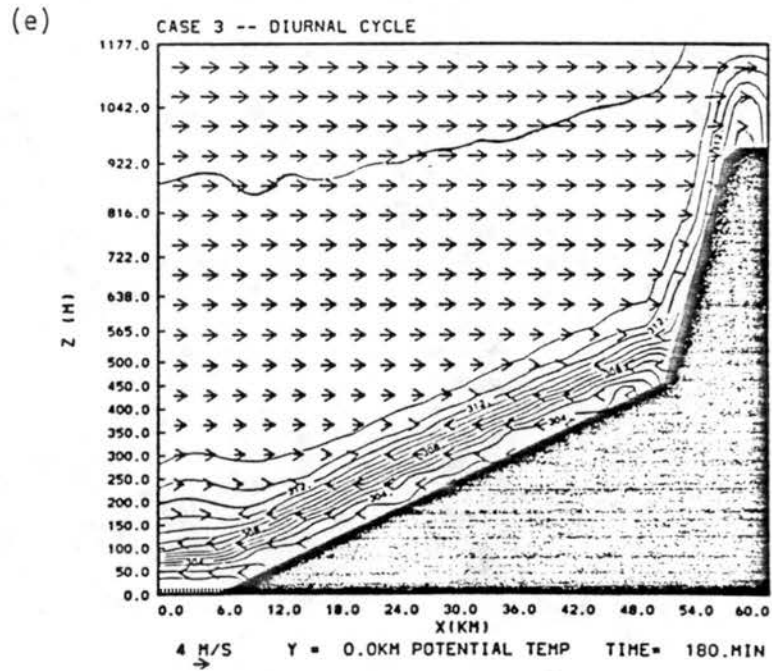


Figure 47. Wind and potential temperature fields for Case 3 (contour interval - 1 K) for (c) at sunset + 1 h and (d) at sunset + 2 h.





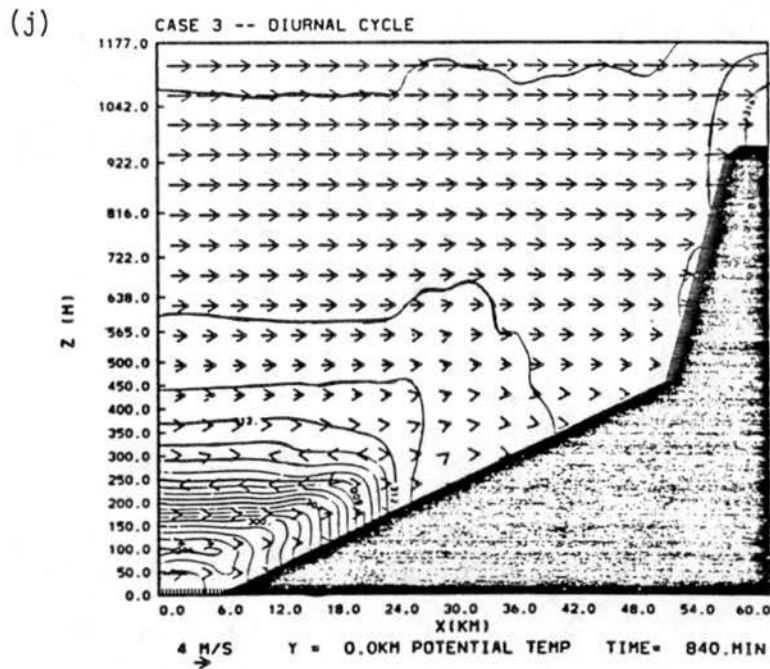
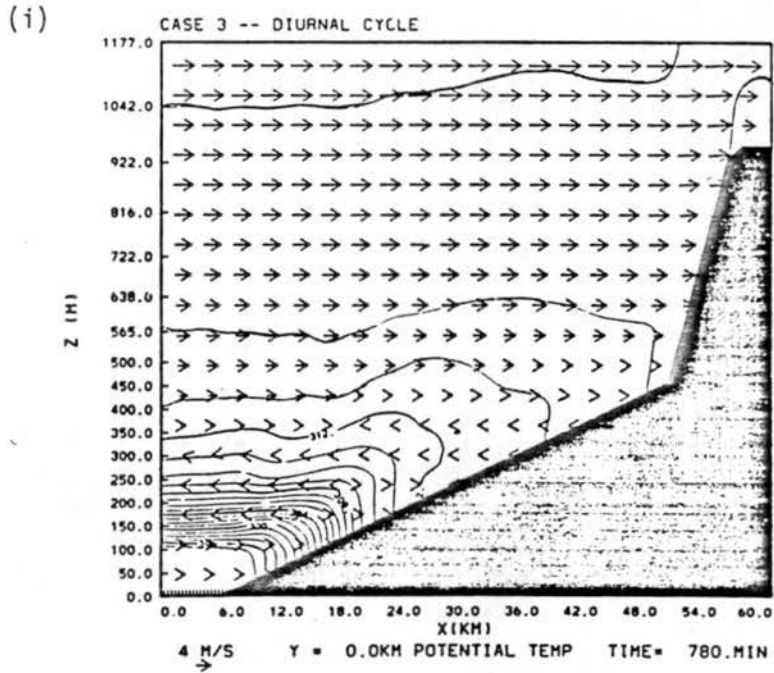
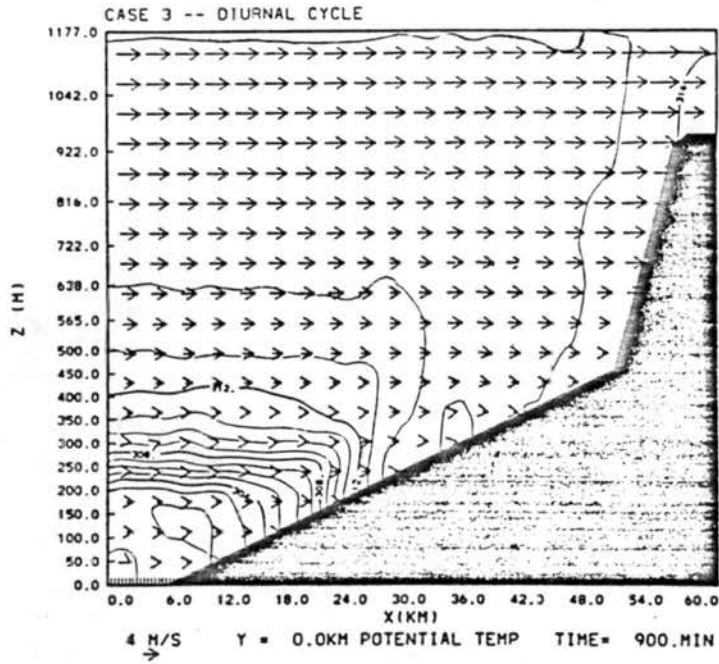


Figure 47. Wind and potential temperature fields for Case 3 (contour interval - 1 K) for (i) at sunrise + 1 h and (j) at sunrise + 2 h.

(k)



(l)

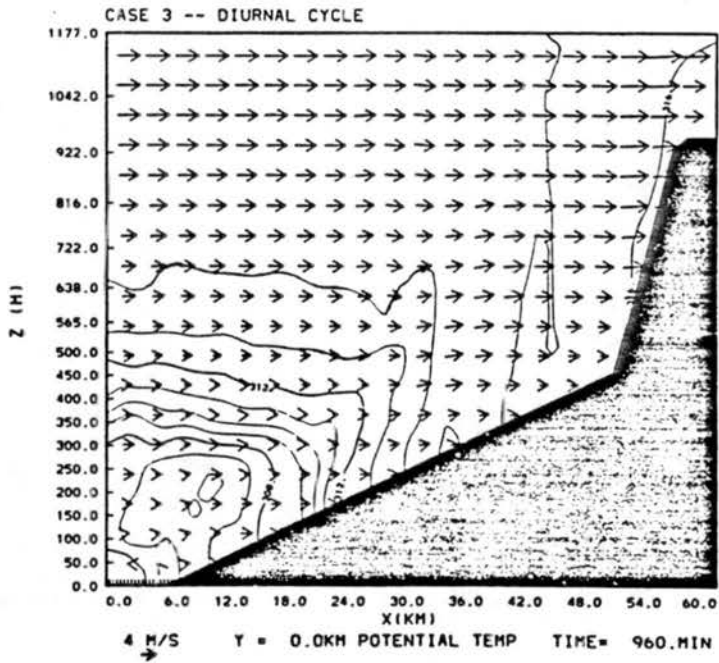


Figure 47. Wind and potential temperature fields for Case 3 (contour interval - 1 K) for (k) at sunrise + 3 h and (l) at sunrise + 4 h.

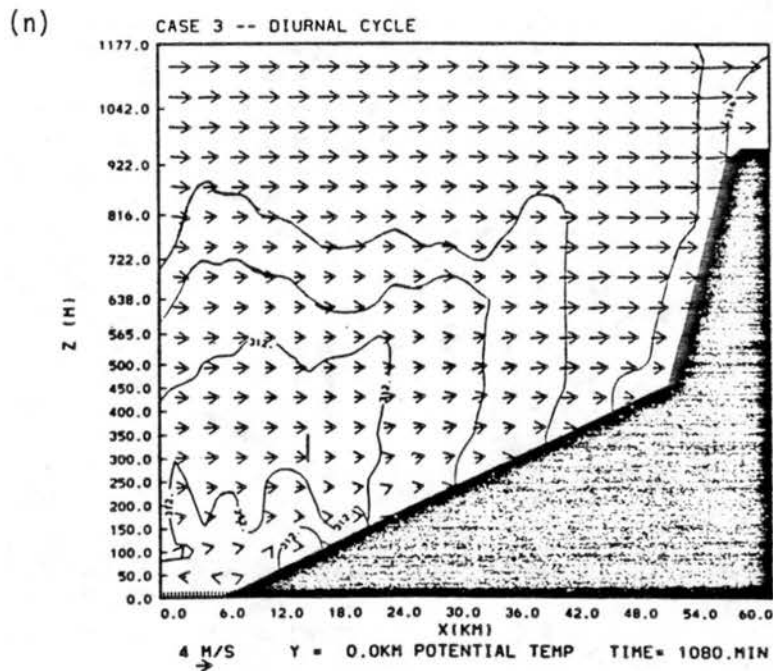
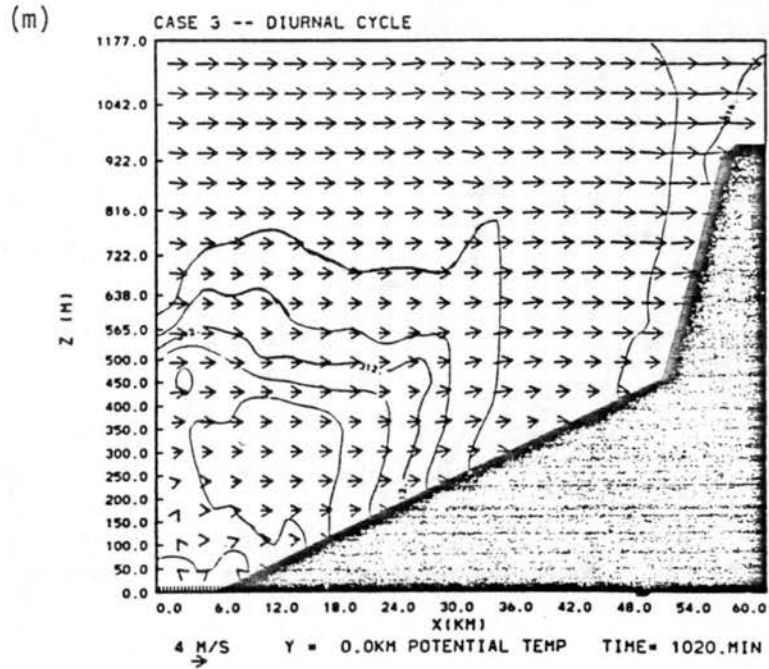


Figure 47. Wind and potential temperature fields for Case 3 (contour interval - 1 K) for (m) at sunrise + 5 h and (n) at sunrise + 6 h.

$3.0 \text{ m s}^{-1}$  and  $7.0 \text{ m s}^{-1}$  respectively. The effects of seasonal differences in NBL development were simulated in Case 6, which was initialized with a much more shallow afternoon CBL, the most significant variable characteristic of daytime boundary layer structure from summer to winter. Cases 7 and 8 were 3-D simulations executed to ascertain the effects of wind direction on NBL structure. Case 7 had an initially southwest flow field and Case 8 was initialized with a south wind; in both cases, total geostrophic wind speeds  $(u_0^2 + v_0^2)^{0.5}$  were  $5.0 \text{ m s}^{-1}$ .

a. Effects of wind speed. Figure 48a shows the initial state in the Case 4 simulation ( $u_0 = 3.0 \text{ m s}^{-1}$ ) with a deep surface based neutral layer and well mixed wind profile. Wind speeds over the flat and sloping plains were less than  $1.0 \text{ m s}^{-1}$  at 25 m AGL but increased logarithmically with height to  $3.0 \text{ m s}^{-1}$  near the CBL top at 1300 m AGL. By 1 h after sunset (Figure 48b), the surface inversion layer had formed over the lower elevations and a  $0.5 \text{ m s}^{-1}$  drainage flow had developed at 25 m AGL. The drainage strengthened to over  $1.0 \text{ m s}^{-1}$  over the steeper slope and extended to the summit of the high plateau. Two hours after sunset, the transition layer had started to develop over the surface inversion layer (Figure 48c). The lapse rate over the sloping plain was  $0.09 \text{ K m}^{-1}$  between 25 m AGL and 125 m AGL and  $0.015 \text{ K m}^{-1}$  in the overlying transition layer which extended to 275 m AGL. A 100 m deep easterly cold thermal wind formed at the top of the surface inversion with maximum speeds between  $3.8 \text{ m s}^{-1}$  and  $4.0 \text{ m s}^{-1}$ , about 1.5 times stronger than those observed in Case 2. West winds were still present in the transition layer, but the speeds there had been reduced to less than  $2.0 \text{ m s}^{-1}$ . Over the steep slope, the layer of east winds remained confined to the lowest 25 m with speeds near  $1.0 \text{ m s}^{-1}$ .

Two hours later (Figure 48d), the layer of easterlies had grown to 175 m AGL as the stable layer cooled slightly. The top of the transition layer was nearly horizontal at this time and extended to 275 m above the reference level. Maximum wind speeds in the easterlies remained steady near  $4.0 \text{ m s}^{-1}$  at 75 m AGL over the sloping plain. Wind speeds 50 m above the maximum had increased in strength from  $0.8 \text{ m s}^{-1}$  2 h previously to near  $2.0 \text{ m s}^{-1}$ , producing wind shears of  $0.027 \text{ m}^{-1}$  through the 150 m deep transition layer. Winds over 275 m AGL had remained nearly constant since sunset. The structure over the steeply sloping section was relatively unchanged during the 2 h period. Analysis of the model solution 5 h after sunset revealed little contrast from the 4 h structure (Figure 48e). Over the lower section of the sloping plain, the surface inversion layer reached 175 m AGL with the overlying transition layer extending to 325 m AGL. These levels are somewhat arbitrary as vertical mixing produced a continuously varying vertical lapse rate. The cold thermal wind had weakened by  $0.3 \text{ m s}^{-1}$ , a result of the reduced surface cooling rate and a slight weakening in horizontal pressure gradient at the top of the surface inversion.

Figure 49a shows the initial state of the boundary layer for Case 5 ( $u_0 = 7.0 \text{ m s}^{-1}$ ). The structure was similar to that in Cases 2 and 4, except that the winds were stronger,  $2.6 \text{ m s}^{-1}$  at 25 m AGL increasing to  $7.0 \text{ m s}^{-1}$  at 1300 m AGL over the lower elevations. Above the high plateau, wind speeds near the surface were over  $7.0 \text{ m s}^{-1}$  and increased with height to a maximum of  $10.0 \text{ m s}^{-1}$  980 m AGL in order to satisfy the domain-wide mass continuity conditions. Initially, the neutral layer top was 1300 m above the reference level and was nearly horizontal over the width of the domain. After 1 h (Figure 49b), the surface inversion

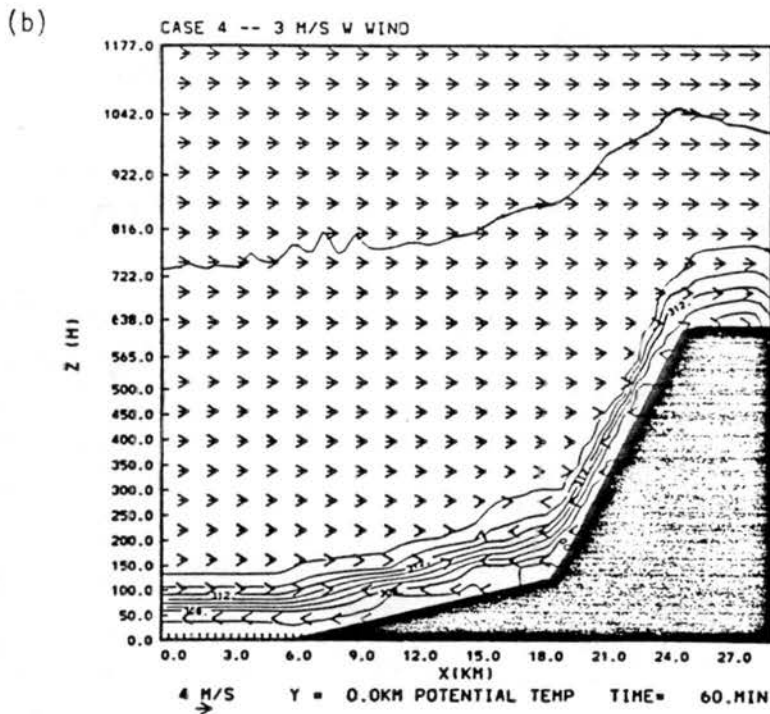
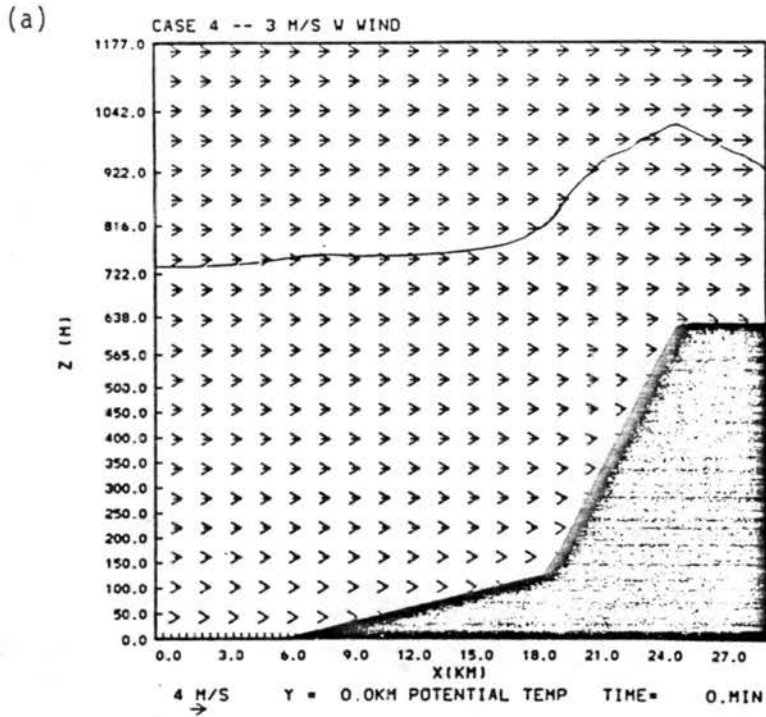


Figure 48. Wind and potential temperature fields for Case 4 (contour interval - 1 K) for (a) at sunset and (b) at sunset + 1 h.



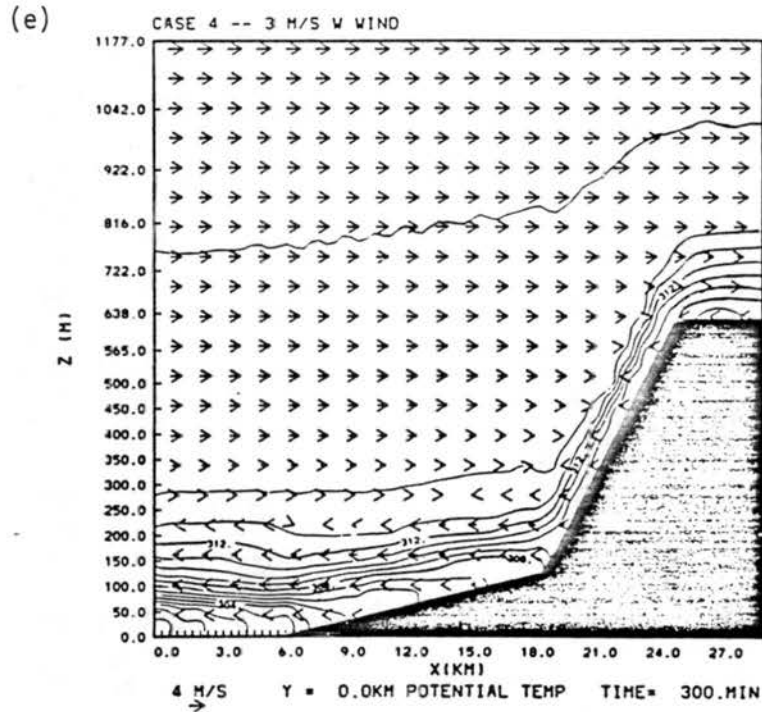


Figure 48. Wind and potential temperature fields for Case 4 (contour interval - 1 K) for (e) at sunset + 5 h.

was 75 m deep and contained a  $0.5 \text{ m s}^{-1}$  drainage flow at 25 m AGL with a weak  $0.1\text{-}0.3 \text{ m s}^{-1}$  westerly flow at 75 m AGL. Unlike the previous cases, the east winds did not appear over the steep slope, but the westerly speeds were reduced by  $1.0\text{-}1.2 \text{ m s}^{-1}$  in the hour since sunset. The transition layer had formed by 1 h later (Figure 49c) and reached 275 m above the reference level. Unlike the other cases, the surface inversion layer depth decreased with increasing surface height, and the transition region had a near constant depth. While the surface inversion extended to 175 m AGL over the plain, it is 50 m lower at  $x = 12.0 \text{ km}$ , roughly the difference in surface elevation between the locations. An inversion layer also formed over the steep slope as the strong westerly wind prevented the cold lower layer air from rapidly draining to lower elevations. A  $1.1\text{-}1.4 \text{ m s}^{-1}$  cold thermal wind was present at 75 m AGL over the sloping plain, producing shears through the transition layer of  $0.03 \text{ s}^{-1}$ .

By three hours after sunset (Figure 49d), the total stable layer depth was over 300 m above the reference level, higher than that found 5 h after sunset in Case 4 and slightly higher than its depth at the same time in Case 2. A small mountain wave started to develop at the base of the sloping plain and the along-slope thermal gradient indicated cold air pooling, a process consistent with the variable inversion layer depth seen 1 h previously. The strong winds forced a low level mass convergence and inhibited the flow of cold air west of the base of the sloping plain. The cold thermal wind retained its  $1.4 \text{ m s}^{-1}$  speed above the sloping plain, but maximum easterly speeds over the flat plain were less than  $1.0 \text{ m s}^{-1}$ . Strong shears were still present through the 150 m deep transition layer, enhancing the vertical mixing of cold air.

Figure 49e shows the pooling effects 4 h after sunset with the isentropic surfaces being nearly horizontal, even in the lowest layers. Elevated flow blocking appeared with the dividing streamline lying approximately 325 m below the elevation of the high plateau over the flat plain to the west. Using the lapse rate in the layer between 175 m AGL and 275 m AGL, a wind speed of  $7.0 \text{ m s}^{-1}$  and a barrier height of 625 m, the theoretical dividing streamline from (7) would be 265 m below the ridge line, which gives reasonably good agreement with that observed in the model solution. Although blocked flow was present in the other simulations, it was mostly confined to the lowest 200 m above the surface. In this case, the stable layer had built through a considerable depth, even above the steep slope where the inhibition of the drainage wind caused a cold air convergence through a 200 m deep stable layer. Vertical mixing produced a 125 m deep stable layer over the high plateau as well.

Figure 49f shows the boundary layer structure 1 h later and it appears that a quasi-steady state was achieved. The low-level cold air pooling resulted in a 275 m deep inversion layer that became more shallow with increased surface elevation. The transition layer top reached 530 m above the reference level, much higher than in either of the previous cases. Low-level winds over the sloping plain remained easterly below 125 m AGL and a weak drainage with speeds less than  $0.5 \text{ m s}^{-1}$  was established over the base of the steep slope. Vertical mixing produced a smoother velocity profile with less shear, resulting in a continuously varying lapse rate with height. Stability over the lower half of the steep slope was reduced as the convergence of air below the dividing streamline formed a near neutral layer, analogous to

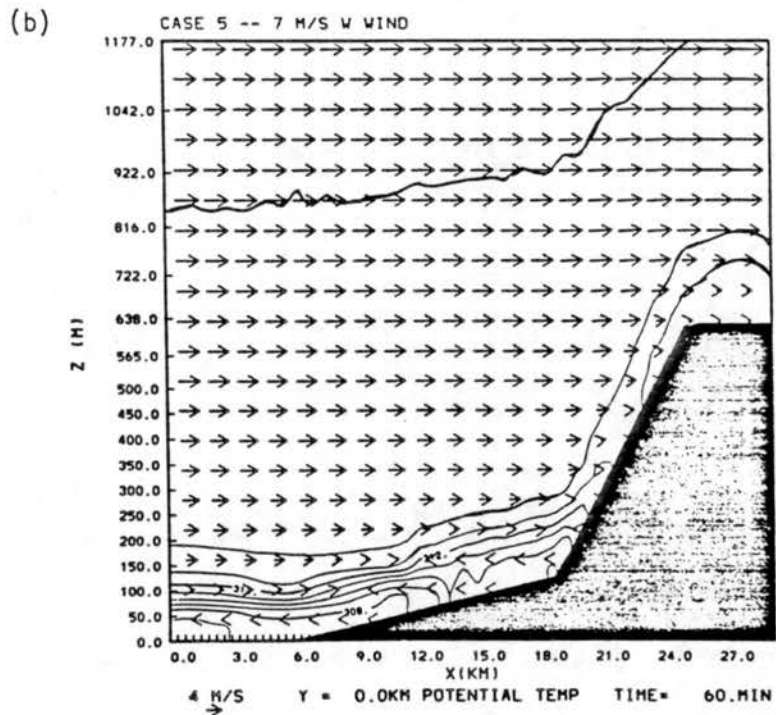
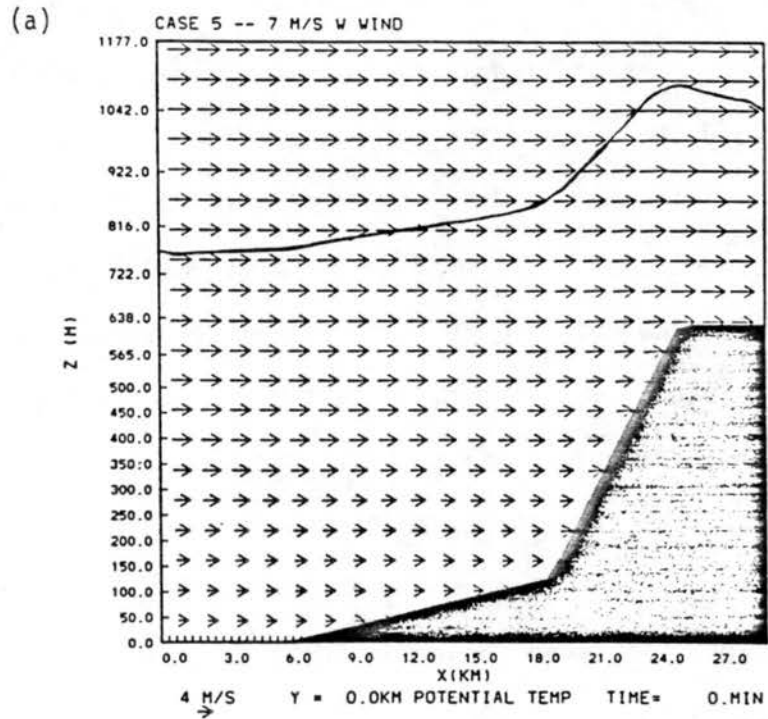


Figure 49. Wind and potential temperature fields for Case 5 (contour interval - 1 K) for (a) at sunset and (b) at sunset + 1 h.

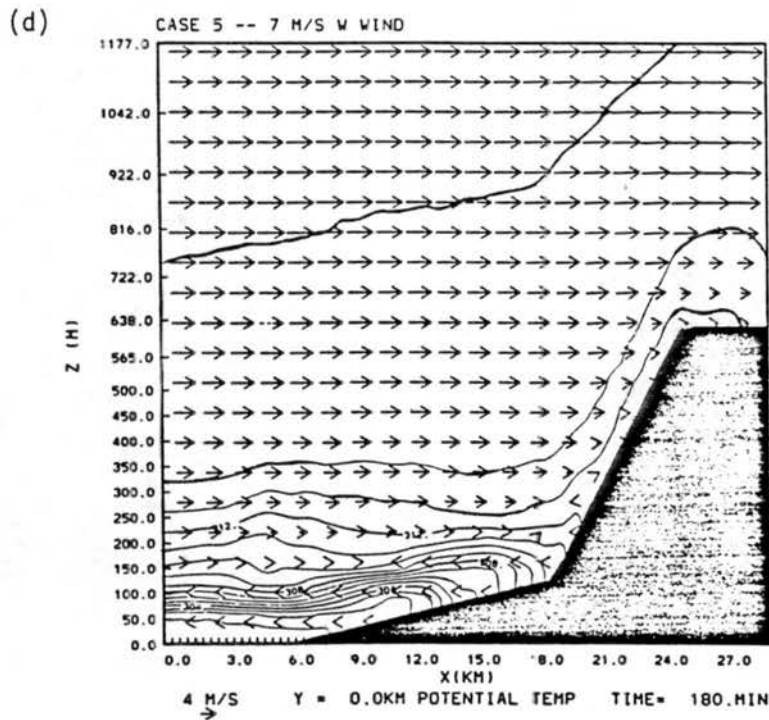
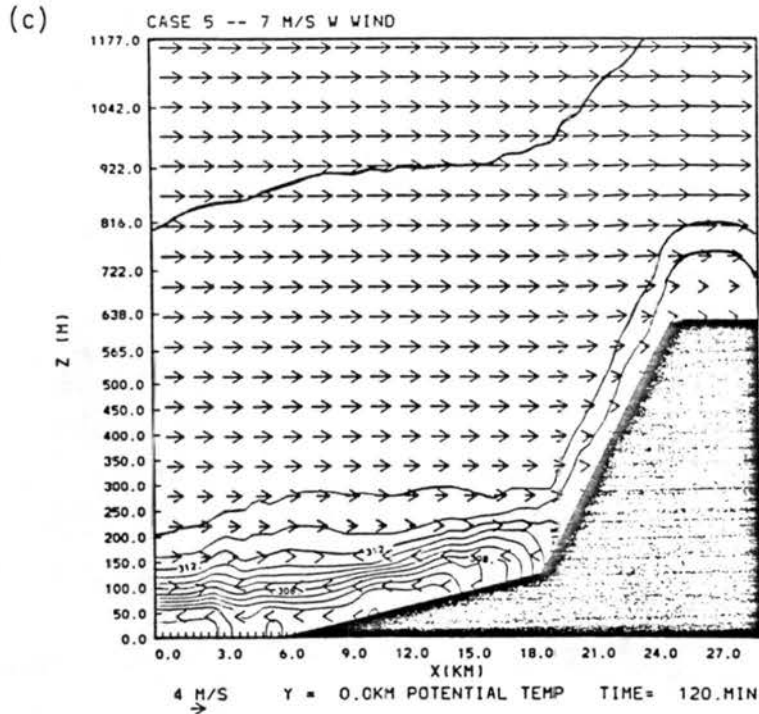


Figure 49. Wind and potential temperature fields for Case 5 (contour interval - 1 K) for (c) at sunset + 2 h and (d) at sunset + 3 h.

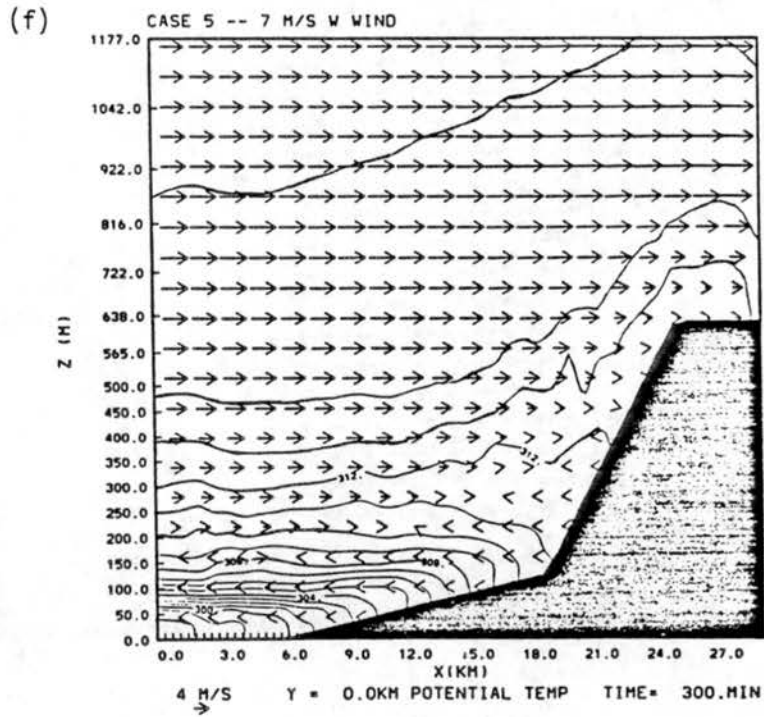
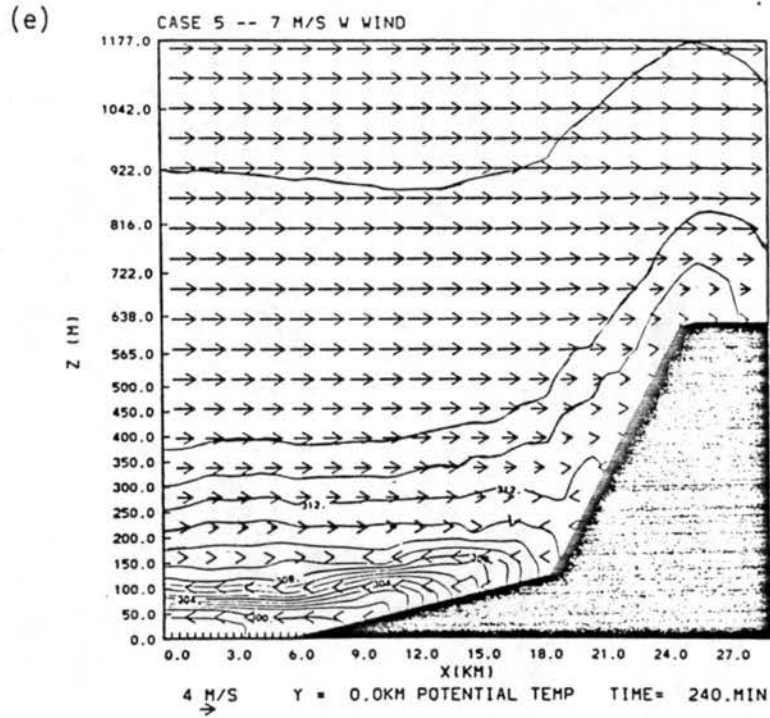


Figure 49. Wind and potential temperature fields for Case 5 (contour interval - 1 K) for (e) at sunset + 4 h and (f) at sunset + 5 h.

the constant density layer observed by Baines (1985) in laboratory studies of blocked flow.

b. Effects of afternoon boundary layer depth. This simulation required a different initialization procedure to properly form the desired "sunset" state. The specified potential temperature profile prior to dynamic initialization replaced the surface based neutral layer with an isothermal lapse rate that extended to 1250 m above the reference level. Following the 1 h dynamic initialization with  $u_0 = 5.0 \text{ m s}^{-1}$ , surface heating was initiated for a 3 h long period with  $\overline{w'\theta'}_s = 0.10 \text{ K m s}^{-1}$ . After the 3 h heating period, surface cooling was initiated with a reduced cooling rate more typical of winter conditions. The resulting boundary layer structure is shown in Figure 50a. The neutral layer extended to 530 m above the reference level over the lower elevations and sloped slightly upward toward the east so that it was 800 m above the reference level over the high plateau. Winds were from the west throughout the domain, but, unlike the other cases, the initialization significantly altered the logarithmic profile. Over the low-lying plains, wind speeds in the neutral layer ranged from  $0.8 \text{ m s}^{-1}$  at 25 m AGL to  $1.2 \text{ m s}^{-1}$  at 475 m AGL. Above this level, strong shear was present and the speeds increased to near  $7.5 \text{ m s}^{-1}$  at 980 m AGL and reached a maximum over  $8.0 \text{ m s}^{-1}$  at 1420 m AGL. Above the steep slope, wind speeds at 25 m AGL increased with distance up the slope from  $1.0 \text{ m s}^{-1}$  at the base to over  $4.0 \text{ m s}^{-1}$  at the summit. As before, wind speeds above the elevated terrain were higher than those over the lower elevations to insure mass continuity. Maximum speeds reached  $10.0 \text{ m s}^{-1}$  at 650 m AGL over the high plateau. This initial condition may not have been in steady state because of the nearly blocked flow below the

elevation of the high plateau. However, based on the CSU 84 observations, it was a realistic initial condition.

One hour after sunset (Figure 50b), the surface inversion layer had formed over the lower elevations, but was slightly deeper and less stable than those simulated in the other experiments at the same time because of the lower surface cooling rate. The lapse rate through the lowest 175 m was  $0.025 \text{ K m}^{-1}$ , a much more realistic value than was found in the other simulations. The shear produced by a weak low-level drainage flow formed a thin transition layer over the surface inversion. Above the sloping plain, the drainage flow was 50 m deep with a maximum speeds near  $1.5 \text{ m s}^{-1}$  at the base of the steep slope that decreased to  $0.5 \text{ m s}^{-1}$  at the western end. A weak  $0.3\text{-}1.4 \text{ m s}^{-1}$  easterly flow extended halfway up the steep slope with westerly flow over its upper section. Wind speeds through the neutral layer remained less than  $2.0 \text{ m s}^{-1}$  although slight increases were noticed in the hour since sunset, most probably because of the reduced surface friction.

After 2 h, the two layer thermal structure evident in prior simulations was seen in the solution to this case as well (Figure 50c). Over the lower elevations, both the surface inversion layer and the overlying transition layer generally followed the topography. The inversion layer still extended to 175 m AGL and the transition region occupied a 100 m deep layer above that. Over the steep slope, the inversion extended only to 75 m AGL because of the drainage of cold air westward. A deeper but less stable inversion layer formed over the high plateau to the east and merged with the overlying free atmosphere. As a result, a wedge of neutrally stratified air was all that remained of the afternoon CBL. The layer of easterly winds reached 125 m AGL over the

sloping plain with a maximum of  $1.8-2.0 \text{ m s}^{-1}$  at 75 m AGL. Winds above the easterlies remained nearly steady. Over the steep slope, the drainage was confined to the lowest level and extended eastward to  $x = 23.5 \text{ km}$ . Winds east of this location were westerly, but speeds were less than  $0.5 \text{ m s}^{-1}$  at 25 m AGL. Above this level, the speeds increased sharply with height to  $7.0 \text{ m s}^{-1}$  at 475 m AGL.

Figure 50d shows the state of the boundary layer 3 h after sunset. East winds over the sloping plain reached 175 m AGL with a broad maximum of  $1.4 \text{ m s}^{-1}$  between 125 m AGL and 175 m AGL. Strong shears were present through the transition layer as the wind direction turned abruptly west. Wind speeds above the transition layer were over  $2.5 \text{ m s}^{-1}$  at 325 m AGL and increased in speed with height to  $6.0 \text{ m s}^{-1}$  at 680 m AGL. These values were  $1.0-2.0 \text{ m s}^{-1}$  higher than 1 h previously as the near neutral layer contraction reduced the effective surface friction. The top of the transition layer was more horizontal than was seen earlier, lying at 325 m above the reference level. The cold air pool could be seen forming over the flat plain with the subsequent development of a stronger potential temperature gradient along the sloping plain. An hour later, the development of a blocked flow layer could be seen forming between 300 m and 500 m above the reference level with the 311 K isentrope approximating the dividing streamline (Figure 50e). Pooling reduced the low-level easterly wind speeds to  $0.3-0.6 \text{ m s}^{-1}$  and the isentropic surfaces were nearly horizontal.

Five hours after sunset (Figure 50f), the boundary layer achieved a near steady structure. Above the 175 m deep low-level inversion layer, the transition layer extended to 425 m above the reference level and

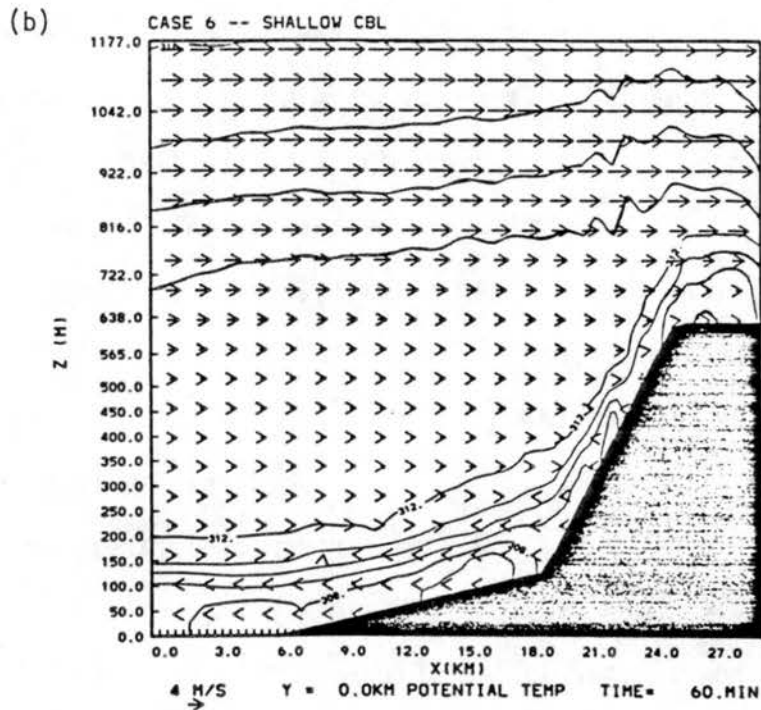
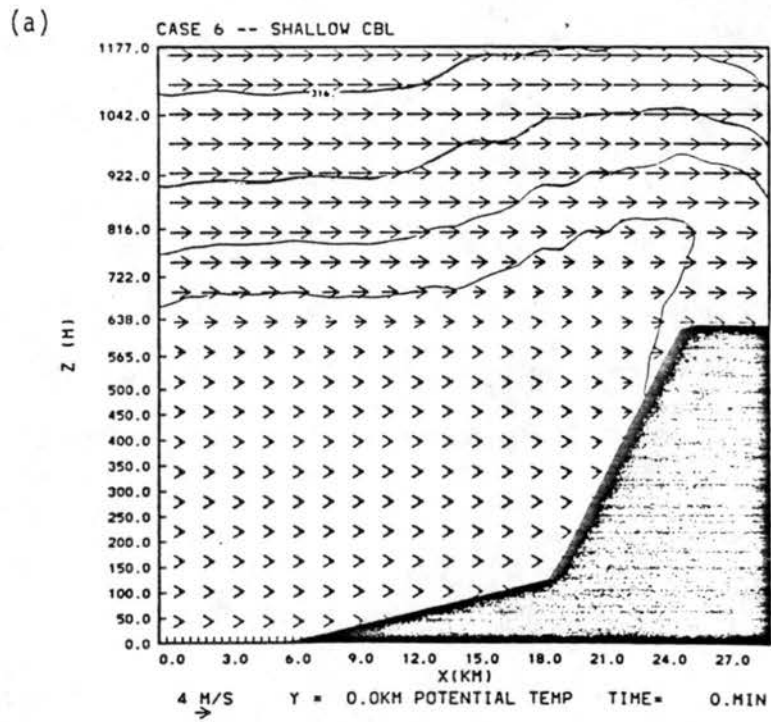


Figure 50. Wind and potential temperature fields for Case 6 (contour interval - 1 K) for (a) at sunset and (b) at sunset + 1 h.

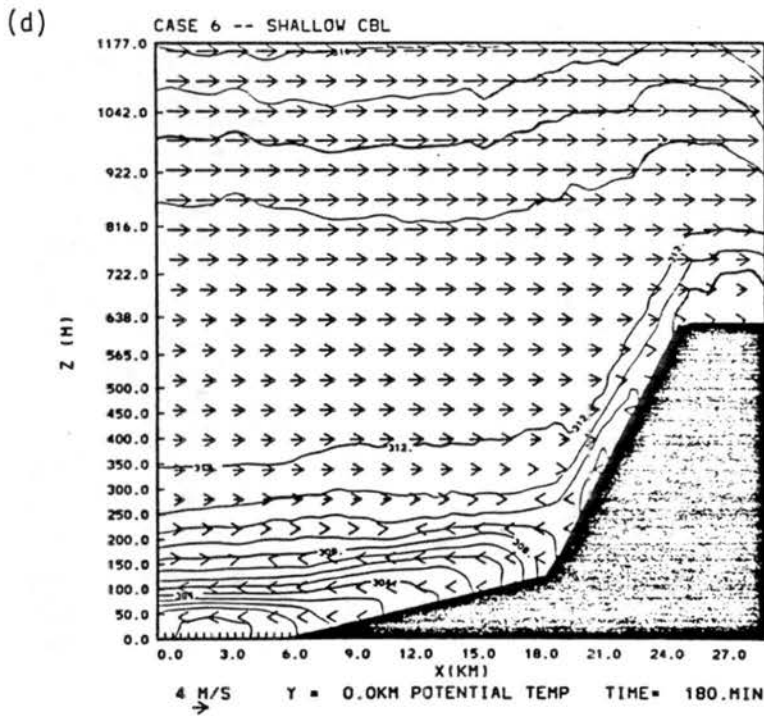
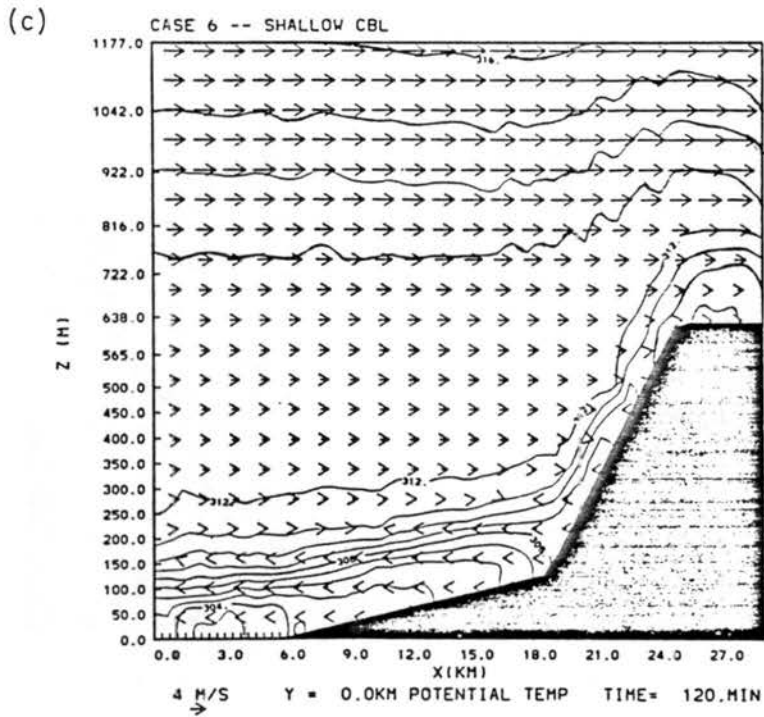


Figure 50. Wind and potential temperature fields for Case 6 (contour interval - 1 K) for (c) at sunset + 2 h and (d) at sunset + 3 h.

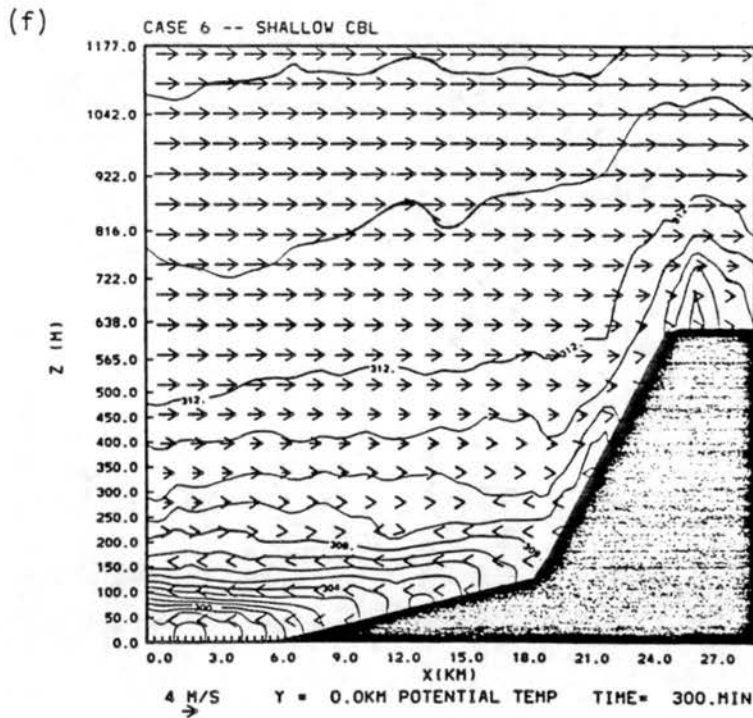
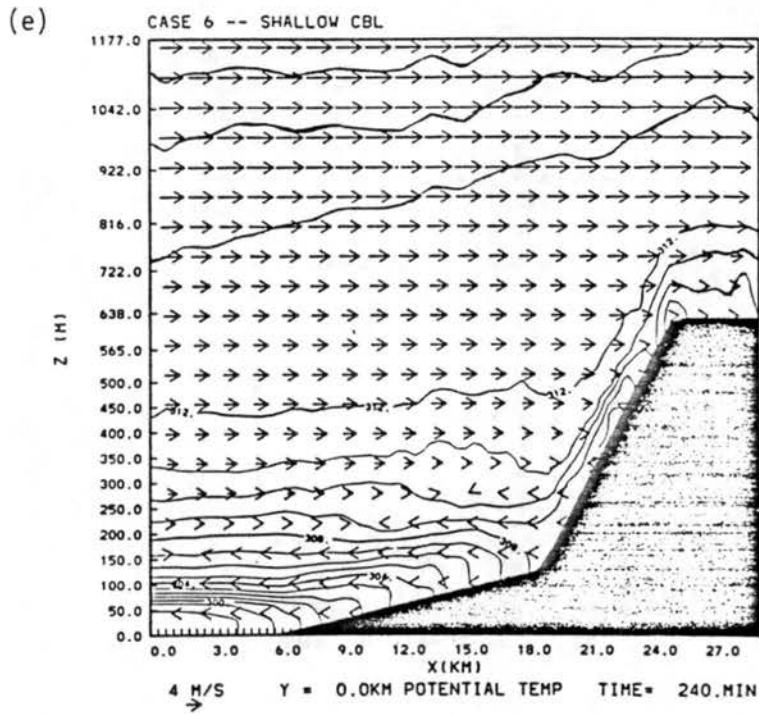


Figure 50. Wind and potential temperature fields for Case 6 (contour interval - 1 K) for (e) at sunset + 4 h and (f) at sunset + 5 h.

smoothly merged with the free atmosphere above it. The stratification lessened with height, similar to the other cases, but unlike those solutions, the mixed layer present at sunset had been completely destroyed by this time. Lapse rates over the plain ranged from  $0.01 \text{ K m}^{-1}$  between 175 m and 275 m above the reference level to  $0.005 \text{ K m}^{-1}$  in the overlying layer. The layer of east winds over the sloping plain remained unchanged from the 4 h structure, but the west winds in the transition layer were  $1.0\text{-}1.5 \text{ m s}^{-1}$  weaker in the blocked flow layer ( $z < 375 \text{ m}$  above the reference level). Winds above this level were unaffected by the increased stability in the layer.

c. Effects of wind direction. The two 3-D simulations executed to determine the effects of wind speed differed from the prior runs in several respects. The biggest change was the doubling of the horizontal grid spacing, thereby reducing the model resolution. The coarse grid was tested in a 2-D simulation with identical boundary conditions as were used in Case 2. Those results appear in Appendix II. This is the largest grid spacing which will still allow proper specification of the lower surface. The model topography was infinite in the north-south direction, resulting in slab-symmetric simulations. However, lateral boundary conditions were used on the northern and southern boundaries to inhibit the development of runaway circulations which can be produced by cyclic boundaries.

The inclusion of full 3-D physics enabled the model to better simulate the time-dependent boundary layer structure produced by the interaction of the 3-D wind field with the 2-D topographical configuration. Although the domain was slab-symmetric in the north-south direction, the asymmetric boundary conditions allowed full 3-D

circulations to be produced. As a result, the simulated boundary layer structure is slab-symmetric when averaged over short time periods, but at any given instant small asymmetric motions representative of local scale circulations appear in the model solution. In this configuration, the model will develop a more realistic structure than would be simulated in 2-D experiments with assumed slab symmetry. Variations in the horizontal velocity field in such 2-D simulations can produce unrealistic vertical motions to maintain continuity. By simulating full 3-D physics, non-divergent horizontal circulations can be produced which would not directly affect the vertical motion fields. In the average, these circulations result in no mean motions, but can produce Reynold's averaged effects on the mean model fields. Initialization was carried out similarly to Case 2 with a 45 min adjustment following the 15 min simultaneous dynamic spinup of both the u and v components.

Figures 51a and 51b show the initial state of the boundary layer for the  $5.0 \text{ m s}^{-1}$  southwest geostrophic wind case ( $u_0 = v_0 = 3.5 \text{ m s}^{-1}$ ). The thermal structure was very similar to that in the reference case. The boundary layer was well mixed from the surface to 1300 m above the reference level; the atmosphere was neutrally stratified and the wind structure paralleled that of the externally imposed logarithmic profile. West winds over the lower terrain increased from  $0.9 \text{ m s}^{-1}$  at 25 m AGL to  $3.4 \text{ m s}^{-1}$  at 1100 m AGL with higher speeds over the higher terrain necessary to satisfy mass continuity. South wind speeds followed the same structure over the lower terrain, and an east-west gradient was present due to the surface effects of the higher terrain. Over the high plateau, the winds developed a more westerly direction because of the acceleration of the west winds over the barrier.

By 1 h after sunset (Figures 51c and 51d), the surface inversion layer had formed with an imbedded easterly wind component. The transition layer also started to develop over the surface inversion and the total stable layer depth was 175 m over the eastern section of the sloping plain and 25 m more shallow over the flat plain. The drainage component was continuous from the summit of the steep slope westward and varied in depth from 25 m over the steep slope and flat plain to 125 m over the middle section of the sloping plain. Wind direction was dominated by the drainage in the inversion layer, but became more southwesterly with height. Speeds in the mixed layer increased 0.3-0.5  $\text{m s}^{-1}$  in the neutral layer due to the reduced surface friction. Over the high plateau, a 125 m deep stable layer produced a narrower shear zone than was present earlier.

Two hours after sunset, the inversion depth was nearly constant over the sloping plain, reaching 125 m AGL, while the top of the transition layer was nearly horizontal at 225 m above the reference level (Figures 51e and 51f). The lapse rate through the lower layer was 0.08  $\text{K m}^{-1}$ , mostly due to the extreme stability in the lowest 75 m, and was 0.007  $\text{K m}^{-1}$  in the transition region. The stable layer depth was only 75 m over the upper steep slope, but increased to 125 m over the high plateau. East component wind speeds peaked at 3.0  $\text{m s}^{-1}$  at 75 m AGL over the sloping plain, the top of the strongly stable layer. Below this level, drainage flow speeds were near 0.5  $\text{m s}^{-1}$  and increased to 1.1  $\text{m s}^{-1}$  over the steep slope where the depth of the layer containing the easterly component was only 25 m deep. At 175 m above the sloping plain, the easterly component was less than 1.0  $\text{m s}^{-1}$  and the profile exhibited a westerly component at higher levels. The south

wind component remained steady during the previous hour throughout the domain. The combination of speed and directional shear through the inversion layer resulted in values near  $0.036 \text{ s}^{-1}$ , sufficient to maintain a high turbulence level despite the moderately strong stability.

After 3 h, the boundary layer appeared to have achieved a quasi-steady structure with little noticeable change from the 2 h fields (Figures 51g and 51h). The strength of the easterly component was  $0.3\text{-}0.5 \text{ m s}^{-1}$  less than before as cold air pooling could be seen over the flat plain. The convergence of the easterly and westerly components in the transition layer resulted in  $0.1\text{-}0.2 \text{ m s}^{-1}$  updrafts above the intersection of the sloping plain and the steep slope. Otherwise, the wind structure was nearly identical to that 1 h previously except that neutral layer speeds were  $0.1\text{-}0.2 \text{ m s}^{-1}$  higher. The top of the transition layer was 50-100 m higher than before as vertical mixing gradually extended the cooling deeper into the neutral layer. By 1 h later (Figures 51i and 51j), the cooling extended to 375 m above the reference level and the lapse rate through the depth of the stable layer decreased smoothly with height. In the lower levels, it was  $0.025 \text{ K m}^{-1}$  while it was  $0.006 \text{ K m}^{-1}$  near the top of the transition region underlying the neutral layer. As before, the wind field appeared to be in a near steady-state structure with a slight increase in speed apparent in the neutral layer.

Five hours after sunset (Figures 51k and 51l), cold air pooling west of  $x = 8.0 \text{ km}$  had reduced the strength of the easterly component to less than  $1.6 \text{ m s}^{-1}$  west of this location,  $1.2 \text{ m s}^{-1}$  less than the maximum speed at  $x = 12.0 \text{ km}$ . Although the stable layer had

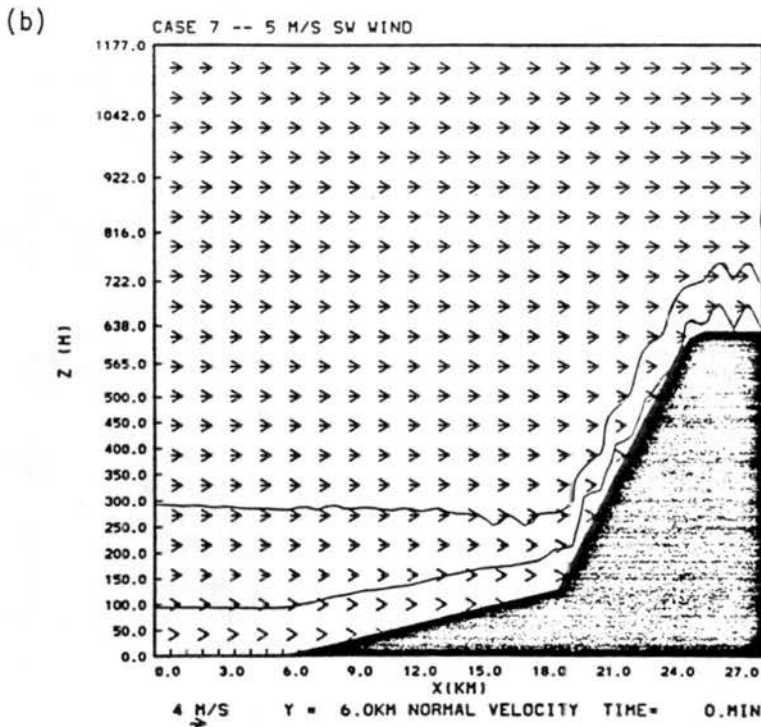
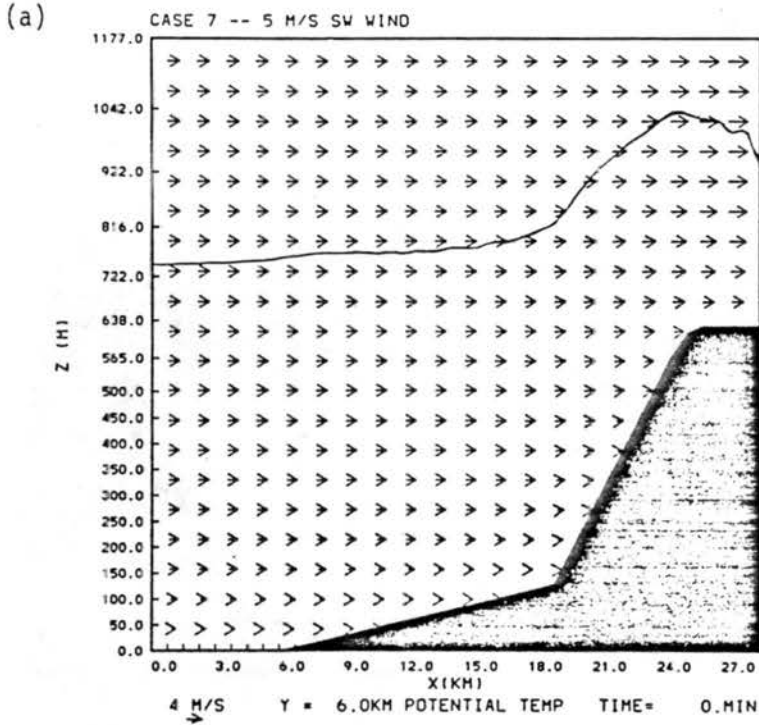


Figure 51. Case 7 fields. Vectors -  $u$  velocity component for (a) sunset potential temperature (contour interval - 1 K) and (b) sunset  $v$ -velocity component (contour interval -  $1 \text{ m s}^{-1}$ ).

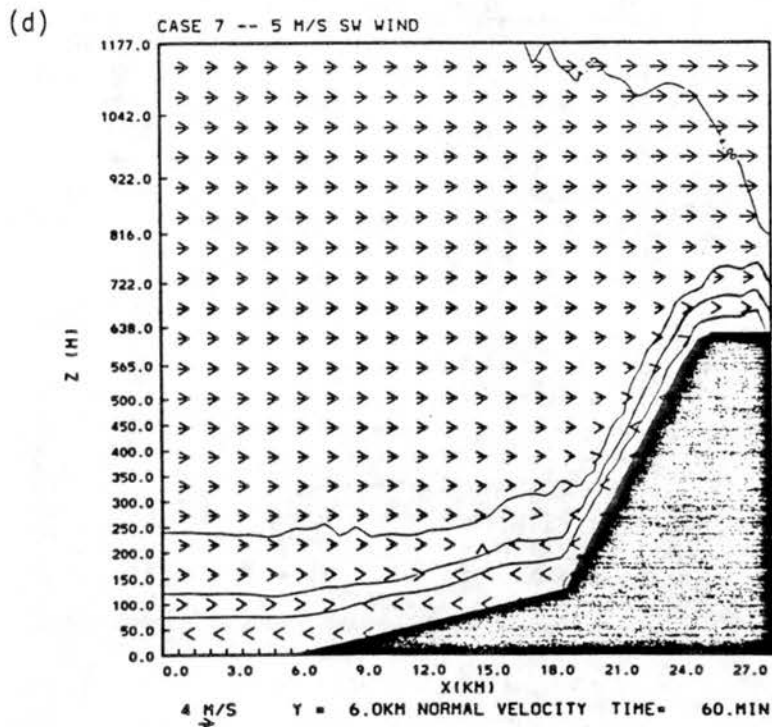
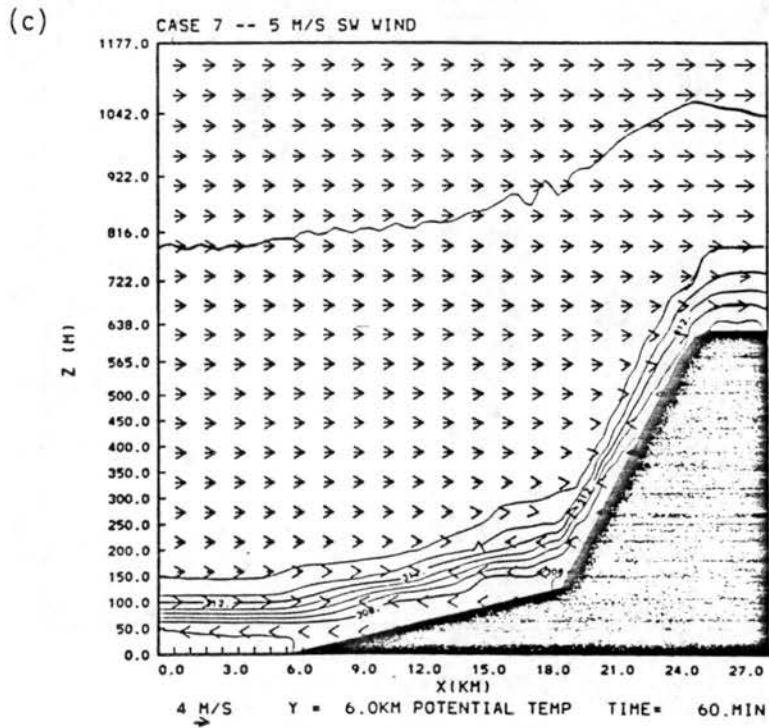
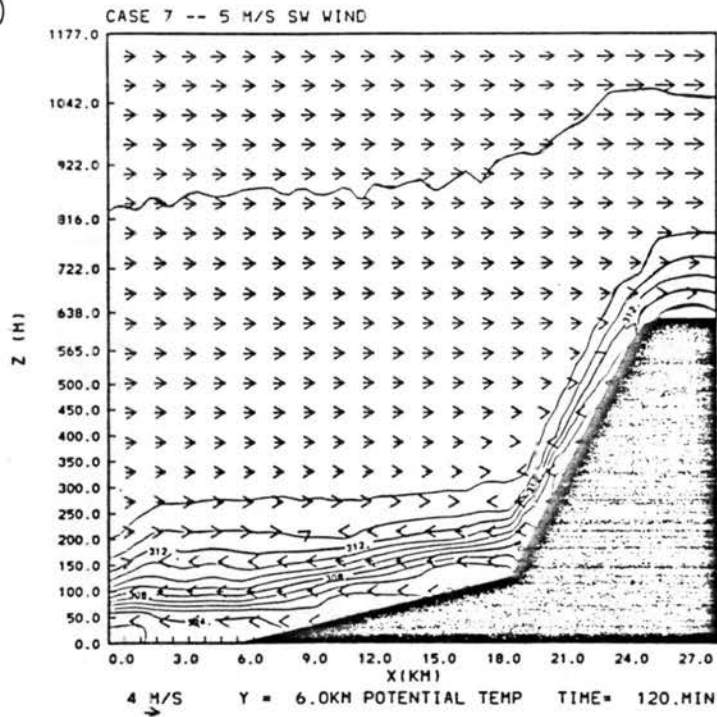


Figure 51. Case 7 fields. Vectors -  $u$  velocity component for (c) sunset + 1 h potential temperature (contour interval - 1 K) and (d) sunset + 1 h  $v$ -velocity component (contour interval - 1  $m\ s^{-1}$ ).

(e)



(f)

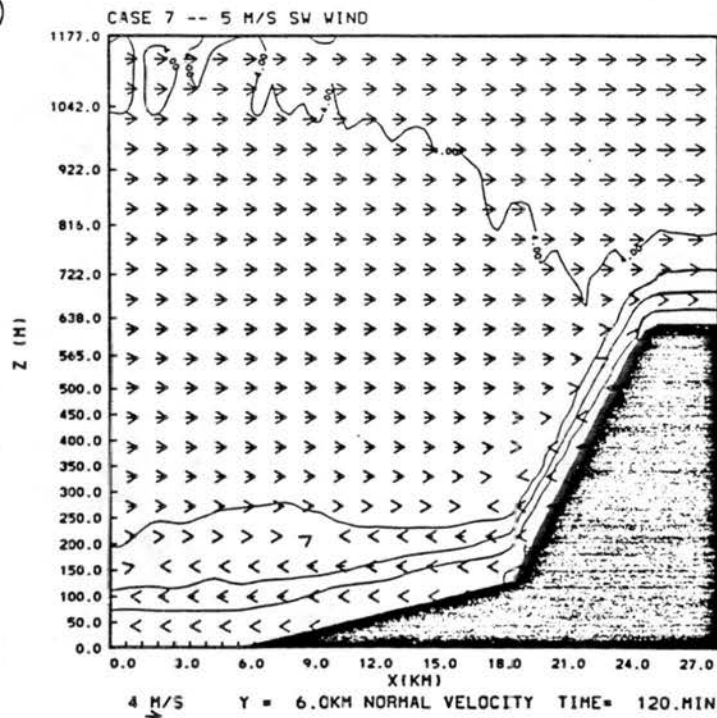


Figure 51. Case 7 fields. Vectors -  $u$  velocity component for (e) sunset + 2 h potential temperature (contour interval - 1 K) and (f) sunset + 2 h  $v$ -velocity component (contour interval - 1  $\text{m s}^{-1}$ ).

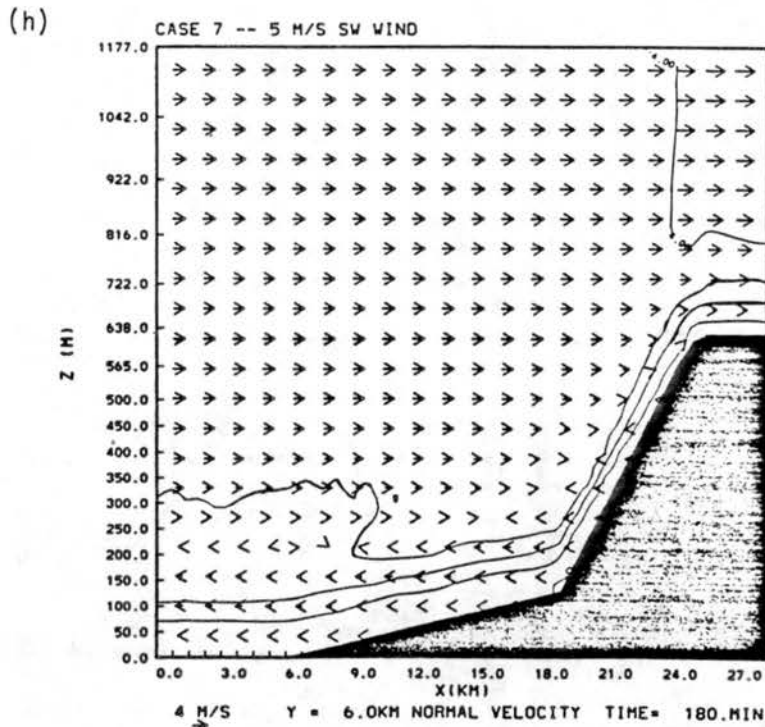
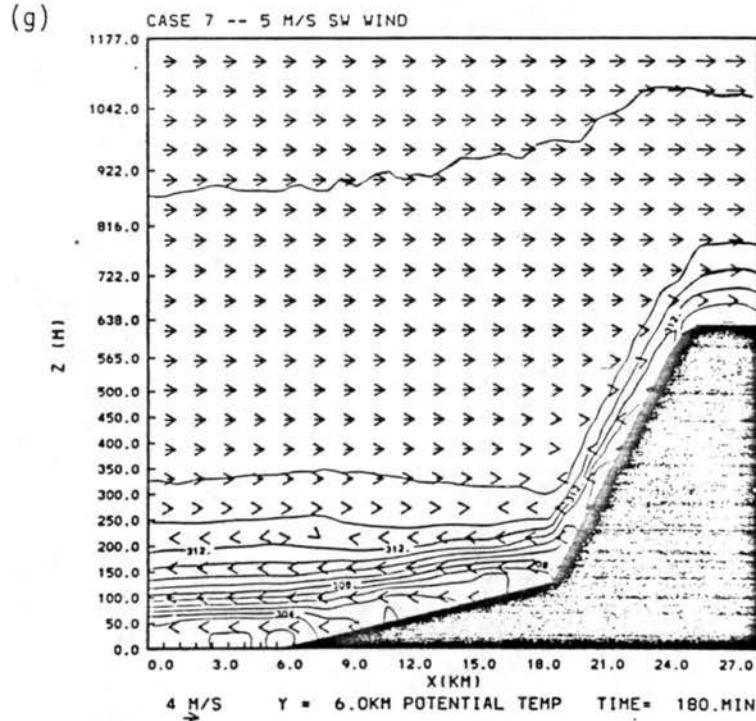
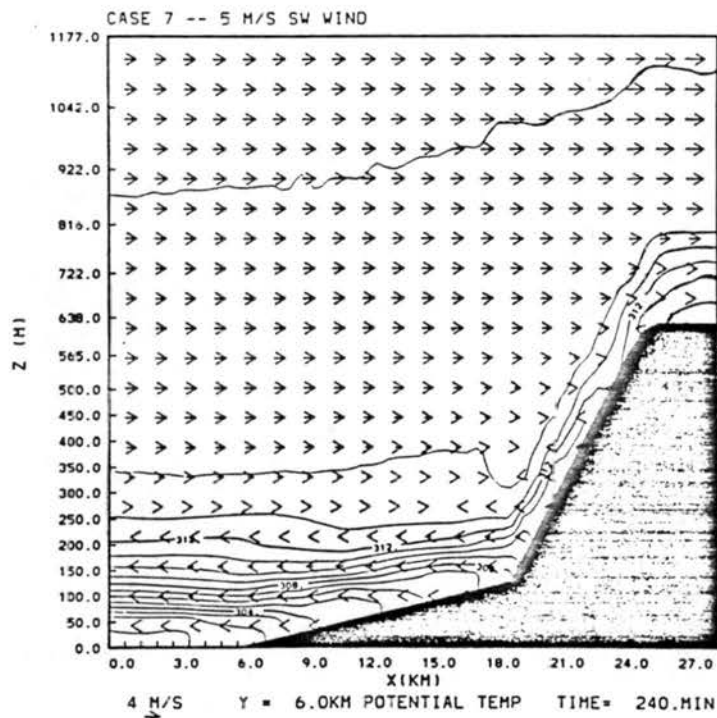


Figure 51. Case 7 fields. Vectors -  $u$  velocity component for (g) sunset + 3 h potential temperature (contour interval - 1 K) and (h) sunset + 3 h  $v$ -velocity component (contour interval - 1  $\text{m s}^{-1}$ ).

(i)



(j)

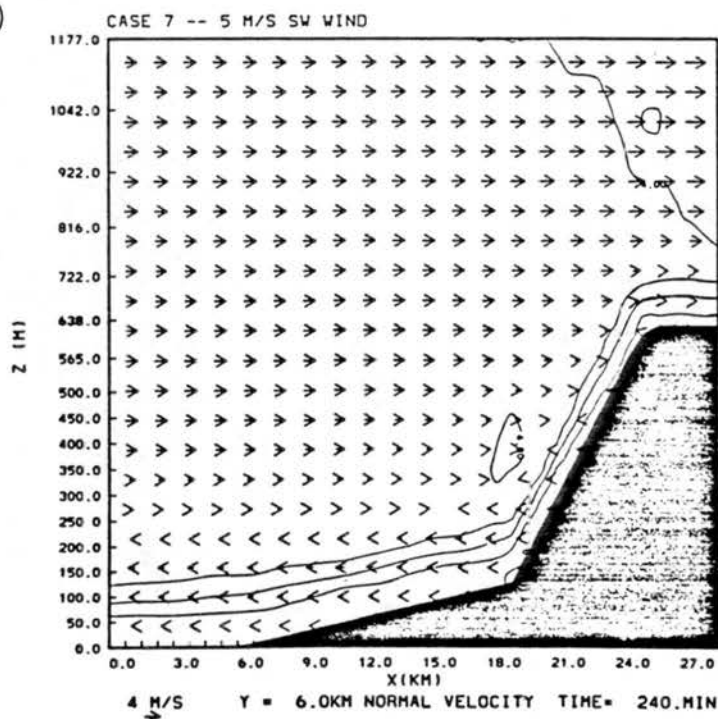


Figure 51. Case 7 fields. Vectors -  $u$  velocity component for (i) sunset + 4 h potential temperature (contour interval - 1 K) and (j) sunset + 4 h  $v$ -velocity component (contour interval -  $1 \text{ m s}^{-1}$ ).

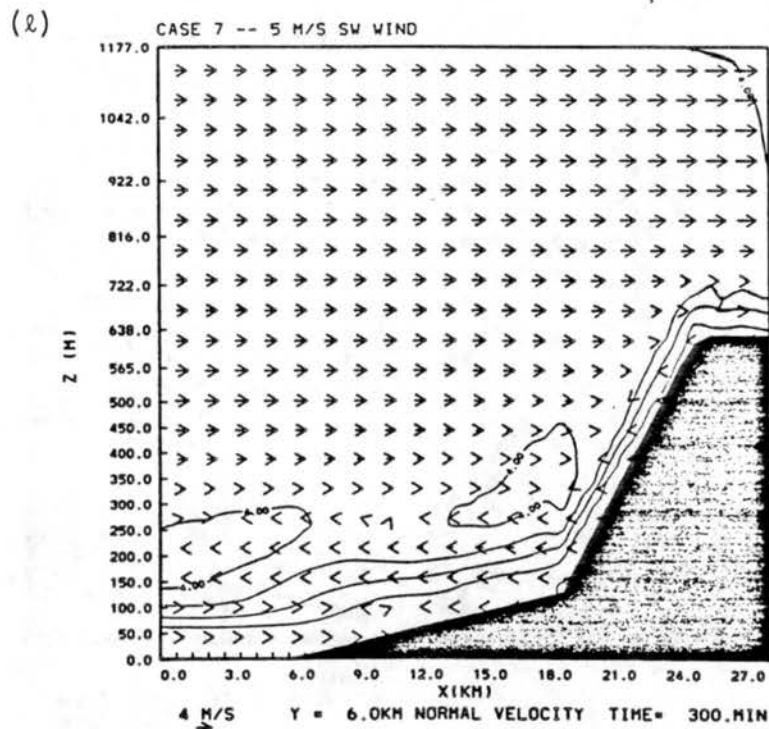
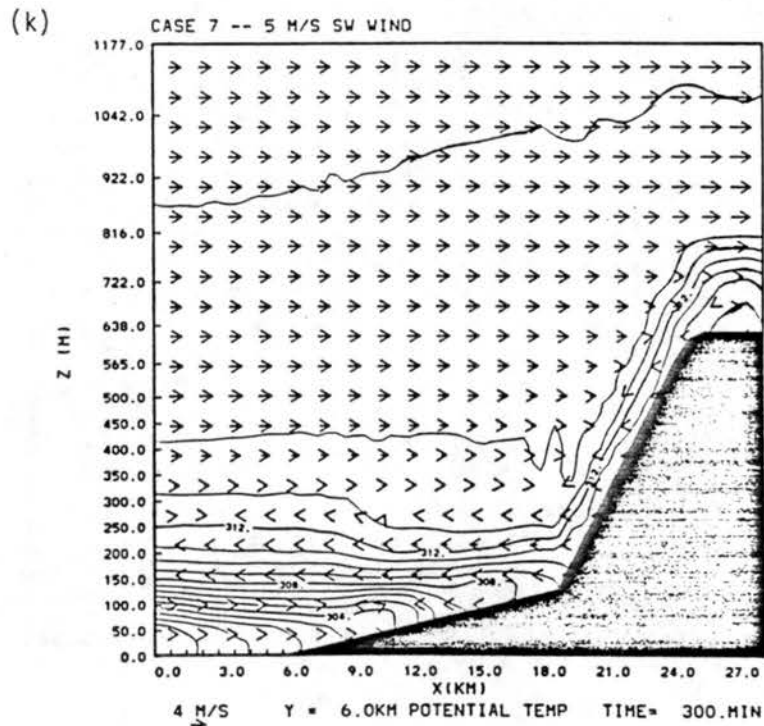
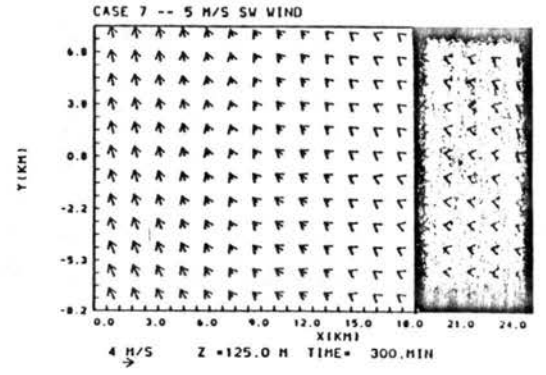
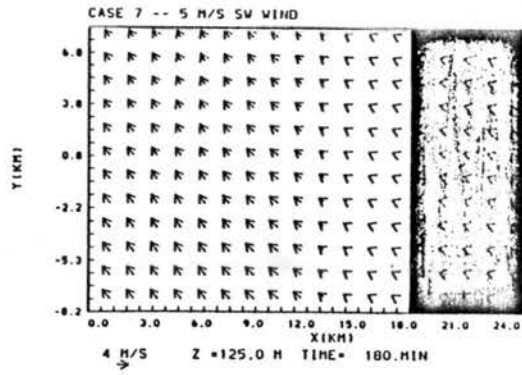
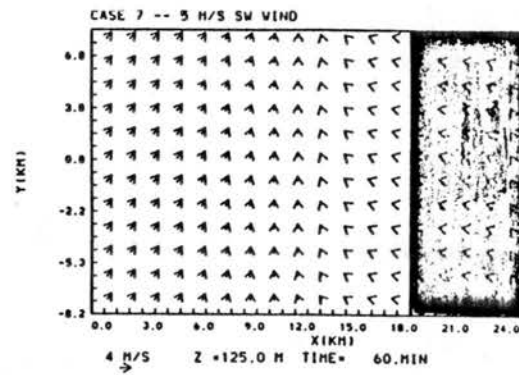
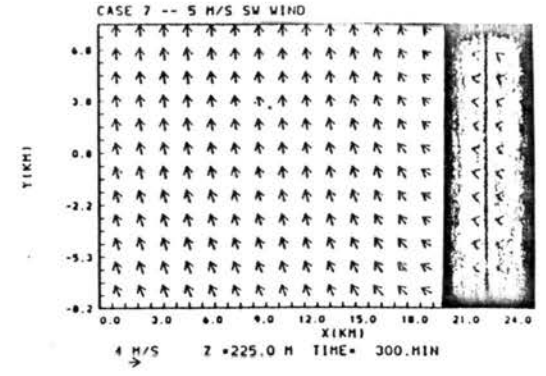
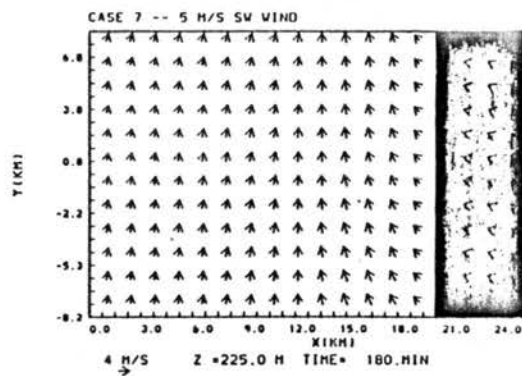
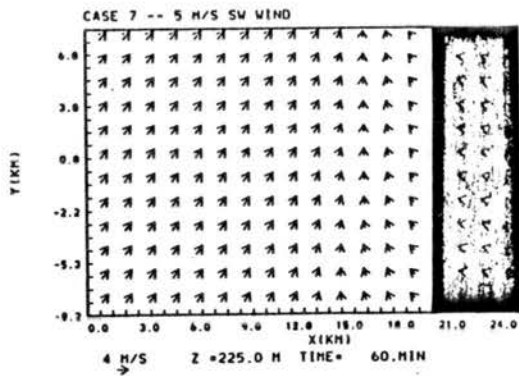
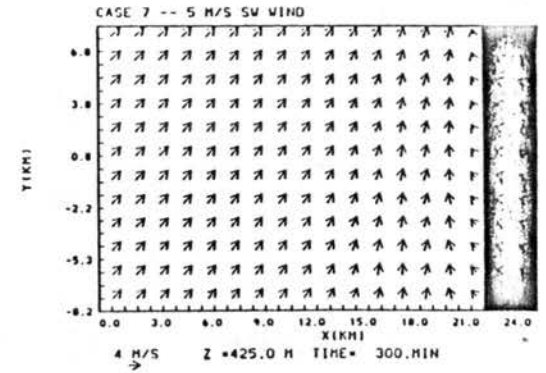
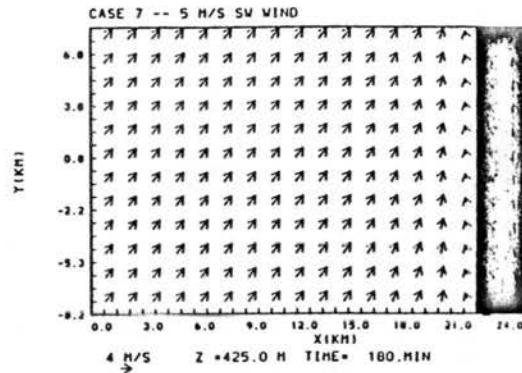
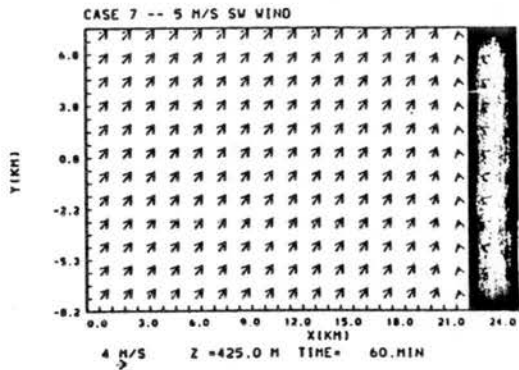


Figure 51. Case 7 fields. Vectors -  $u$  velocity component for (k) sunset + 5 h potential temperature (contour interval - 1 K) and (l) sunset + 5 h  $v$ -velocity component (contour interval - 1  $\text{m s}^{-1}$ ).

continuously variable stratification with height, the approximate elevation of the top of the surface inversion appeared to be 275 m AGL with the transition layer reaching 475 m AGL over the flat plain. An easterly component was present in the lowest 175 m over the sloping plain with maximum speeds of  $2.8 \text{ m s}^{-1}$  at 75 m AGL. Over the steep slope, both the inversion layer and the layer containing an easterly component were more shallow. Cooling only extended to 125 m AGL and the layer of easterlies reached the same level with maximum speeds less than  $1.0 \text{ m s}^{-1}$ , showing that the stronger elevated winds over the sloping plain were not pure drainage phenomena. Over the high plateau, the stable layer top was located at 125 m AGL, slightly higher than over the steep slope. The south wind component continued to remain steady, showing little time variability after the completion of the evening transition period.

The development of the NBL structure is further detailed in Figure 52 which shows the time evolution of the Case 7 wind fields on horizontal cross-sections at 125 m, 225 m and 425 m above the model reference level ( $z=0$ ). After 1 h, the cold thermal effects near the surface has resulted in the inhibition of the westerly wind component at 125 m. Southwesterly flow still dominates at 225 m and 425 m, except over the steep slope immediately west of the intersection of the cross-section with the lower boundary. By 3 h after sunset, the transition layer extend to 325 m above the reference level and the winds below this elevation have an easterly thermal component. At 125 m,  $4\text{-}5 \text{ m s}^{-1}$  southeast winds are found while at 225 m the westerly component of the large scale wind balances the thermal easterlies, resulting in a weak  $2\text{-}3 \text{ m s}^{-1}$  south wind. The flow field at 425 m remains unaffected by the

Figure 52. Case 7 horizontal wind fields.



cooling of the layer below, except over the steep slope. Five hours after sunset the 125 m winds have weakened to  $2-3 \text{ m s}^{-1}$  with the decrease in surface cooling rate. At 225 and 425 m, the wind fields exhibit a slightly stronger thermal component than 2 h previously, but the increase is only  $0.5-1.0 \text{ m s}^{-1}$ , showing the achievement of a quasi-steady structure.

Contrasted with this experiment are the results from the  $5.0 \text{ m s}^{-1}$  south geostrophic wind case (Case 8) in which there was initially no wind component into the barrier. In this case, vertical wind shear was present, but the forced lifting of the flow and the existence of a synoptic scale wind opposing the drainage and cold thermal winds was absent. Figures 53a and 53b show the sunset boundary layer structure at the completion of the initialization-adjustment period. As in the other simulations, the boundary layer was neutrally stratified to 1300 m above the reference level and the wind profile followed the logarithmic distribution imposed at the north and south boundaries. Over the low plain, initial southerly wind speeds were  $1.5 \text{ m s}^{-1}$  at 25 m AGL and increased to  $5.0 \text{ m s}^{-1}$  at 980 m AGL. A small west wind component developed as a result of the dynamic initialization, but speeds were less than  $0.1 \text{ m s}^{-1}$ . A southerly jet with maximum speeds near  $10.0 \text{ m s}^{-1}$  at 225 m AGL developed over the high plateau during the initialization because mass continuity requirements imposed at the boundaries and the proximity of the overlying free atmospheric stable layer to the surface channeled the mixed layer air through a more shallow depth.

One hour after sunset (Figures 53c and 53d), the surface inversion layer had formed over the low-lying area and extended to 75 m AGL. A

thin transition layer had also developed over the surface inversion, reaching 125 m AGL. South component wind speeds over the sloping plain were unchanged since sunset. At 25 m AGL, a  $0.5-0.7 \text{ m s}^{-1}$  easterly drainage flow developed along the entire length of the sloping plain. A cold thermal easterly component also had formed at the top of the surface inversion layer with a speeds increasing from  $1.0 \text{ m s}^{-1}$  at the eastern end of the flat plain to  $3.5 \text{ m s}^{-1}$  at the base of the steep slope. The depth of the layer containing a significant easterly component ( $u$  greater than  $0.5 \text{ m s}^{-1}$ ) also increased with distance eastward along the sloping plain from 75 m at  $x = 10.0 \text{ km}$  to 175 m at  $x = 18.0 \text{ km}$ . Above the layer of east winds, a weak  $0.1-0.4 \text{ m s}^{-1}$  westerly return component was present in the lowest 300 m of the overlying neutral layer. Total stable layer depth was only 125 m over the steep slope and high plateau as much of the cold air drained west at  $0.5-1.0 \text{ m s}^{-1}$ . With the development of the near-surface easterly component, the south component speeds decreased to less than  $1.0 \text{ m s}^{-1}$  from nearly  $3.0 \text{ m s}^{-1}$  at sunset, resulting in a total speed decrease of  $1.5 \text{ m s}^{-1}$ . This reduction was caused by the elimination of the downward flux of high momentum air by the stability in the surface inversion layer.

The surface inversion layer extended to 175 m AGL over the sloping and flat plains and the top of the transition layer was nearly horizontal 275 m above the reference level 2 h after sunset (Figures 53e and 53f). Lower layer lapse rates ranged from  $0.10 \text{ K m}^{-1}$  below 75 m AGL, which is unrealistically stable, to a more reasonable value of  $0.04 \text{ K m}^{-1}$  between 75 m AGL and 175 m AGL. Stability in the transition layer was similar to that found in other simulations, approximately

$0.01 \text{ K m}^{-1}$ . The stable layer only reached 175 m AGL over the steep slope, but was 50 m deeper over the high plateau with lapse rates ranging between  $0.015 \text{ K m}^{-1}$  and  $0.030 \text{ K m}^{-1}$ . The south component speeds changed little during the period between 1 h and 2 h, except for a slight increase of  $0.5\text{-}1.0 \text{ m s}^{-1}$  above the stable layer over the steep slope. The layer of east component winds was 175 m deep over the sloping plain, and increased to 225 m deep at the base of the steep slope. Over the upper section of the steep slope and over the high plateau, the layer shrunk to 175 m in depth. East component speeds reached a maximum between  $3.5 \text{ m s}^{-1}$  and  $4.0 \text{ m s}^{-1}$  at 75 m AGL and decreased with height through the inversion layer to  $0.5\text{-}1.0 \text{ m s}^{-1}$  at its top. Above the inversion layer, the winds acquired a small westerly component with speeds less than  $0.3 \text{ m s}^{-1}$  over the flat plain which increased to  $0.6 \text{ m s}^{-1}$  400 m AGL over the intersection of the plain with the steep slope. East of this location, the west component decreased with distance eastward. A  $0.1\text{-}0.2 \text{ m s}^{-1}$  subsidence was present in the lowest 400 m above the base of the steep slope which marked the descending branch of the mountain-plain circulation, a phenomenon which could not be discerned in the other simulations.

Three hours after sunset, pooling over the flat plain started to back up onto the lower section of the sloping plain (Figures 53g and 53h). The surface inversion layer was still 175 m deep over the lower elevations, but the top had less slope than the underlying surface. The top of the transition layer reached 325 m above the reference level and the stable layer had grown to 175 m AGL over the steep slope. The large region of subsidence moved eastward and was directly above the summit of the steep slope with vertical wind speeds of  $0.1\text{-}0.2 \text{ m s}^{-1}$ . As before,

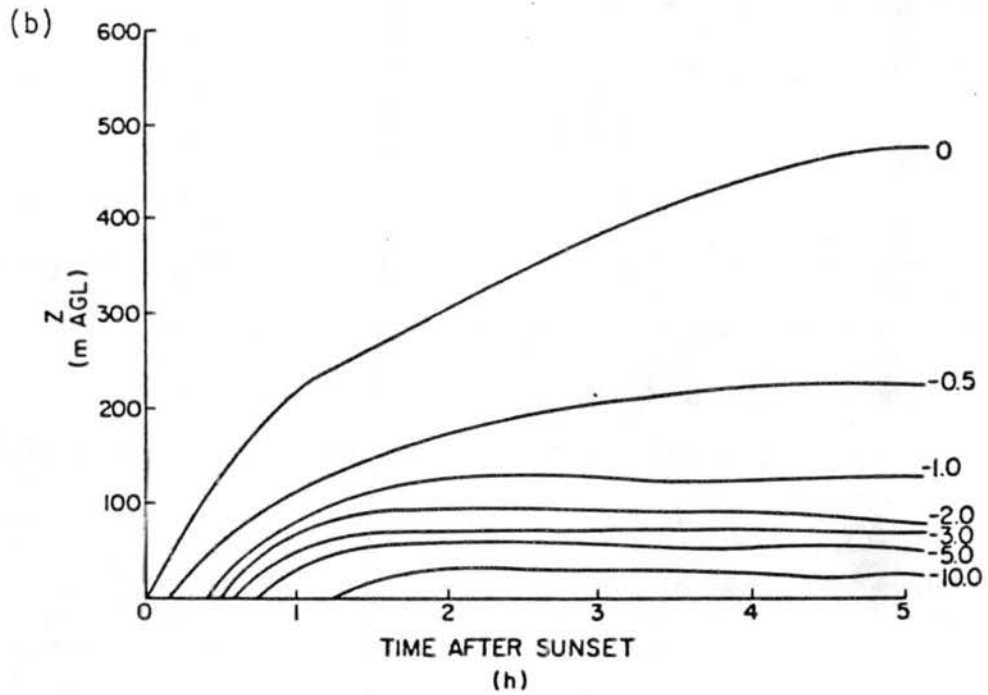
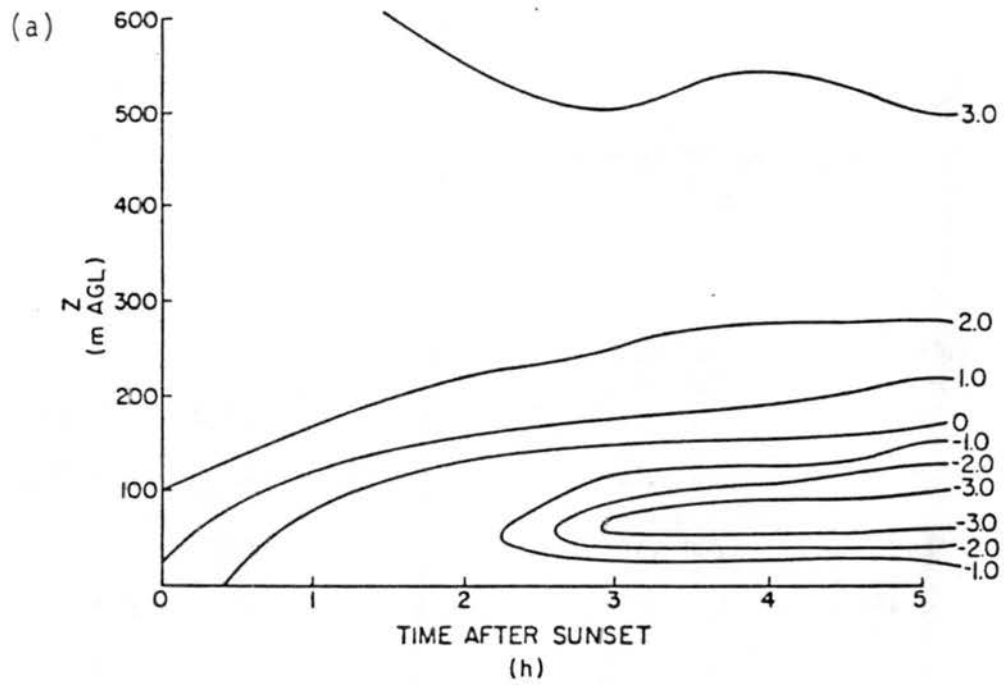


Figure 56. Time-height cross-sections at  $x = 15$  km of (a)  $u$  velocity component and (b) potential temperature deviations for Case 4.

winds remained steady while the transition layer continued to grow. By 5 h after sunset, the top of the transition layer was 350 m above the surface due to the continued diffusion of cold air upward through the shear layer.

For contrast, Figures 56 and 57 show similar diagrams for the weaker wind (Case 4) and stronger wind (Case 5) cases, respectively. Not surprisingly, the easterly wind speeds were higher and the transition layer depth was much less in the weak wind case than the reference case. Even the transition layer achieved a steady structure by 3 h after sunset, a result not seen in the other simulations. In the strong wind case, the opposite was found. The drainage flow speeds remained small and the transition layer continued to deepen throughout the simulation due to the increased shear. The transition layer was still growing at a relatively fast rate at the conclusion of the simulation 5 h after sunset. In both cases, the velocity difference between the easterly flow 5 h after sunset and the sunset westerly winds was nearly the same as that in the reference case,  $4\text{-}5\text{ m s}^{-1}$ .

The time-height cross-sections for the southwest geostrophic wind case (Case 7) are shown in Figure 58. The simulated structure had characteristics resembling a combination of both the Case 2 results, which had the same geostrophic wind speed, and Case 4, which had a similar barrier wind component. The surface inversion layer containing the easterly flow developed much like that in the weak wind case, with a more shallow depth and slightly higher east wind speeds than in the reference case. Unlike Case 4, however, the transition layer continued to grow through the evening, much in the same way as that simulated in the reference case. Throughout the simulation, the

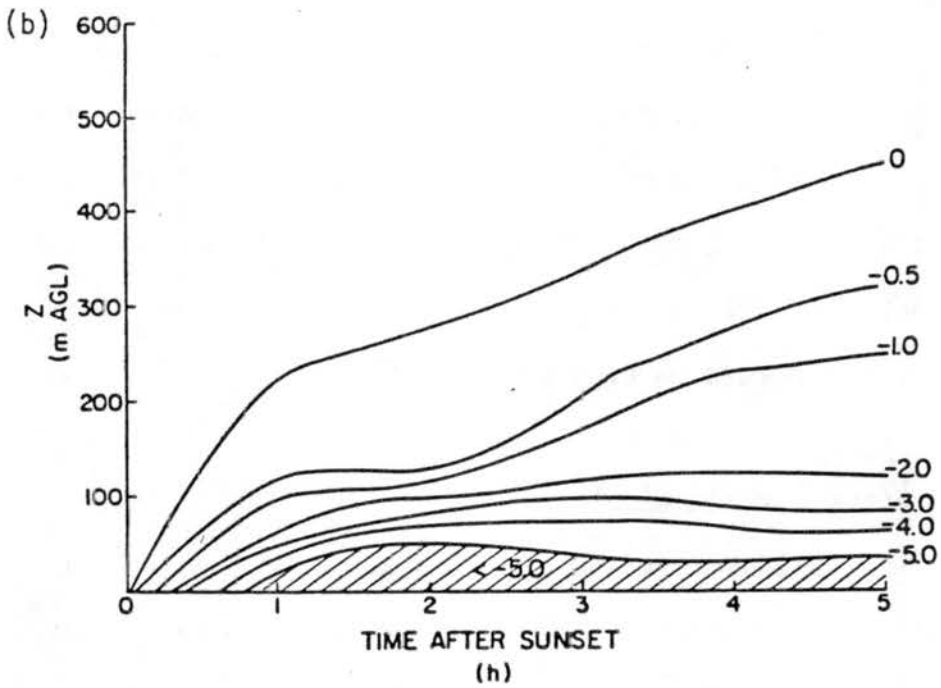
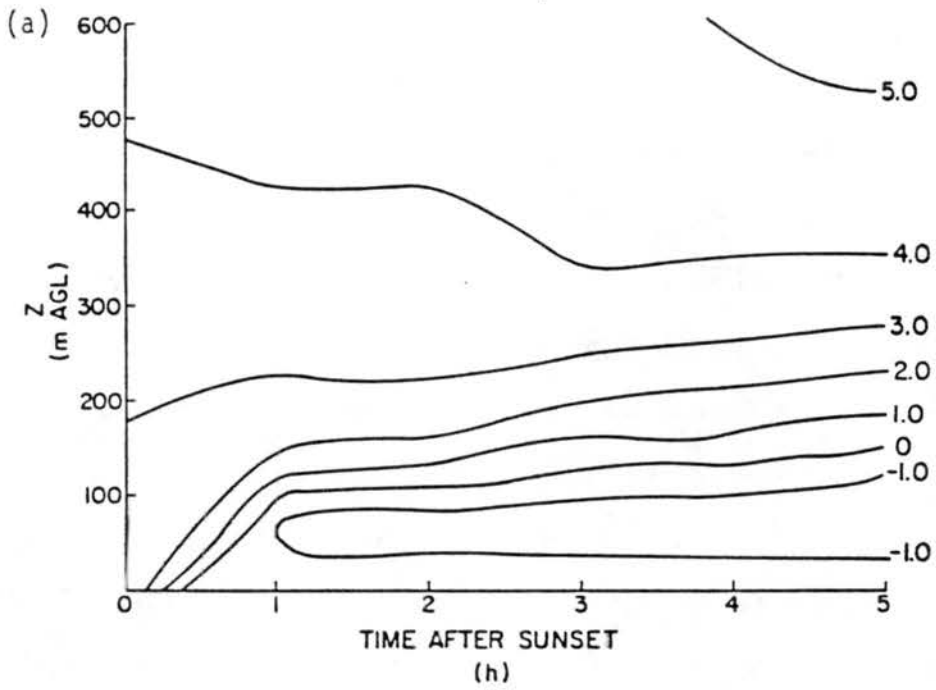


Figure 55. Time-height cross-sections at  $x = 15$  km of (a)  $u$  velocity component and (b) potential temperature deviations for Case 2.

elevations. A similar recession of the stable air away from the high barrier was modeled by Banta (1982). At the completion of the morning transition, the model boundary layer again resembled its initial state with a deep surface based neutral layer and well mixed westerly winds.

Not simulated were the rotational wind components which would develop as the easterly flow persisted through the night. Assuming the externally forced winds were in gradient balance, Coriolis turning of a steady  $3 \text{ m s}^{-1}$  thermal easterly component would generate a  $3 \text{ m s}^{-1}$  south wind after 1 h if frictional effects were negligible. Rotation of the winds to such a large degree cannot occur because of the large turbulent drag in the thermal wind layer. The easterly winds were quasi-steady with the large pressure gradient produced by the surface cooling being approximately balanced by the turbulent momentum flux divergence. On the other hand, it is not unreasonable to assume that a noticeable Coriolis component would develop through the night if it had been simulated. However, this effect is only of secondary importance and would not significantly affect the diurnal boundary layer processes. Further, the simulation of the rotational wind components would add another process in the simulated dynamical structure and make interpretation of the model results more difficult.

Figure 55 shows time-height cross-sections of potential temperature deviations and wind speeds for the reference simulation (Case 2) taken at  $x = 15.0 \text{ Km}$ . The evening transition period was complete 2-3 h after sunset with the 100 m deep inversion layer underlying a thin transition layer. Easterly wind speeds ranged between  $1.5 \text{ m s}^{-1}$  and  $2.0 \text{ m s}^{-1}$ , a total velocity difference of  $4\text{-}5 \text{ m s}^{-1}$  from the sunset structure. As the simulation progressed, the surface inversion layer and easterly

layer containing a well-mixed westerly wind bounded at the top by the overlying free atmosphere. During the evening transition, a shallow stable inversion layer formed over the lower surface and developed an imbedded easterly drainage flow. By 2 h after sunset, the transition period was nearly complete and a quasi-steady structure appeared which lasted until late at night. The surface cooling rate was strong enough in the early evening to maintain a  $1-3 \text{ m s}^{-1}$  drainage and elevated easterly cold thermal flow over the sloping plain. As a result, vertical wind shear between the layers of easterly and westerly flow enhanced the upward diffusion of cold air in the inversion layer to form a less stable, quasi-isothermal transition layer ( $\partial\theta/\partial z \approx 0.01 \text{ K m}^{-1}$ ). This layer was initially less than 100 m deep, but continued to grow through the night, despite the weakening of the surface inversion and easterly winds in the last several hours before sunrise. By sunrise, the reduced surface cooling rate and diffusion of the inversion layer resulted in a less distinct stable layer structure with a top near 500 m above the reference level. The easterly thermal circulations were maintained by the weak pressure gradient produced by the cooling of the elevated terrain to the east.

After sunrise, a shallow CBL formed along the surface with a westerly warm thermal wind, while the overlying easterlies persisted in the stable layer for 1-2 h. The CBL depth increased with distance eastward, as would be expected considering the reduction in stability with elevation. As a result, the CBL first became recoupled with the overlying neutral layer over the high plateau and steep slope. As the morning progressed, the CBL continued to grow over the lower elevations and the edge of the stable air mass slowly receded westward toward lower

the overlying air. There were two primary causes for this problem. First, the vertical grid resolution was too coarse to properly describe the very small scale processes which dominate the dynamics in strongly stable layers. Secondly, unlike real topography, the western boundary condition prevented the proper continuation of the low-level easterly flow. This problem was not very severe in the first several hours after model sunset when the pooling was confined principally to the flat plain on the western edge of the domain and did not significantly affect the simulated structure over the elevated terrain.

The coarse vertical resolution near the surface also prevented a detailed reproduction of surface-based slope wind layers which are frequently only several meter thick. However, the bulk effects of the flow layers were adequately simulated. For example, the total potential temperature deficit and mass flow in the simulated flow layers are consistent with the structures observed in the field experiments. A finer vertical grid resolution would provide a more detailed simulated structure, but this information would be superfluous unless a more detailed representation of the topography, including small scale valleys, hills and depressions, was also put into the model. Since the investigation focuses primarily on the larger mesoscale boundary layer structure, greater resolution was unnecessary. This would not be the case if one attempted to simulate the very small scale slope flows or possibly even the valley scale winds modeled by McNider and Pielke (1984).

The diurnal cycle simulation defined several stages of the mesoscale boundary structure as the diurnal evolution continued. The solution started from an afternoon steady-state with a deep surface based neutral

to near  $11 \text{ m s}^{-1}$  at 225 m. A small easterly component is present at 425 m, showing the greater depth of the thermal circulation in this simulation than in the others.

#### D. Analysis of Numerical Model Results

In order to properly use the results of the numerical modeling experiments to better understand simulated atmospheric processes, one must determine the limits and conditions for which the results are valid. Conversely, it is just as important to be able to identify unrealistic properties in the model solutions which exist due to either the assumptions made in the model formulation or by the improper treatment of spatially and temporally continuous atmospheric phenomena by the finite difference scheme. Based on these considerations, the level of "realism" in the model solutions must be ascertained. This task is more easily facilitated if past results of modeling and observational programs are used as aids in the analysis. Using these guidelines, analysis of the model results in this study greatly enhanced the knowledge of the processes contributing to the development of the mesoscale boundary layer in western Colorado.

From the sensitivity studies, it was determined that vertical wind shear was important in the development of the mesoscale NBL. Without its presence, the model was unable to properly simulate the boundary layer evolution. Another problem found in the model solutions was the pooling of cold air in the lowest layers overlying the flat plain and lower section of the sloping plain. Once the cold air collected in these lower elevation regions, stability prevented any vertical mixing of the air and the parameterized surface cooling became decoupled from

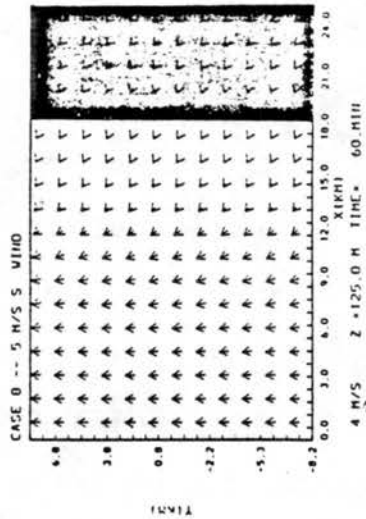
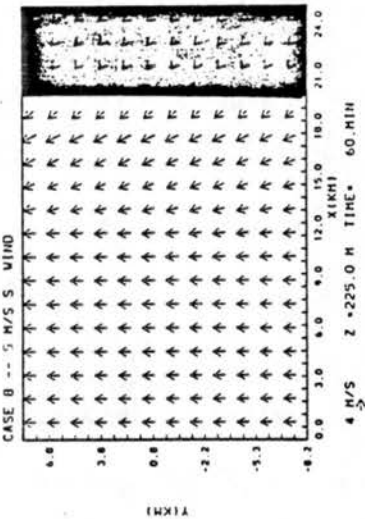
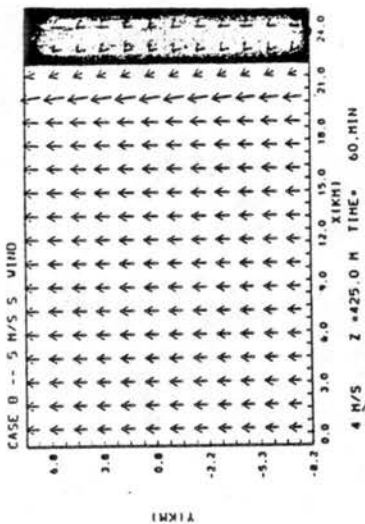
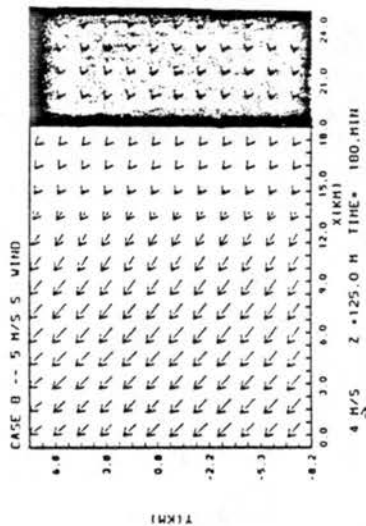
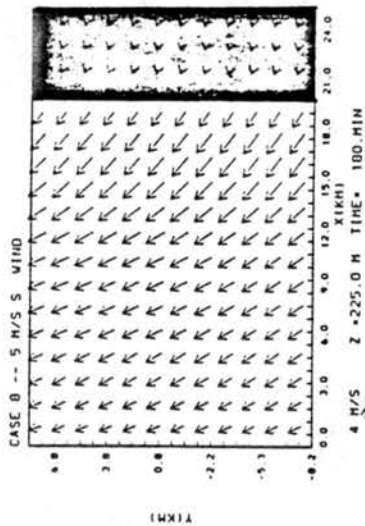
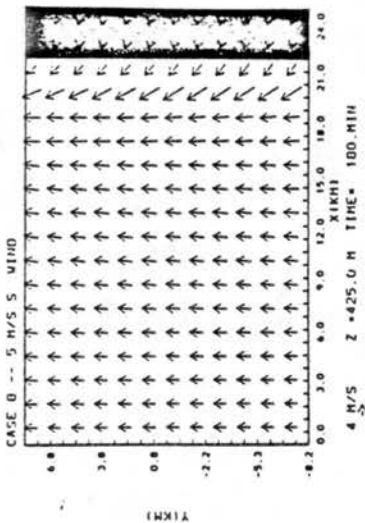
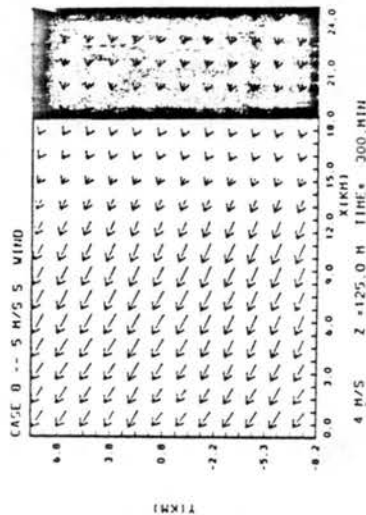
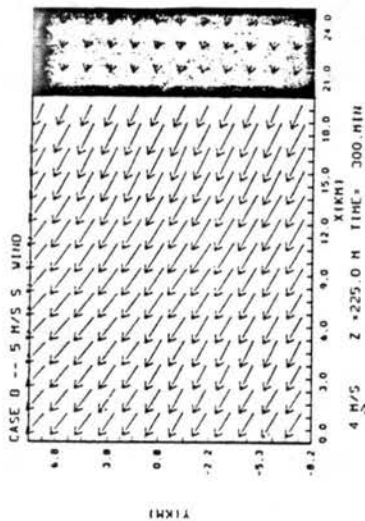
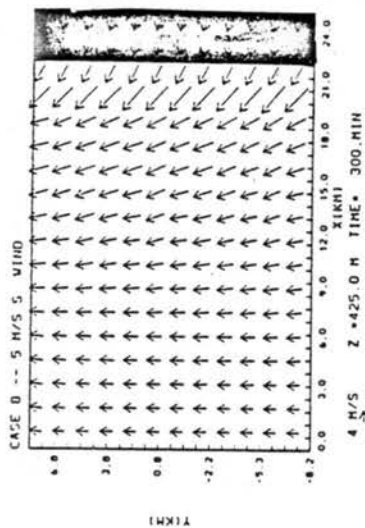
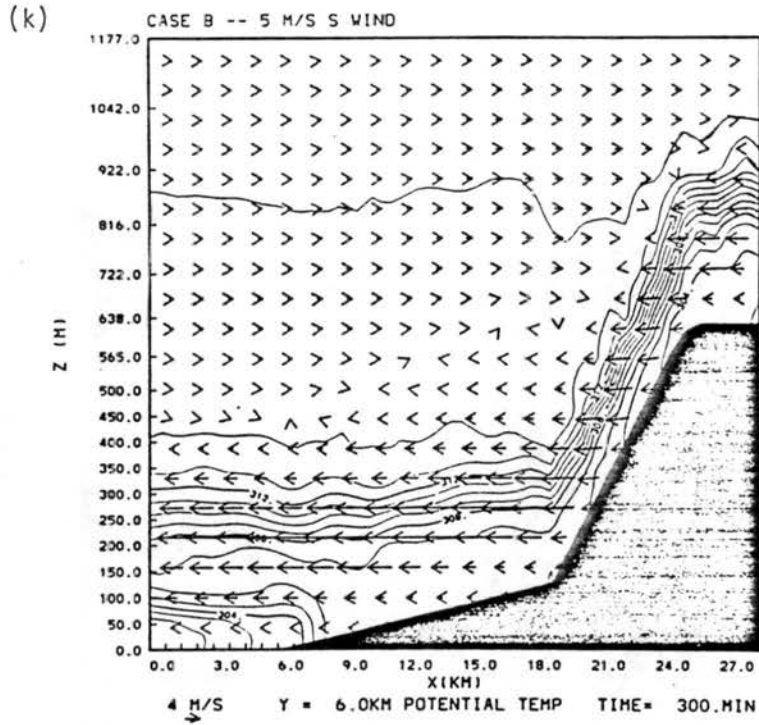


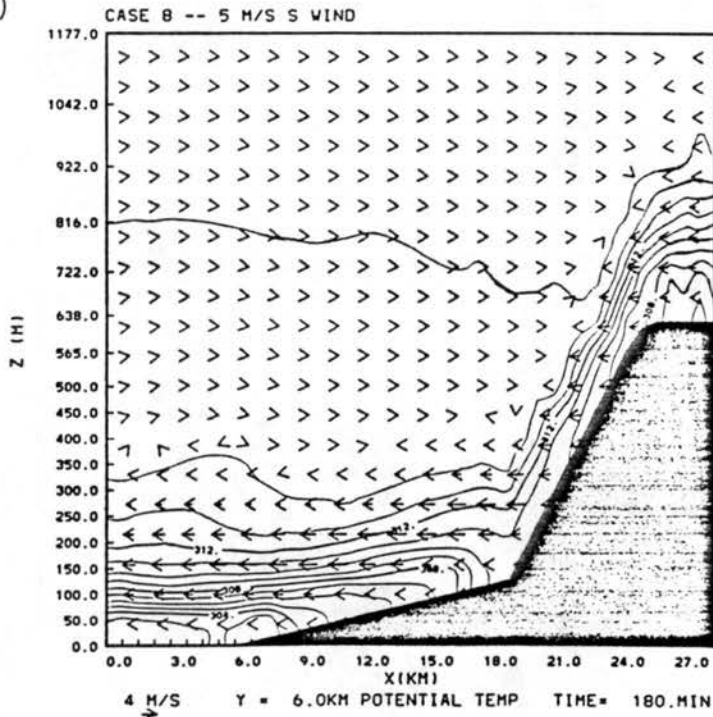
Figure 54. Case 8 horizontal wind fields.

pressure gradient resulting from the small slope of the inversion layer over the low-lying elevations combined with the larger scale temperature contrast to produce a  $9.0-11.0 \text{ m s}^{-1}$  east-southeast jet from 125 m to 275 m above the reference level. Above this level, higher momentum air near the barrier was rapidly diffused as it flowed into the elevated mixed layer in the western region of the domain. Southerly component speeds were still very steady, increasing  $0.3-0.5 \text{ m s}^{-1}$  in the previous hour. As was found over the low plains, drainage and shear weakened the near-surface stability over the high plateau. A broad subsidence region was present in the lowest 350 m AGL from  $x = 20.0 \text{ km}$  to  $x = 23.0 \text{ km}$  with speeds averaging  $0.2-0.3 \text{ m s}^{-1}$ . Also apparent at this time was the development of a  $1.0-1.2 \text{ m s}^{-1}$  return flow between 600 m and 800 m above the reference level.

Figure 54 shows the horizontal cross-sections at 125 m, 225 m and 425 m above the model reference level 1 h, 3 h and 5 h after sunset for Case 8. After 1 h the only thermal effects evident in the wind fields are over the more elevated terrain where the cross-section height approaches the surface elevation. By 3 h after sunset, a strong  $2-4 \text{ m s}^{-1}$  easterly thermal component develops through the transition layer, as can be seen in the 125 m and 225 m sections. At 425 m the winds remain southerly at  $5-6 \text{ m s}^{-1}$  and are unaffected by the cooling except over the eastern portion where the cross-section intersects the stable layer. The 3 h cross-sections also give a good depiction of the strong vertical wind shear which provides the turbulent energy necessary to extend the stable layer higher into the atmosphere. The strong jet which develops in the elevated stable layer appears in the 5 h cross-sections. The  $8-9 \text{ m s}^{-1}$  southeast winds present at 125 m increased in strength with height



(g)



(h)

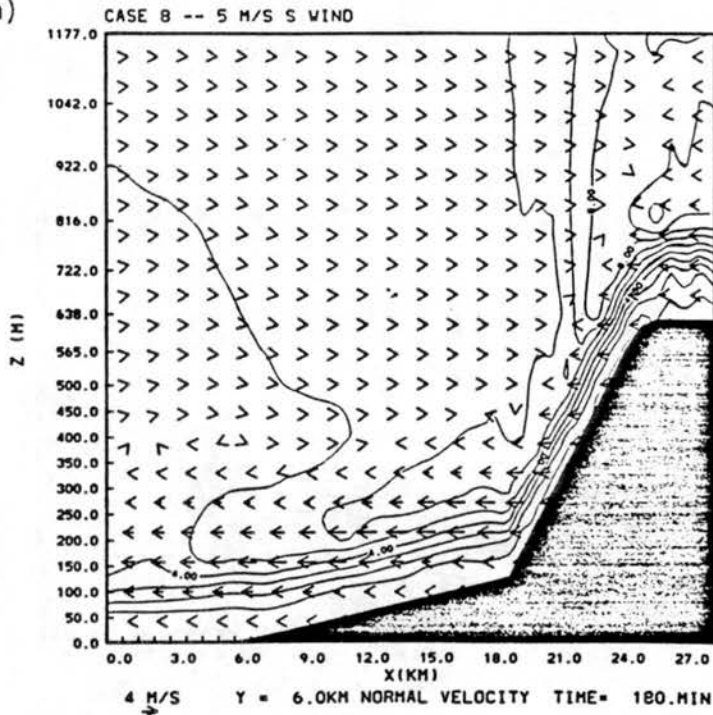


Figure 53. Case 8 fields. Vectors -  $u$  velocity component for (g) sunset + 3 h potential temperature (contour interval - 1 K) and (h) sunset + 3 h  $v$ -velocity component (contour interval - 1  $\text{m s}^{-1}$ ).

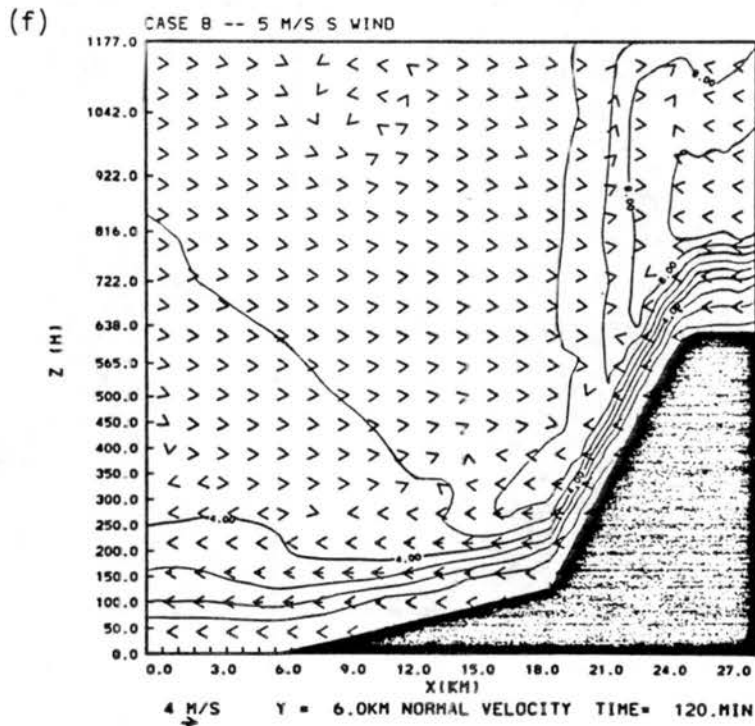
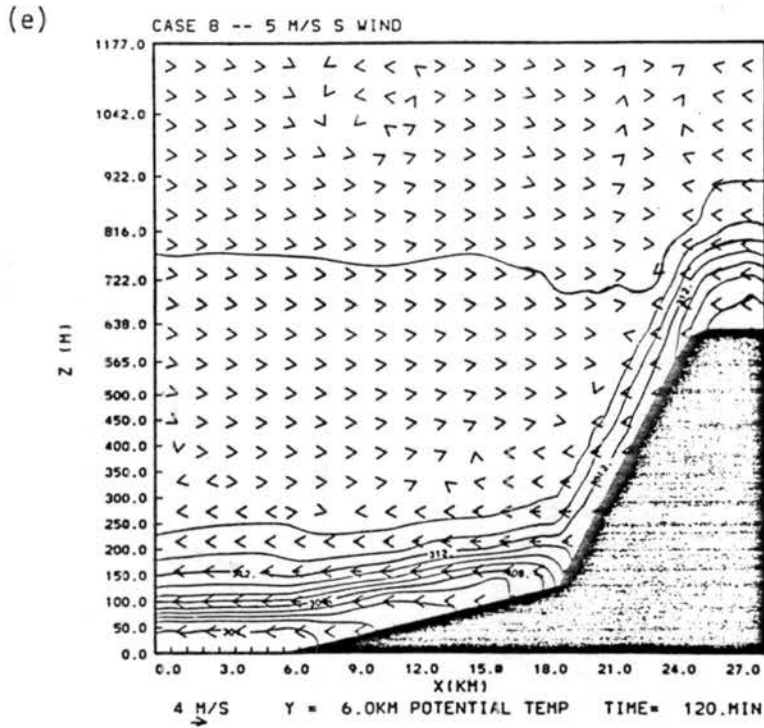


Figure 53. Case 8 fields. Vectors -  $u$  velocity component for (e) sunset + 2 h potential temperature (contour interval - 1 K) and (f) sunset + 2 h  $v$ -velocity component (contour interval - 1  $\text{m s}^{-1}$ ).

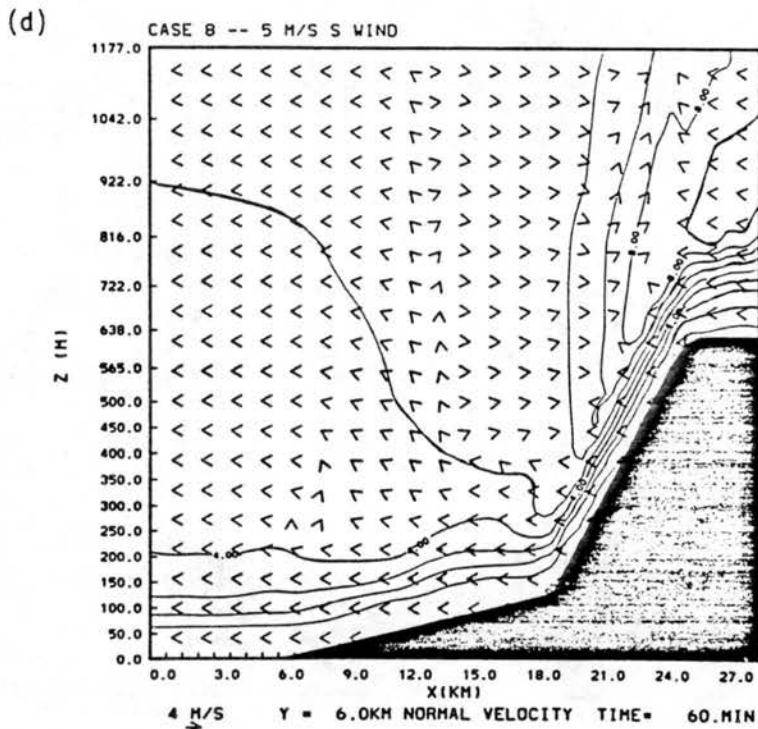
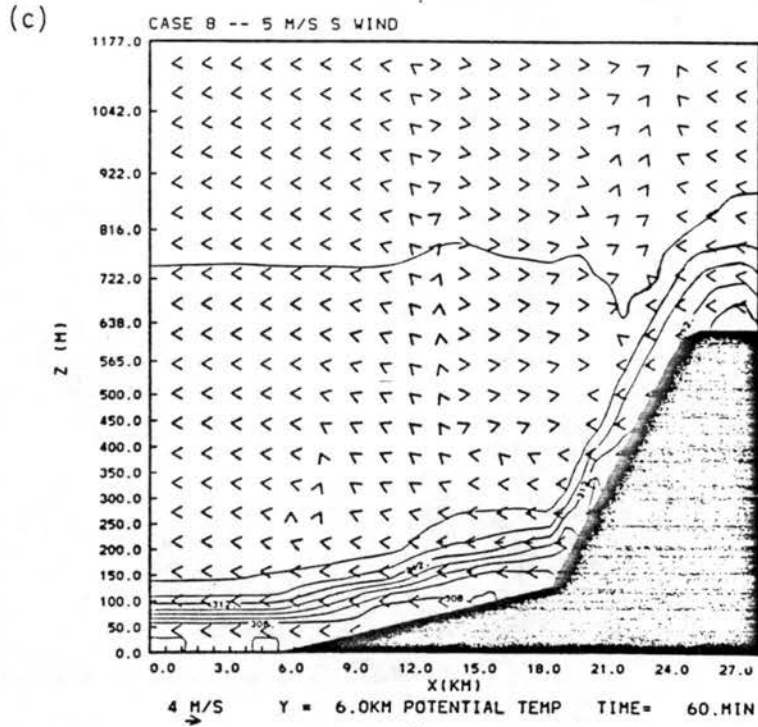


Figure 53. Case 8 fields. Vectors -  $u$  velocity component for (c) sunset + 1 h potential temperature (contour interval - 1 K) and (d) sunset + 1 h  $v$ -velocity component (contour interval -  $1 \text{ m s}^{-1}$ ).

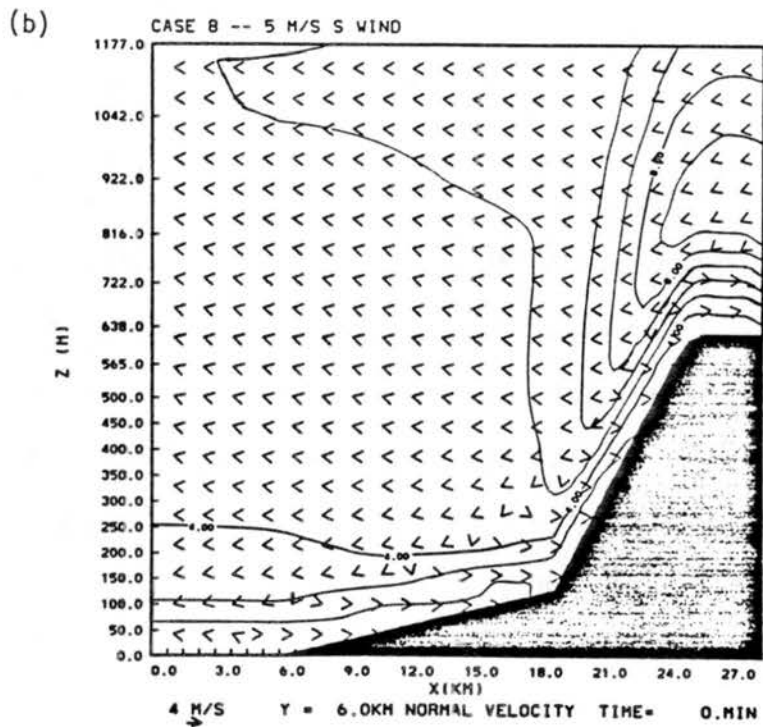
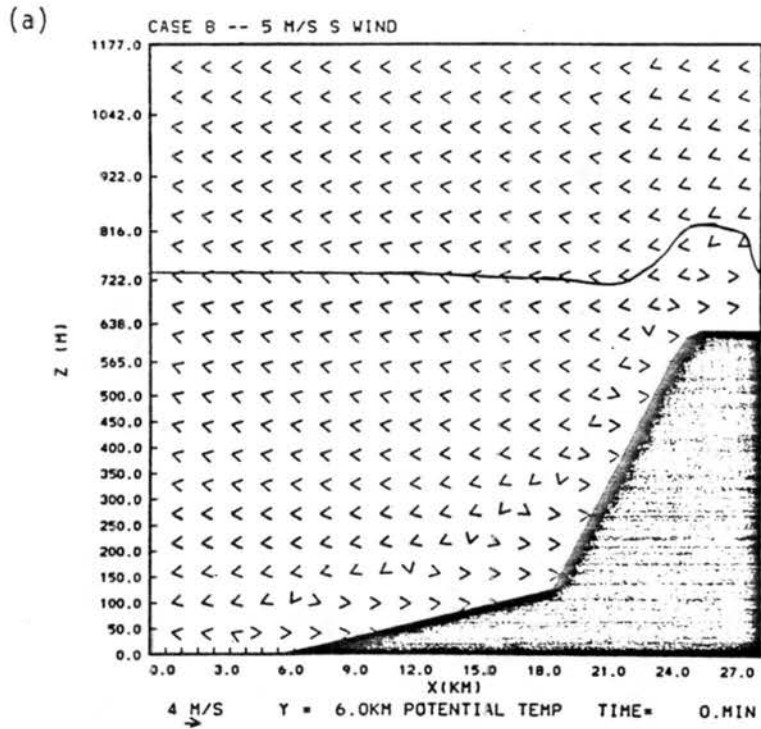


Figure 53. Case 8 fields. Vectors -  $u$  velocity component for (a) sunset potential temperature (contour interval - 1 K) and (b) sunset  $v$ -velocity component (contour interval -  $1 \text{ m s}^{-1}$ ).

south component wind speeds remained relatively steady, but the continued strengthening of the easterly thermal circulation produced a strong  $8.0\text{-}9.0\text{ m s}^{-1}$  southeast flow at the top of the surface inversion layer. At higher elevations, the predominantly southerly flow over the western half of the domain intensified and turned southeasterly near the barrier. One hour later (Figures 53i and 53j), the thermal structure was altered by the low level flow. East wind components with speeds between  $5.0\text{ m s}^{-1}$  and  $7.0\text{ m s}^{-1}$  were present through a 100 m deep layer between 150 m and 250 m above the reference level over the lower terrain. Cold air advection resulting from the strong flow and the small slope at the top of the surface inversion layer, produced an elevated inversion layer over the flat plain. Because of the reduced surface cooling rate, winds in the lowest 100 m over the lower elevations were relatively weak from the southeast with speeds of  $1.0\text{-}2.0\text{ m s}^{-1}$ . Consequently, the colder surface air drained westward toward the lower elevations and the low level stability over the upper section of the sloping plain and the higher terrain to the east was reduced.

Quasi-steady structure was achieved by 5 h after sunset (Figures 53k and 53l). The elevated inversion layer reached 325 m above the reference level and extended to the surface only over the flat plain. Over the sloping plain, the southeasterly drainage, weak cooling and large vertical wind shear produced a 125 m deep neutral layer. Over the steep slope, a strong horizontal potential temperature gradient responsible for the acceleration of the easterly wind component was very evident. A weak surface based stable layer was still present over the steeper slope. As the air drained onto the sloping plain, it was quickly mixed through the near-neutral layer over the surface. The

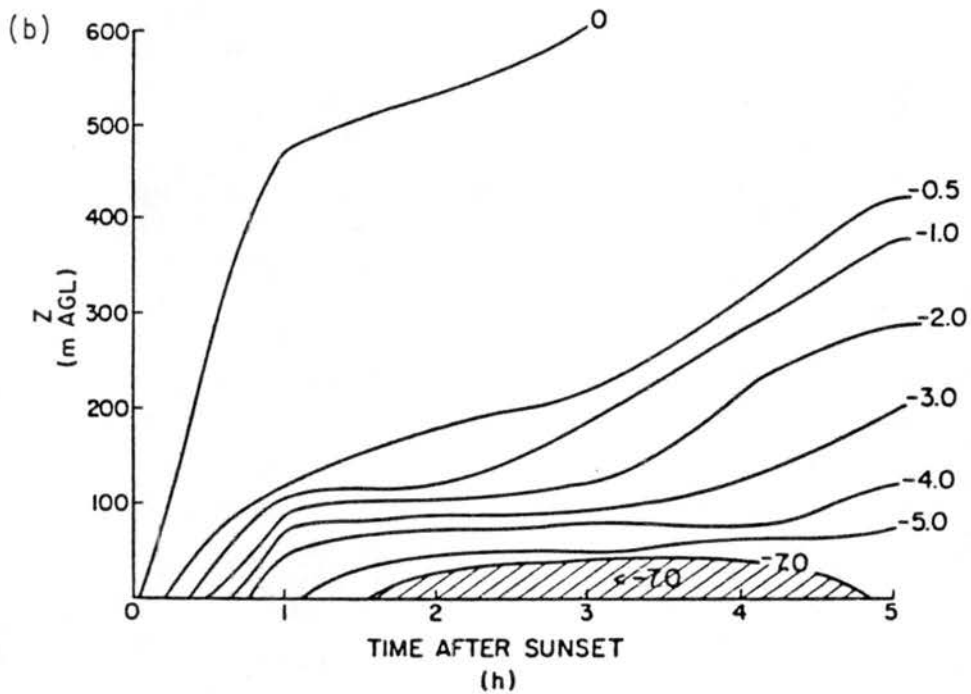
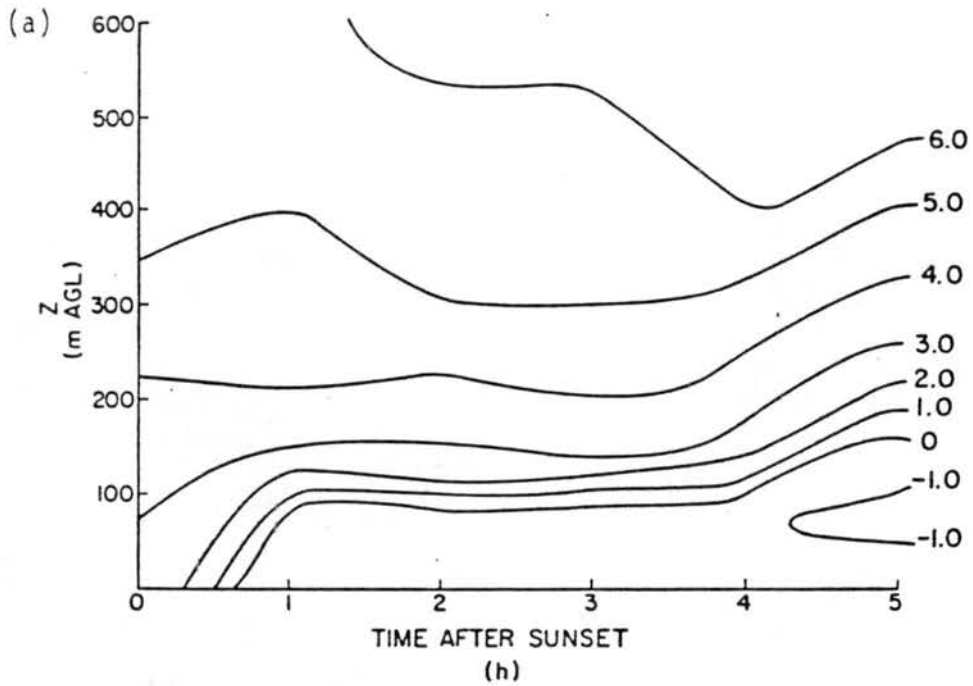


Figure 57. Time-height cross-sections at  $x = 15$  km of (a)  $u$  velocity component and (b) potential temperature deviations for Case 5.

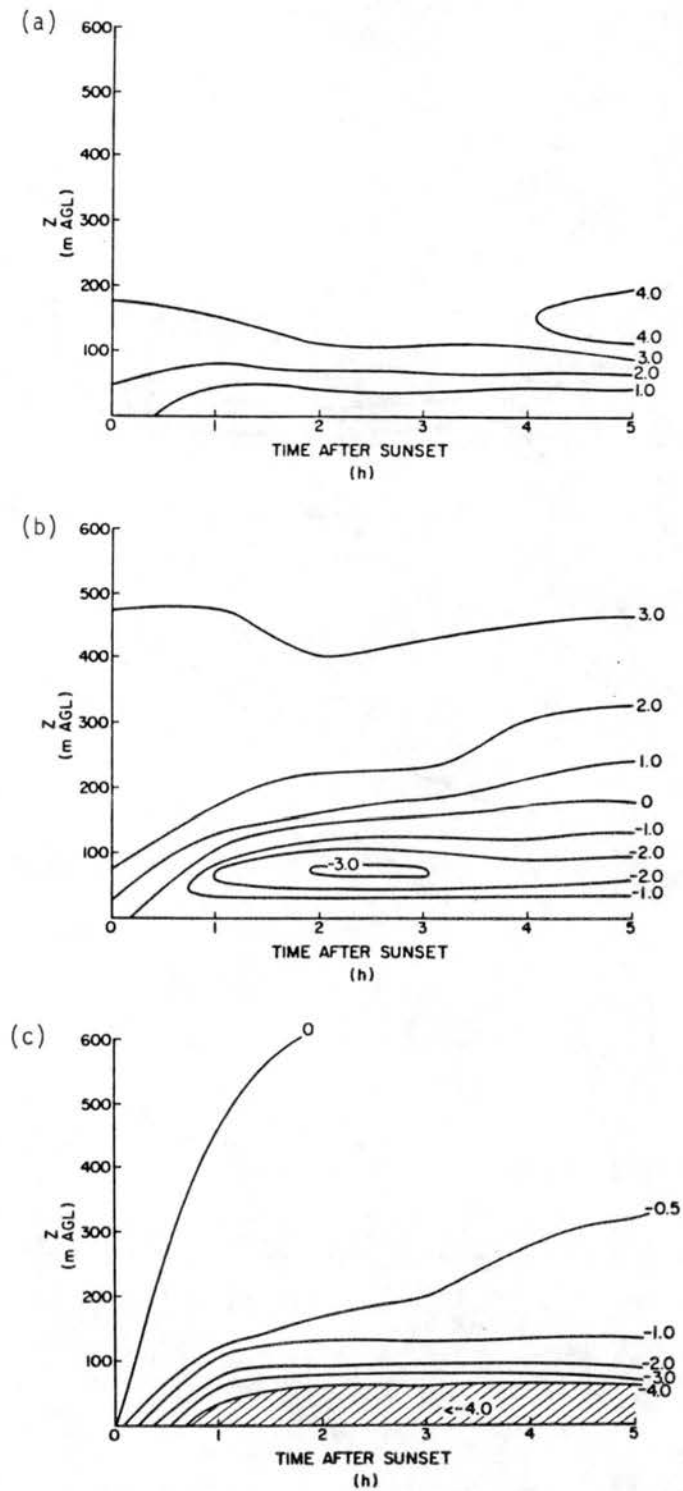


Figure 58. Time-height cross-sections at  $x = 15$  km of (a)  $v$  velocity component, (b)  $u$  velocity component and (c) potential temperature deviations for Case 7.

southerly component remained very steady, increasing in speed slightly as the effective surface friction was reduced by the inversion layer. It appeared from these results that the total NBL depth scaled with the geostrophic wind speed, like idealized boundary layers over flat terrain. However, the surface inversion depth and easterly wind speeds scaled with the into the barrier component of the geostrophic wind. The determination of the exact relationship requires more information, but the relation  $h_s \propto u_0^{0.5}$  implied from (3) agrees well with the three cases presented here.

The Case 6 simulation, which was initiated with a much more shallow neutral layer depth, had a boundary layer structure approximating the winter conditions encountered during the CSU 84 field experiment. The development of the simulated structure shown by the time-height cross sections in Figure 59 show good agreement with observations taken at the Rifle site, which was located slightly upwind of the barrier, in a similar location to the model "sounding site" at  $x = 15.0$  km. In this simulation, the mixed layer present at sunset was completely destroyed in the first several hours after sunset and the simulated NBL was difficult to discern from the overlying free atmosphere. One indication of the vertical extent of the surface influence was the height to which surface cooling extended, 400 m AGL in this case. Corresponding to the 400 m deep cooled layer was the deep blocked flow region present 5 h after sunset. The CSU 84 data show that the boundary layer was already stably stratified through its depth at sunset. The air continued to cool 0-2 K through a 500-900 m deep layer above the valley ridgetop despite the synoptic scale weak warm air advection. Winds were blocked

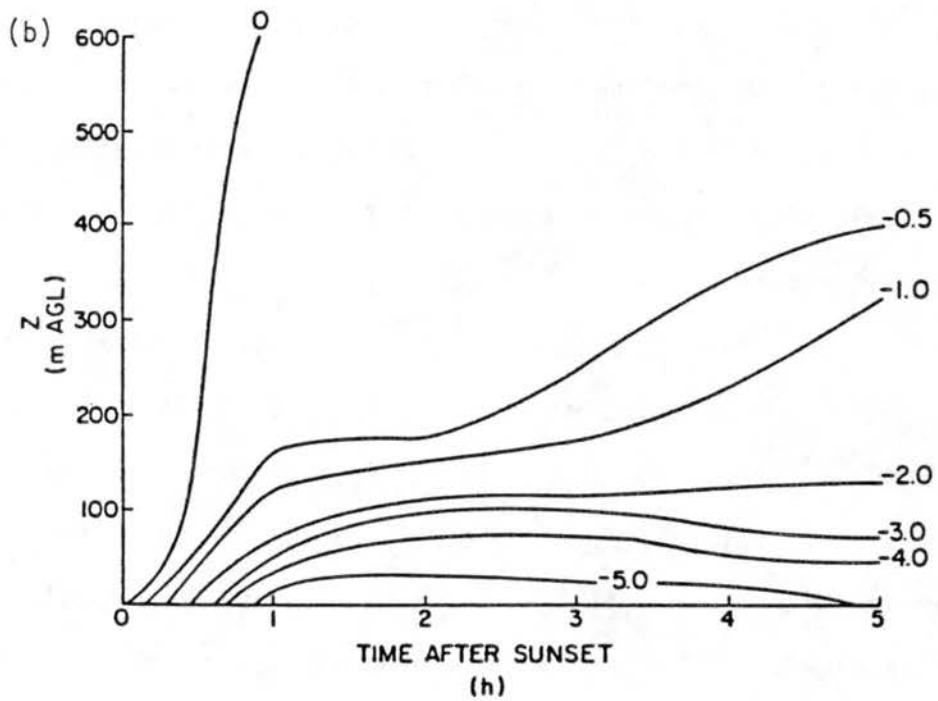
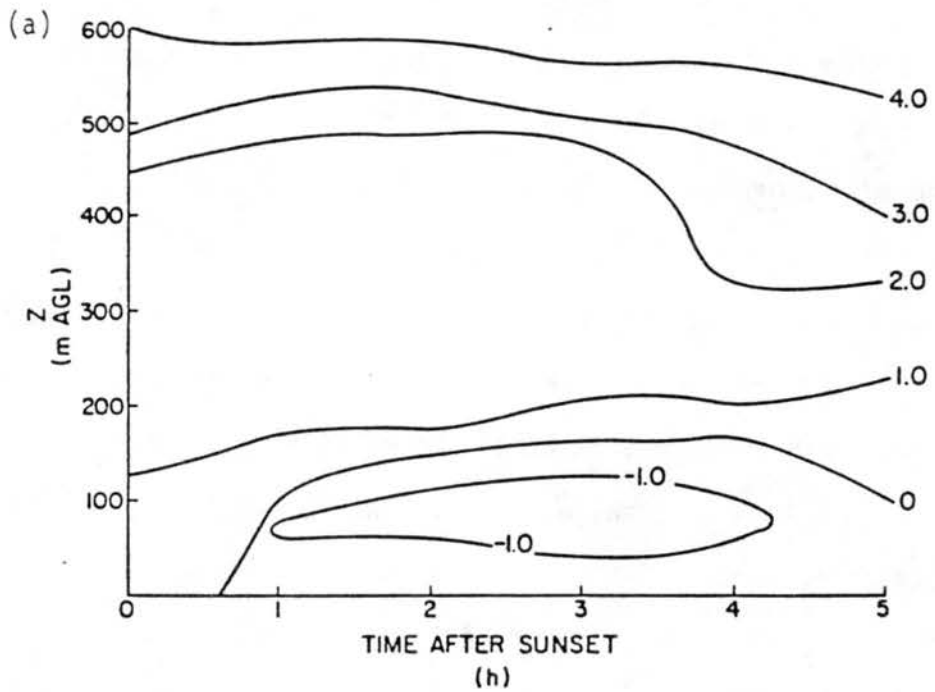


Figure 59. Time-height cross-sections at  $x = 15$  km of (a)  $u$  velocity component and (b) potential temperature for Case 6.

through the cooled boundary layer in the same way as those produced by the model simulation.

The south geostrophic wind case (Case 8) was the only simulation in which the prevailing synoptic scale wind did not oppose the easterly thermal and drainage flows. As a result, the simulated boundary layer structure differed significantly from that found in the other numerical experiments. Figure 60 shows time height cross-sections of potential temperature deviations and both wind components in a column above  $x = 15.0$  km. A very strong easterly  $7-9 \text{ m s}^{-1}$  jet formed between 100 m AGL and 200 m AGL over the lower terrain in response to the thermal pressure gradient formed at the top of the surface inversion layer. Significant easterly winds extended as deep as 400 m AGL and the resulting cold air advection helped form an elevated inversion layer over the eastern half of the domain. The total depth of the NBL was 100 m greater, than in the reference case. The advective influence revealed in this simulation limits the aforementioned NBL depth-wind speed relationships to those situations in which there is a significant barrier normal wind component to inhibit thermal advection in the topographically induced circulations. Another feature present in this solution which was absent in the other cases was the development of a complete mountain-plain circulation cell. Subsidence was present over the high plateau and steep slope to the east and a well developed return flow was apparent above the plateau elevation.

The observations taken during the ASCOT 82 experiment can be explained to a large degree by using the results of the Cases 7 and 8 simulations. Case 8 was the only simulation in which there was no geostrophic wind component into the barrier, as was observed during the

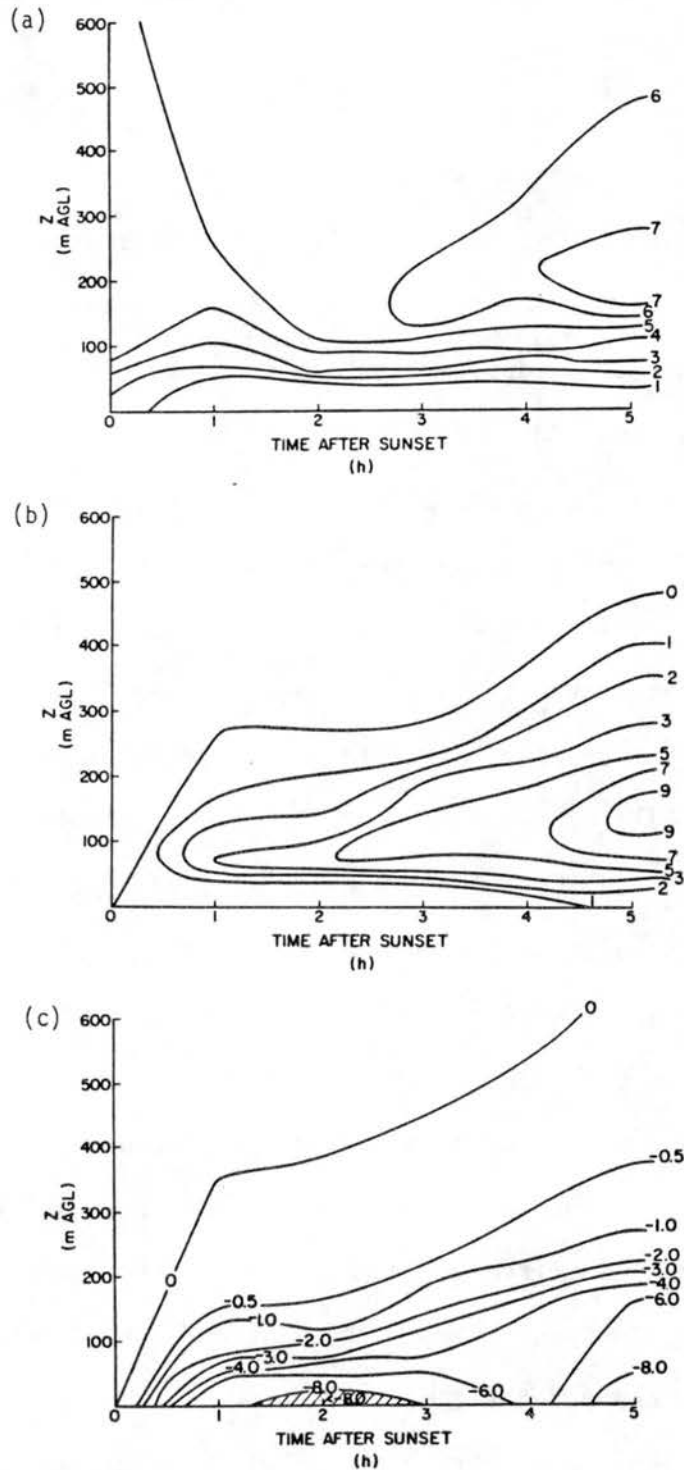


Figure 60. Time-height cross-sections at  $x=15$  km of (a)  $v$  velocity component, (b)  $-u$  velocity component and (c) potential temperature deviations for Case 8.

early part of the experimental night. The observational data revealed an apparent 300 m descent of the mixed layer top before the geostrophic wind shifted to provide a small component into the barrier. The descending branch of the mountain-plain circulation produced by the model resulted in subsidence rates of  $0.1-0.2 \text{ m s}^{-1}$  above the high terrain 3 h after sunset. This is more rapid than was actually observed, but not so much different as to discount this effect in the analysis of the field data. Also, the formation of the elevated inversion was not seen in the observations and the strength of the observed thermally forced winds was much less than those produced by the model. These features most probably result from the overly uniform topography in the model.

Following the late night shift from northeasterly to northwesterly geostrophic flow, the observed boundary layer evolution paralleled that in the Case 7 simulation. The large scale subsidence ceased and 0-3 K cooling occurred above ridgetop as the wind shear mixed the cold air vertically. Although the wind data from the field experiments are not complete, they do show mesoscale easterly  $3-5 \text{ m s}^{-1}$  thermal component in the NBL above ridgetop, like that produced by the model. Based upon these analyses of the model results and comparisons of observational and model data, a conceptual model of mesoscale boundary layer evolution has been formulated and is presented in the succeeding chapter.

## CHAPTER V

### CONCEPTUAL MODEL OF MESOSCALE BOUNDARY LAYER EVOLUTION

A generalized conceptual model of the diurnal evolution of the mesoscale boundary layer can be constructed from the results of the observational and numerical modeling programs. For this purpose, only the simplest case of ideal boundary layer evolution upwind of a high mountain barrier is considered. The underlying terrain is generally smooth compared to the scale of the regional circulations and the synoptic scale wind and thermal fields are stationary and barotropic. Although these conditions are unrealistic, they do form the simplest base state from which the general characteristics of mesoscale boundary layer development can be described.

Starting at sunset (Figure 61a), the boundary layer is neutrally stratified to a depth well above the top of the elevated terrain. The initial winds have a significant component (greater than  $3 \text{ m s}^{-1}$ ) into the barrier and are well mixed through the boundary layer. After the initiation of surface cooling, the lower layers over the surface start to stabilize, marking the onset of the evening transition period. As the cooling proceeds, a shallow drainage flow with speeds of  $0.5\text{-}2 \text{ m s}^{-1}$  develops over the sloping surfaces which opposes the overlying flow. During this period, drainage flows also become established in the lower creek and river valleys as some of the cooled air at slides off the mesas. Toward the end of the transition period 1-3 h after sunset, a 75-150 m deep surface inversion layer has developed over the region with

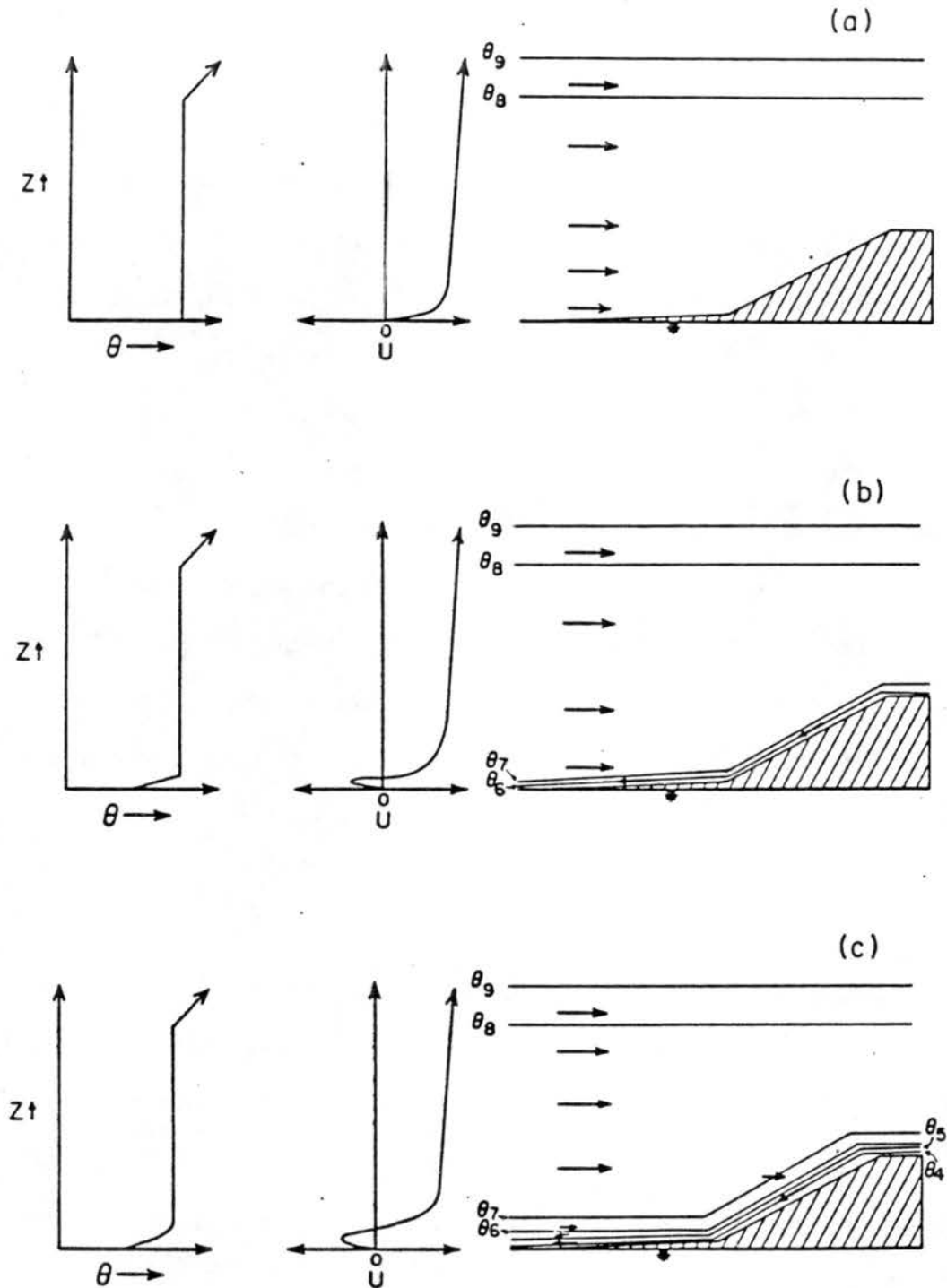


Figure 61. Idealized mesoscale boundary layer evolution for (a) sunset state, (b) end of evening transition period, 1-3 h after sunset and (c) early evening, 5-7 h after sunset.

the larger scale cold thermal circulation beginning to appear over the low-level drainage circulations (Figure 61b).

Shear induced mixing builds a shallow, quasi-isothermal transition layer over a more stable surface inversion ( $\partial\theta/\partial z \approx 0.02 \text{ K m}^{-1}$ ) once a near steady structure is achieved in the lower layers (Figure 61c). As the evening progresses, this layer continues to grow, while in the lower layers, the cold thermal flow slowly intensifies to speeds over  $3 \text{ m s}^{-1}$ , resulting in the late night structure appearing in Figure 61d. The large shear in the transition layer continues to mix the colder inversion air deeper into the overlying neutral layer. Late at night, however, the surface cooling rate driving the NBL development decreases substantially and the cold thermal winds weaken to  $1\text{-}3 \text{ m s}^{-1}$ . By sunrise (Figure 61e), the inversion and transition layers have merged smoothly into a deep surface-based stable layer with a continuously decreasing lapse rate with height. This layer typically extends 300-500 m above the mesa elevations and contains the weak cold thermal circulation.

After sunrise, surface heating starts to form a shallow CBL containing warm thermal winds under the nocturnal stable layer. The CBL depth increases with surface elevation since the stability (from the remnants of the nocturnal layer) weakens with height. By mid-morning, the boundary layer structure resembles Figure 61f. Remnants of the cold thermal winds are still present in the elevated stable layer while the CBL warm thermal winds are flowing in the opposite direction with speeds of  $1\text{-}3 \text{ m s}^{-1}$ . As the morning progresses, the heating intensifies so that the stable layer is removed first over the higher terrain when the CBL merges with the neutral layer aloft (Figure 61g). The winds are

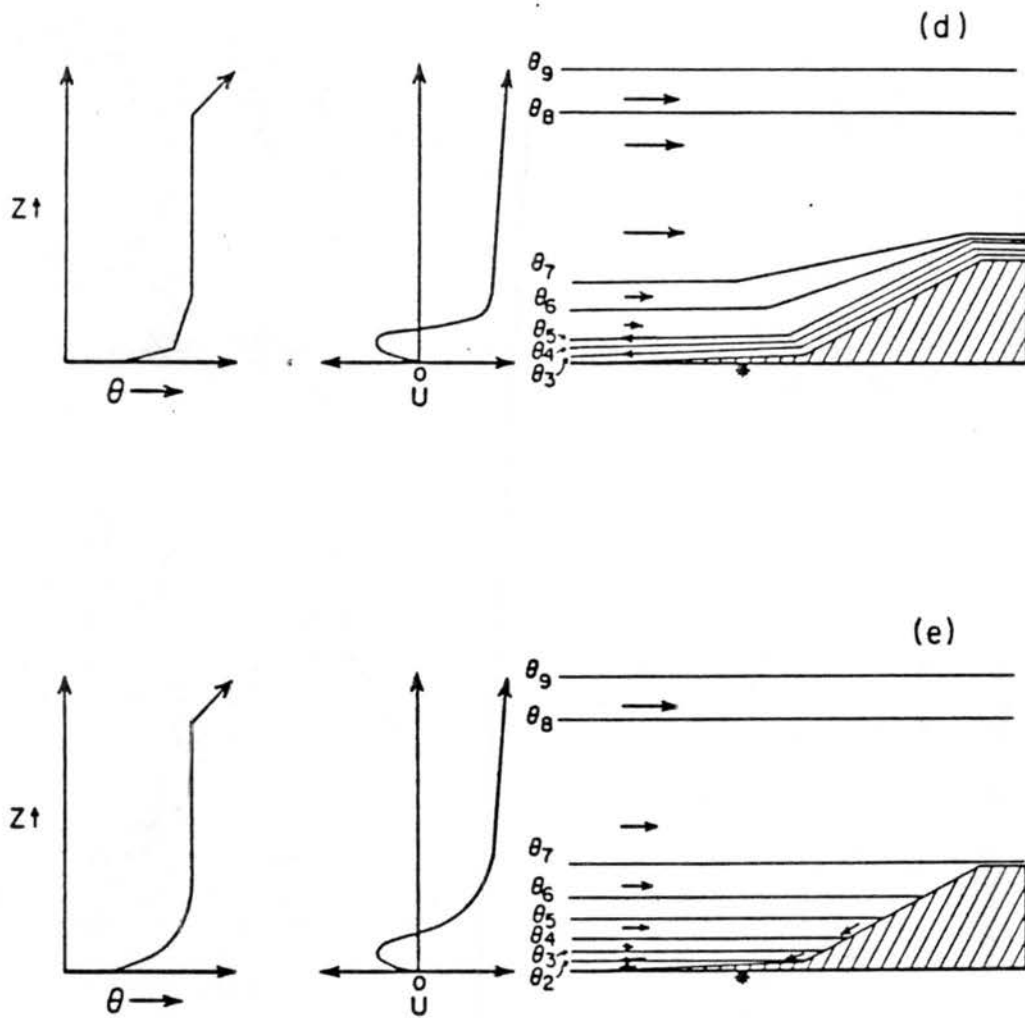


Figure 61. Idealized mesoscale boundary layer evolution for (d) late night steady state, 8-10 h after sunset and (e) sunrise state.

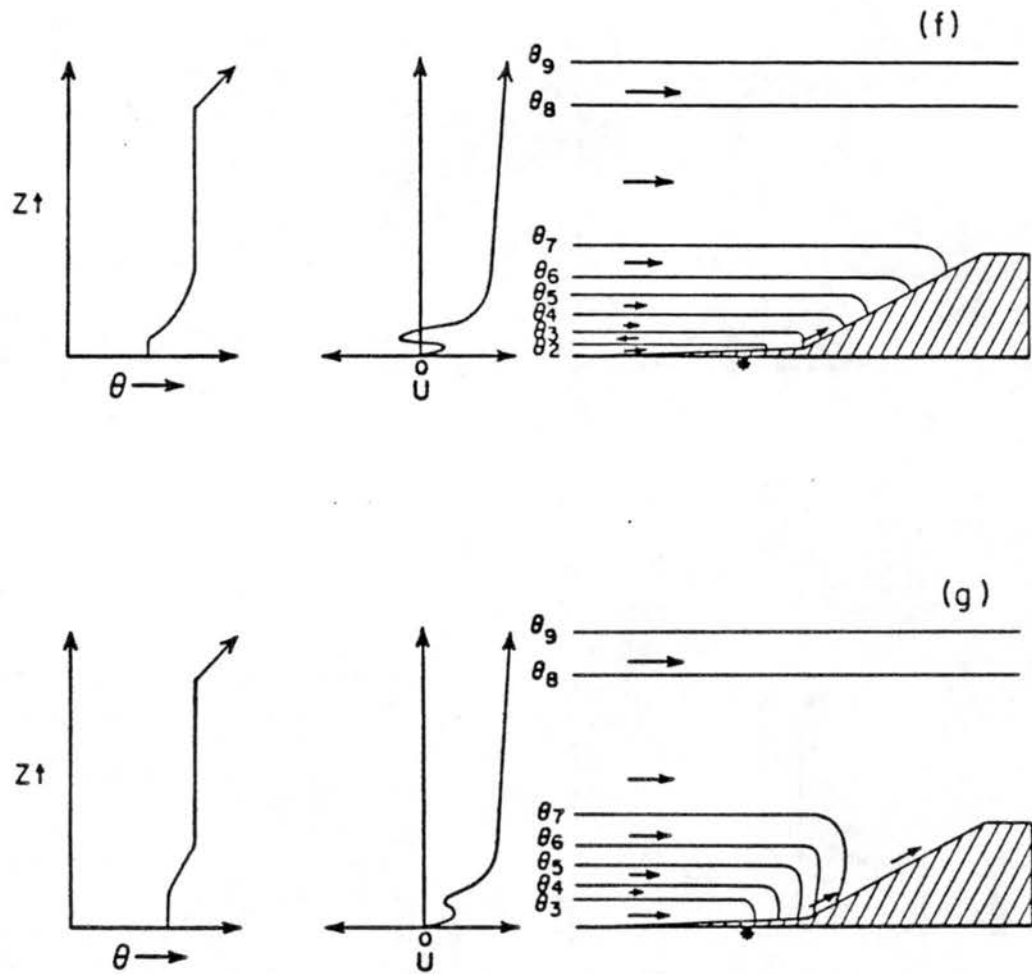


Figure 61. Idealized mesoscale boundary layer evolution for (f) early morning, 2-3 h after sunrise and (g) late morning, 5-6 h after sunrise.

uniform in direction, but the profile shows a speed minimum near  $1 \text{ m s}^{-1}$  in the elevated stable layer. The edge of the stable air layer slowly recedes toward the lower elevations as the CBL continues to grow above the higher terrain. By the end of the morning transition period near midday, the stable layer is completely destroyed and the boundary layer has again attained the steady daytime structure shown in Figure 61a.

The simplified conceptual model cannot account for all of the observed and modeled variability of mesoscale boundary layer evolution. This is particularly true of the cases in which the sunset mixed layer depth does not exceed the height of the downwind barrier. In that situation, a blocked flow layer develops and a steady-state structure is never achieved. However, the dominant boundary layer dynamical mechanisms responsible for the boundary layer evolution in these cases are present in the conceptual model. Specifically, the growth of the surface-based stable layer at night through shear induced mixing and the development of decoupled wind layers are important in all of the observed and modeled cases.

## CHAPTER VI

### CONCLUSIONS AND SUGGESTIONS FOR FUTURE RESEARCH

#### A. Conclusions from Research

Evidence has been presented from both field observations and numerical model results documenting the diurnal evolution of a mesoscale (~50 km) boundary layer in mountainous terrain. Emphasis was placed on the formation and destruction of a 300-500 m deep nocturnal stable layer over sloping terrain upwind of a high mountain barrier. This layer cools 1-4°C in the first 3-5 h after sunset and separates the larger synoptic scale flow field from the small scale circulations in the underlying river and creek valleys. The layer grows slowly from turbulent mixing of cold air upward due to the shear between the topographically induced circulations and the overlying flow field. Destruction of the layer is accomplished by a growing convective boundary layer above the surface in the first several hours after sunrise.

Observational data from the two field experiments executed in western Colorado show that the boundary layer evolution can exhibit wide variability with season and location, but both cases contain similarities as well. In the ASCOT 82 summer case, relationships among the geostrophic wind direction, the mesoscale boundary layer structure and the valley wind structure were seen. When the prevailing wind direction had no component into the barrier, the growth of the mesoscale

nocturnal boundary layer was inhibited by the descending branch of the mountain plain circulation, resulting in a 300 m subsidence in the first 6-8 h after sunset and a slight 1-2 K cooling in the 200 m deep layer above ridgetop. At the same time, a very strong valley wind developed with peak speeds over  $6 \text{ m s}^{-1}$ . After the wind shifted slightly to provide a component into the barrier, the strong subsidence was halted by the upwind convergence of the large scale flow. After this time, the NBL deepened to 500 m above the ridgetop height and cooled over 3 K in the 200 m deep layer immediately above the Roan Plateau. The valley winds weakened to less than  $4 \text{ m s}^{-1}$  following the synoptic wind shift and the valley layer stability simultaneously increased. The CSU 84 observations also showed a deep cooling above the ridgetop elevation, but exhibited other characteristics which are representative of the winter seasonal effects. The stronger synoptic scale winds and inhibited daytime mixed layer development resulted in the formation of a deep surface-based stable layer extending into the free atmosphere. At the Rifle site, the winds below the level of the high barrier to the east were blocked, an observation not made at the other sites. While the winds above the blocking elevation remained westerly with speeds over  $5 \text{ m s}^{-1}$ , the flow below this level was predominantly southerly with speeds near  $2 \text{ m s}^{-1}$ . The extent of cooling above the ridgetop also varied with location from a 2 K advective warming observed at Ca to a 1 K cooling observed at Rifle despite the large scale warm advection.

Results from the numerical model experiments provided insight into the physical processes responsible for the observed nocturnal boundary layer evolution and offered possible explanations for the observed variability. Vertical diffusion of cold air was found to be the primary

mechanism by which the nocturnal boundary layer deepened. Therefore, it is necessary for a synoptic scale wind field to be present in the model for the proper simulation of nocturnal boundary layer formation. In the simulations, the development of a surface inversion in the first 1-2 h after sunset led to the formation of a 1-3 m s<sup>-1</sup> cold thermal flow away from the barrier. The shear between these flows and the synoptic scale wind field resulted in the late night development of a 300-500 m deep quasi-isothermal transition layer overlying a 75-125 m deep surface inversion ( $\partial\theta/\partial z \approx 0.02 \text{ K m}^{-1}$ ). Stronger synoptic winds produce deeper nocturnal layers and more shallow sunset neutral layers depth result in the merging of the stable nocturnal boundary layer with the overlying free atmosphere. In all cases in which the initial mixed layer was deep and there was a wind component into the barrier, the total magnitude of the wind speed change was 4-5 m s<sup>-1</sup>. The absence of an into the barrier wind component leads to the formation of a 500 m deep topographically induced cold thermal circulation with maximum speeds over 7 m s<sup>-1</sup>. Daytime destruction of the nocturnal boundary layer results from the growth of a turbulent, surface-based convective boundary layer under the stable airmass. The layer is first destroyed over the elevated terrain as the cold thermal circulations flowing away from the barrier are replaced by warm thermal winds which move toward it. More importantly, for the first time a boundary layer model has successfully simulated the continuous diurnal evolution of meso- to meso- $\beta$  scale boundary layer over complex terrain. The conceptual model based on the results of the modeling program accounts for the primary factors contributing to the diurnal mesoscale boundary layer evolution, although its applicability is limited by the assumptions under which it was formulated.

## B. Suggestions for Future Research

Obviously, more research is necessary to understand more fully the simple concepts which have been presented in this paper. This should include more field experiments designed specifically to explore some unresolved issues such as the horizontal extent of the downwind barrier effects on the mesoscale boundary layer. Additionally, a more detailed observational data set is necessary to gain a better understanding of the morning transition period when the nocturnal stable layer is destroyed. Ideally, these field programs will include detailed surface observations and high frequency sounding data from a network of locations covering the region. They should be conducted under a variety of synoptic conditions and in all seasons. The use of radio theodolites would provide a significant improvement in both the quality and quantity of wind measurements from the rather sparse wind measurements made in this study. One such experiment was conducted in the fall of 1984 by the ASCOT program, but more are needed.

The model capability demonstrated in this study could be used to explore a variety of topics associated with mesoscale boundary layer structure. The incorporation of more realistic topographical configurations and the addition of a better surface energy budget parameterization could be used to perform case studies now that a basic understanding of regional boundary layer behavior has been achieved. The inclusion of the moist physics and atmospheric radiative transfer model parameterizations already available would enable the model to simulate a wider variety of behavior. Since the model is not bound by the hydrostatic approximation it is also ideally suited for studies of the interactions between the regional boundary layer circulations and the

local scale circulations in complex terrain. These include the details of the coupling and decoupling mechanisms between the valley and regional flow systems as well as the interrelationships between the local, mesoscale and synoptic scale features.

## REFERENCES

- Andre, J. C., and L. Mahrt, 1982: The nocturnal surface inversion and the influence of clear air radiative cooling. J. Atmos. Sci., 39, pp. 864-878.
- Arritt, R. W., and R. A. Pielke, 1984: Numerical investigations of terrain induced mesoscale circulations and pollutant transport in the Shenandoah Valley. Paper presented at the Third AMS Conference on Mountain Meteor., 16-19 October 1984, Portland, OR, pp. 1-4.
- Bader, D. C., and T. B. McKee, 1983: Dynamical model simulation of the morning boundary layer development in deep mountain valleys. J. Climate Appl. Meteor., 22, pp. 341-351.
- Bader, D. C., and T. B. McKee, 1985: Effects of shear, stability and valley characteristics on the destruction of temperature inversions. J. Climate Appl. Meteor., 24, pp. 805-815.
- Bader, D. C., T. B. McKee, and G. J. Tripoli, 1983: Three dimensional simulation of the daytime boundary layer evolution in a deep mountain valley. Preprints, AMS Sixth Symposium on Turbulence and Diffusion, 22-25 March 1983, Boston, MA, pp. 196-197.
- Baines, P. G., 1984: A unified description of two-layer flow over topography. J. Fluid Mech., 146, pp. 127-167.
- Ball, F. K., 1960: Control of inversion height by surface heating. Quart. J. Roy. Meteor. Soc., 86, pp. 483-494.
- Banta, R. M., 1982: An observational and numerical study of mountain boundary-layer flow. Atmos Sci. Paper No. 350, Colo. State Univ., Fort Collins, CO, 203 pp.
- Banta, R. M., 1984: Daytime boundary layer evolution over mountainous terrain. Part 1: Observations of the dry circulations. Mon. Wea. Rev., 112, pp. 340-356.
- Banta, R., and W. R. Cotton, 1981: An analysis of the structure of local wind systems in a broad mountain basin. J. Appl. Meteor., 20, 1255-1266.
- Barr, S., and W. E. Clements, 1981: Nocturnal wind characteristics in high terrain of the Piceance Basin, Colorado. AMS Second Conf. on Mountain Meteor., Nov 9-12, 1981, Steamboat Springs, CO, Preprints, pp. 325-330.

- Bell, R. C., and R. O. R. Y. Thompson, 1980: Valley ventilation by cross winds. J. Fluid Mech., 96, pp. 757-767.
- Blackadar, A., 1957: Boundary layer wind maxima and their significance for the growth of nocturnal inversions. Bull. Amer. Meteor. Soc., 38, pp. 283-290.
- Blackadar, A. K., and H. Tennekes, 1968: Asymptotic similarity in neutral barotropic planetary boundary layers. J. Atmos. Sci., 25, pp. 1015-1020.
- Brost, R. A., and J. C. Wyngaard, 1978: A model study of the stably stratified planetary boundary layer. J. Atmos. Sci., 35, pp. 1427-1440.
- Buettner, K. J. K., and N. Thyer, 1966: Valley winds in the Mount Ranier area. Arch. Meteor. Geophys. Bioklim., B14, pp. 125-147.
- Businger, J. A., J. D. Wyngaard, Y. Izumi, and E. F. Bradley, 1971: Flux profile relationships in the atmospheric surface layer. J. Atmos. Sci., 28, pp. 181-189.
- Caughey, S. J., J. C. Wyngaard and J. C. Kaimal, 1979: Turbulence in the evolving stable layer. J. Atmos. Sci., 36, pp. 1041-1052.
- Cermak, J. E., 1984: Physical modeling of flow and dispersion over complex terrain. Bound.-Layer Meteor., 30, pp. 261-292.
- Chimonas, G., and J. R. Grant, 1984a: Shear excitation of gravity waves. Part 1: Modes of a two-scale atmosphere. J. Atmos. Sci., 41, pp. 2269-2277.
- Chimonas, G., and J. R. Grant, 1984b: Shear excitation of gravity waves. Part 2: Upscale scattering from K-H waves. J. Atmos. Sci., 41, pp. 2278-2288.
- Clark, T. L., 1977: A small-scale dynamic model using a terrain following coordinate transformation. J. Comput. Phys., 24, 186-215.
- Cotton, W. R., and G. J. Tripoli, 1978: Cumulus convection in shear flow--three dimensional numerical experiments. J. Atmos. Sci., 35, pp. 1503-1521.
- Davidson, B., 1961: Valley wind phenomena and air pollution problems. J. Air Poll. Cntl. Assoc., 11, pp. 364-368.
- Davidson, B., and P. K. Rao, 1958: Preliminary report on valley wind studies in Vermont, 1957. Final report, Contract AF19(604)-1971, AFCRC-TR-58-29, College of Engineering, New York University, 54 pp.
- Davidson, B., and P. K. Rao, 1963: Experimental studies of the valley-plain wind. Int. J. Air Water Pollut., 7, pp. 907-923.

- Defant, F., 1949: Zur theorie der hangwinde, nebst bemerkungen zur theorie der berg- und talwinde [A theory of slope winds, along with remarks on the theory of mountain winds and valley winds]. Arch. Meteor. Geophys. Bioklim., A1, pp. 421-450.
- Delage, Y., 1974: A numerical study of the nocturnal atmospheric boundary layer. Quart. J. Roy. Meteor. Soc., 100, pp. 351-364.
- Dickerson, M. H., and P. H. Gudiksen, 1980: The Department of Energy's atmospheric studies in complex terrain program. Preprints, AMS Second Joint Conf. Applications of Air Pollution Meteorology, New Orleans, LA, March 24-27, 1980, pp. 469-473.
- Dirks, R. A., 1969: A theoretical investigation of convective patterns in the lee of the Colorado Rockies. Atmos. Sci. Paper No. 145, Colo. State Univ., Fort Collins, CO, 122 pp.
- Doran, J. C., and T. W. Horst, 1981: Velocity and temperature oscillations in drainage winds. J. Appl. Meteor., 20, pp. 361-364.
- Doran, J. C., and T. W. Horst, 1983: Observations and models of simple nocturnal slope flows. J. Atmos. Sci., 40, pp. 708-717
- Dyer, A. J., and B. B. Hicks, 1970: Flux-gradient relationships in the constant flux layer. Quart. J. Roy. Meteor. Soc., 93, 501-508.
- Egger, J., 1981: Thermally forced circulations in a valley. Geophys. Astrophys. Fluid Dyn., 17, pp. 255-279.
- Einaudi, F., and J. J. Finnigan, 1981: The interaction between an internal gravity wave and the planetary boundary layer. Part I: The linear analysis. Quart. J. Roy. Meteor. Soc., 107, pp. 793-806.
- Ekhart, E., 1944: Beitrage zur alpinen meteorologie [Contributions to alpine meteorology]. Meteorologische Zeitschrift, 61(7), pp. 217-231.
- Ekhart, E., 1948: De la structure thermique de l'atmosphere dan la montagne [On the thermal structure of the mountain atmosphere]. La Meteorologie, 4(9), pp. 3-26.
- Ekman, V. W., 1927: Eddy-viscosity and skin-friction in the dynamics of winds and ocean-currents. Memoirs of the Royal Meteor. Soc., 2, No. 20.
- Eymard, L., and A. Weill, 1979: A study of gravity waves in the planetary boundary layer by acoustic sounding. Bound.-Layer Meteor., 17, pp. 231-245.
- Finnigan, J. J., and F. Einaudi, 1981: The interaction between an internal gravity wave and the planetary boundary layer. Part II: Effert of the wave on the turbulence structure. Quart. J. Roy. Meteor. Soc., 107, pp. 807-832.

- Finnigan, J. J., F. Einaudi, and D. Fau, 1984: The interaction between an internal gravity wave and turbulence in the stably-stratified nocturnal boundary layer. J. Atmos. Sci., 41, pp. 2409-2436.
- Fitzjarrald, D. R., 1984: Katabatic wind in opposing flow. J. Atmos. Sci., 41, pp. 1143-1158.
- Fleagle, R. G., 1950: A theory of air drainage. J. Meteor., 7, pp. 227-232.
- Gal-Chen, T., and R. C. J. Somerville, 1975a: On the use of a coordinate transformation for the solution of the Navier-Stokes equations. J. Comp. Physics, 17, pp. 209-228.
- Gal-Chen, T., and R. C. J. Somerville, 1975b: Numerical solution of the Navier-Stokes equations with topography. J. Comp. Physics, 17, pp. 276-310.
- Garratt, J. R., and R. A. Brost, 1981: Radiative cooling effects within and above the nocturnal boundary layer. J. Atmos. Sci., 38, pp. 2730-2746.
- Garrett, A. J., 1983: Drainage flow prediction with a one-dimensional model, canopy, soil and radiation parameterization. J. Climate Appl. Meteor., 22, pp. 79-91.
- Gleeson, T. A., 1953: Effects of various factors on valley winds. J. Meteor., 10, pp. 262-269.
- Gudiksen, P. H., 1985: Categorization of nocturnal drainage flows within the Brush Creek Valley in western Colorado and the variability of sigma theta in complex terrain. Report UCID-20414. University of California-Lawrence Livermore National Laboratory, 20 pp.
- Hanna, S. R., 1969: The thickness of the planetary boundary layer. Atmos. Environ., 3, pp. 519-536.
- Heywood, G. S. P., 1933: Katabatic winds in a valley. Quart. J. Roy. Meteor. Soc., 59, pp. 47-59.
- Holton, J. R., 1977: An Introduction to Dynamic Meteorology. Academic Press, New York, NY, 319 pp.
- Holzworth, G. C., and R. W. Fisher, 1979: Climatological summaries of the lower few kilometers of rawinsonde observations. U.S. Environmental Protection Agency, Environmental Sciences Research Laboratory, Research Triangle Park, NC, 141 pp.
- Hootman, B. W., and W. Blumen, 1983: Analysis of nighttime drainage winds in Boulder, Colorado during 1980. Mon. Wea. Rev., 111, 1052-1061.

- Howard, L. N., 1961: Comment on a paper of John W. Miles. J. Fluid Mech., 10, pp. 509-512.
- Hunt, J. C. R., and W. H. Snyder, 1980. Experiments on stably and neutrally stratified flow over a model three-dimensional hill. J. Fluid Mech., 96, 4, pp. 671-704.
- Kaimal, J. C. (ed.), 1983: Studies of nocturnal stable layers of BAO. Report No. 4, NOAA Boulder Atmospheric Observatory, Boulder, CO, 129 pp.
- Kao, T. W., 1965: The phenomenon of blocking in stratified flow. J. Geophys. Res., 70, pp. 815-822.
- Kao, K.S., and H. F. Snodgrass, 1981: A nonstationary nocturnal drainage flow model. Bound.-Layer Meteor., 20, pp. 309-320.
- Kazanski, A. B., and A. S. Monin, 1961: On the dynamical interaction between the atmosphere and the earth's surface. Bull Acad. Sci. USSR, Ser. Geophys., 5, pp. 786-788.
- Kitabayashi, K., 1977: Wind tunnel and field studies of stagnant flow upstream of a ridge. J. Meteor. Soc. Japan, 55, pp. 193-203.
- Klemp, J. B., and R. B. Wilhelmson, 1978: The simulation of three-dimensional convective storm dynamics. J. Atmos. Sci., 35, pp. 1070-1096.
- Lee, J. T., S. Barr, R. E. Lawson, Jr., W. H. Snyder, and G. L. Marsh, 1984: Towing tank studies of stratified flow over ridges and valleys. Preprints, Third AMS Conference on Mountain Meteorology, 16-19 October 1984, Portland, OR, pp. 37-41.
- Lenschow, D. H., and P. L. Stephens, 1980: The role of thermals in the convective boundary layer. Bound.-Layer Meteor., 19, pp. 511-532.
- Lilly, D. K., 1968: Models of cloud-topped mixed layers under a strong inversion. Quart. J. Roy. Meteor. Soc., 94, pp. 292-309.
- Long, R. R., 1955: Some aspects of the flow of stratified fluids. Part III. Continuous density gradients. Tellus, 7, pp. 341-357.
- Louis, J., 1979: A parametric model of vertical eddy fluxes in the atmosphere. Bound.-Layer Meteor., 17, pp. 187-202.
- Mahrt, L., 1981: Modeling the depth of the stable boundary layer. Bound.-Layer Meteor., 21, pp. 3-19.
- Mahrt, L., J. C. Ande, and R. C. Heald, 1982: On the depth of the nocturnal boundary layer. J. Appl. Meteor., 21, pp. 90-92.
- Mahrt, L., R. C. Heald, D. H. Lenschow, B. B. Stankov, and I. Troen, 1979: An observational study of the nocturnal boundary layer. Bound.-Layer Meteor., 17, pp. 247-264.

- McBean, G. A. (ed), 1979: The planetary boundary layer. Technical note 165. WMO-530, World Meteor. Organization, 201 pp.
- McNider, R. T., 1982: A note on velocity fluctuations in drainage flows. J. Atmos. Sci., 39, pp. 1658-1660.
- McNider, R. T., and R. Arritt, 1984: Transferability of critical dividing streamline models to larger scale terrain. Preprints, Third AMS Conference on Mountain Meteorology, 16-19 October 1984, Portland, OR, pp. J25-J27.
- Melgarejo, J. W., and J. W. Deardorff, 1974: Functions for the boundary layer resistance laws based on observed boundary layer heights. J. Atmos. Sci., 31, pp. 1324-1333.
- Mellor, G. L., and T. Yamada, 1982: Development of a turbulence closure model for geophysical fluid problems. Rev. of Geophysics and Space Phys., 20, pp. 851-875.
- Mellor, G. L., and T. Yamada, 1984: A hierarchy of turbulence closure models for planetary boundary layers. J. Atmos. Sci., 31, pp. 1791-1806.
- Merrill, J. T., 1977: Observational and theoretical study of shear instability in the airflow near the ground. J. Atmos. Sci., 34, pp. 911-921.
- Miles, J. W., 1961: On the stability of heterogeneous shear flows. J. Fluid Mech., 10, pp. 496-508.
- Moll, E., 1935: Aerologische untersuchung periodischer gebirgswinde in V-formigen alpentälern. Beitr. Physik fr. Atmos., 22, pp. 177-197.
- Monin, A. S., and A. M. Yaglom, 1971: Statistical Fluid Mechanics: Mechanics of Turbulence, Vol. 1. The MIT Press, Cambridge, MA, 769 pp.
- Neff, W. D., 1983: Personal communication.
- Nieuwstadt, F. T. M., 1981: The steady state height and resistance laws of the nocturnal boundary layer: theory compared with Cabauw observations. Bound.-Layer Meteor., 20, pp. 3-17.
- Nieuwstadt, F. T. M., and A. G. M. Driedonks, 1979: The nocturnal boundary layer: a case study compared with model computations. J. Appl. Meteor., 18, pp. 1397-1405.
- Nieuwstadt, F. T. M., and H. Tennekes, 1981: A rate equation for the nocturnal boundary layer height. J. Atmos. Sci., 38, pp. 1418-1428.
- Orlanski, I., 1975: A rational subdivision of scales for atmospheric processes. Bull. Amer. Meteor. Soc., 56, pp. 527-530.

- Orlanski, I., 1976: A simple boundary condition for unbounded hyperbolic flows. J. Comp. Physics, 21, pp. 251-269.
- Orville, H. D., 1964: On mountain upslope winds. J. Atmos. Sci., 21, pp. 622-633.
- Panofsky, H. A., and J. A. Dutton, 1984: Atmospheric Turbulence. John Wiley and Sons, New York, 397 pp.
- Pielke, R. A., 1984: Mesoscale numerical modeling. Academic Press, Orlando, FL, 612 pp.
- Prandtl, L., 1942: Flow Theory. Verlay Vieweg and Sohn, Brunswick, pp. 367-375.
- Raymond, D., and W. Wilkening, 1980: Mountain-induced convection under fair weather conditions. J. Atmos. Sci., 37, pp. 2693-2706.
- Rossby, C. G., and R. B. Montgomery, 1935: The layer of frictional influence n wind and ocean currents. Papers Phys. Oceanogr. Meteor., MIT and Woods Hole Oceanogr. Inst., 3, 101 pp.
- Start, G. E., C. R. Dickson, and L. L. Wendell, 1975: Diffusion in a canyon within rough mountainous terrain. J. Appl. Meteor., 14, pp. 333-346.
- Stull, R. B., 1973: Inversion rise model based on penetrative convection. J. Atmos. Sci., 30, pp. 1092-1099.
- Stull, R. B., 1983a: A heat flux history length scale for the nocturnal boundary layer. Tellus, 35A, pp. 219-230.
- Stull, R. B., 1983b: Integral scales for the NBL: Part I, Empirical depth relationships. J. Climate Appl. Meteor., 22, pp. 673-686.
- Tang, W., 1976: Theoretical study of cross-valley wind circulation. Arch. Meteor. Geophys. Bioklimat., A25, pp. 1-18.
- Tennekes, H., 1973: A model for the dynamics of the inversion above a convective boundary layer. J. Atmos. Sci., 30, pp. 558-567.
- Thorpe, S. A., 1973: Turbulence in stably stratified fluids: A review of laboratory experiments. Bound.-Layer Meteor., 5, pp. 95-119.
- Thyer, N. H., 1966: A theoretical explanation of mountain and valley winds by a numerical method. Arch. Meteor. Geophys. Bioklimat., A15, pp. 318-348.
- Tremback, C., G. J. Tripoli, and W. R. Cotton, 1985: A comparison between a hydrostatic and non-hydrostatic compressible numerical model in several mesoscale simulations. In preparation.

- Tripoli, G. J., and W. R. Cotton, 1980: A numerical investigation of several factors contributing to the observed variable intensity of deep convection over south Florida. J. Appl. Meteor., 19, pp. 1032-1063.
- Tripoli, G. J., and W. R. Cotton, 1982: The Colorado State University three-dimensional cloud/mesoscale model--1981. Part 1: General theoretical framework and sensitivity experiments. J. Rech. Atmos., 16, pp. 185-219.
- von Karman, T., 1930: Mechanische ahnlichkeit und turbulenz. Nachrichten von der Gesellschaft der Wissenschaften zu Gottingen, Math.-Phys. Klasse, Heft I, pp. 58.
- Wagner, A., 1938: Theorie und beobachtung der periodischen gebirgswinde [Theory and observation of periodic mountain winds], Gerlands Beitr. Geophys., 52, pp. 408-449.
- Warner, J., and J. W. Telford, 1967: Convection below cloud base. J. Atmos. Sci., 24, pp. 374-382.
- Wenger, R., 1923: Zur theorie des berg- und talwindes [Theory of the mountain and valley wind.]. Meteor. Z., 193.
- Wetzel, P. J., 1982: Toward parameterization of the stable boundary layer. J. Appl. Meteor., 21, pp. 7-13.
- Whiteman, C. D., 1980: Breakup of temperature inversions in Colorado mountain valleys. Atmospheric Science Paper No. 328, Colo. State Univ., Fort Collins, CO, 250 pp.
- Whiteman, C. D., 1982: Breakup of temperature inversions in deep mountain valleys. Part 1. Observations. J. Appl. Meteor., 21, 270-289.
- Whiteman, C. D., 1985: Personal communication.
- Whiteman, C. D., and E. Dreiseitl, 1984: Alpine Meteorology: Translations of classic contributions by A. Wagner, E. Ekhardt, and F. Defant. Pacific Northwest Laboratory, PNL-5141, ASCOT-84-3, Richland, WA, 121 pp.
- Whiteman, C. D., A. H. Huber, R. W. Fisher, and B. D. Zak, 1984: Atmospheric tracer experiments in a deep narrow valley. Preprint, Third AMS Conference on Mountain Meteorology, 16-19 October, 1984, Portland, OR, pp. J1-J4.
- Whiteman, C. D., and T. B. McKee, 1977: Observations of vertical atmospheric structure in a deep mountain valley. Arch. Meteor. Geophys. Bioklim., A26, pp. 39-50.
- Wyngaard, J. C., 1975: Modeling the planetary boundary layer -- extension to the stable case. Bound.-Layer Meteor., 9, pp. 441-460.

- Yamada, T., 1979: Prediction of the nocturnal surface inversion height. J. Appl. Meteor., 18, pp. 526-531.
- Yamada, T., 1983: Simulations of nocturnal drainage flows by a  $q^2$  turbulence closure model. J. Atmos. Sci., 40, pp. 91-106.
- Yu, T.-W., 1978: Determining the height of the nocturnal boundary layer. J. Appl. Meteor., 17, pp. 28-33.
- Zeman, O., 1979: Parameterization of the dynamics of stable boundary layers and nocturnal jets. J. Atmos. Sci., 36, pp. 792-804.
- Zilintekevich, S. S., 1972: On the determination of the height of the Ekman boundary layer. Bound.-Layer Meteor., 3, pp. 141-145.
- Zilitinkevich, S. S., 1975: Resistance laws and predictive equations for the depth of the planetary boundary layer. J. Atmos. Sci., 32, pp. 741-752.
- Zilitinkevich, S. S., and J. W. Deardorff, 1974: Similarity theory for the planetary boundary layer of time-dependent height. J. Atmos. Sci., 31, pp. 1449-1452.

## APPENDIX I

### ROSSBY SIMILARITY IN THE ATMOSPHERIC BOUNDARY LAYER

Dynamic similarity analysis is an important tool used to theoretically describe properties of fluid turbulence. Its basic premise is that fluid properties can be non-dimensionalized using appropriate scaling parameters so that a single theory can be used to cover a wide variety of observed behavior provided that the dominant forcing mechanisms are dynamically similar. The scaling parameters must be chosen to reflect this restriction. Modern atmospheric boundary layer (ABL) similarity theories stem from the two layer model first proposed by Rossby and Montgomery (1935) for neutral, stationary and barotropic flow. In that paper, it was proposed that the velocity structure of the ABL could be determined from three externally specified parameters, the geostrophic wind speed,  $G$ , the surface roughness height,  $z_0$ , and the Coriolis parameter,  $f$ . These three parameters form a non-dimensional quantity known as the surface Rossby number defined by

$$R_0 = \frac{Gf}{z_0} . \quad (I.1)$$

This theory has since been revised and updated by Kazanski and Monin (1962) and Blackadar and Tennekes (1968).

From Blackadar and Tennekes, the equations for neutral barotropic boundary layer flow in the northern hemisphere can be written as

$$f(v-v_g) + \frac{d}{dz} \overline{u'w'} = 0 , \quad (I.2)$$

$$-f(u-u_g) + \frac{d}{dz} \overline{v'w'} = 0 \quad (\text{I.3})$$

with the boundary conditions  $\overline{u'w'} = u_*^2$ ,  $\overline{v'w'} = 0$ , and  $u = v = 0$  at  $z = z_0$  and  $\overline{u'w'} = \overline{v'w'} = 0$  at  $z = h$ , the top of the ABL. The ABL is divided into two layers, an inner or surface layer encompassing the lowest few percent and an outer or Ekman layer extending from the top of the surface layer to  $h$ . In the surface layer, the frictional effects are the strongest and the flow is maintained by the momentum flux to the surface through the layer. Consequently, it is appropriate for velocities to be scaled by  $u_*$  and heights by  $z_0$ . In the outer layer, the flow field approaches geostrophic balance with increasing height, losing all boundary effects at  $h$ . However, the frictional influence of the underlying surface is still significant through the depth of the ABL. Therefore, the appropriate scaling parameters are  $h$  for heights and  $u_*$  for velocities. Since  $h$  is proportional to  $u_*/f$ , this parameter can be used in its place.

Using Prandtl's surface layer theory which assumes that  $h \gg z_0$  and that the surface layer wind does not turn with height, I.2 can be rewritten in non-dimensional form for the surface layer as

$$\frac{u}{u_*} = f_x \left( \frac{z}{z_0} \right) \quad (\text{I.4})$$

After scaling I.2 and I.3, the outer layer equations are

$$\frac{u-u_g}{u_*} = F_x \left( \frac{zf}{u_*} \right) \quad (\text{I.5})$$

$$\frac{v-v_g}{u_*} = F_y \left( \frac{zf}{u_*} \right) \quad (\text{I.6})$$

In the solution of the two-layer model, the solutions to  $F_x$  and  $f_x$  must approach the same asymptotic value in the double limit  $z/h \rightarrow 0$  and  $z/z_0 \rightarrow \infty$ . Likewise,  $F_y$  must asymptotically approach 0 in the same double limit. From Blackadar and Tennekes, solutions meeting this requirement are Prandtl's equation for the surface layer,

$$\frac{u}{u_*} = \frac{1}{k} \ln \frac{z}{z_0} \quad (1.7)$$

and

$$\ln R_0 = A - \ln \frac{u_*}{G} + \left( \frac{k^2 G^2}{u_*^2} - B^2 \right)^{1/2}, \quad (1.8)$$

$$\sin \alpha = \frac{B}{k} \frac{u_*}{G} \quad (1.9)$$

for the outer layer; A and B are universal constants and  $\alpha$  is the angle between the surface layer and geostrophic wind directions. Equation 1.7 is the well known surface layer "constant stress" or logarithmic profile. The outer layer solutions do not define the shape of the universal functions  $F_x$  and  $F_y$ , which must be determined experimentally, but they do quantify the effect of the underlying surface on the geostrophic wind from the externally defined parameters. It should be noted that in the Soviet and European literature, the constants A and B are reversed, an unfortunate consequence of independently conducted research.

Diabatic extensions to Rossby similarity apply similar methods to match the solutions in the surface layer to those in the outer layer when a turbulent heat flux is also present through the ABL. For this purpose, Monin-Obukhov similarity is used in the surface and outer layers (Zilitinkevich and Deardorff, 1974). In the surface layer, the non-dimensional wind shear  $\phi_M$  and potential temperature gradient  $\phi_H$  defined by

$$\phi_M = \frac{kz}{u_*} \frac{du}{dz} , \quad (I.10)$$

$$\phi_N = \frac{kzu_*}{\overline{w'\theta'_s}} \frac{d}{dz} \quad (I.11)$$

are universal functions of  $z/L$  where  $L$  is the Monin-Obukhov length. Businger et al. (1971) and Dyer and Hicks (1970) have independently determined the form of these functions from experimental data. In the outer layer, I.8 and I.9 are still valid, but  $A$ ,  $B$ ,  $F_x$  and  $F_y$  are functions of the stability parameter ( $u_*/fL$ ). Additionally, a third equation is necessary for the outer layer to describe the non-dimensional turbulent heat flux,

$$\frac{\theta(z) - \theta(h)}{\theta_*} = \frac{1}{k} F_\theta \left( R_o, \frac{u_*}{fL} \right) , \quad (I.12)$$

where  $\theta_* = \overline{w'\theta'_s}/u_*$ . Integration of I.12 yields an expression for the bulk potential temperature gradient,

$$\frac{\theta(h) - \theta(z_o)}{\theta_*} = \frac{1}{k} \left[ \ln \frac{u_*}{fz_o} - C \left( \frac{u_*}{fL} \right) \right] . \quad (I.13)$$

Values of the functions  $A$ ,  $B$  and  $C$  have been determined experimentally by several authors and are summarized in McBean (1979).

Rossby similarity breaks down when the assumptions inherent in its formulation are no longer valid, which is most often the situation. For example, Rossby similarity does not describe very convective or very stable boundary layers, situations in which the velocity scaling parameter  $u_*$  is no longer appropriate. Similarity theory is also incapable of describing the time dependent behavior of non-stationary

and inhomogeneous flow fields. However, Rossby similarity does form the basis for the development of ABL theory and therein is found its importance.

## APPENDIX II

### MODEL SENSITIVITY EXPERIMENTS

In addition to the two sensitivity experiments described in Chapter IV, simulations were executed to test the initialization procedure, the turbulence parameterization and the grid spacing to guarantee that the model was producing physically consistent solutions. The test of the initialization procedure consisted of a 4 h simulation using the short plain with no surface heating or cooling. Subsequently, three simulations with differing terrain configurations and turbulence closures were run to check the performance of the turbulence parameterization. Finally, a single simulation was run to determine the differences produced by doubling the grid spacing in a two-dimensional simulation prior to the execution of the course grid three-dimensional simulations described in Chapter IV.

#### A. Test of Model Initialization Procedure

For the test of the initialization procedure, the Case 2 simulation was continued for 4 h with no heating following the 1 h initialization period. The model fields at the start and the end of the 4 h test simulation are shown in Figure II.1 for comparison. Wind speeds in the lowest layer increased slightly from  $1.5 \text{ m s}^{-1}$  to  $1.6 \text{ m s}^{-1}$  over the flat and sloping plains. Since lower level wind speeds increased with increasing elevation, it was difficult to discern any change that occurred during the 4 h simulation, but speeds appeared to

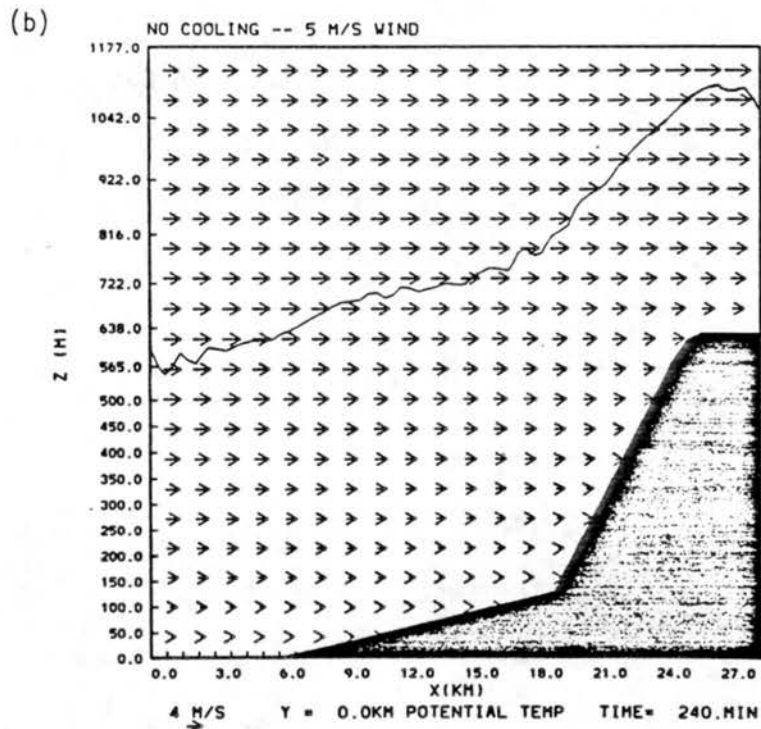
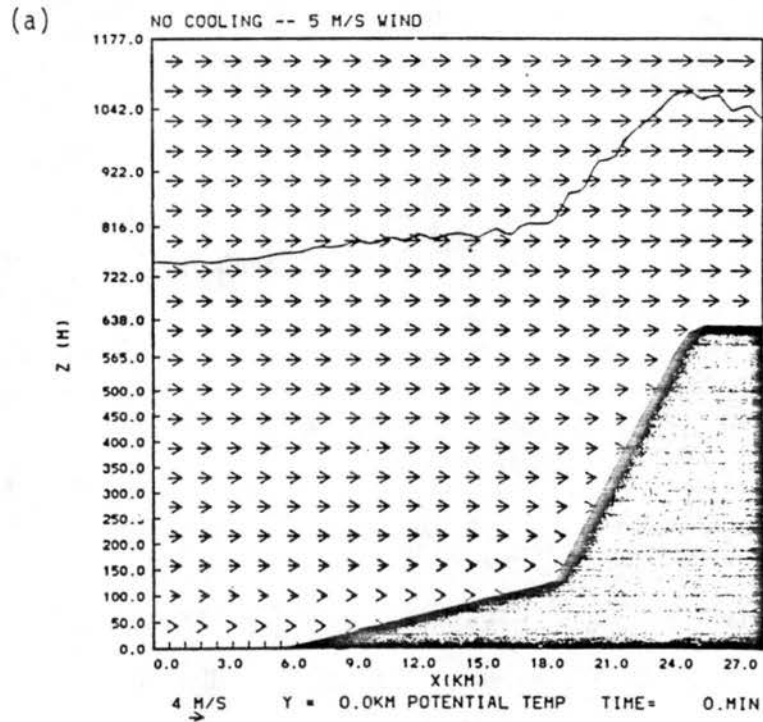


Figure II.1. Wind and potential temperature fields for initialization test case (contour interval - 1 K) for (a) after initialization and (b) 4 h after initialization.

be  $0.0-0.1 \text{ m s}^{-1}$  higher at the end of the run. Between 200 m AGL and 500 m AGL at any location, the wind speeds decreased  $0.0-0.1 \text{ m s}^{-1}$  over the same time period. Above 500 m AGL, the wind speed differences were less than  $0.2 \text{ m s}^{-1}$  in magnitude and random in sign. Likewise, the potential temperature deviations throughout the domain were less than  $0.2 \text{ K}$  with no systematic change in sign. Based upon these results, it was determined that the 45 min adjustment period following the imposition of winds at the external boundaries was sufficient to allow the model to achieve a steady-state structure.

#### B. Tests of Turbulence Closure

In addition to the Case 2 simulation described in Chapter IV, three model simulations were performed to test both the diagnostic turbulence closure used in previous studies (Bader and McKee, 1983, 1985; Banta, 1982) and the Yamada scheme which was used in the present study. Results from the diagnostic scheme test showed that the solution was inadequate in stable regimes. Sub-grid scale fluxes were strongly suppressed by the slightest degree of static stability, resulting in an underestimation of downward turbulent transports of heat and momentum. Despite the presence of vertical wind shears on the order of  $10^{-1} - 10^{-2} \text{ s}^{-1}$  in a layer with a lapse rate of only  $0.002 \text{ K m}^{-1}$ , the sub-grid scale fluxes remained near the values produced by the arbitrarily specified minimum mixing coefficient. The failure of the parameterization to suppress the very small wavelength features compounded by the dynamical forcing of the terrain resulted in the production of growing numerical instabilities appearing in the solution after 2 h. Consequently, one should have little confidence in this

parameterization except in the strongly convective cases for which it was designed.

Although the Yamada scheme performed satisfactorily in Case 2, two additional model simulations were executed to ascertain whether the scheme was overly diffusive in stable lapse rates when used with the model configuration employed in this study. In the first case, the terrain was removed from the model and a simulation was executed with an identical initialization procedure and surface cooling function as were used in the Case 2 simulation. At sunset, the boundary layer was well mixed with a potential temperature ranging from 314.6 K near the surface to 315.2 K at 1400 m AGL. Wind speeds followed the externally imposed profile with  $u_0 = 5 \text{ m s}^{-1}$ . After 4 h, the surface cooling had produced a strong 14 K surface based inversion extending to 175 m AGL topped by a 50 m deep transition layer lying between it and the overlying mixed layer. Wind speeds in the lowest model layer decreased from  $1.1 \text{ m s}^{-1}$  to  $-0.5 \text{ m s}^{-1}$ , however wind speeds in the higher levels changed less than  $0.2 \text{ m s}^{-1}$  with a slight deceleration found in the inversion layer and a small acceleration found in the mixed layer. Considering the course grid resolution, the model realistically simulated the NBL development and was not overly diffusive.

The second test of the Yamada scheme consisted of reversing the initial wind direction and repeating the Case 2 simulation. In such a configuration, the model should produce mountain wave features and thereby provide a good test of the horizontal diffusion in the model. Although the model was not configured to produce a realistic simulation of mountain waves, the simulated structure consisted of a standing wave typical of downslope windstorms associated with mountain waves.

Figure II.2a shows the initial state of the model following the 1 h initialization period. The relatively high wind speeds (over  $12 \text{ m s}^{-1}$ ) above the high plateau have produced a hydraulic jump on the lee side of the slope with a small separated stagnant zone over the lower part of the sloping plain. Four hours of surface cooling resulted in the structure appearing Figure II.2b. The increased stability produced by the cooling has intensified the standing wave and formed a three layer vertical structure over the flat and sloping plains. Since the flow was decoupled from the overlying winds at sunset, an inversion had formed in response to the surface cooling. A nearly neutral layer laid between the top of the inversion at 225 m AGL and the base of the standing wave at 400 m AGL. From this solution it was concluded that the Yamada scheme successfully preserved the dominant structures and did not diffuse the larger scale horizontal features.

### C. Test of Horizontal Grid Spacing

Since the three-dimensional simulations required the doubling of the horizontal grid spacing and the small timestep, the Case 2 simulation was repeated using a 750 m grid spacing and a 1:6 time-step ratio to test the model's performance in the coarse resolution configuration. Figure II.3a shows the simulated structure 4 h after sunset. The surface inversion layer extended to 275 m AGL over the flat and sloping plains which is surmounted by a 100 m deep quasi-isothermal transition layer. Overlying the 0.5 m s drainage flow in the lowest layer was 100 m deep easterly thermal circulation with speeds of  $2.3 \text{ m s}^{-1}$  at 75 m AGL and  $0.1 \text{ m s}^{-1}$  at 125 m AGL as compared to  $1.7 \text{ m s}^{-1}$  and  $0.6 \text{ m s}^{-1}$  speeds found at the same elevations in the

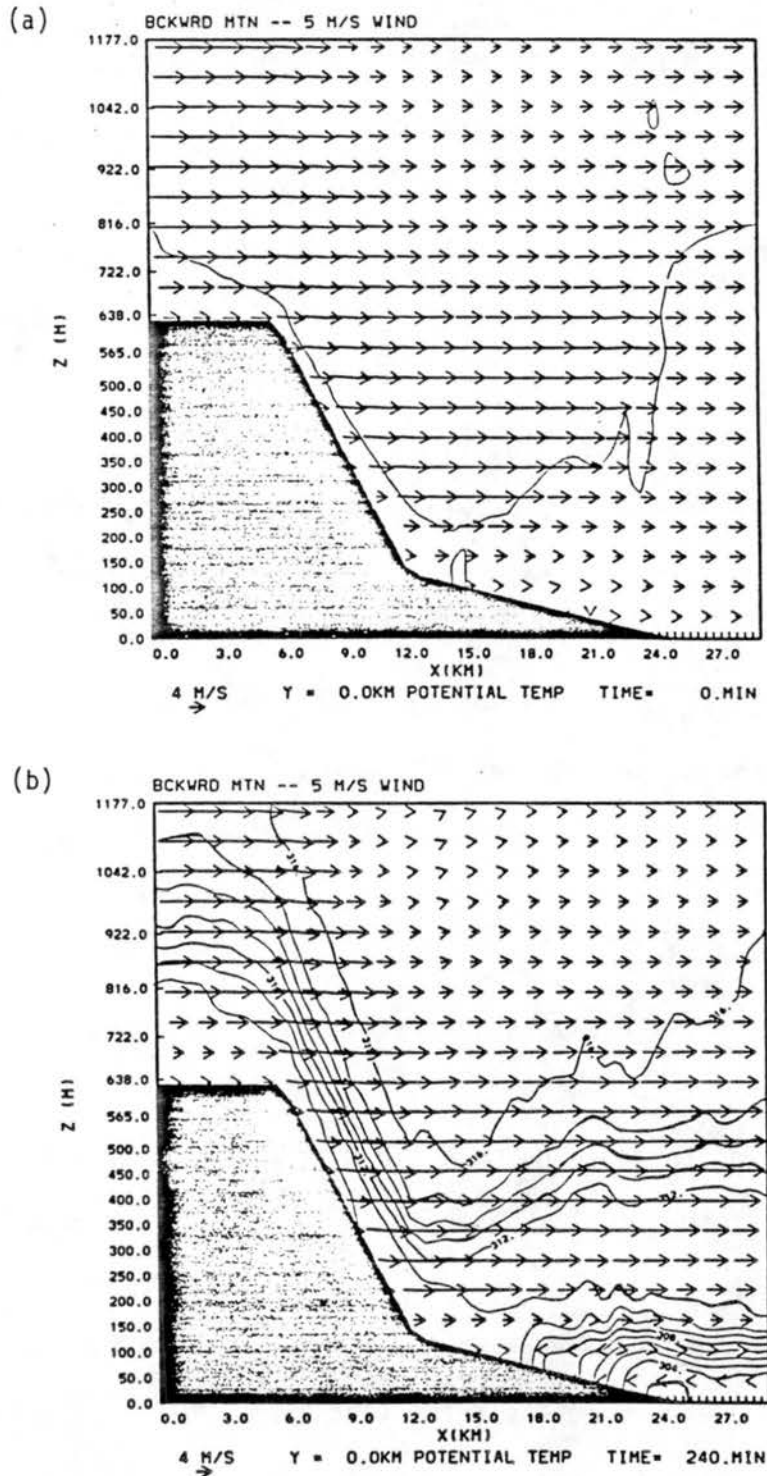


Figure II.2. Wind and potential temperature fields for reversed topography turbulence scheme test case (contour interval - 1 K) for (a) at sunset and (b) 4 h after sunset.

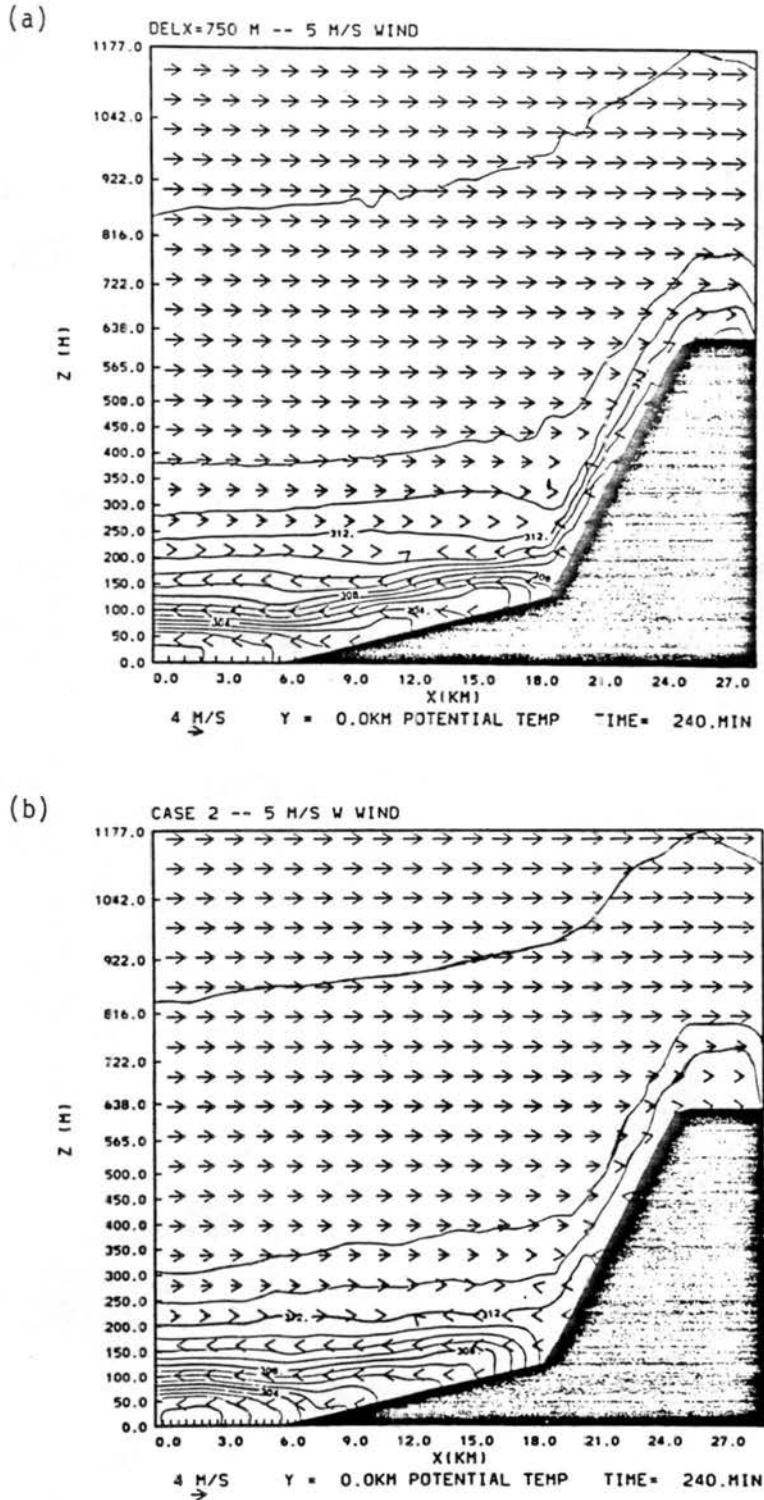


Figure II.3. Wind and potential temperature fields 4 h after sunset (contour interval - 1 K) for (a) 750 m grid spacing test case and (b) Case 2.

Case 2 experiment (Figure II.3b). Also like the Case 2 simulation, strong shears were present through the transition layer which continued to mix the cold air vertically and slowly deepened the transition layer. The stable layer depth decreased with increasing surface elevation with differences in simulated lapse rates between the Case 2 and coarse resolution solutions being negligible. However, systematic temperature differences of  $-0.5$  K were noticed in the lower layers of the coarse resolution results. Despite these deviations, it was determined that the coarse resolution configuration adequately reproduced the boundary layer structure found in the Case 2 results.

1. Geographic Data T	1. Report No. Atmospheric Science Paper No. 396	2.	3. Recipient's Accession No.
4. Title and Subtitle Mesoscale Boundary Layer Development over Mountainous Terrain		5. Report Date November 1985	6.
7. Author(s) David C. Bader		8. Performing Organization Report No. 396	
9. Performing Organization Name and Address Department of Atmospheric Science Colorado State University Fort Collins, CO 80523		10. Project/Task/Work Unit No.	
		11. Contract/Grant No. ATM83-04328	
12. Sponsoring Organization Name and Address NSF Washington, DC		13. Type of Report & Period Covered	
		14.	

15. Supplementary Notes  
Principal Investigator: Thomas B. McKee

16. Abstracts  
The diurnal evolution of the mesoscale boundary layer (~50km) over gently sloping terrain upwind of a high mountain barrier is described using both observational data and results from numerical model simulations. Atmospheric sounding data are presented from two nights, one during the summer and the second during the winter, when the mesoscale nocturnal boundary layer development was observed. Subsequently, a series of two and three-dimensional numerical model experiments are presented which identify the important physical processes responsible for the observed features. A conceptual model of mesoscale boundary layer evolution is then presented that accounts for the principle dynamic mechanisms discerned from analysis of the observational and simulated cases.

17. Key Words and Document Analysis. 17a. Descriptors  
complex terrain  
boundary layer  
numerical modeling

18. Identifiers/Open-Ended Terms

19. COSATI Field/Group

Availability Statement Available at no cost until supply runs out, then available at .15/page	19. Security Class (This Report) UNCLASSIFIED	21. No. of Pages 251
	20. Security Class (This Page) UNCLASSIFIED	22. Price